Numerical Modelling of Surface Subsidence Induced by Underground Coal Gasification

by Yury Derbin, MSc

Thesis submitted to the University of Nottingham
for the degree of Doctor of Philosophy, January 2018

Abstract

Underground coal gasification (UCG) is an alternative method of energy extraction from coal. This method has significant advantages over traditional coal mining. Because the coal is combusted in situ, there is no need for underground labour and the environmentally unfriendly products of burning remain underground. The method can be applied to the coal seam of poor quality and deep underground where traditional mines would not be profitable. Although the method has been known for a century, there are only a few projects that exist on an industrial scale. One of the obstacles of UCG implementation is surface subsidence, which can damage infrastructure, UCG equipment and boreholes. To organize UCG in the most efficient way, the surface subsidence should be predicted.

This work shows that none of the popular constitutive models can predict surface subsidence correctly. To demonstrate, investigate, and find the reasons of the incorrect predictions, the surface subsidence after an uncontrolled collapse of the traditional Longwall mine in Naburn, UK is modelled. The surface subsidence is assumed as a plain problem in the commercial finite-difference software FLAC3D by Itasca. The 2D problem is modelled in the 3D software to demonstrate that FLAC3D's results can be improved for two dimensions before extending the model to three dimensions.

Before developing the model, the method of deriving elastic stiffness, friction angle, cohesion, and tensile strength from the boreholes description is developed and described in detail. FLAC3D's embedded Mohr-Coulomb, modified Hoek-Brown and strain-softening constitutive models are implemented to model behaviour of the rock. The simulations of the collapse of the conventional mine indicate two possible reasons of the poor performance of the model, i.e. mesh density and constitutive models. It is noticed that the results depend on mesh density. The detailed mesh analysis is carried out to eliminate the first reason of poor model performance and to recommend some optimal mesh for modelling surface subsidence at a UCG station.

To eliminate the second reason of the poor model performance, the more advanced constitutive model is recommended. Historically, the double-yield model is utilized in the goaf; however, this model fails to predict the behaviour of the goaf. In an attempt to improve predictions, the built-in modified Cam-clay model, which employs the Critical State concept, is implemented. The model results are closer to the expectations. Since the Critical State model improves the result, CASM and the bubble model are programmed. Both of the models can replicate the modified Cam-clay model under certain conditions for their validation . The programming is started from the elastic, isotropic model, then the von Mises, Drucker-Prager, Tresca, and Mohr-Coulomb models are coded.

After validation, CASM and the bubble model are implemented to simulate the clay overburden of the Shatsk UCG station in the Moscow basin. The UCG features, such as ash left in the UCG reactor, the complicated geometry of the UCG reactor, thermal stresses are also considered. The simulations show that CASM (Yu, 1998) and the modified Cam-clay predictions coincide. At the same time, the bubble model (Al-Tabbaa and Wood, 1989) results agree much better with the field measurement.

Acknowledgements

The research described in this Thesis was carried out at the University of Nottingham Ningbo China (UNNC) during the period from March 2013 to December 2017. This work was to a great extent made possible thanks to financial support from the Nottingham University and a grant from the State Key Laboratory for Geomechanics and Deep Underground Engineering of the China University of Mining and Technology (CUMT).

First and foremost, I thank my supervisor, Dr James Walker, for inspiration, encouragement, and guidance throughout this research. My PhD journey was colorful and thrilling due to Dr James Walker. It was a great story of the constantly repeating periods of challenges and success in the British transnational campus of the University of Nottingham. Dr James Walker showed me how to survive and improve the transnational education by knowing and precisely following policies.

I am also very grateful to my other supervisors, Dr Alec M Marshall and Dr Dariusz Wanatowski, for their advice and financial support.

My thanks go to all my friends, colleagues, and teachers.

I am indebted to Dr Juan Wang for her help with technical Chinese translations.

My thanks are extended to Dr Richard Hoban, Dr Paul Dempster, and Dr Matthew Pike for giving me opportunities to gain practice of teaching at the British University and earn some money for my PhD study.

I am grateful Giovanna Comerio for her friendship.

My special appreciations go to $\boxed{\text{Dr Vadim Kuzmin}}$ who was the head of the State Hydrological Institute in Saint Petersburg, Candidate for Master of Sport in freediving, and talented shot-story writer for his support, cheerfulness, and example of a strong and courage man.

Exclusively, I wish to thank my friend, Liphapang Khaba, for his support during all my hard work at the University and for his proofreading of this Thesis.

My warm thanks go to the librarians of the largest library in Russia, Russian State Library in Moscow, and very special thanks go to the librarians of the unique National Library of Russia in Saint Petersburg for providing me the old and valuable literature.

Last but not least, I would like to thank my grandparents, $\boxed{\text{Nina Derbina}}$, $\boxed{\text{Oleg Derbin}}$, $\boxed{\text{Lydia Vasilieva}}$, and $\boxed{\text{Konstantin Vasiliev}}$. The great thankfulness is extended to my parents, Galina Derbina and German (Herman) Derbin. I thank them simply for everything.

Contents

List of Figures

List of Tables

Chapter 1

Introduction

1.1 UCG, Surface Subsidence, FLAC

Despite the slight reduction of recent coal consumption, coal has regained its position as a main energy source in the 21st century (BP, 2017). According to Kavalov and Peteves (2007), the increased interest in coal is a result of three salient factors of coal:

- wider geopolitical distribution of reserves;
- a higher reserves-to-production ratio; and
- lower price per energy unit over oil and gas.

However, speaking about traditional coal mining, many challenges appear, such as miners' safety, deep and poor quality seams, and serious ecological and environmental issues, i.e. soil erosion, surface subsidence, dust, noise, air and water pollution, and impacts on local biodiversity. A solution to some of these problems could be a long-known but not well-investigated method of coal extraction known as Underground Coal Gasification or UCG. During UCG, coal is combusted at the place of its deposit, in situ. This gives several advantages over conventional coal mining, for instance, the liberation of man from dangerous and hard underground work and exploitation of poor quality coal at great depths. The disadvantages of this method include water pollution, gas leakage, and surface subsidence (Su et al., 2013).

Surface subsidence is one of the obstacles to commercialization of UCG (Gunn, 1977) and considered one of the most serious environmental impacts of UCG (Kapusta et al., 2013). Surface sinking and displacements of country rock may damage equipment for coal conversion and gas transportation systems causing gas leakage (US Department of Energy, 1979). Younger (2011) points to the scarcity of research on surface subsidence during UCG. This unwanted phenomenon is less predictable during UCG than during traditional coal mining (Zamzow, 2010) because it happens in a less uncontrolled manner. Additionally, the surface subsidence process could be sensitive to high temperatures.

This work is aimed to enhance numerical predictions of surface subsidence. The outcomes of this work can be extended to investigations of the surface subsidence that is caused by controlled and uncontrolled tunnel collapses. Strokova (2009) noted the importance of the prediction of surface subsidence during tunneling. For example, in 1974, a collapse of the tunnel of the Saint Petersburg subway at a depth of about 70m caused road deformations and cracks in the buildings (Derbin, 2018). The collapse occurred due to an unusual unfavorable geological condition, i.e. the neotectonic fault (Dashko and Malov, 1997).

Shell and France (1977) emphasized the importance of the prediction of surface and subsurface movements to remedy the consequences of the movements. The movements could be predicted using numerical analysis, but it is known that the current constitutive models cannot give adequate results for all cases of surface subsidence. For example, Guarascio et al. (1999) reported successful implementation of two-dimensional model FLAC2D for subsidence prediction validating the results against the empirical subsidence trough obtained with help of the Subsidence Engineer's Handbook (NCB, 1975); but it was mentioned that the elasticity assumption leads to unrealistic horizontal displacements. Earlier, Lloyd et al. (1997) concluded that it was impossible to achieve accurate results with the constitutive models embedded in FLAC2D, i.e. isotropic and transversely isotropic elastic, Mohr-Coulomb, ubiquitous-joint, and strain-softening models. Mead et al. (1981) reported the difference between modelled results and in situ measurement and blamed the deficit on the constitutive models. Singh and Yadav (1995) also noticed the difficulties of modelling surface subsidence in cases of weak overburden when the narrower and deeper trough was expected.

To investigate these difficulties, the commercial explicit finite difference package FLAC3D was chosen to simulate surface subsidence. For example, FLAC3D has previously been used by Herrero et al. (2012) and Xu et al. (2013), to model surface subsidence. However, these cases mostly involved elastic deformations. Xu et al. (2013) acknowledged the complex behavior of the rock-soil interaction and encouraged more investigations.

Using FLAC3D, this work shows that the popular plastic constitutive models do not predict surface subsidence correctly. FLAC3D has built-in popular constitutive models, i.e. Mohr-Coulomb, modified Hoek-brown, strain-softening, double-yield, and modified Cam-clay. These models were used to show that the popular constitutive models fail to predict measurements and to help validate user-defined constitutive models (UDCM). FLAC2D was also implemented to validate UDCM by comparing it with the results obtained with FLAC3D.

FLAC is an abbreviation of Fast Lagrangian Analysis for Continuum. It utilizes an explicit finite difference formulation. FLAC calculates strain rates from velocities and stress from strain rates within one very small time step which is small enough to prevent information from passing between elements. Therefore, the iteration process is not required when computing stress from strain inversion of the stiffness equations for the system at each step, which shortens the run time (Frydman and Burd, 1997). The stiffness matrix is determined by Lame's constants. In FLAC, any constitutive model uses the same solution algorithm and is solved exactly in one step, which makes this software easier for implementing UDCMs.

1.2 Sign Conventions

During programming a constitutive model, sign notation should be implemented with great care. The theory of plasticity was originated for metals where tensile stresses are usually positive. Alas, geotechnics uses the opposite sign convention, the compressive stress is positive because compressive normal stresses are more common than tensile ones in mechanics. FLAC uses tension as positive and therefore clockwise shear stress as positive. This work follows the sign convention adopted in FLAC. The tension is positive, and the compression is negative.

1.3 Aims and Objectives

The aim of this research is to improve the accuracy of numerical predictions of surface subsidence caused by any underground extractions focusing on UCG. This is achieved through pursuing the following objectives:

- Literature review on UCG and surface subsidence to model surface subsidence at a UCG site.

- Development of an approach to model surface subsidence and modelling of surface subsidence at a conventional coal mine to investigate what should be improved in the current models, i.e. goaf behaviour, model mesh, and constitutive models.

- Improvement of modelling predictions of surface subsidence at the UCG site by following means: mesh analysis in FLAC3D; consideration of the specifics of UCG in simulation of surface subsidence, such as thermal analysis, geometry of the UCG reactor, and combustion ash left in the UCG reactor; programming UDCMs in C++ and their embedment in FLAC3D, validation of UDCMs, increasing stability and optimization of the codes of UDCMs and implementation of UDCMs in FLAC3D to model surface subsidence.

1.4 Outline of the Thesis

Chapter 1 introduces the background and context of the work, presents aims and objectives of the research, and describes the outline of the thesis.

Chapter 2 reviews the literature on UCG and surface subsidence. The review is focused on the Soviet trials of UCG because of the uniqueness of the industrial implementation of UCG and the scarce availability of the information in English. The UCG features are also in focus, such as thermal conductivity in the overburden, a complicated geometry of the UCG reactor, thermal impact on the overburden, and thermal expansion of geomaterial.

Chapter 3 lays out the way of building a model of surface subsidence after an uncontrolled collapse of a mine. The method of deriving model parameters from the borehole description is presented. The chapter shows that popular constitutive models cannot recreate a subsidence profile which would be close to the measurements. The modelling results are also compared with the predictions of the Subsidence Engineers' Handbook (NCB, 1975). Additionally, the chapter describes the challenges of simulation of the goaf behaviour.

Chapter 4 studies the influence of different mesh densities, zone shapes and sizes on deformations in FLAC3D. In the end, the chapter proposes recommendations on mesh density and shapes of zones in the area of large deformations.

Chapter 5 explains the method of implementation of a UDCM into FLAC3D. The chapter includes all necessary equations and solutions obtained during implementing the UDCM into FLAC3D.

Chapter 6 presents a simulation of the surface subsidence during UCG. This chapter includes the results of UDCMs. The UCG features, such as thermal stresses, ash left in the reactor, and complicated geometry of the reactor, are also considered in the model.

Chapter 7 concludes and gives recommendations for further work.

Chapter 2

Literature Review

This chapter begins with a statement of the problem. Before delving into solving the problem, the literature survey on the UCG trials and surface subsidence is presented in this chapter. The main source of the literature on the Soviet trials is the National Library of Russia in Saint Petersburg, and several papers are also obtained from the Russian State Library in Moscow. In the literature, the following topics are reviewed: UCG methods, UCG history, and its current state, surface subsidence and its numerical modelling. The chapter ends with the possible solutions of improving the surface subsidence numerical predictions and their adaptations to modelling of surface subsidence at the UCG site.

2.1 The Problem

Any underground activities can cause surface subsidence. In turn, surface subsidence can damage buildings, infrastructure, and mining or UCG equipment. Prediction and remediation of these unwanted consequences of surface subsidence need a reliable model that could predict surface subsidence for different cases.

The careful literature review shows that the modern numerical tools can predict surface subsidence; however, in case of the complicity of an investigation site, the prediction of surface subsidence becomes a nontrivial task for the modern numerical tools. Additionally, some papers reported satisfactory outcomes of modelling of surface subsidence, but most of the numerical results were not compared with field observations. Pongpanya et al. (2017) studied the impact of sizes of the panels and pillars, mining depth, and backfill on surface subsidence without reference of modelling results to the field measurements. Earlier Lloyd et al. (1997) measured surface subsidence and compared the modelling results with the empirical solution by the Subsidence Engineer's Handbook

(NCB, 1975). Later, Esterhuizen et al. (2010) managed to obtain good agreement between field measurements and modelled results, but modelling needs extensive calibrations. Deck and Anirudh (2010) pointed out that modelled horizontal strain was different from the observed strain. To improve predictions, Vyazmensky et al. (2007) combined continuum and discrete element methods to model block caving; however, the coupling makes the numerical tool is complicated and takes long computational time.

Additionally, the task of modelling of surface subsidence can be complicated by different factors, for example, excavations of multi-seams or inclined seams. After modelling multi-seam surface subsidence with the Mohr-Coulomb failure criteria, Iwanec et al. (2016) encouraged more investigations. Ghabraie et al. (2017) developed the method to model multi-seam subsidence, and compared with two available numerical models, but admitted that there was no sufficient research on modelling of the multi-seam surface subsidence. In this work, modelling of surface subsidence is complicated by differences between conventional coal mining and UCG are considered in Section 2.3. With this, Nusimov (1941) pointed out that deformations of the roof of the UCG reactor and surface subsidence were one of the most important problems connected to UCG.

2.2 Introduction to UCG and Surface Subsidence

This section introduces UCG, its history and gives a general understanding of the UCG process. The section considers the subsidence mechanism and four types of surface responses to the mining activity. This section also describes the underground conditions at the site of surface subsidence and ends with surface subsidence at UCG sites.

2.2.1 UCG Methods

The simplest UCG method is called a Link Vertical Wells (LVW) method. The more advanced method of UCG is The Controlled Retracting Injection Point or CRIP method developed in the USA. For the LKW method, only two wells are needed at the site. One injects air or oxygen, and the other one extracts UCG product - the synthetic gas, so-called Syngas. Syngas can be used as fuel. The research of Pei et al. (2016) showed that UCG syngas can be competitive with natural gas when natural gas is expensive. The price of UCG syngas depends on the depth and thickness of the coal seam (Pei et al., 2016). The thicker and shallower the coal seam is, the cheaper it is gasified. The principle of UCG is illustrated in Figure 2.1.

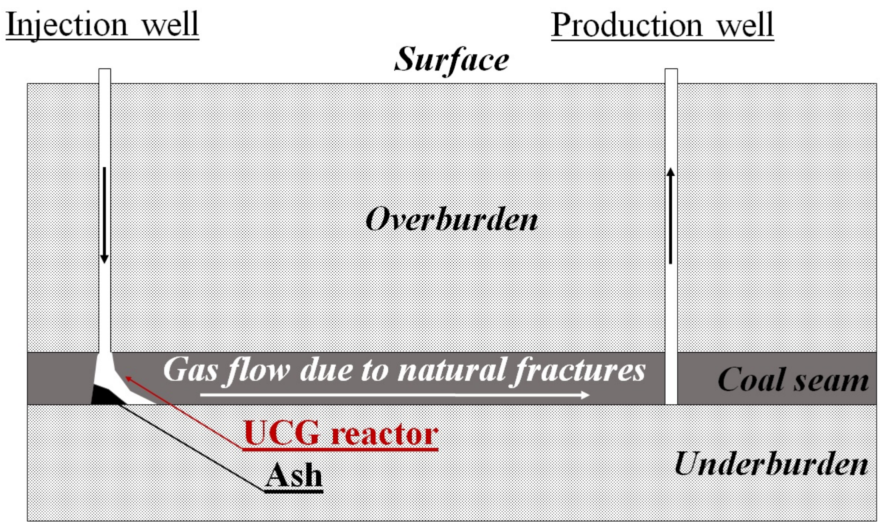

Figure 2.1: Simplified Sketch of UCG

Figure 2.1 presents two wells. They are drilled in the coal seam through the overburden. The wells are interconnected by natural cracks in the coal seam. This interconnection lets the coal combust in the UCG reactor. The temperature reaches above 1000°C there. The UCG reactor gets larger in the direction from the well of air injection to the production well. Occasionally, the reactor collapses provoking surface subsidence. The sketch of CRIP is shown in Figure 2.2.

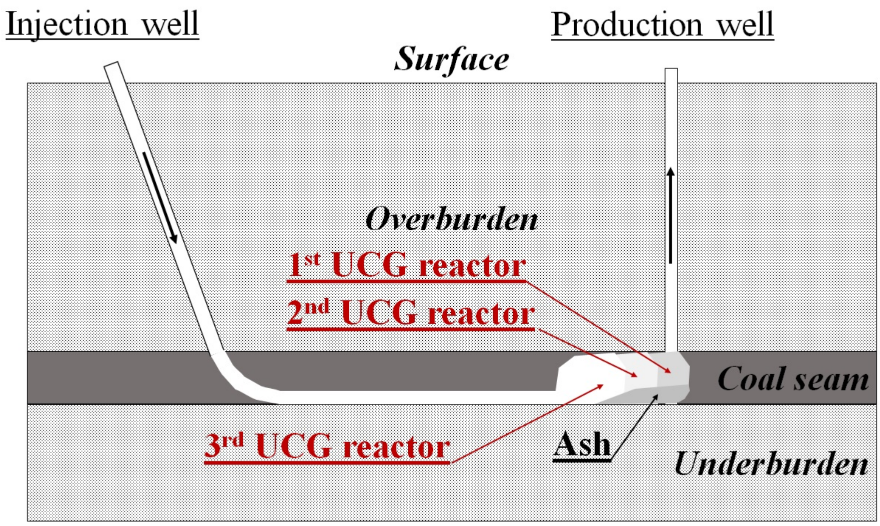

Figure 2.2: Sketch of CRIP

The production and injection wells are drilled with the angle into the coal seam and then the injector well is drilled horizontally in the coal seam to the production well. The ignition is carried out at the place of connection of two wells. Once the coal is burnt there, the ignition point is retracted to a new location closer along the horizontal well to the injection well. Once the fresh coal is burnt up, the ignition point is moved to the location closer to the injection well again. At times, the UCG reactor collapses as in the case of the LVW method.

2.2.2 Soviet UCG and Surface Subsidence

Despite many reviews of the UCG projects in English, this work is unique because it covers large-scale UCG experience in the Soviet Union with emphasis on surface subsidence and the material is collected from the sources in Russian. Gregg et al. (1976) described UCG projects conducted until 1976. however, Trent and Langland (1983) noticed that the USA did not have field experience of surface subsidence induced by large-scale UCG projects and advised to take a look at the Soviet projects. Shafirovich and Varma (2009) reviewed the current state of UCG. Klimenko (2009) revised the early UCG trials. Bhutto et al. (2013) collected information on the application and history of UCG. The latest review was by Khan et al. (2015) with a focus on modelling of the UCG processes.

The Russian Empire and later the Soviet Union developed the idea of UCG at the same time as the USA, but due to political reasons, the Soviet UCG programme was bigger. In agreement to the theory of Multiple Discovery, which states that most scientific discoveries and inventions are made independently and more or less simultaneously by multiple scientists and inventors, the idea of UCG was suggested by both William Siemens in the USA and Dmitry Mendeleev in the Russian Empire presumably independently and almost at the same time, at the end of the 19th century (Burton et al., 2006). Lenin (1913) was embraced by the idea, and this possibly was a key factor of the active development of UCG projects in the Soviet Union. However, the wide UCG development in the Soviet Union was postponed due to World War I, the Civil War, and post-war reconstructions. World War II also postponed the UCG development imposing two milestone decades of the beginning of the Soviet UCG projects, i.e. before the war - the 30s, and after the war years - the 50s.

Although the preparation of a UCG trial was firstly started at the Lysychansk station in the Donetsk Basin, the actual first UCG test occurred at the Krutova station in the Moscow Basin in 1932 (Klimenko, 2009). The Lysychansk station became the second UCG trial, which was followed by the third UCG station Leninsk in the Kuznetsk Basin. The first stations implemented for the industry were in the Moscow Basin, but they were abandoned because of the Nazi-German invasion. UCG efforts were regained after the war, and their peak was in the late 60s. Then the interest in UCG fell off sharply because of a cheaper and more convenient source of energy, natural gas. Nowadays, only one UCG station out of all Soviet stations operates, i.e. the Angren station in the former Soviet republic Uzbekistan (Sury et al., 2004).

To sum up the Soviet UCG experience, Table 2.1 collects data on the surface subsidence for all significant Soviet UCG projects in four basins, i.e. the Moscow, Kuztensk, Dontesk, and Angren Basins. Table 2.1 includes the project start year and the coal seam characteristics.

Table 2.1: Characteristics of the Soviet UCG Projects

Station/ ***Seam***	**Start**	**Thickness (m)**	**Inclination (°)**	**Depth (m)**	**Subsidence (m)**
Moscow Basin					1.2[4]
Krutovsk	1932[8]	1.8[5]	0[5]	-	
Podmoskovnaya	1940[8]	2.5[5]	0[5]	40-50[2]	
Shatsk	1955[4]	2.6[5]	0[5]	45[4]	
Kuznetsk Basin					2.2 collapses[7] up to 10[4]
Leninsk	1933[8]	-	-	-	
Yuzhno-Abinsk	1955[1]	9.2-9.8[7]	68-70[7]	43[3]-53[7]	
Stalinsk	1960[8]	-	-	-	
Donetsk Basin				up to 400[8]	0.5[1]
Lysychansk	1933[8]				
Bobrovsk seam		0.75[5]	30-40[5]		
k_8		1.8-2.1[5]	40-60[5]		
l_8		0.8[5]	41[5]		
Shakhta	1933[8]				
k_4 *Rozovy*		0.4[5]	15-18[5]		
Gorlovka	1935[8]				
k_3 *Derezovka*		2.0[5]	80[5]		
Kamensk	1960[8]				
Angren Basin					1.0[6]
Angren	1960[6]				
Upper		0.3-3.8[6]	-	-	
Interlayer (clay)		0.7-4.7[6]	-	-	
Lower (main)		2.0-7.3[6]	5[6]	115-126[6]	

[1]Semenenko and Turchaninov (1957); [2]Turchaninov (1957a);
[3]Turchaninov and Zabrovsky (1958); [4]Turchaninov and Sazonov (1958);
[5]Kazak and Semenenko (1960); [6]Zhukov and Orlov (1964);
[7]Ovchinikov et al. (1966); [8]Gregg et al. (1976)

Table 2.1 shows that the surface subsidence took place in all Soviet UCG projects and had different magnitudes. The sites with deeper and thiner seams experienced less surface subsidence. The inclination of the overburden layers caused deeper surface subsidence. For example in the Donetsk Basin, the UCG stations with the seams at a depth of 400m had the smallest surface subsidence, 0.5m. At the same time, the stations in the other basins with the seams at a depth of about 40m-100m had surface subsidence of 1m-2m. The stations in the Moscow and Angren Basins experienced moderate surface subsidence, i.e. 1.2m and 1.0m, respectively. The surface subsidence in the Angren Basin was slightly smaller due to its twice deeper gasified coal seam than the seam in the Moscow Basin. Despite the equality of the seam depths, the Kuznetsk Basin experienced the biggest surface subsidence due to the thick coal seam and inclination of the overburden layers.

2.2.3 Surface Subsidence

Surface subsidence can be caused by a collapse or deformation of any underground voids, such as pores, fractures, mines, tunnels, and UCG reactors, and the response of the country geomaterial, and underground movements. The voids can occur due to change of soil-rock temperature or groundwater level, dissolution of soluble rocks (karst), soil suffusion, and underground human activities, i.e. tunnel constructions and underground mineral extractions, for example, by mines or UCG. The geomaterial response depends on several factors. According to Lee and Abel (1983), there are 10 interconnected factors i.e. mining method, multiple seam mining of coalbeds, depth of extraction, rate of advance, the thickness of seam or deposit, lithology and structure, in-situ stresses, topography and time.

This work deals with surface subsidence at the Longwall mining and UCG sites; therefore, the factors relevant to these sites are considered. Brady and Brown (2013) defined Longwall mining as a high rock mass response to mining. UCG should be considered equally to mining in terms of surface subsidence; however, UCG has several mitigation factors such as a slower descending roof layer and ash left in the void (Kreinin, 2010). The depth of extraction impacts the underground disturbance zone. The deep extractions have a bigger disturbance zone. The disturbed geomaterial is larger in volume; therefore, the deep extractions have less surface subsidence. NCB (1963) found that the rate advance is transmitted to the rate of surface subsidence. The thickness of the deposit increases the surface subsidence and structured and lithologically-strong geomaterial decreases surface subsidence as shown in section 2.2.2. The strong horizontal in situ stresses mitigate surface subsidence forming an arch as reported by Kendrich (1973). Contrary, the strong in situ vertical stresses force the host geomaterial to move downwards increasing surface subsidence. The topographical ups and lows caused maximum and minimum subsidence, respectively (Gentry and Abel, 1978). The time factor is interconnected with lithology and final surface subsidence as Knothe (1953) showed in the time function:

$$W(t) = W_0(1 - e^{-ct}) \tag{2.1}$$

where W is the subsidence, W_0 is the final subsidence, c is a time influence coefficient related to lithology. However, traditionally the assessments of the final surface subsidence is assessed and it is fine if the subsidence basin can be considered as constantly flat Cui et al. (2001).

The factors determine the distribution of the zones of disturbance. After a collapse of a UCG reactor, Iofis and Shmelev (1985) distinguished several underground zones of disturbance (Figure 2.3). Zone I is a highly crushed material. Zone II is the zone of bending with vertical fractures where gas and water can easily migrate. Zone III has vertical fractures which do not easily let gas and water go through. Zones II and III constitute the so-called fractured zone. Zone IV does not have vertical fractures. Zone V is curved but has no fractures. Zone VI is the zone of high tension.

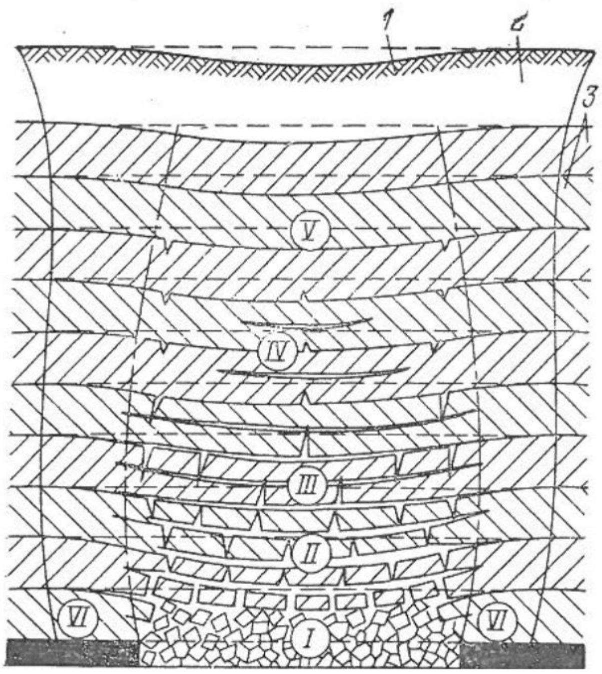

Figure 2.3: Underground Disturbance Zones of Surface Subsidence (after Iofis and Shmelev (1985))
I zone of highly crushed material, which Kreinin et al. (2010) divides into two subzones: disordered lower part, goaf and well-ordered upper part; II zone of bending with fractures with low aerodynamic friction; III - zone of bending with fractures with high aerodynamic friction; IV - zone of bending with fractures without air/water conductivity; V - zone of bending without fractures; VI zone of high tension;
1 - surface; 2 - top seal; 3 - overburden.

The zones of disturbance determine types of surface subsidence. Skafa (1960) recognized four types of surface response to underground mineral extraction. Figure 2.4 shows these types: (1) no surface movements; (2) smooth banding, when no fractures appear in the overburden; (3) bending with fractures; and (4) craters or so-called sink holes, where the deep surface sinking can be observed. The waste material or goaf is pointed by the bold line.

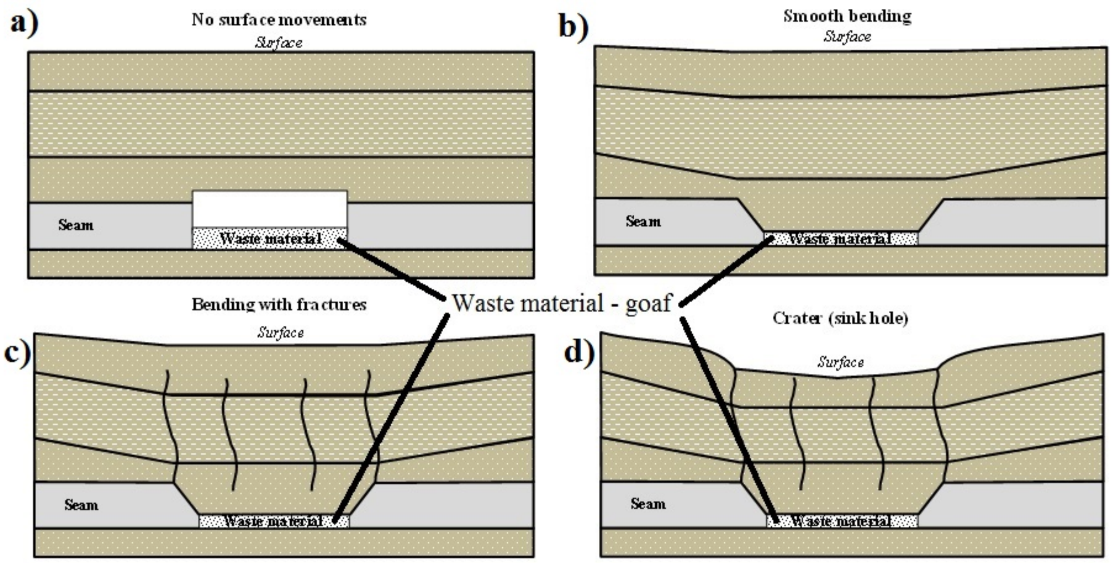

Figure 2.4: Types of Surface Response to Mining
a) No surface movement; b) Smooth bending; c) Bending with fractures; d) Crater (Sink hole)

Figure 2.4 illustrates that the 'no surface movement' type is caused as a result of non-collapsed mine. In this study, this subsidence type is not considered since modelling of surface subsidence is of interest. This type causes an underground void at the place where a mineral was extracted. There is some waste material left after mining or material fallen from the roof in the void. In the case of UCG in this type, the ash remains in this void. In three other types, the sinking roof collapses and then the waste material, collapsed roof material and the ash in case of UCG are compressed. As a result of this process, two different parts of highly disturbed material appear. According to Iofis and Shmelev (1985), the upper part is well-ordered, whereas the lower disordered part is refereed to as a goaf. The two parts together comprise a caving zone.

After a collapse of the mine, surface subsidence does not take place ('no surface movement' type) if only Zone VI is present underground. Zones III and IV predominate in the profile of 'smooth bending' subsidence. The large extension of Zone II contributes to 'crater-type subsidence'. Zone IV and V are absent in this subsidence type. It is the most unwanted type of subsidence since it has the deepest trough with long vertical fractures. For UCG, these fractures disturb isolation of the UCG reactor. These large fractures along with caving need some special treatment in the continuous method of modelling. Since the continuous method of modelling is employed in FLAC, in this work, the first three types of surface response to coal mining or to the UCG are modelled. In this research, highly disturbed material in the caving and fractured zones with moderate heights are considered by altering parameters of the constitutive models, or by introducing a new yield surface, for example, double-yield model, or by implementing some advanced constitutive models.

The types of surface response to mining differ in the extension of the zone of highly-disturbed material. These zones are absent in the 'no surface movements' type. The fractured zone is absent in the 'smooth bending' type. Both zones are presented in the 'with fractures' and 'crater' types. In the 'crater' type, the fractured zone does not end until the surface. Usually, the high-disturbance zone is distinguished from the just disturbance zone. The extension of the highly disturbed material is especially important for modelling of surface subsidence because it has different constitutive behaviour from the intact rock or soil. The zones of highly-disturbed material include Zone II and partly Zones I and III of Figure 2.3.

2.2.4 Disturbance Zones Extension

Since the highly disturbed material needs special treatment in the continuous method of modelling, the heights of the caving and fractured zones are important to be determined. According to Karacan (2010), the height of caving zone created by Longwall mining could reach 4 - 11 times the height of excavation if the overburden is weak and porous. Lama (1973) stated that the height of the primary caving zone is usually taken to be about five times the thickness of the seam, and the total height of the primary and secondary zones about 8 - 10 times the thickness of the seam under extraction. Proskuryakov (1947), Turchaninov et al. (1977), Kratzsch (1983), Smart and Aziz (1989), Ren et al. (1989), Palchik et al. (1991), Karfakis and Akram (1993), Singh and Dhar (1997), Singh and Singh (1999), and Gan et al. (2012) calculated the height of the caving zone according to the following equation:

$$H = h/(k-1) \tag{2.2}$$

where h is the height of excavation, k is the bulking factor.

According to Palchik (2002), the bulking factor could be estimated by the equation:

$$k = 1 + 0.05\sqrt{\sigma} \tag{2.3}$$

where σ is the uniaxial compression strength of the roof material.

Whilst Equation 2.2 is popular, there are other empirical equations for estimation of the height of the caving zone. Majdi et al. (2012) and Mohammadi et al. (2013) extracted the empirical relations to calculate heights of caving (H_c) and fractured (H_f) zones in Table 2.2 from the literature.

Table 2.2: Equations of Heights Estimation of Caving and Fractured Zones modified after Majdi et al. (2012)

Empirical Formulas	**Overburden Conditions**	**Property constants a**	**b**	**c**	**Reference**
$H_{c,f} = [100h/(a \cdot h + b)] \pm c$	hard	0.640	16	8.2	Zhou (1991)
	medium	1.433	19	7.2	
	soft	1.890	32	4.9	
	weathered	2.134	63	3.9	
$H_f = 100h/(a \cdot h + b)$	weak	3.1	5.0		Chuen (1979)
	medium	1.6	3.6		
	strong	1.2	2.0		
$H_f = a \cdot w - b$		0.83	11		Fawcett et al. (1986)
$H_f = 105$ if $h \leqslant 1.7$	minimum cover				NCB (1975)
$H_f = 43h + a$ if $1.7 \leqslant h \leqslant 4.0$		32			
$H_c = h(h + 3d)/2d$, where d= the expansion factor $d = k \cdot h$					Majdi et al. (2012)
$H_f = 56(h)^{1/2}$ $0.0 \leqslant h \leqslant 3.5$					Singh and Kendorski (1981)
$H_c = (h - Ss)/(k - 1)$, if the lowest strata sagging (Ss)					Peng and Chiang (1984)
$H_c = h/(k - 1)$, if the strata fails without sagging					

Table 2.2 provides evidence that the heights of the caving and fractured zones mostly depend on the height of excavation (h). The higher the excavation is, the higher the caving and fractured zones. In one case, calculations of the height of these zones are complicated by influences of panel width (w) by increasing the height with increasing the width. The overburden condition also plays an important role. Stronger overburden increases the height of the fractured zone but decreases the height of the caving zones and vice versa. This tendency is schematized in Figure 2.5. In the equations presented in Table 2.2, the influence of overburden properties is considered by including either the constants, which are selected according to the overburden conditions or by the bulking factor (k). Peng and Chiang (1984) suggested that sagging of the overburden is important for the calculations. The site, where the strata fail without sagging, has higher caving and fractured zones.

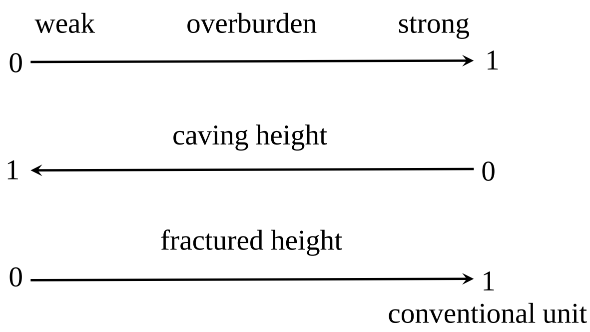

Figure 2.5: Tendency of Heights of Caving and Fractured Zones vs Overburden Strength

Figure 2.5 illustrates the tendency of the height of caving and fractured zones against overburden strength by three arrows. Two arrows point to the right. One of them represents an increase of the strength of the overburden from left to right, the other one stands for the increase of the height of the fractured zone. In other words, strengthening of the overburden increases the fractured zone height. One of the three arrows point to the right and represents the decrease of the caving height with the increasing strength of the overburden and height of the fractured zone.

To verify the tendency for the real cases presented in Figure 2.5, Table 2.3 presents in situ measurements of the height of caving and fractured zones. Table 2.3 also shows the overburden conditions and heights of excavations.

Table 2.3: Heights Measurements of Caving and Fractured Zones

Site	**Overburden Description**	h **(m)**	H_c **(m)**	H_f **(m)**	**References**
Donetsk	shell	1	up to 8		Chernyak et al. (1981)
USA and GB	unknown	unknown	8-12	50	Styler et al. (1984)
unknown	unknown	unknown	4-6	30	Hasenfus et al. (1988)
Donetsk	shale, argillite, sandstone	0.8-1.6	4-11	20-100	Palchik (1989), Palchik (2002), Palchik (2003)
Mu Us Desert	sandstone, mudstone	$\sim$6	5-6	10-11	Zhang et al. (2011)
Anhui	sandstone, claystone	3	2-3	48-49	Guo et al. (2012)

Table 2.3 shows that the height of the caving zone is withing 2-12m, whereas the height of the fractured zone can exceed up tp 100m. The higher caving zone develops at the sites with weaker overburden; however, at the same time, weaker overburden causes lower fractured zone. Table 2.3 suggests that shale argillite and sandstone in the Donetsk Basin resulted in smaller caving zone but larger fractured zone than sandstone and mudstone in the Mu Us desert. Table 2.3 gives an

idea that the depth of excavations plays a role in the development of caving and fractured zones. When comparing the Mu Us and Anhui sites with similar geological conditions, the smaller heights of the extractions result in smaller caving height and bigger fractured zone height. The depth of the seam at the Anhui site is 734m (Guo et al., 2012) whereas the depth of the seam at the Mu Us desert is smaller, 40-210m (Zhang et al., 2011).

Regarding the UCG cases, Kapralov (2013) collected the heights of goaf (H_g), fractured and caving zones in Table 2.4. Table 2.4 also presents the overburden description and the depth of the UCG.

Table 2.4: Heights Measurements of Disturbance Zones at the UCG Sitesafter Kapralov (2013)

Station	**Depth (m)**	**Overburden Description**	h **(m)**	H_g **(m)**	H_c **(m)**	H_f **(m)**
Podmoskovnaya	40-50	clay, sand, limestone	2.0-3.5	1.2-1.4	3.2-3.9	6.0-8.0
Angren	115-126	clay	2.0-6.0	1.6-1.8	5.5-6.5	8.5-9.0
Yuzhno-Abinsk	43-53	siltstone, sandstone	3.9-9.0	2.0-4.0	3.0-6.0	7.0

Table 2.4 shows that the weak overburden of the Podmoskovnaya station results in a comparable high caving zone and low fractured zone. The Yuzhno-Abinsk station has a strong overburden; therefore, the site should have a comparably low caving zone, but a high fractured zone. However, at the Yuzhno-Abinsk station, the heights of the caving and fractured zones do not show this tendency. This is because the inclination of the seam of the Yuzhno-Abinsk station is 70°and the layers slide between each other instead of cracking (Ovchinikov et al., 1966). The next subsection will proceed with the review of the surface subsidence at the UCG sites in the world and the attempts to model it.

2.2.5 World UCG, Surface Subsidence, and Modelling

Surface subsidence is also influenced by the properties of the overburden material. Turchaninov (1957b) noticed that the limestone, which was the strongest material in the Moscow Basin, reduced surface subsidence; however, the state of integrity of overburden geomaterial had a greater impact on surface movements. The comparison of surface subsidence at the Hanna and Hoe Creek sites in the USA also confirms the mitigating effect of limestone overburden (Youngberg et al., 1983). Taking a broader view of UCG projects, Table 2.5 collects world UCG projects with the seam depths and thicknesses, duration, and surface subsidence.

Table 2.5: Surface Subsidence of the World UCG Projects

UCG Sites Dates	**Thickness/ Depth (m)**	**Duration (month)**	**Overburden**	**Subsidence (m)**
Hanna I-V, (WY, USA) 1973-81[1,2]	4.3/ 244-274	4-5	shale, soft sandstone, siltstone	0.3 (model)
Hoe CreekII Felix II seam Felix I and II (USA) 1977[3,4]	7.6/44.2 3.0/25	∼1.5	fissured claystone, uncemented sandstone	for Felix II no subsidence for Felix I II 4.6
Hoe Creek III (USA) 1973[5,6,7]	3.0 - 7.6/ 42.7 - 55.5	∼1.5	feldspathic sandstone, shales, thin limestone	0.9 sink holes
Centralia (WA, USA) 1981-82[8,9]	15.0/175	∼1	siltstone, soft sandstone, moderately stiff sandstone	0.8(model) none observed
Chinchilla (Australia) 80s, 1999-2003[9, 10, 11]	8.0-10.0/ 130-140	30	gneiss, microgabbro, gabbro-diorite	minimal
Wulanchabu, (China) 2008-09[12, 13]	-	2-3	basalt, sandstone, siltstone, mudstone	no subsidence
Majuba (South Africa) 2007-09[12]	300/3.5	7-8	no data	no subsidence

[1]Virgona (1978); [2]Stephenson et al. (1983); [3]Aiman et al. (1980) [4]Trent and Langland (1983); [5]Campbell et al. (1974); [6]Trent and Langland (1983); [7]Ganow (1984); [8]Trent and Langland (1983); [9]Zamzow (2010); [10]Benson (1970); [11]Khadse et al. (2007); [12]Mellors et al. (2012); [13]Wagoner (2011)

Table 2.5 shows that some UCG projects did not experience or experienced insignificantly surface subsidence, i.e. Hanna and Centralia in the USA, Chinchilla in Australia, Wulanchabu in China, and Majuba in South Africa. This can be explained by the short-term duration of these projects, except Chinchilla, where during 30 months of gasification no subsidence was noticed. This could be because of the good quality overburden of rock mass. The condition of the overburden was reported by Benson (1970) after geological studies. Chinchilla UCG site had strong overburden, i.e. gneiss, microgabbro, and gabbro-diorite. The deepest subsidence of 4.6m was noticed in Hoe Creek II (USA) when Felix I and II seams were developed. At the same time, when first Felix II, the deepest seam, was developed no subsidence was noticed.

Table 2.5 also presents the results on trials of modelling surface subsidence and the difference between the observations and modelled expectations. For the Hanna site, Stephenson et al. (1983) implemented the finite element code DAPROK (D'Applonia Consulitng Engineers, 1981). The Mohr-Coulomb model was assigned for the overburden, and the null model, which automatically set the stresses to zero, was used for the reactor. The depth of subsidence trough was modelled at a level of 0.1-0.3m, which is greatly underestimated if it is compared with the prediction of the Subsidence Engineers' Handbook (NCB, 1975). This handbook was used to estimate surface subsidence empirically before the conduction of sophisticated numerical analyses became possible.

The numerical thermal analysis showed that the depth of the subsidence trough reduced during the thermal loading. For the Centralia site, Trent and Langland (1983) used the finite difference code STEALTH (Hofmann, 1976) and finite element code ADINA developed by Dr. K.J. Bathe. Both codes produced identical results, underpredicted surface displacements, and showed the importance of surface subsidence of one of the UCG features, i.e. thermal effects on surface subsidence (Trent and Langland, 1983).

2.3 UCG Features

In the context of surface subsidence, the main differences, or call them UCG features, between UCG and conventional coal mining are the exposure of the geomaterial to high temperatures, products of burning left in the UCG reactor and complicated shape of the reactor. High-temperature influences the stress-strain state and physical-mechanical properties of the overburden. Information on geomaterial thermal conductivity, calculation of heat loss and thermal expansion are discussed and an example of the shape of the UCG reactor is given.

2.3.1 Distribution of High Temperatures

It is important to determine the high-temperature distribution to adjust physical-mechanical properties and impose the thermal strain on the overburden. Semenenko and Turchaninov (1957) argued that UCG heats rock and soil over a relatively small distance away from the UCG reactor. Russo and Kazak (1958) agreed on this argument but pointed out that the spread of heat mainly occurs due to the convection of hot gas through fractures near the reactor. Kolesnikov (1935) gave the energy conductivity of the coal seam, which is very small 0.14-0.17 W/m°C, but noticed that the real conductivity can be much higher due to fractures. Kolesnikov (1935) measured horizontal conductivity in the seam at the Krutovsk UCG station, and found it was 10°/m. Based on the materials of Agroskin and Kazak (1959) and Kazak and Semenenko (1960) for the Lysychansk UCG station, a temperature profile is provided in Figure 2.6.

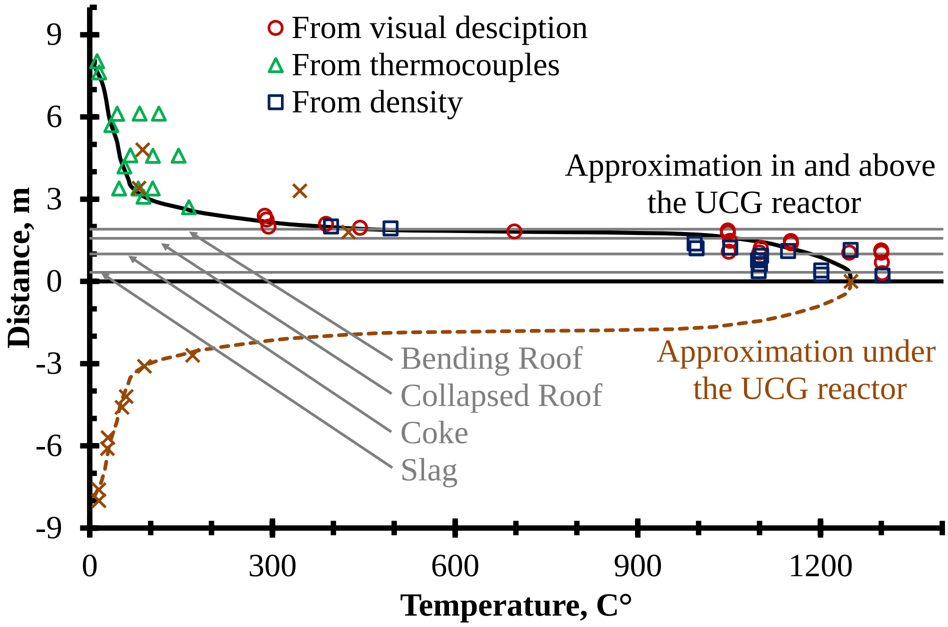

Figure 2.6: Distribution of Temperature at the Lysychansk UCG Station based on Agroskin and Kazak (1959) and Kazak and Semenenko (1960)

Figure 2.6 presents approximations of the geomaterial temperature in and above the UCG reactor (solid black line) and under the UCG reactor (dash brown line) from the field measurements and observations. For the first time, the All-Union Research and Designed Institute of Underground Coal Gasification or VNIIPodzemgaz, now known as Gazprom Promgaz, measured the temperature in the UCG reactor and in its roof and floor during UCG. After UCG, boreholes were drilled. The temperature below 200°C was determined by thermocouples. The temperature above 200°was determined by visual descriptions and data on density and porosity. In the zones of slag and coke, the temperature was almost constant at 1250°C. In the roof, the temperature decreased dramatically and became less than 100°C at a distance of 3m above the seam. At a distance of 9m above the seam, the thermal effect of UCG was not observed. The measurements in the floor showed the identical temperature pattern as for the roof. At a distance of 3m from the reactor floor, the temperature dropped to 200°C, and the thermal effect disappeared at a distance of 9m from the reactor floor.

Empirical Equation 2.4 derived from the field measurements at the UCG stations (Kazak et al., 1990) also shows that temperature should decrease fast with the distance from the reactor. Equation 2.4 calculates heat losses in the overburden, which is proportional to the height of isothermic area m_c (area of temperature between 800-1000°C), m.

$$\frac{Q_1 + Q_2}{Q} = \frac{350}{q_y} \cdot \frac{m_c}{m} + \frac{100.7\sqrt{l}}{m\sqrt{v}q_y} \tag{2.4}$$

where Q_1 is the convectional heat losses; Q_2 is the conductive heat losses; Q is the general heat amount produced by UCG; m_c is the thickness of the isothermic area (area of temperature between 800-1000°C), m; l is the width of the isothermic area, m; m is the thickness of the gasified area; v is the velocity of burning advance, m/day; q_y is the heat of the coal burn.

2.3.2 Thermal Impact on Strata

Gerdov (1940) highlighted that the thermal impact on different strata could vary a lot during UCG. Each case needs to be studied individually. Under high temperatures, the compressive strength of rock or soil can either increase or decrease. Tian (2013) analyzed different experiments on the thermal impact and distinguished three types of compressive strength changing properties (Figure 2.7). The normalized strength is the ratio between the results of the test during high temperature and room temperature. The normalized temperature is the ratio between test temperature and threshold temperature, which is the incipient temperature of changing the strength. The threshold temperature usually corresponds to the lowest melting point of one of the geomaterial minerals.

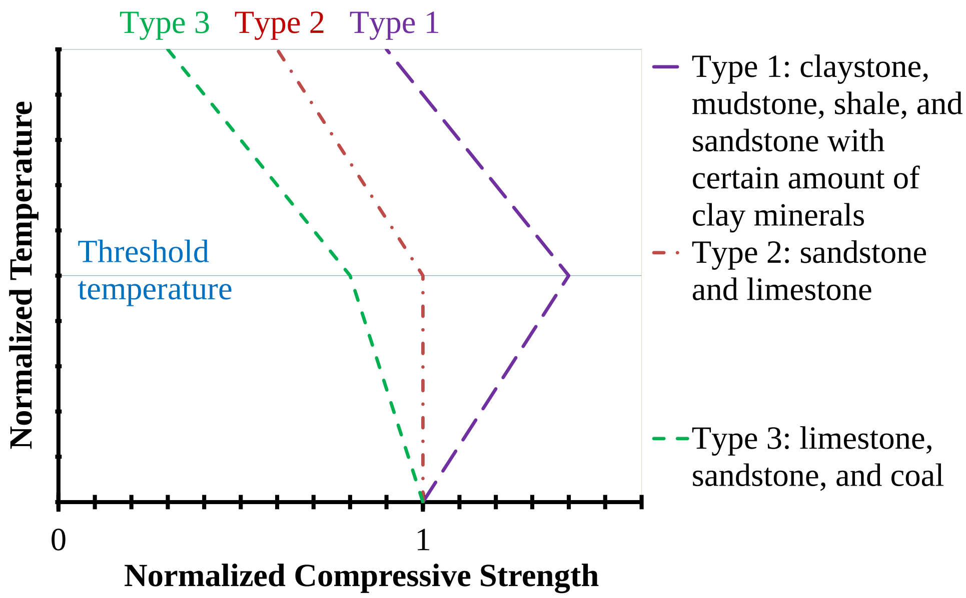

Figure 2.7: Types of Relationships between Rock Strength and Temperature modified after Tian (2013)

Figure 2.7 illustrates three curves, i.e. Type 1, 2 and 3, which relate normalized temperature and normalized compressive strength in the linear fashion for simplicity. Type 1 is typical for clayey material. With increasing temperature, the strength of this material constantly increases below the threshold temperature, and then the strength decreases. Types 2 and 3 are typical for sandstones and limestones. The rock of Type 2 keeps the same strength with increasing temperature and after the threshold, the strength decreases. The strength of the rock of Type 3 decreases with rising temperature. The weakening of the geomaterial accelerates after the threshold temperature.

The compressive strengths of the geomaterial of the Soviet stations under high temperatures were reported by Semenenko and Turchaninov (1957) for soils and Antonova et al. (1990) for rock and were depicted in Figure 2.8.

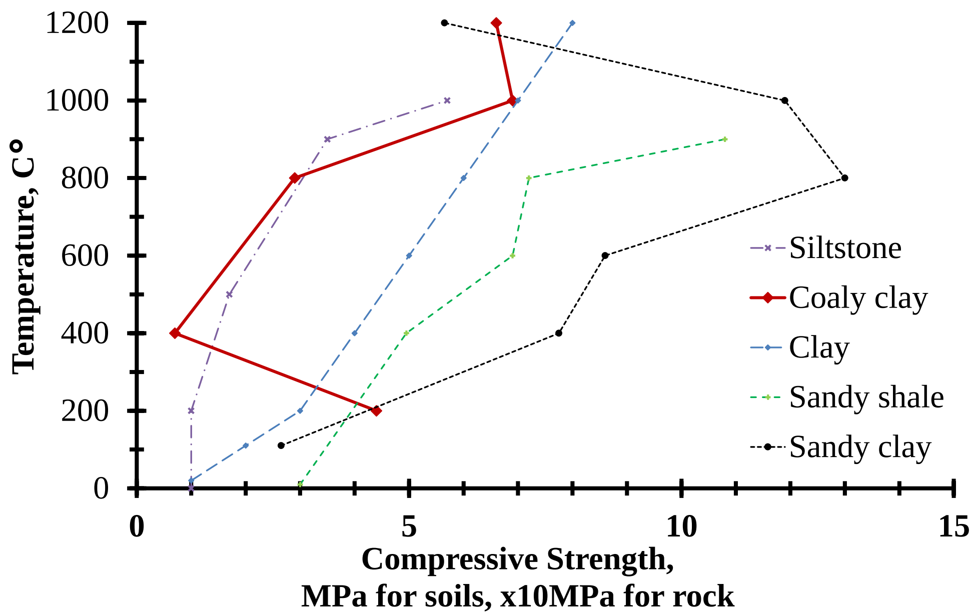

Figure 2.8: Compressive Strength under Different Temperatures after Semenenko and Turchaninov (1957) for soils and Antonova et al. (1990) for rocks

Figure 2.8 illustrates that the geomaterial at the Soviet UCG sites generally followed the pattern of Type 1 by Tian (2013). Russo and Kazak (1958) reported, the shale of the Lysychansk station also follows the pattern of Type 1, when the uniaxial compressive strength increases from 7.7MPa to 40.7MPa under high temperatures. However, in Figure 2.8, there is one exception, which is the coaly clay. At the very beginning, its strength reduces and then increases. This unusual behavior is due to burning coal particles at the first stage. After coal combustion, the soil follows the general patten.

2.3.3 Geometry of the Reactor

One more UCG feature, which should be considered in any numerical model, is the geometry of a UCG reactor that is more like a trapezoid, whereas traditional coal mining leaves a rectangular cave. During conventional mining, the shape of a cave is perfectly controlled (Laouafa et al., 2016). Contrary, the void left after UCG has an uncontrolled complicated geometry. Tian (2013) claims that it has complex shapes in space. After excavation, Kuznetsov (1935) described the sidewall of the experimental UCG reactor (Figure 2.9).

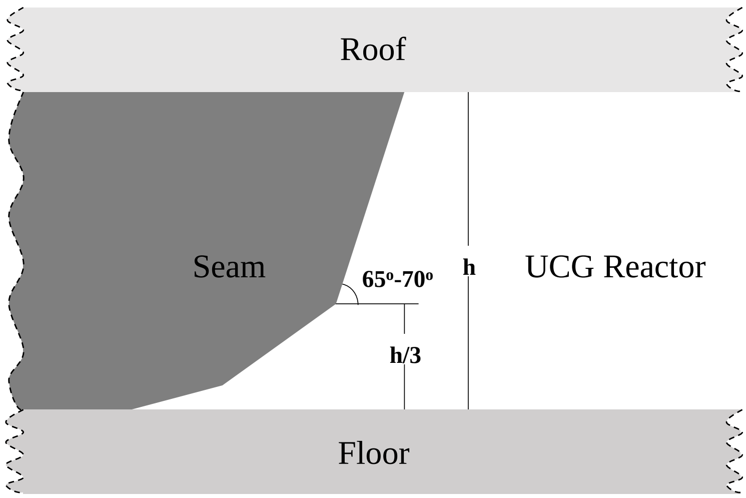

Figure 2.9: Cross-Section of the UCG Rector after Kuznetsov (1935)

Figure 2.9 illiterates the coal seam and the UCG reactor between seam roof and floor. The coal wall of the UCG reactor, the edge of the burn, is inclined. Combustion spreads under the seam at a height of one-third of the reactor. At this place, the angle between the coal overhang and the horizontal line is 65-70°. Above a height of one-third of the reactor, the inclination gets steeper. Gerdov (1940) indicated two main factors that determine the shape of the reactor, i.e. natural conditions (dipping angle, the thickness of the seam, rock properties, groundwater, and the depth) and the method of UCG implementation (temperature of coal burning, the rate of burning, the oxidative and reducing zones).

2.4 State-of-the-Art

Considering the UCG differences from conventional mining (described in Section 2.3) improves the prediction of the surface subsidence at the UCG site. For example, Wu et al. (2017) showed that even small changes of temperature of soil-rock (within 30 °C) influenced on modelling surface subsidence. Thermos-mechanical coupling was mostly achieved by including an expansion coefficient of geomaterial. Najafi et al. (2014) conducted thermal analyses in FLAC3D for UCG. Yang et al. (2014) investigated the thermal stress at the UCG site in the ABAQUS software (ABAQUS, 2012), but these authors did not have a measured temperature profile. Some thermal-mechanical coupling was fulfilled for nuclear waste sites, for example, Nguyen and Selvadurai (1995) and Yow and Hunt (2002). However, the temperatures were considerably lower at the nuclear waste sites than at the UCG sites (200°versus 1250°).

The thermos-mechanical coupling does not solve the challenge (described in Subsection 2.1) of the poor numerical prediction of surface subsidence. The new constitutive model should be implemented to simulate behaviours of overburden or a goaf. The goaf experiences both low and high stresses during its formation. The rockfill material is close to the goaf material in terms of particle sizes; therefore at the particle level, the behavior of the goaf and rockfill agree. The British Soil Classification System (BS 5930:1981, 1981) states that the rockfill is a very coarse granular type of soil, which are cobbles, boulders, and large boulders. According to Singh and Singh (2011), the goaf consists of 22.5% boulders and 77.5% large boulders. Under a low level of stress, the plastic flow of the rockfill is mainly due to interparticle slippage and rotation. Under this theory, many constitutive models available have been successfully utilised in engineering applications. However, when considering high stress level, several authors reported different behaviours of rockfill materials, and grain crushing is identified as a key factor resulting in the different behaviours of rockfill materials under high stress levels (Chávez and Alonso, 2003). According to Russell and Khalili (2004), particle crushing leads to volumetric contraction under drained loading and a suction effect under undrained loading. Chávez and Alonso (2003) concluded that the rockfill material's particle breakage is controlled by the inherent grain strength, grain size distribution, stress level and the relative humidity prevailing in the rockfill voids. Several constitutive models have been developed based on the basis of general elastic-plastic theory, distributed state concept, bounding surface plasticity and hyper-elasticity of energy theory in order to simulate the grain crushing and particle breakage effect rockfill, or more generally, crushable granular materials.

In this work, two constitutive models, CASM (Yu, 1998) and the bubble (Al-Tabbaa and Wood, 1989) model, will be programmed in Chapter 5. CASM can be used for the granular material in contrast to the modified Cam-clay model, and the bubble model was extended from the modified Cam-Clay model by introducing an inner kinematically hardening bubble, which reduces the elastic zone of the model. The bubble model is developed for structured soil. Structured soil is the most typical type of soil. It is defined for natural soil following Mitchell (1976) as having different mechanical behaviour after being remoulded due to damage to its initial structure, i.e. particle arrangement and bonding.

For the first time, these two models will be applied to model surface subsidence at the UCG site in Chapter 6. These models can be considered as the next step of programming after the modified Cam-clay model, in an attempt to implement a model that could capture the phenomena described above. Both CASM and the bubble model can replicate the modified Cam-clay model, which is embedded in FLAC3D, under certain conditions. This makes possible to verify these models against the modified Cam-Clay model embedded in FLAC.

2.5 Summary

The chapter started with the description of the problem, which resides in poor modelling results of surface subsidence. Since the surface subsidence at the UCG site was considered in this work, the chapter presented the UCG process and its history, the surface subsidence mechanism, and an overview of surface subsidence during UCG. The Soviet documents showed that the surface subsidence took place at all the industrial UCG sites. Sometimes, it was the most unwanted type of subsidence, sink holes, as it happened in the Kuznetsk Basin; however, this type of surface subsidence was not modelled in this work. As for the world experience, it does not include many UCG industrial stations; however, it was possible to conclude that surface subsidence was typical for most large UCG projects. Thus, reliable surface subsidence models are required.

Then this chapter discussed differences between surface subsidence at the conventional mine site and UCG site to implement these differences into modelling surface subsidence at the UCG site. The chapter described the measured trapezoid-shaped geometry of the UCG reactor. The chapter also showed that the UCG heat does not spread far from the UCG reactor and gave mean values of the thermal properties of rock-soil. The general patterns of changing properties under high temperatures were considered. In the end, the chapter presented the solution, implementation of a more advanced constitutive model. The review of the constitutive models was fulfilled.

This review information helps develop a model of surface subsidence after a UCG reactor collapse; however, surface subsidence is known to be often modelled incorrectly. To improve surface subsidence perditions and to investigate what is wrong with the current models, the next chapter develops a model of surface subsidence due to a collapse of a conventional mine.

Chapter 3

Surface Subsidence Simulations

This chapter identifies problems and solutions for precise numerical modelling of surface subsidence at the site of a conventional mine. For this, a computer model is developed to predict surface subsidence after the collapse of a mine at Naburn in North Yorkshire. The chapter aims to explain the procedure of modelling surface subsidence, to show that none of the popular constitutive models, i.e. Mohr-Coulomb, modified Hoek-Brown, strain softening, and double-yield cannot predict the field observations, and to recommend the implementation of an advanced constitutive model. The study of the chapter also reveals the great influence of mesh density on the model results.

3.1 Model of the Naburn Site

Thousands of households and businesses are affected by surface subsidence in the UK. The UK has precise maps and measurements of surface subsidence in the whole country. UK Coal Production Ltd kindly provided a measured surface subsidence profile and boreholes logs at a Naburn mine in North Yorkshire. The surface subsidence was measured on September 6, 2004. Figure 3.1 shows the location of the Naburn site.

Figure 3.1: Location of the Naburn Site. Yandex.Maps (https://maps.yandex.ru)

Figure 3.1 is part of the map of Great Britain. The Naburn site of modelling is located in the middle of Nottingham and Newcastle upon Tyne where the author studied. A wide range of rock was presented at the site, i.e. coal, mudstone, sandstone, seatearth, and siltstone. The coal seam was slightly inclined. The inclination was so small that it was neglected in the model. Coal was excavated from the 2.8m-Barnsley seam at a depth of 716.8m using a method of Longwall mining. The excavation caused surface subsidence. The rock domain was discretised into a mesh 104 zones wide, 570 zones deep and one zone in plane. The general layout of the model domain is depicted in Figure 3.2.

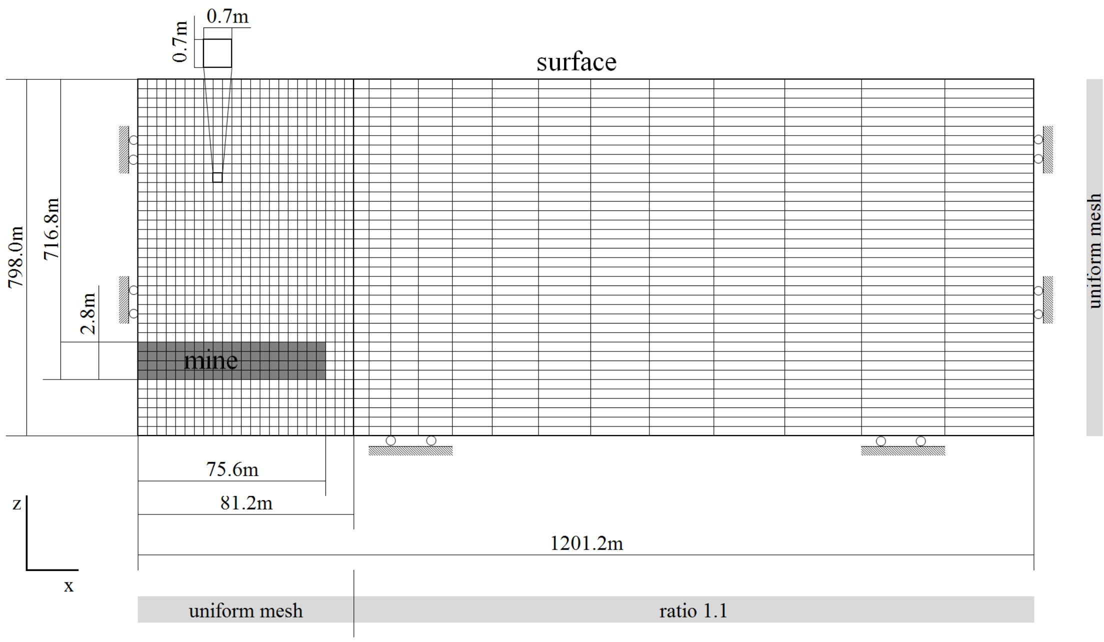

Figure 3.2: Layout of the Naburn Model

Figure 3.2 shows the x–z orientation of the model, the size of the model domain, boundary conditions, and the mine location. The labels of axes were assigned in the following way: x was the horizontal axis in the plane direction, z was the vertical axis, and y was the axis out of the plane. The roller boundary conditions were imposed to the bottom and both ends of the model not to overconstrain the model. By increasing the width of the model, it was checked that theses roller boundary conditions have a minimum impact on the modelling results.

The roller boundary conditions were imposed by fixing the model left and right ends in the x-direction and the bottom in the z-direction. The y-direction of the model was fixed and had only one zone in the y-direction making the problem plane in the 3D software. The model height (z- dimension) was 798.0m and the width (x-direction) was 1201.2m because the values could be divided by 2.8m (the height of the coal seam) with no remainder. The width of 1201.2m could provide the distance of the minimum impact to the right boundary of the model. The depth to the coal seam was 716.8m. It was checked that the used distance between the goaf and the model bottom had a minimum impact on the modelled goaf behaviour. Utilising the symmetry of the problem, a plane strain model was used to reduce the model domain. Hence, just the half of 151.2m-long panel was modelled. It was examined that the reduction of the model domain due to the symmetry does not influence the results.

Figure 3.2 also illustrates that the size of the cube-shaped zone was 0.7m in the area above and under the mine. The width (x-direction) of the zones increased from the mine to the right side of the model with a ratio of 1:1.1. This helped reduce the run-time of the model, which was usually several hours. The cube-shaped zones were kept from the left side of the model at a distance 81.2m to exclude the influence of the zone size change on the numerical results at the mining border. A hydrostatic stress field was imposed on the mesh. A gravity constant of 10 m/s^2 was used throughout the model. The mechanical properties of the rock were calculated based on the method of derivation of the mechanical properties from the borehole logs.

3.2 Deriving Model Parameters from Boreholes Data

This section explains the method of deriving the appropriate parameters of the model, i.e. elastic stiffness, friction angle, cohesion, and tensile strength, using the boreholes data. This method was developed after an extensive literature search and based on the works of Balmer (1952), Deere (1968), Hoek and Brown (1980), Hansen (1988), Palmström (1995), Hoek and Brown (1997), Palmström and Singh (2001), and Hoek and Diederichs (2006). The rock was assumed to be isotropic.

3.2.1 Elastic Stiffness

The elastic stiffness is a key geomechanical property for any material. To estimate this parameter, Serafim and Pereira (1983) performed an extensive parametric study and suggested the following popular relationship between rock mass stiffness (E_{rm}) and Rock Mass Rating (RMR) in GPa.

$$E_{rm} = 10^{\frac{RMR-10}{40}} \tag{3.1}$$

A comparison of empirical equations on the determination of the elastic stiffness of various rocks was carried out by Hoek and Diederichs (2006). Hoek and Diederichs took high-quality data and approximated the trend of the rock mass stiffness (E_{rm}) with the Geological Strength Index (GSI) using a sigmoid. The following formula was derived.

$$E_{rm} = E_i \left(0.02 + \frac{1 - \frac{D}{2}}{1 + e^{60+15D-\frac{GSI}{11}}} \right) \tag{3.2}$$

The GSI is a system for estimating the rock mass strength for different rock types in varying geological conditions. Its role will be explained in greater detail later in this section. In Figure 3.3, a GSI of 100 represents a very good, undisturbed rock mass whereas a GSI of 0 represents a very poor quality, disintegrated rock mass.

D is called the disturbance factor, which was first introduced by Hoek et al. (2002), it ranges from 0 to 1 and provides a measure of how much the rock has been disturbed i.e. blasting a rock face will give the rock a disturbance factor of 1.0 while careful excavation will yield a disturbance factor of 0.0. The influence of D on the elastic modulus can be seen in the following graph taken from Hoek and Diederichs (2006).

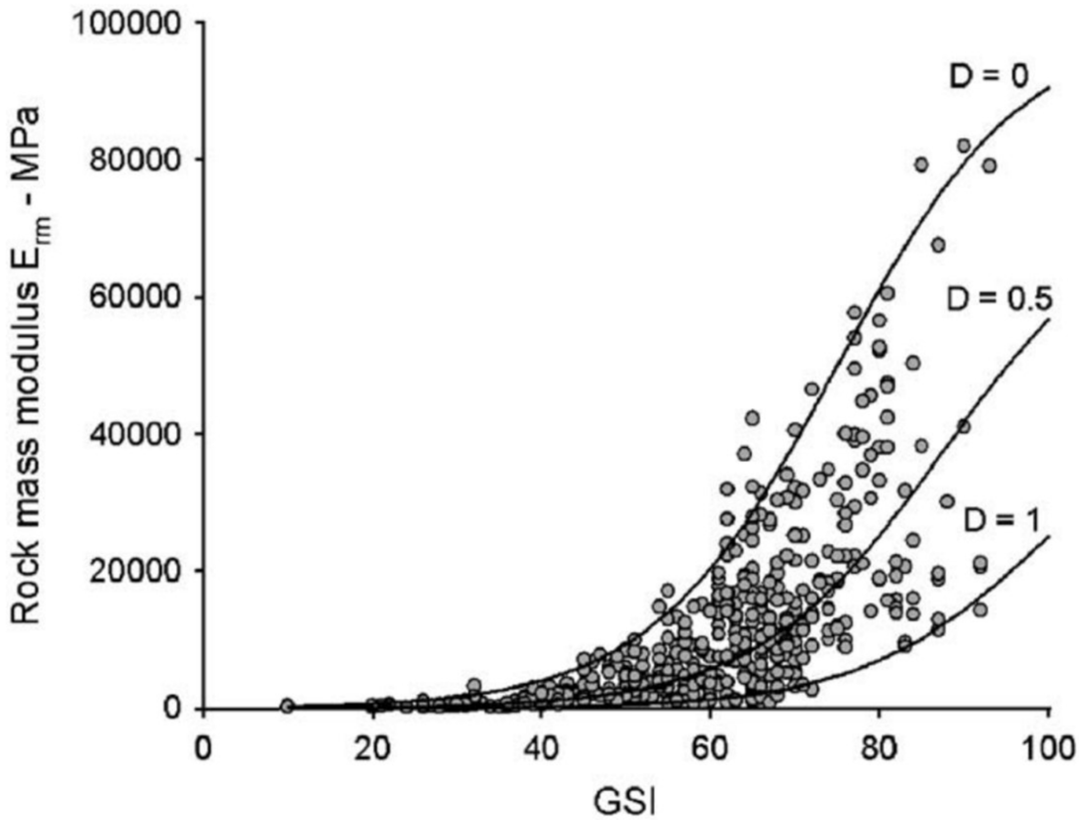

Figure 3.3: Elastic Modulus Measured from Insitu Tests vs GSI and Disturbance after Hoek and Diederichs (2006)

In Figure 3.3, each circle represents the result of a specific in situ test. It is clear that the disturbance factor has a large effect on the elastic modulus of the rock. Equation 3.1 has a second term that has not been described, namely E_i. E_i is given by

$$E_i = MR \cdot \sigma_{ci} \tag{3.3}$$

where MR is the modulus ratio and σ_{ci} is the uniaxial compressive strength (UCS) of the intact rock.

The modulus ratio (MR) was first proposed by Deere (1968) and later modified by Palmström and Singh (2001). The MR is classified by rock type and presented in Table 3.1.

Table 3.1: Guidelines for the Selection of the Modulus Ratio based on Deere (1968) and Palmström and Singh (2001)

Rock type	**Class**	**Group**	**Texture**			
			Coarse	**Medium**	**Fine**	**Very Fine**
Sedimentary	Clastic		Conglomerates 300-400 Breccias 230-350	Sandstones 200-350	Siltstones 350-400 Greywackes 350	Claystones 200-300 Shales 150-250[a] Marls 150-200
	Non-clastic	Carbonates	Crystalline limestones 400-600	Sparitic limestones 600-800	Micritic limestones 800-1000	Dolomites 350-500
		Evaporates		Gypsum (350)[b]	Anhydrite (350)[b]	
		Organic				Chalk 1000+
Metamorphic	Non-foliated		Marble 700-1000	Hornfels 40-700 Metasandstone 200-300	Quartzites 300-450	
	Slightly-foliated		Migmatite 350-400	Amphibolites 400-500	Gneiss 300-750[a]	
	Foliated			Schists 250-1100[a]	Phyllites/ Mica Schist 300-800[a]	Slates 400-600[a]
Igneous	Plutonic	Light	Granite[c] 300-550 Granodiorite[c] 400-500		Diorite[c] 300-350	
		Dark	Gabbro 400-500 Norite 350-400	Dolerite 300-400		
	Hypabyssal		Porphyries (400)[b]		Diabase 300-350	Peridotite 250-300
	Volcanic	Lava		Rhyolite 300-500 Andesite	Dacite 350-450 Basalt	
				300-500	250-450	
		Pyroclastic	Agglomerate 400-600	Volcanic breccia (500)[b]	Tuff 200-400	

[a]Highly anisotropic rocks: the value of MR will be significantly different if normal strain and/or loading occurs parallel (high MR) or perpendicular (low MR) to a weakness plane. Uniaxial test loading direction should be equivalent to field application.
[b]No data available, estimated on the basis of geological logic.
[c]Felsic Granitoids: coarse grained or altered (high MR), fined grained (low MR)

By appropriate selection of the disturbance factor, the GSI, and the MR, the elastic modulus of the rock can be estimated. Tables 3.2 and 3.3 shows that the UCS can be estimated by rock type. While the MR is given in Table 3.1 and the GSI later in Table 3.5, which selection of the disturbance factor is subsequently discussed. Ideally, the disturbance factor would be equal to 0 throughout the subsurface rock except close to the mine collapse where the disturbance factor would increase to 1 in proportion to the degree of plastic strain. However, many commercial numerical packages do not allow the user to prescribe a relationship between the elastic modulus and the plastic strain when using the Mohr-Coulomb failure criterion. Hence, it is suggested a disturbance factor of 0 is used throughout the model and strain softening is used to weaken the model in the area of disturbance.

3.2.2 Failure Parameters

To ascertain failure parameters based upon rock type without UCS data, the parameter values from Hansen (1988) and Hoek and Brown (1980) can be adopted. Palmström (1995) conveniently summarises these parameter values for different soils and rocks in the following table.

Table 3.2: Summary of UCS Data Based on Rock Type after Palmström (1995)

Rock name	**UCS** σ_c,			m_i[1)]	**Rock name**	**UCS** σ_c,			m_i[1)]
	low	**average**	**high**			**low**	**average**	**high**	
Sedimentary					**Metamorphic**				
Anhydrite		120’?		13.2	Amphibolite	75	125	250	31.2
Coal	16”	21”	26”		Amphibolitic				
					gneiss	95	160	230	31?
Claystone	2’	5’	10	3.4	Augen gneiss	95	160	230	30?
Conglomerate	70	85	100	(20)	Black shale	35	70	105	
Coral chalk	3	10	18	7.2	Garnet				
					mica schist	75	105	130	
Dolomite	60’	100’	300’	10.1	Granite gneiss	80	120	155	30?
Limestone	50*	100’	180*	8.4	Granulite	80’	150	280	
Mudstone	45	95	145		Gneiss	80	130	185	29.2
Shale	36”	95”	172”		Gneiss granite	65	75	85	
Sandstone	75	120	160	18.8	Greenschist	65	75	85	
Siltstone	10’	80’	180’	9.6	Greenstone	120’	170*	280*	20?
Tuff	3’	25’	150’		Graywacke	100	12	145	
Igneous									
Andesite	75’	140’	300’	18.9	Marble	60’	130’	230’	9.3
Anorthosite	40	125	210		Mica gneiss	55	80	100	30?
Basalt	100	165	355”	(17)	Mica quartzite	45	85	125	25?
Diabase									
(dolerite)	227”	280”	319”	15.2	Mica schist	20	80*	170*	15?
Diorite	100	140	190	27?	Mylonite	65	90	120	
Gabbro	190	240	285	25.8	Phyllite	21	50	80	13?
Granite	95	160	230	32.7	Quartz sandstone	70	120	175	
Granodiorite	75	105	135	20?	Quartzite	75	145	245	23.7
Monozonite	85	145	230	30?	Quartzitic				
Nepheline					phyllite	45	100	155	
syenite	125	165	200		Serpentinite	65	135	200	
Norite	290”	298”	326”	21.7	Slate	120’	190’	300”	11.4
Pegmatite	39	50	62		Talc schist	45	65	90	10?
Rhyolite		85’?		(20)					
Syenite	75	150	230	30?					
Ultra basic									
rock	80’	160	360						

Soil materials[2)]**:**
Very soft clay $\sigma_c = 0.025$MPa Soft clay $\sigma_c = 0.025 - 0.05$MPa Firm clay $\sigma_c = 0.05 - 0.1$MPa
Stiff clay $\sigma_c = 0.1 - 0.25$MPa Very stiff clay $\sigma_c = 0.25 - 0.5$MPa Hard clay $\sigma_c > 0.5$MPa
Silt, sand: assume $\sigma_c = 0.0001 - 0.001$MPa

*Values found by the Technical Universoty of Norway (NTH) Inst. for rock mechanics.
’Values given in Lama and Vutukuri (1978)
”Values given by Bieniawski (1984)

[1)] m_i refers to the value of m for intact rock in the Hoek-Brown model. Values in brackets have been estimated by Hoek et al. (1992) while those with a question mark have been assumed by Palmstrom.
[2)] For clays, the values of the UCS is based on ISRM (1988)

The UCS of a geomaterial that is not presented in Table 3.2, can be derived from Table 3.3 of classification of the rocks and soils according to their strength. Table 3.3 includes Protodyakonov’s coefficient f, density, and bulking factor. This coefficient was introduced by Porododyakonov at the beginning of the 20th century (Lomtadze, 1984) and calculated as

$$f = 0.1\sigma_c \tag{3.4}$$

where σ_c is the UCS, MPa. Knowing this coefficient, it is trivial to estimate the UCS.

Table 3.3: Classification of Geomaterial According to Their Strength after Lomtadze (1984)

Strata name	f	**Density ($\mathbf{g/cm^3}$)**	**Bulking factor**
Basalt, Quartzite	20	2.8–3.8	2.2
Strong granite, the strongest limestone and sandstone	15	2.6–2.7	2.2
Granite, very strong limestone and sandstone	10	2.5–2.0	2.2
Pyrites, strong limestone	8	2.5	2
Sand-shale, normal sandstone	5–6	2.5	2
Strong shale, weak sandstone and limestone	3–4	2.5	2
Anthracite, soft limestone, soft schist, chalk, rock salt, gypsum, frozen soil, distorted sandstone	2	2.4	1.8
Strong coal, distorted schist, very strong clay	1.5	1.8–2.0	1.5
Coal, strong clay	1	1.8	1.4
Weak coal, weak sandy clay	0.8	1.6	1.3
Peat, wet sand	0.6	1.5	1.2
Sand, seatearth	0.5	1.7	1.1
Quicksand	0.3	1.5-1.8	1.05

Table 3.2 and Table 3.3 provide slightly different values of UCS, for example, sandstone 120MPa vs 150MPa, coal 21MPa vs 10MPa, Seatearth 16MPa vs 5MPa. Palmström (1995) compiled the data into Table 3.2 from all over the world; whereas Lomtadze (1984) based Table 3.3 on the data from the Soviet experience. The values which were based on the world observations were chosen for the site in England. If a site of the countries of the former Soviet Union is considered, it would be recommended to use the values which were suggested by Lomtadze (1984).

Table 3.2 also presents the value of m_i. m_i is important for calculations of the failure parameters. Table 3.4 gives more values from the paper by Hoek and Brown (1997) for the subsequent discussion.

Table 3.4: Determination of m_i after Marinos et al. (2000) in Hoek and Brown (1997)

Rock type	Class	Group	Texture: Coarse	Medium	Fine	Very Fine
Sedimentary	Clastic		Conglomerates (22)	Sandstones 19	Siltstones 9	Claystones 4
				——Greywackes—— (18)		
	Non-clastic	Organic		——Chalk—— 7		
				——Coal—— (8-12)		
		Carbonate	Breccia (20)	Sparitic Limestone (10)	Micritic Limestone 8	
		Chemical		Gypstone 16	Anhydrite 13	
Metamorphic	Non-foliated		Marble 9	Hornfels (19)	Quartzites 24	
	Slightly-foliated		Migmatite (30)	Amphibolite 25–31	Gneiss (6)[a]	
	Foliated*		Gneiss 33	Schists 4–8	Phyllites (10)	Slates 9
Igneous	Light		Granite 33		Rhyolite (16)	Obsidian (19)
			Granodiorite (30)		Dacite (17)	
			Diorite (28)		Andesite (19)	
	Dark		Gabbro 27	Dolerite (19)	Basalt (17)	
			Norite 22			
	Extrusive pyroclastic type		Agglomerate (20)	Breccia (18)	Tuff (15)	

*These values are for intact rock specimens tested normal to bedding or foliation.
The value m_i will be significantly different if failure occurs along a weakness plane.

The Hoek-Brown failure-criterion is for jointed rock masses, the criterion is empirical and given by the following equation:

$$\sigma_1' = \sigma_3' + \sigma_{ci}\left(m_b \frac{\sigma_3'}{\sigma_{ci} + s}\right)^a \tag{3.5}$$

where σ_1' and σ_3' are the maximum and minimum principal stresses, m_b is the value of the Hoek-Brown constant m for the rock mass, and s and a are constants that depend upon the characteristics of the rock mass.

Hoek (1994) and Hoek et al. (2000) introduced the concept of a Geological Strength Index (GSI), which is a system for estimating the reductions in rock mass strength in different geological conditions. The value of the GSI can be estimated from the following table.

Table 3.5: Determination of the GSI after Hoek and Brown (1997)

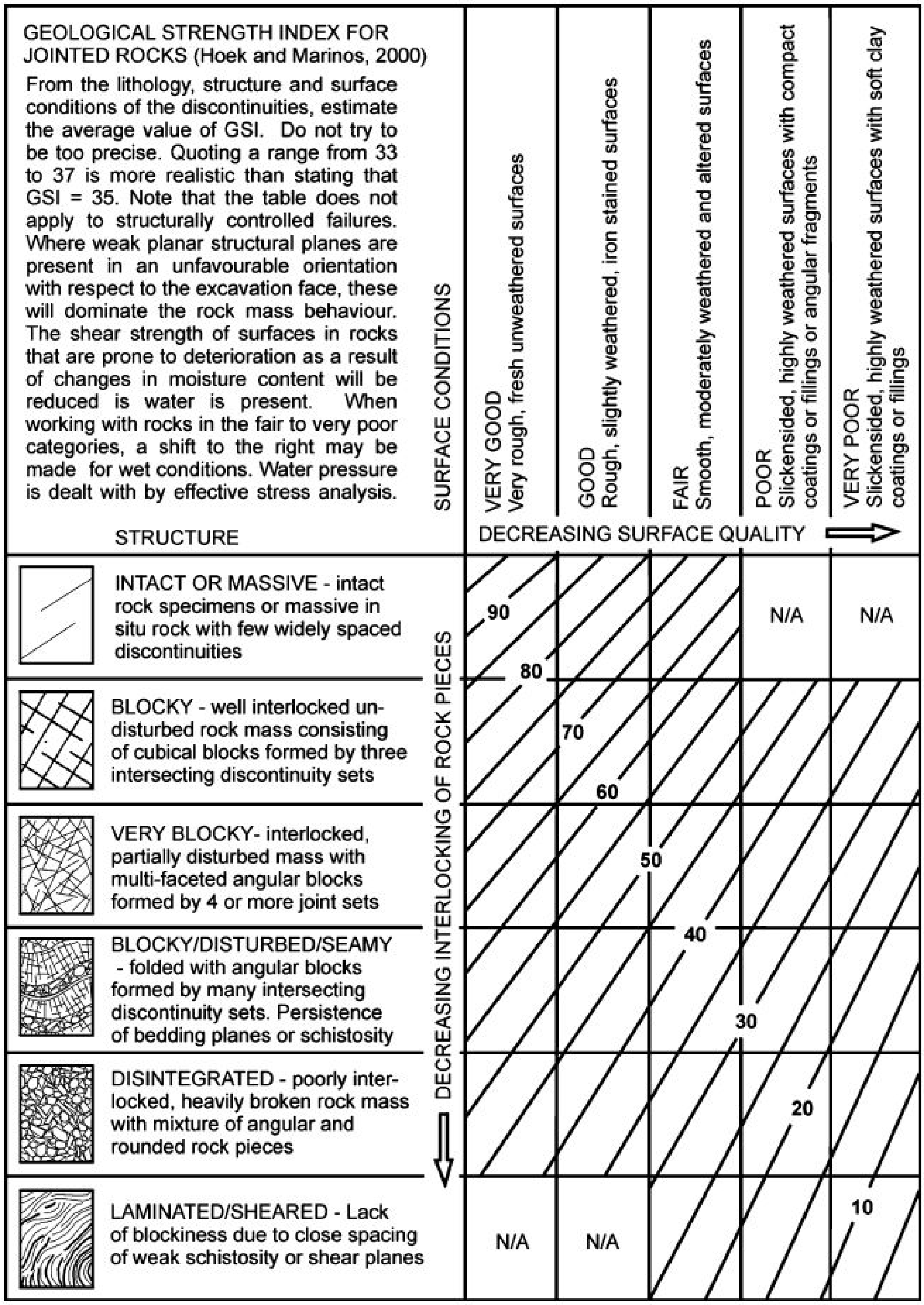

Table 3.5 shows that the GSI depends on the surface quality and structure of the geomaterial. Once the value of the GSI has been estimated, then the following calculation can be used to find m_b:

If the GSI is greater than 25, then m_b can be found by

$$m_b = m_i \cdot exp\left(\frac{GSI - 100}{28}\right) \tag{3.6}$$

Correspondingly, the values of a and s in Equation 3.5 are given by

$$s = exp\left(\frac{GSI - 100}{9}\right); a = 0.5 \tag{3.7}$$

where, σ_{ci} is given by Table 3.2 and m_i is given by Table 3.4.

Next, the Hoek-Brown failure criterion is approximated with a Mohr-Coulomb failure surface. Following Hoek and Brown (1997), the most practical solution is to treat this approximation as a set of full-scale triaxial strength tests. Equation 3.5 provides values of σ_1 that lay on the yield surface for different values of σ_3 hence it can be used to generate the maximum and minimum principal stresses for the rock in question. The user must select the values for σ_3 used in the analysis and Hoek and Brown found that the most consistent results are obtained when 8 equally spaced values between $0 < \sigma_3 < 0.25\sigma_{ci}$ are used.

To find the tangent of the failure surface at the appropriate stress level, first the non-linear analytical solution for the Mohr's envelope is found and then a linear regression analysis is used to find the equation of the tangent at that point. The analytical solution of Balmer (1952) to Mohr's envelope describes the relationship between the normal and shear stresses (σ'_n and τ) in terms of the principal stresses as

$$\sigma'_n = \sigma'_3 + \frac{\sigma'_1 - \sigma'_3}{\frac{\delta\sigma'_1}{\delta\sigma'_3} + 1}; \tau = (\sigma'_1 - \sigma'_3)\sqrt{\frac{\delta\sigma'_1}{\delta\sigma'_3}} \tag{3.8}$$

Provided that the GSI is greater than 25, then it can be calculated as

$$\frac{\delta\sigma'_1}{\delta\sigma'_3} = 1 + \frac{m_b\sigma_{ci}}{2\left(\sigma'_1 - \sigma'_3\right)} \tag{3.9}$$

The tensile strength of the rock is then calculated as

$$\sigma_{tm} = \frac{\sigma_{ci}}{2}\left(m_b - \sqrt{m_b^2 + 4s}\right) \tag{3.10}$$

The equivalent Mohr's envelope may be written as

$$Y = log(A) + B \cdot X \tag{3.11}$$

where A and B are constants and X and Y are unknown values.

The values of X and Y can be calculated using Equations 3.8 and

$$Y = log\left(\tau/\sigma_{ci}\right); X = log\left(\frac{\sigma'_n - \sigma_{tm}}{\sigma_{ci}}\right) \tag{3.12}$$

The constants A and B can then be calculated using a linear regression analysis, i.e.

$$A = 10^{\left(\sum Y/T - B\left(\sum X/T\right)\right)}; B = \frac{\sum X \cdot Y - \left(\sum X \cdot \sum Y\right)/T}{\sum X^2 - \left(\sum X\right)^2/T} \tag{3.13}$$

where, T is the number of values in the sequence, i.e. 8, if the earlier suggestion is followed.

Finally, the Mohr-Coulomb parameters (internal friction angle ϕ and cohesion c) can be deduced from the following two equations:

$$\phi = arctan\left(A \cdot B \cdot \left(\frac{\sigma'_{ni} - \sigma_{tm}}{\sigma_{ci}}\right)^{B-1}\right) \tag{3.14}$$

$$c = 0.75\left(\tau - \sigma'_{ni} tan(\phi)\right) \tag{3.15}$$

Since A and B are known, then using σ_{ni} in place of σ_n in Equation 3.12 will evaluate an expression for X which can be used in Equation 3.10 to find a value of Y. This can be used to calculate τ from the first equation in Equation 3.12.

It can be seen that another new parameter σ_{ni} has been introduced, and this is the value of the normal stress at the point of interest at a certain depth (z). To determine this value, Martin et al. (2003) collected all available information on the subsurface vertical stress gradient ($\Delta\sigma_v$) in Table 3.6.

Table 3.6: Summary of Measured Vertical Stress Gradients in Various Rock Types after Martin et al. (2003)

$\Delta\sigma_v$ (MPa/m)	Location [rock type]	Depth (m)	Reference
0.0249	Elliot Lake, Canada (Quartzites)	900	Hedley and Grant (1972)
0.0266 ±0.0028	World data	0-2400	Herget (1974)
0.027	World data	0-3000	Brown and Hoek (1978)
0.0265	World data	100-3000	McGarr and Gay (1978)
0.026 ±0.0324	Canadian Shield	0-2200	Herget (1987)
0.0266 ±0.008	Canadian Shield	0-2200	Arjang (1989)
0.027	URL[1], Granite	0-440	Martin (1990)
0.0285	Canadian Shield	0-2300	Herget (1990)
0.026	Canadian Shield	0-2200	Arjang and Herget (1997)
0.0264	Aspo HRL[2], Diorite	150-420	Andersson and Ljunggren (1997)
0.0249±0.00025	Sellafield, UK [Sandstones/Volcanics]	140-1830	Batchelor et al. (1997)

[1]AECLs (Atomic Energy of Canada Limited) Underground Research Laboratory, Canada
[2]Hard Rock Laboratory in Sweden

Using Table 3.6, the vertical stress can be calculated by Equation 3.16.

$$\sigma_{ni} = \Delta\sigma_v \cdot z \tag{3.16}$$

This value (σ_{ni}) is equivalent to the normal stress and enables us to completely specify the mechanical properties of the rocks underground in the surface subsidence model. The description of the model, the mine, and the results are presented in the following section. The results of the Hoek-Brown model were compared with the results of the Mohr-Coulomb model to check the equations and conclusions in this chapter. If the results of both models agreed, the theory in this chapter is corrected.

3.3 Modelling

This section describes the process of modelling starting with the derivation of the primary model parameters and proceeding with a method of modelling goaf. Then the modelling results are presented and later the challenges, i.e. stresses in the goaf and unsystematic impact of the mesh density on the results.

3.3.1 Primary Model Parameters

The method of deriving parameters from borehole log (from Subsection 3.2) was implemented. This method is direct and has advantages over a back analysis of deriving parameters. In the direct method, the characteristics of the geomaterial are known, and the parameters can be derived based on these characteristics. In the back analysis, the parameters are adjusted to observed results. The back analysis is widely used (Fakhimi et al., 2004); however, the method requires a large number of model runs and obtained parameters could not correspond to reality.

The overburden consists of siltstone, sandstone, seatearth, mudstone, and coal at the Naburn site. The bulk and shear moduli were calculated using Equations 3.1 and 3.2 for Young's modulus and assuming the same Poisson's ratio of 0.2 for all layers. The choice of the GSI for the calculation of Young's modulus was based on Table 3.5 and two principals:

- Firstly, simulations with a GSI of 100 suggested that the mine did not collapse because of too strong overburden. An investigation was carried out to find GSI which causes the mine to collapse. For this, FLAC's null model, which set stresses to zero, was assigned to the zone of the excavation to represent material that was removed. The GSI of the roof layer was gradually reduced. It was determined that the roof collapses when the GSI was less than approximately 60.

- Secondly, the strength of the soils and rocks increases with the depth (Lel et al., 2000). The strengthening of the overburden with the depth can be achieved by increasing GSI with the depth. A GSI of 25, as the minimum possible, was chosen for the rock in the caving zone and near the surface because it is a disintegrated rock. The largest GSI was taken as 60 at the bottom of the model because the simulations show that a GSI of 60 reached the maximum value when the mine collapsed. The GSI of other layers was linearly interpolated according to the depth. Figure 3.4 shows the GSI and the stiffness vs depth.

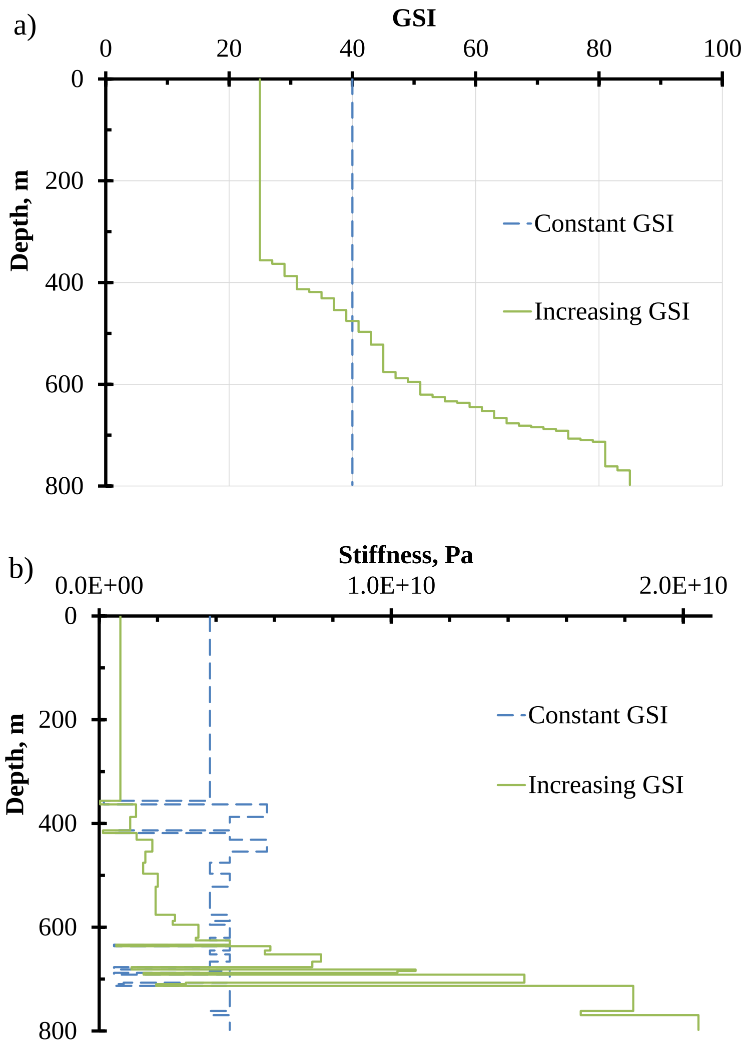

Figure 3.4: a) GSI vs Depth and b) Stiffness vs Depth

Internal friction angle and cohesion were derived from Equations 3.14 and 3.15. The tensile strength was calculated by Equation 3.10. Nonassociated flow rules were used (dilatancy angle = 0) because the overburden was rock, solid aggregate as concrete, at the Naburn site and the nonassociated flow rule showed better results for concrete than the associated flow rule did (Hu and Schnobrich, 1989). Table 3.7 presents the calculated rock parameters, i.e. bulk and shear moduli, internal friction, cohesion, and tension with the rock type and depth. A density of 2700 kg/m ^{3} was taken as an average value for these types of rock following Table 3.3.

Table 3.7: Rock Properties for the Naburn Model (if not mentioned, in Pa)

Depth (m)	**Geomaterial**	**Bulk Modulus**	**Shear Modulus**	σ_{ci}	m_b **(-)**	**s (-)**	a **(-)**	**Friction (degree)**	**Cohision**	**Tensile Strength**
355.6	mudstone	4.02E+08	3.02E+08	9.50E+07	0.16	0.00005	0.5	21.16	7.06E+05	2.68E+04
364	sands	2.84E+07	2.13E+07	5.00E+06	0.25	0.00018	0.5	7.8	4.97E+05	3.53E+03
386.4	sandstone	1.08E+09	8.11E+08	1.20E+08	1.22	0.00020	0.5	35.41	2.20E+06	1.93E+04
414.4	siltstone	9.25E+08	6.94E+08	8.00E+07	0.62	0.00024	0.5	25.63	1.73E+06	3.09E+04
417.2	seatearth	1.12E+08	8.43E+07	1.60E+07	0.57	0.00027	0.5	15.61	1.05E+06	7.51E+03
431.2	siltstone	1.02E+09	7.65E+08	8.00E+07	0.65	0.00029	0.5	25.7	1.84E+06	3.49E+04
453.6	sandstone	1.41E+09	1.06E+09	1.20E+08	1.44	0.00033	0.5	35.6	2.61E+06	2.72E+04
476	siltstone	1.20E+09	9.03E+08	8.00E+07	0.72	0.00038	0.5	25.85	2.03E+06	4.28E+04
495.6	mudstone	1.12E+09	8.40E+08	9.50E+07	0.67	0.00045	0.5	26.1	2.19E+06	6.36E+04
520.8	siltstone	1.46E+09	1.10E+09	8.00E+07	0.80	0.00054	0.5	26.08	2.25E+06	5.35E+04
576.8	mudstone	1.48E+09	1.11E+09	9.50E+07	0.78	0.00072	0.5	26.46	2.52E+06	8.74E+04
588	siltstone	2.03E+09	1.52E+09	8.00E+07	0.95	0.00092	0.5	26.54	2.62E+06	7.73E+04
596.4	mudstone	1.80E+09	1.35E+09	9.50E+07	0.87	0.00099	0.5	26.76	2.75E+06	1.08E+05
621.6	siltstone	2.29E+09	1.72E+09	8.00E+07	1.01	0.00112	0.5	26.73	2.77E+06	8.81E+04
624.4	mudstone	2.08E+09	1.56E+09	9.50E+07	0.93	0.00125	0.5	26.99	2.93E+06	1.27E+05
632.8	siltstone	2.53E+09	1.90E+09	8.00E+07	1.07	0.00131	0.5	26.89	2.89E+06	9.82E+04
635.6	seateath	2.96E+08	2.22E+08	1.60E+07	0.96	0.00137	0.5	16.48	1.70E+06	2.27E+04
644	siltstone	2.66E+09	2.00E+09	8.00E+07	1.09	0.00142	0.5	26.98	2.95E+06	1.04E+05
652.4	mudstone	2.34E+09	1.76E+09	9.50E+07	0.99	0.00151	0.5	27.2	3.09E+06	1.45E+05
666.4	siltstone	2.90E+09	2.17E+09	8.00E+07	1.14	0.00164	0.5	27.13	3.06E+06	1.14E+05
677.6	mudstone	2.60E+09	1.95E+09	9.50E+07	1.05	0.00179	0.5	27.39	3.23E+06	1.62E+05
683.2	seatearth	3.62E+08	2.72E+08	1.60E+07	1.07	0.00190	0.5	16.73	1.85E+06	2.84E+04
686	siltstone	3.22E+09	2.42E+09	8.00E+07	1.21	0.00195	0.5	27.33	3.21E+06	1.29E+05
688.8	mudstone	2.77E+09	2.08E+09	9.50E+07	1.09	0.00200	0.5	27.51	3.32E+06	1.75E+05
691.6	seatearth	3.79E+08	2.85E+08	1.60E+07	1.09	0.00205	0.5	16.8	1.89E+06	2.99E+04
705.6	siltstone	3.46E+09	2.60E+09	8.00E+07	1.26	0.00220	0.5	27.47	3.30E+06	1.40E+05
708.4	seam	6.76E+08	5.07E+08	2.10E+07	2.57	0.00235	0.5	24.66	2.67E+06	1.92E+04
711.2	seatearth	4.18E+08	3.13E+08	1.60E+07	1.15	0.00241	0.5	16.93	1.97E+06	3.34E+04
761.6	siltstone	4.09E+09	3.07E+09	8.00E+07	1.38	0.00292	0.5	27.82	3.55E+06	1.69E+05
770	mudstone	3.90E+09	2.93E+09	9.50E+07	1.31	0.00361	0.5	28.23	3.86E+06	2.61E+05
798	siltston	4.78E+09	3.58E+09	8.00E+07	1.51	0.00387	0.5	28.17	3.80E+06	2.05E+05

3.3.2 Excavation Collapse

A collapse of the excavation was simulated by replacing the excavated coal with the goaf. The goaf was modelled using a double-yield model, which allows both shear and volumetric compression. The properties of the roof material (siltstone), i.e. bulk and shear moduli, internal friction angle and cohesion, were used from Table 3.7. As for the volumetric properties of the double-yield model in FLAC, the stress-strain curve is approximated by a table to generate a linear piecewise curve. In the developed model, the table has 10 rows. Salamon (1983) described the volumetric compression properties of the goaf material by the following equation:

$$\sigma = \frac{\alpha \cdot \epsilon}{\beta - \epsilon} \tag{3.17}$$

where α and β are empirical constants. To eliminate the need for the empirical constants, Salamon (1990) rewrote Equation 3.17 using certain physical parameters:

$$\sigma = \frac{E_0 \cdot \epsilon}{1 - \epsilon/\epsilon_m} \tag{3.18}$$

where E_0 is the initial tangent modulus and ϵ_m is the maximum strain of the goaf material. Since the parameters are difficult to estimate, Equation 3.18 is rewritten.

$$\sigma = \frac{E_0 \cdot \epsilon}{\gamma - \epsilon} \tag{3.19}$$

where γ is used to adjust the height of the goaf after a simulation, and E_0 is the Young's modulus of the roof material. The required height (RH) of the goaf after the simulation was calculated according to Equation 3.20:

$$RH = H \cdot (1 - a) \tag{3.20}$$

where H is the height of the excavation and a is the subsidence factor, which ranges from 0.1 to 0.9 and presented in Table 3.8.

Table 3.8: Subsidence Factor and Ratio of Maximum Horizontal Displacement to Maximum Possible Subsidence after Bräuner (1973) in Bell and Donnelly (2006))

Coal Field and Method of Packing	**Subsidence Factor**
British coal fields	
Solid stowing	0.45
Caving or strip packing	0.9
Ruhr coal field, Germany	
Pneumatic stowing	0.45
Other solid stowing	0.5
Caving	0.9
North and Pas de Calais coal field, France	
Hydraulic stowing	0.25–0.35
Pneumatic stowing	0.45–0.55
Caving	0.85–0.90
Upper Silesia, Poland	
Hydraulic stowing	0.12
Caving	0.7
Russia and Ukraine	
Donbass district	0.8
Lvov-Volyn district	0.80–0.90
Kizelov district	0.40–0.80
Donetzk, Kuznetsk and Karaganda districts	0.75–0.85
Sub-Moscow and Cheliabinski districts	0.85–0.90
Pechora	0.65–0.90
United States	
Central	0.50–0.60
Western	0.33–0.65

Hence, the subsidence factor of the mines that have longwall excavations is 0.9 for mines in the UK. For the case at hand with a height of the excavation of 2.8m, the required final height of the goaf (RH) was estimated as 0.28m using Equation 3.20. Altering the empirical parameter γ, the simulation was repeated until the error in the goaf height after the simulation reaches 5% or less of the required height. In Table 3.8, it can also be seen that stowing the mine reduces the subsidence factor by two-three times depending on the method of stowing. The ash left after UCG may be considered as stowing, and this is discussed later in Chapter 6.

3.3.3 Modelled Surface Subsidence

To investigate the influence of the failure model on the surface subsidence profile, three popular constitutive models embedded in FLAC, i.e. the Mohr-Coulomb, modified Hoek-Brawn, and strain-softening constitutive models were implemented for the overburden. Table 3.7 in Subsection 3.3.1 presents the elastic, Hoek-Brown and Mohr-Coulomb parameters for the simulations. The elastic part of the model required the bulk and shear moduli. The Hoek-Brown parameters included uniaxial compressive strength (σ_{ci}), m_b, s, and a. The Mohr-Coulomb parameters were friction angle and cohesion, which were calculated out of the Hoek-Brown parameters as described in Subsection 3.2.2.

Figure 3.5 shows the obtained surface settlement profiles with the modified Hoek-Brown, Mohr-Coulomb, and strain-softening models, measurements, and empirical estimations of the surface subsidence trough by the Subsidence Engineers' Handbook (NCB, 1975). The distance zero corresponded to the centre line of the excavation, and it was assumed that there was little or no gradient across the longwall face so that the subsidence profile is symmetrical about the excavation's centre line.

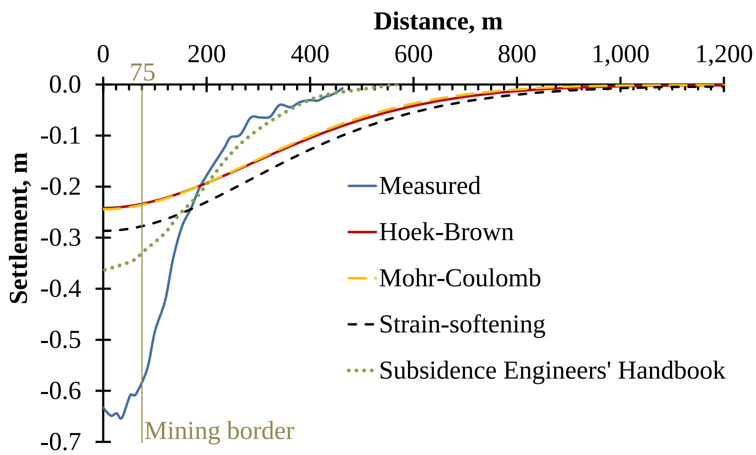

Figure 3.5: Surface Settlement Half-Profile Obtained with Different Constitutive Models

Figure 3.5 illustrates that the empirical method provided in the Subsidence Engineers Handbook (NCB, 1975) failed to predict the correct depth of the trough. Therefore, there was a need for a better tool, for example, numerical modelling. However, the modelling worsened predictions as it can be seen in Figure 3.5. At the same time, the results of the Mohr-Coulomb and Hoek-Brown failure criteria agreed closely with each other. This result agreement means that the calculation of the Mohr-Coulomb parameters out of the Hoek-Brown parameters was correct.

The further investigation includes the implementation of the strain-softening model available in FLAC. The model uses the Mohr-Coulomb failure-criterion to detect failure, and cohesion of the rocks would suffer a post-failure reduction in strength. Using test results, Pourhosseini and

Shabanimashcool (2014) proved that the post-failure friction angle of rocks is constant, which agrees with the kinked-cracking theory. During kinging, the frictional component of the rock material is unchangeable because of the constant mechanical properties of the crack surface (Bieniawski, 1967). For post-peak variations of inherent cohesion, Pourhosseini and Shabanimashcool (2014) suggested a function:

$$c = c_o \left(1 - \frac{tanh(100\gamma_p)}{tanh(10)} + 0.001\right)^n \tag{3.21}$$

where γ_p is the plastic shear strain, %; c_0 is the cohesion at peak strength of the rock where γ_p=0, and n is the fitting parameter, which depends on rock type and its magnitude varies from 0.29 for sandstone to 0.34 for mudstone (Pourhosseini and Shabanimashcool, 2014). During the evaluation of the effect of this parameter on the subsidence profile, the only small effect was noticed. Figure 3.6 presents the subsidence troughs obtained with different parameter n.

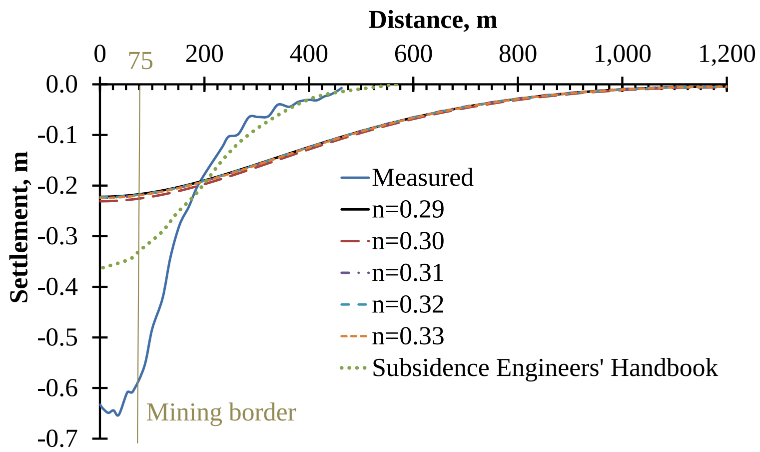

Figure 3.6: Surface Settlement Half-Profile Obtained with Different Parameter n

3.3.4 Caving Extension

Besides gradually increasing the input GSI with the depth, the extension of the plastic zone above the excavation is provoked by the size of the caving zone. Subsection 2.2.4 listed equations to estimate GSI. Equation 2.2 is the most popular. According to Table 3.3 for the Naburn site, the bulking factor of the roof layer is between 1.4 - 1.5, or more precisely, it is 1.447 using Equation 2.3 and uniaxial compression strength of 80MPa from Table 3.2. Hence, the caving height is about 5.6m - 7.0m. The equations from Table 2.2 estimates the caving height from 4.1m to 152.4m for the Naburn site.

In this work, there are two caving heights considered: a caving roof layer of 15m and 29.9m. The caving zone, which corresponds to the disintegrated rock, can be described by a GSI of 25 (Table 3.5). Figure 3.7a depicts that the model without a caving area predicts the plastic deformation above and under the goaf is in equal proportion. The model with caving heights of 15m and 29.9m result in a larger area of plastic deformation above the goaf than the area of plastic deformation under the goaf (Figure 3.7b and Figure 3.7c), respectively. At the same time, the model with a caving height of 15m experienced more plastic deformation than the model with a caving height of 29.9m. It is interesting to notice that in the case of the model without a caving zone, shear localization appears (Figure 3.7a).

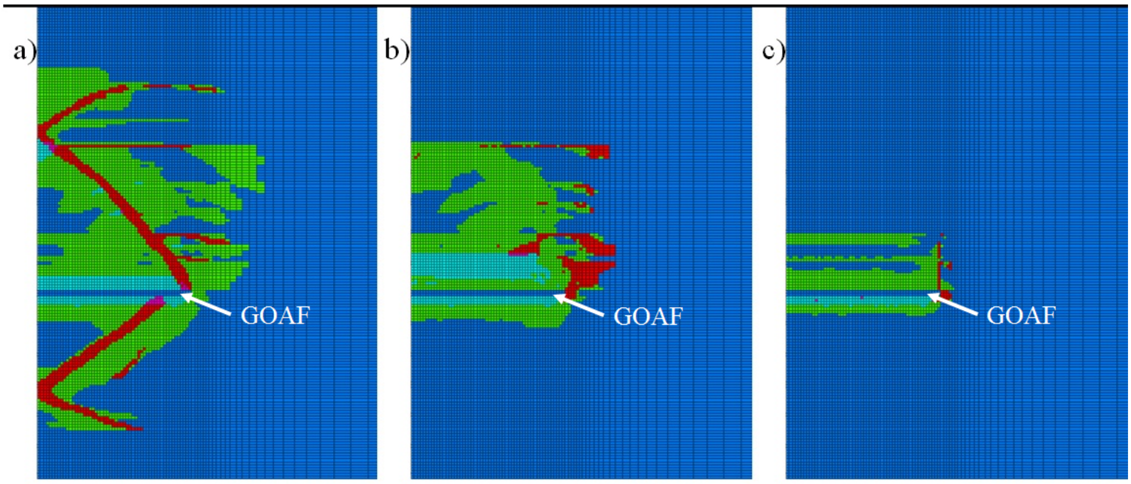

Figure 3.7: Shear Strain Localization and Caving Zone. a) no caving; b) 15m caving; c) 29.9m caving. Green - shear failure in the past. Red - shear failure now

Investigations of the subsidence trough showed that the depth of subsidence was inversely correlated with caving height (Figure 3.8). The deepest and closest to the field measurements trough was modelled without the caving zone. A caving height of 29.9m resulted in the shallowest trough. The larger extent of the plastic zone above the goaf caused the deeper trough.

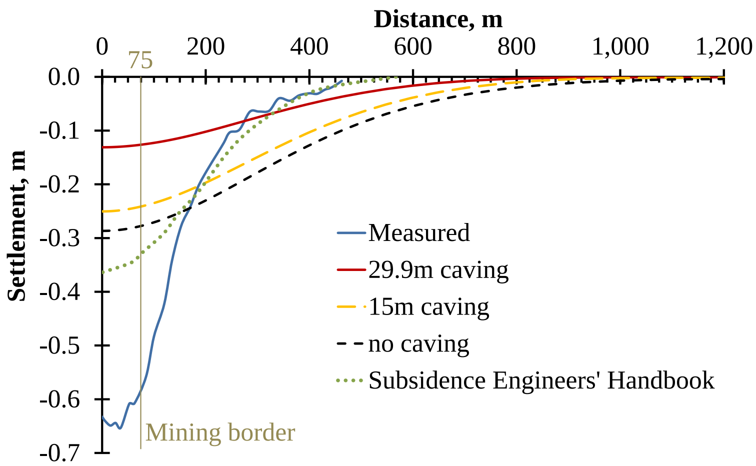

Figure 3.8: Surface Subsidence Half-Profile for Different Caving Heights

Figure 3.8 also shows that altering the caving height does not help achieve the measured depth of the subsidence trough; therefore, the caving height cannot play a role in improving modelled predictions.

3.3.5 Goaf Behaviour

A collapse of a mine causes perturbations of the stresses. The exact perturbations are difficult to estimate since the stresses alter deep underground. However, the theory says that three distances of the stress behavior can be distinguished, namely $D1$, $D2$, and $D3$. $D1$ is the distance of the recovering vertical stresses to the primary values in the goaf. $D2$ is the distance of the recovering vertical stresses in the seam between its peak value at a goaf rib and the vertical stress completely recovered to the primary state. If the coal is crushed at the goaf rib, $D3$ is the distance of the crushed coal between the goaf rib and intact coal. These distances are illustrated in Figure 3.9.

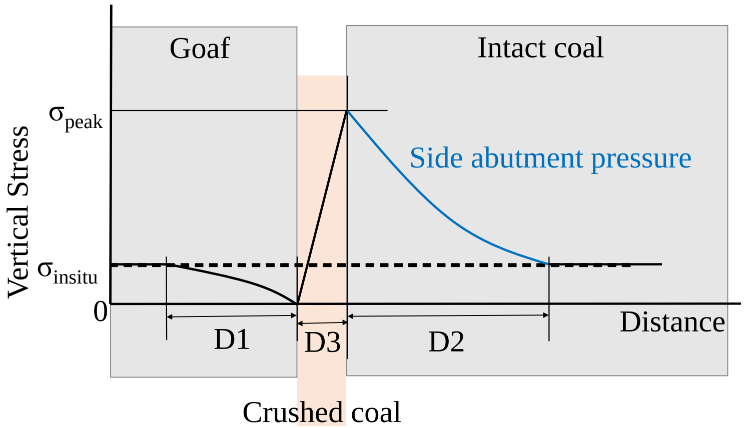

Figure 3.9: Theoretical Vertical Stress in the Vasinity of the Goaf after Wilson (1982)

After careful literature search on the goaf behavior, it was concluded that the vertical stresses in the goaf after perturbation should recover to the natural stresses at distance $D1$ from the goaf rib as shown in Figure 3.9. Wilson (1982) suggested that $D1$ was 30-40% of the overburden thickness. To obtain distance $D1$ sufficiently long for recovering stresses of the primary values, a fictitious surface subsidence model was developed by reducing the Naburn model to accelerate calculations and increasing the width of the goaf from 75m to 180m. Figure 3.10 illustrates the layout of the model.

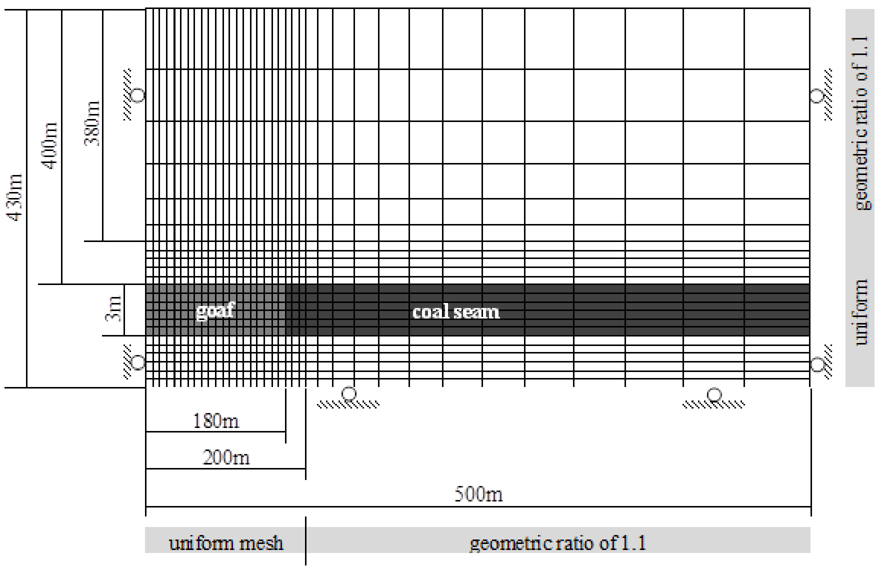

Figure 3.10: Layout of the Fictitious Model

Figure 3.10 depicts the dimensions of the fictitious model. The height was 430m and the width was 500m. The depth of the coal seam was 380m. The increase in the width of zones started at 200m from the right side of the model. The increase of the height of zones started at 130m from the bottom. This mesh configuration let the model run fast. Additionally, to reduce run-time, the simple elastic constitutive model was implemented in the overburden, instead of the plastic models. An elastic modulus of 5.25e+8Pa and Poissons ratio of 0.25 were assigned.

The fictitious model was run for two cases with both the traditional double-yield, which has been earlier used in Subsection 3.3.2, and modified Cam-clay models in the goaf. The principle of implementation of the modified Cam-Clay model into goaf is discussed later. Figure 3.13 illustrates the results of the model.

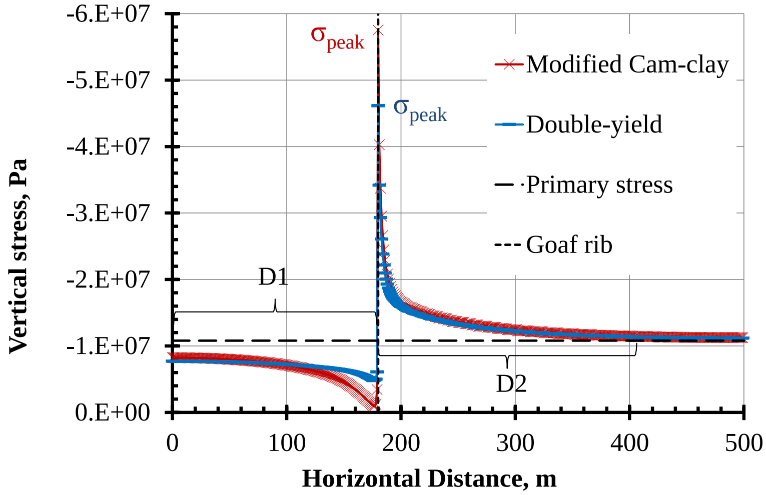

Figure 3.11: Modelled Vertical Stress in the Goaf

Figure 3.11 shows that the stresses did not recover to the primary stresses in the models with the double-yield and modified Cam-clay materials in the goaf. However, the modified Cam-clay model predicted the stresses in the goaf closer to the theoretical. The peak and stresses at the rib of the goaf were higher, which corresponded better to the theory.

In an attempt to repeat this improvement, the modified Cam-clay model was implemented into the goaf of the Naburn model. The goaf material is coarse granular material as it was justified in Section 2.4. After triaxial tests on the crushed rock, Indraratna and Salim (2002) obtained Cam-clay parameters, i.e. lambda (λ)=0.188, kappa (κ)=0.007, and a frictional constant (M)=1.9 were assigned. The required height (RH) of the goaf after the simulation (aforementioned in Subsection 3.3.2) was obtained by altering the specific volume at reference pressure on the normal consolidation line or the pre-consolidation pressure. Figure 3.12 depicts curves of the relationship between the obtained goaf height and specific volume for pre-consolidation pressures of 1e5Pa, 1e4Pa, and 1e3Pa.

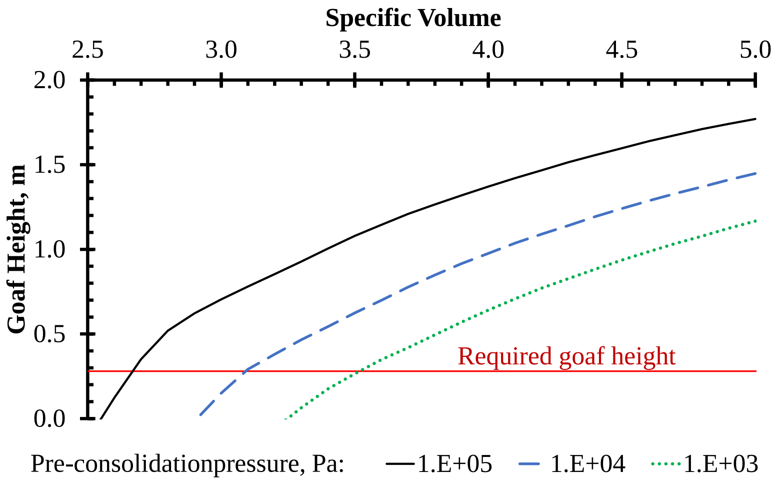

Figure 3.12: Obtaining the Required Height of the Goaf

Figure 3.12 illustrates that the required height of the goaf after simulation can be obtained with the modified Cam-clay model for specific volumes of 2.65, 3.1, and 3.55 when the pre-consolidation pressure is 1e5Pa, 1e4Pa, and 1e3Pa, respectively. Unfortunately, the Naburn mine does not have a sufficiently-long goaf, and the recovering of the primary stresses with the modified Cam-clay model cannot be checked. The stress results with the double yield and modified Cam-clay models are two identical curves as shown in Figure 3.13.

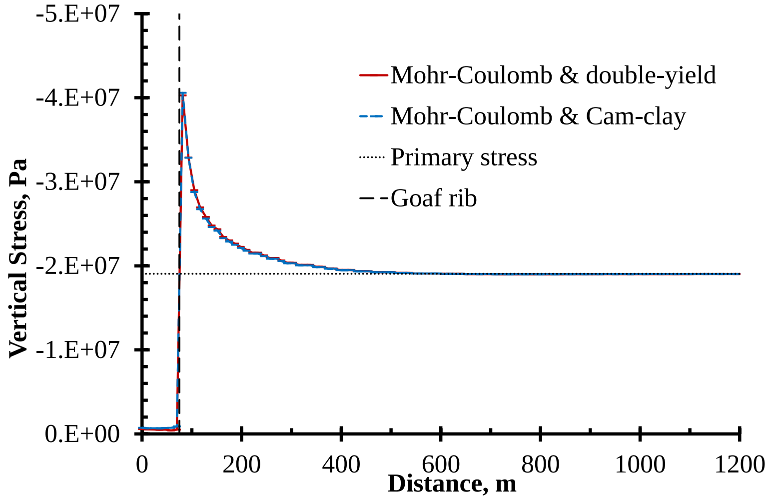

Figure 3.13: Vertical Stress within the Goaf in the Naburn Model

Figure 3.13 depicts two identical stress curves which were obtained with the double-yield model and the modified Cam-clay model at the level of the goaf roof. In the case of the short Naburn mine, the goaf was a highly distressed zone shown as a deep flat curve in the left part of the chart and rising highly up in the rib of the goaf. Figure 3.14 overviews stresses in the whole model domain including the detailed view of the goaf area.

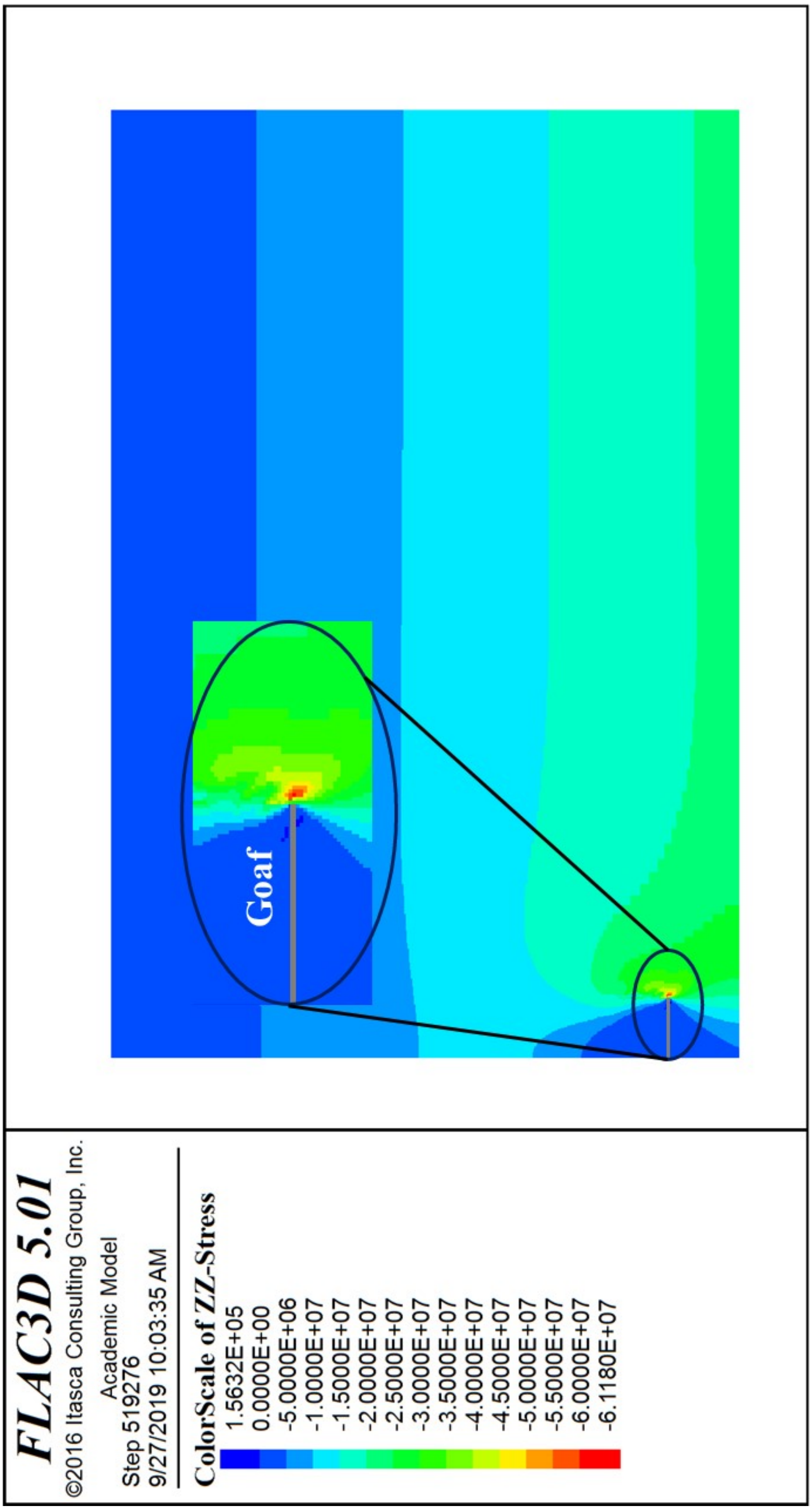

Figure 3.14: Contour of the Vertical Stresses in the Naburn Model

Figure 3.14 is a contour map of the stresses induced by the surface subsidence. The contours are like a wave when the left part of the wave is much deeper than the right part of the wave. The highly-distressed zone (in blue) can be seen in the area near the goaf.

3.3.6 Mesh Density

During simulations, one difficulty was noticed, i.e. mesh density influenced the modelling results, i.e. the goaf height. The mesh with cube-shaped zones, 2.8m on a side, was densified gradually by reducing the size of the zone. Figure 3.15 illustrates that the goaf height after the simulation becomes larger with reducing the size of the zone.

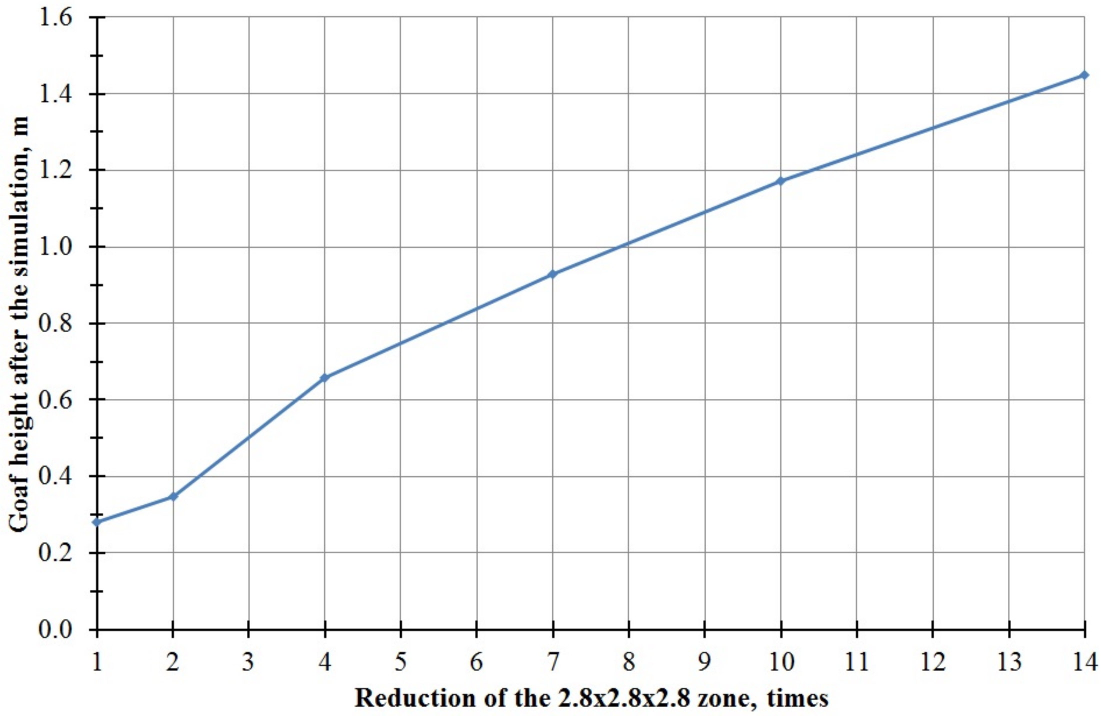

Figure 3.15: Goaf Height after the Simulation vs Mesh Density

Figure 3.15 shows the relationship between mesh density and the height of the goaf after simulation. The mesh was densified twice each time from the least dense mesh with a cube-shaped zone of 2.8m. The final cube-shaped zone was of 0.2m when the mesh was densified in 14 times in total. Further densification of the mesh caused model crash due to insufficient computer memory. Figure 3.15 shows that the denser the mesh was, the higher the goaf was modelled. Since the research aims to improve modelling of surface subsidence, investigation of the influence of mesh density on surface subsidence was carried out. The mesh density was twice decreased. The next chapter will investigate the impact of the mesh density on model results in detail.

3.4 Summary

The chapter started with a description of the site of interest, Naburn. Then the method of derivation of the model parameters using borehole data was developed based on the extensive literature search. Using this method, the parameters were calculated for the Naburn site. Then the model of surface subsidence after the mine collapse was developed. The model results showed that it was impossible to correctly predict the subsidence trough using the constitutive models built in FLAC3D, i.e. Mohr-Coulomb, strain-softening, and modified Hoek-Brown models. Therefore, some advanced constitutive model should be programmed and embedded in FLAC3D. The chapter shows that the stresses in the goaf, which were modelled with the double-yield and modified Cam-clay models did not correspond to the theoretical stresses. Therefore, some advanced constitutive model is required. Finally, one more difficulty was pointed out, which was the impact of the mesh density and shapes of the zone on the model results. Therefore, thorough mesh density analysis is required. The next chapter deals with the mesh difficulty in detail.

Chapter 4

Model Mesh for Better Surface Subsidence Predictions

This chapter aims to find a FLAC3D mesh that is most suitable to model the collapse of a shallow UCG reactor and surface subsidence. The research shows some error abnormalities for modelling of stress and deformation with different mesh density and sizes in FLAC3D. These abnormalities are crucial to modelling of surface subsidence correctly. Therefore, the extensive exercises with different mesh configurations are carried out before modelling of surface subsidence at the UCG site. The explanation of the abnormalities is beyond the scope of this work.

4.1 Overview

The chapter investigates mesh configurations to model stresses and displacements in small errors while modelling of surface subsidence. The investigations reveal that six cube-shaped zones in the height of the goaf are the optimal number of zones to model correctly stresses and strains in the goaf. Two cuboid-shaped zones that are three times larger in the goaf height result in small error too. The mesh configuration of the cube-shaped zones of 200x1x60 or denser can be used to model surface subsidence in FLAC3D.

In FLAC3D and FLAC2D, the selection of the appropriate mesh density and zone size affects both displacements and stresses. For example, when the end deflection of a cantilever with elastic properties is simulated, the solution is extremely sensitive to the mesh density and zone ratios. FLAC2D and FLAC3D user manuals (Itasca, 2008, 2011) recommend keeping a high number of zones in areas of non-linear stress change and keeping zone aspect ratios as close as possible to 1:1. However, after attempting to model the deflection of an elastic cantilever and the deflection of a thin cylinder under a point load in FLAC2D, Pound (2006) argued that a high-density mesh was not a panacea.

In this work, a great number of scenarios was considered in FLAC3D to justify the mesh for modelling of surface subsidence. The analysis can be divided into two parts, i.e. the mesh justification for modelling of the goaf behaviour and modelling of the behaviour of the whole domain. For these tasks, a cantilever under a point load, a thin-walled hollow cylinder under a point load, a thick-walled hollow cylinder with a uniformly distributed pressure on its inner side, cylindrical hole in an infinite Hoek-Brown medium, and the rough strip footing on a cohesive frictionless material were considered. The three aspects of the model mesh geometry were addressed, i.e. the relative dimensions of the modelled object, the mesh density, and the aspect ratios of the zones.

4.2 Cantilever

4.2.1 Model Description

The general layout of the cantilever model is illustrated in Figure 4.1. x is the horizontal direction (the longitudinal direction of the beam), z is the vertical direction, and y is the out-of-plane direction, coinciding with the width of the beam. For convenience, the capital letters X, Y, and Z indicate the physical dimensions of the beam, and the small letters x, y, and z indicate the sizes of the zones in their corresponding directions. Sometimes the ratio a:1, where a is some value, is called a ratio a for simplicity, especially in the figures. The zonal points were prevented from translating in the y-direction using an appropriate boundary condition. The left end of the beam had a fixed boundary condition, and the right end was placed under a point load P of 50kN at distance X from the point of fixity. The direction of bending was in the z-direction as shown in Figure 4.1.

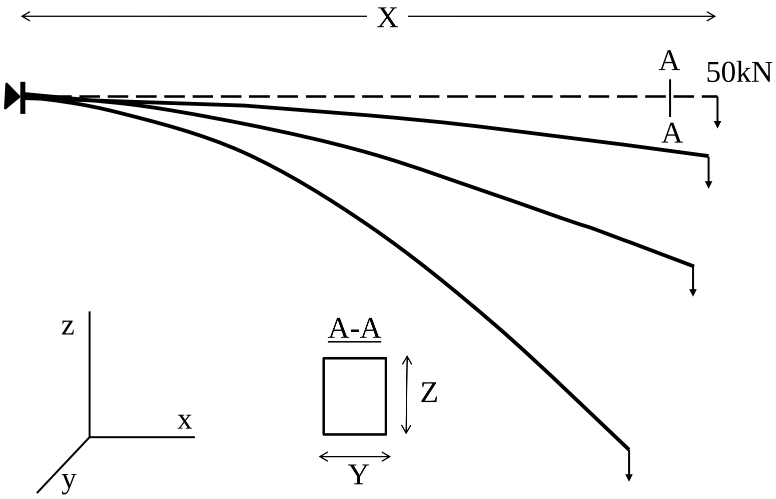

Figure 4.1: Layout of the Cantilever Model

The cantilever was modelled as a purely elastic material with Young's modulus E of 150GPa. The theoretical maximum deflection (d) was found using the standard closed-form solution presented in Equation 4.1.

$$d = \frac{-PX}{3EI} \tag{4.1}$$

where I = the second moment of inertia of the beam's cross-section.

Using standard mechanics, the stress distribution throughout the beam in the z-direction was calculated according to Equation 4.2.

$$\sigma = \frac{XZP}{2I} \tag{4.2}$$

The size of the beam was changed during the study; hence, the theoretical displacements had to be calculated for each case.

4.2.2 First Trial Tests

In the beginning, the trial cases with different mesh configurations were run to understand how the mesh should be analyzed. Pound (2006) demonstrated that in the 2D case, the most accurate simulation occurred when six square zones were used over the depth of the beam, or two rectangular zones were used over the depth of the beam with the zone ratios three times taller than the width in the direction of bending. This investigation focused on a three-dimensional model; hence, there was a need to study the out-of-plane number of zones. Following the procedure of Pound (2006), three beams were considered. The arrangements of the number of zones and zone sizes are presented in Table 4.1. One of the mesh configurations had cuboid-shaped zones which were three times larger in the direction of bending. The other configurations consisted of cube-shaped zones. The results were obtained by altering the number of zones in the y-direction while keeping the same size of the zones. The error was calculated as a percentage of the difference between theoretical and modelled solutions divided by the theoretical solution. The error against the beam size and its mesh arrangements are presented in Table 4.1.

Table 4.1: Error of the Model with Different Beam Size and Mesh Arrangement

	Number of Zones in x- y- z-directions	**Zone Size, m** x-y-z	**Beam Size** X-Y-Z	**Diflection Error, %**
a	226-40-6	1-3-3	226-120-18	0.84
b	226-6-2	1-3-3	226-18-6	0.82
c	226-2-2	1-3-3	226-6-6	0.74
d	180-6-6	0.05-0.05-0.05	9-0.3-0.3	1.8
e	180-4-6	0.05-0.05-0.05	9-0.2-0.3	1.8
f	180-2-6	0.05-0.05-0.05	9-0.1-0.3	1.8
g	450-6-6	0.02-0.02-0.02	9-0.12-0.12	26.1
h	450-4-6	0.02-0.02-0.02	9-0.08-0.12	26.4
i	450-2-6	0.02-0.02-0.02	9-0.04-0.12	26.1

Table 4.1 presents nine different solutions for the cantilever with a different number of zones. Table 4.1 shows that the number of zones in the out-of-plane direction had no significant effect on the calculation of the cantilever deflection. This small impact took place when the number of zones in the x-z plane caused FLAC3D to calculate deflections with the big error. These results were anticipated because the model was fixed in the out-of-plane direction, and the problem of the cantilever deflection was reduced to the 2D problem. The small impact of the number of zones in the out-of-plane direction meant that the number of zones in the out-of-plane direction should not be investigated in this section.

When the beam was very long and thin, i.e. a beam of 9m length (X) and less than 0.3m height (Z), the model did not perform well. Please see lines g, h, and i of Table 4.1. The unsatisfactory results were caused by the Z/X ratio (slenderness ratio), which played a significant role in the accuracy of deflection calculation. The significance of the slenderness ratio is presented in Subsection 4.2.6. Keeping the size of zones and increasing the number of zones in the y-direction, the size of the beam into the page (Y) did not play a significant role when the Y/X and Y/Z ratios were greater than 0.04:1. This issue is addressed in Subsection 4.4.3.

4.2.3 Out-of-Plane Zone Ratio y/x

The previous subsection demonstrated that the number of zones in the y-direction has a negligible effect on the result. However, it is also important to investigate the effect of the out-of-plane zone ratio in the y-direction. Hence, by using two zones in the z-direction, the aspect ratio y/x was investigated when z = $x/3$ (aspect ratio z/x was chosen to be consistent with the analysis of Pound (2006)). This mesh arrangement can be seen in Figure 4.2.

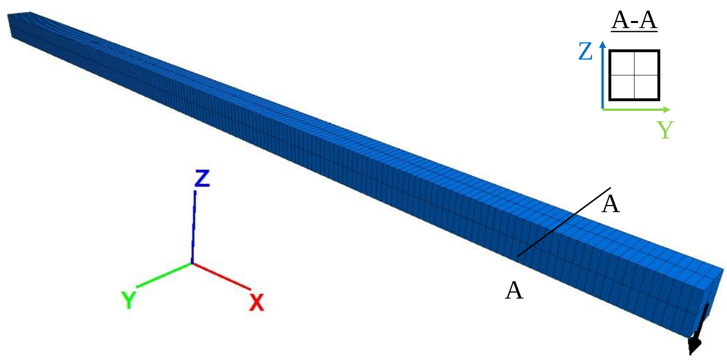

Figure 4.2: Cantilever in FLAC3D

Figure 4.2 illustrates the beam with 226 zones in the x-direction and two zones in the y- and z-directions, cross-section A-A of the beam and the black downward arrow of the applied force. In comparison with the previous study, these numbers of zones were kept. To broaden the range of possible ratios y/x and to reduce computational time, four beams of different widths were considered, i.e. 0.3m, 0.6m, 0.9m, and 3.6m (y-direction), whilst the height of the beam was kept constant at 0.3m. Figure 4.3 is a graph of the relationship between errors and aspect ratio y/x.

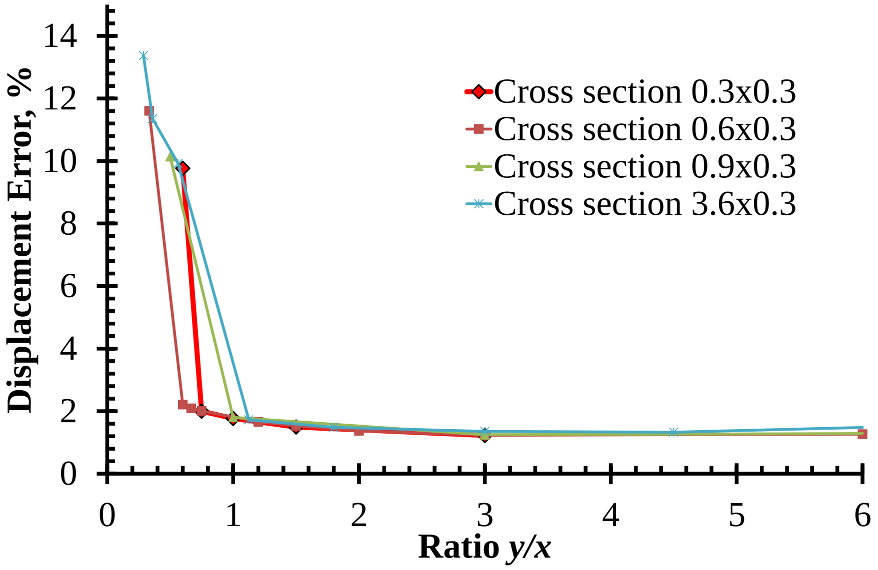

Figure 4.3: Displacement Error versus Ratio y/x When z/x=3

Figure 4.3 shows that all four curves of the results of the different width beams agreed well. This agreement was expected in accordance with the primary investigation on different width beams in Subsection 4.2.2. Figure 4.3 also illustrates that the dependence between the displacement error and ratio y/x was inversely exponential. The error rapidly decreased from large values to small values of y/x until a ratio of three was reached. From this point, the error mildly increased with increasing y/x and stayed below 2% error.

Based on the modelling results described above, it could be concluded that for a three-dimensional model, the optimal zone ratios y/x and z/x were three for the model in simple bending. Let's call this zone configuration **the optimal zone configuration**. There was no need to check ratio z/y because it was interconnected with ratios y/x and z/x; hence the optimal ratio z/y was three as well.

4.2.4 In-Plane Ratio z/x

The previous section exploited the result by Pound (2006), which said that the most efficient in-plane zone aspect ratio (z/x) was equal to three. This section successfully checked this conclusion for the three-dimensional model. This investigation was carried out by keeping aspect ratio y/x equal to three and altering zone size z as shown in Figure 4.4.

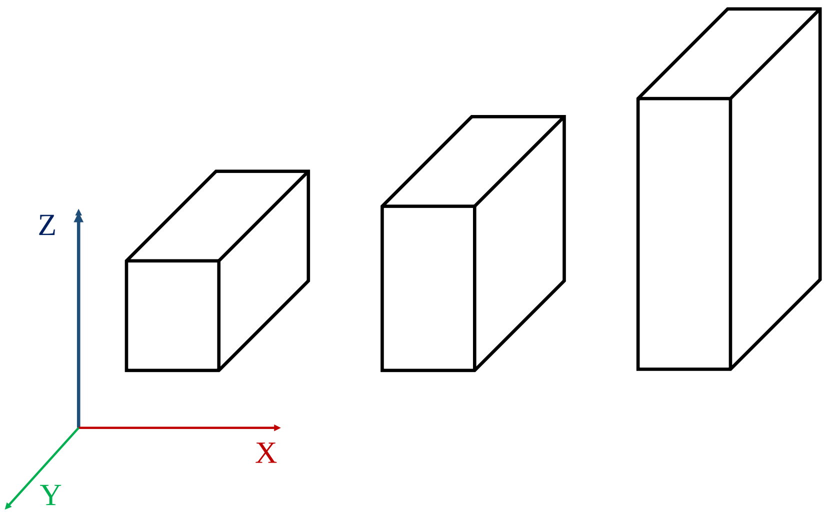

Figure 4.4: Altering Zone Size in the z- direction

The beam mesh was created so that there were two zones across both the height and width of the cross-section of the beam. Figure 4.5 is a relationship between deflection error and aspect ratio z/x.

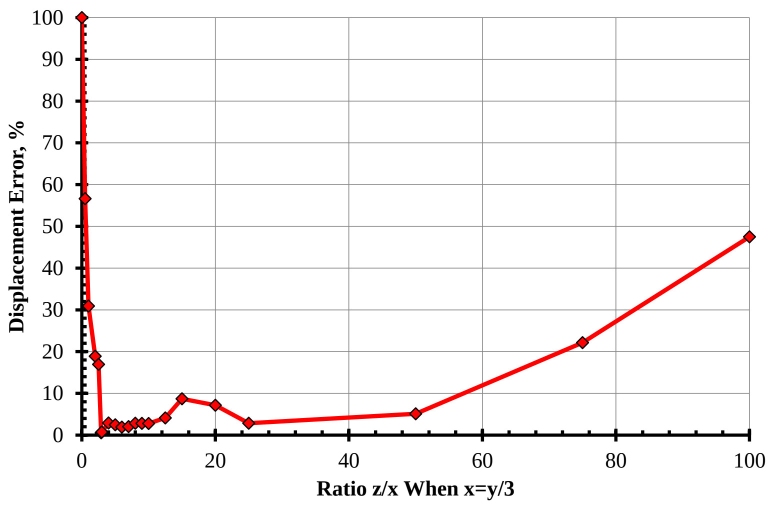

Figure 4.5: Displacement Error versus Ratio z/x When y/x=3

Figure 4.5 illustrates that z/x of between three and ten provided a deflection error of less than 3%. Smallest errors of 0.55% and 0.74% were obtained for ratios z/x of 2.9:1 and 3:1, respectively. The error increased non-monotonically for larger zone ratios. After a ratio of approximately 21:1, the error reduced to a small value. For zone ratios of greater than 21:1, the displacement error started to increase monotonically, and the error rose dramatically after a ratio of 50:1. The optimal aspect ratio z/x was concluded to be between three and ten when two zones were used across the height of the cross-section of the cantilever and when the out-of-plane zone ratio was 3:1. The smallest error was found when a zone ratio of approximately three was used; therefore, the analyses and assumptions in Subsections 4.2.2 and 4.2.3 were justified.

4.2.5 Number of Zones in the z-Direction

Pound (2006) proved that two rectangular-shaped zones which sides in the bending direction were three times smaller than the sides in the direction perpendicular to the bending, or six cube-shaped zones in the beam height were the optimal mesh arrangement for the two-dimensional model. For the three-dimensional model, the optimal zone configuration was found in Subsections 4.2.3 and 4.2.4. This subsection shows that the two-zone arrangement in the height of the cross-section was optimal for the three-dimensional model when the zone sides in the bending direction, three times smaller than the sides in the direction perpendicular to the bending. The six-zone configuration is also optimal for any shape of the zone.

As it was concluded in Subsection 4.2.2, the number of zones in the y-direction did not significantly influence the results. Therefore, in this study, only the effect of the zone in the z-direction was investigated. Starting from two zones, the number of zones was constantly increased in the y- and z-direction. The height and width of the cross-section (Y and Z) were kept constant. Figure 4.6 presents the relationship between the deflection error and the number of zones in the z-direction for the cuboid- and cube-shaped zone meshes.

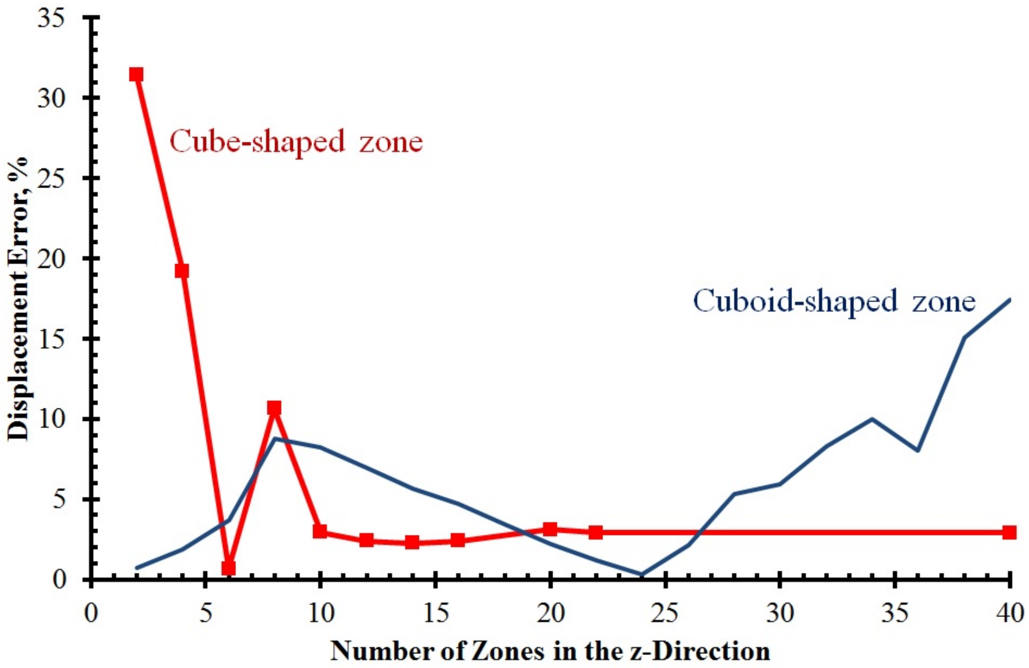

Figure 4.6: Displacement Error versus Number of Zones in the z-Direction

Figure 4.6 shows that the smallest error was calculated when two and 24 cuboid-shaped zones were used in the z-direction. The error is increased when the mesh density from two zones to eight zones increased. The error hit a peak value when the number of zones was eight, and then it decreased until 24 zones were used. Then the error increased non-monotonically. This investigation was repeated using cube-shaped zones (i.e. aspect ratio 1:1) instead of the zones with aspect ratios z/x and z/y of 3:1.

Figure 4.6 also presented the investigation on the number zone in the z-direction keeping the mesh with cube-shaped zones. The smallest error was obtained when six zones were used across the height of the beam (Figure 4.6). Figure 4.6 also shows that using eight zones across the height of the beam caused an unexpected spike in the calculated error. The further increase of the number of zones, more than ten, did not significantly reduce the calculated error. When only two zones were used, errors of more than 30% were calculated. The smallest error was obtained with six zones in the z-direction. This mesh arrangement permitted constant stress zones with a linear stress function representing the non-uniform stress distribution along the beam thickness (z-direction).

4.2.6 Slenderness, Ratio Z/X

Apart from the mesh configuration in the goaf, a suitable mesh should be found for the whole model domain. Since the domain of the surface subsidence model was rectangular, like a very thick beam, the effect of cantilever slenderness on the calculated error should be investigated. For this, the ratio between the length and height of the beam was considered. The size of the cube-shaped zone and the cross-section were kept constant. Figure 4.7 presents three analyses that investigated the relationship between ratio Z/X and the displacement error. The black line indicates the case when $Y = Z = 0.3$m and had six zones of equal size across both the width and height of the beam. To reduce the height to length ratio, the length of the beam was increased by adding zones in the x-direction. The second and third curves of Figure 4.7 are for the same dimensions of the beam, but the density of the mesh was increased two and four times, so the cross-section had 12 and 24 zones across, respectively.

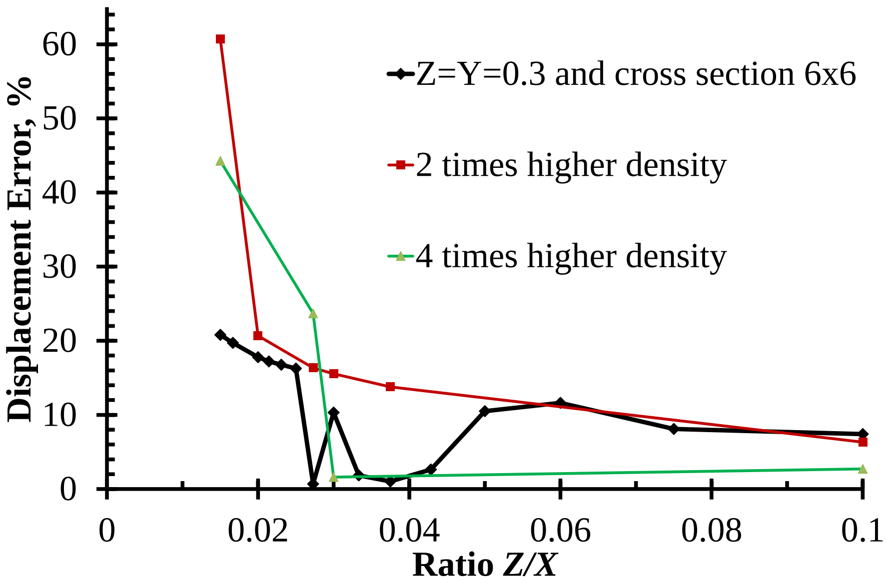

Figure 4.7: Displacement Error versus Ratio Z/X

Figure 4.7 shows that for a ratio Z/X of less than 0.025, the correct solution could not be found even with a high mesh density. All three curves have an inverse exponential behaviour; however, with the 6x6 cross-section, some irregularities were noticed: the smallest errors were obtained with ratios Z/X of 0.027 and 0.037. Errors of less than 5% were obtained when the ratio was 0.033 or 0.037; but when the ratio was 0.03, 0.05 or 0.06, the error was more than 10%. With increasing the ratio from 0.06, the error became gradually less than 10%.

To investigate how tall the beam could be modelled whilst still achieving a reliable solution, the number of cube-shaped zones was gradually increased in the z-direction thus increasing the height of the beam. Subsection 4.2.5 showed that the error would remain below 5% by using a high number of zones in the z-direction. Figure 4.8 presents the results of increasing the value of ratio Z/X.

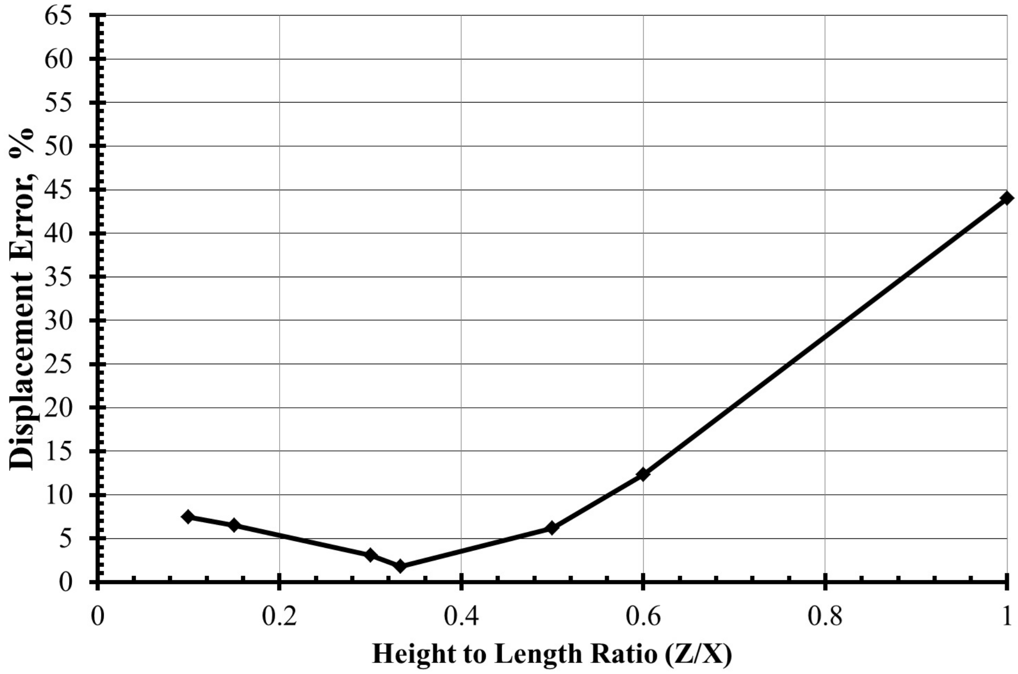

Figure 4.8: Study on How Thick the Beam Can Be Modelled

Figure 4.8 depicts that the minimum error was achievable with ratio Z/X of 0.33:1. Beyond this ratio, the error constantly increased. The 'square' beam, alias beam of equal height and length, resulted in the calculated error of 45%. If Figure 4.7 and Figure 4.8 are juxtaposed, the smallest error was for the height to length ratio of 0.33:1.

The study continued with the investigation of the influence of increasing mesh density on the result when the shape of the beam was a cube, or in other words, when ratios Z/X and Z/Y were equal to one. The sizes of the beam were chosen as 0.3m in all directions. After running the model with higher mesh density, it was concluded that the increase in the density of the mesh did not reduce the error significantly. Table 4.2 presents a number of zones, a zone size, and displacement errors. The total number of zones had an impact on model running time. The largest number of zones, 592704 zones, took several days to run the model. Despite the very dense mesh, the displacement error was always large, about 50%. The smallest error of 44% was achieved for the mesh with six zones in all three directions.

Table 4.2: Error of the Model, 'Cube-Shaped' Beam

Number of Zones in x- y- z- directions	**Zone Size*, m** $x=y=z$	**Total Number of Zones**	**Error, %**
6-6-6	0.05	216	44
12-12-12	0.025	1728	47.2
24-24-24	0.0125	13824	48.1
36-36-36	0.008(3)	46656	48.3
48-48-48	0.00625	110592	48.4
60-60-60	0.005	216000	48.3
72-72-72	0.0041(6)	373248	48.3
84-84-84	0.00357(142857)	592704	48.3

*There are repeating decimals in the brackets.

This study showed that the 'square' beam model predicted the theoretical results with an error of about 50%. The problem could be that the beam theory did not work for 'square' beams, and this shape of the beam should be considered as a plate. However, the attempt to improve the situation is presented in the next subsection.

4.2.7 'Square' Beam

Subsection 4.2.6 demonstrated that it was not possible to obtain the theoretical solution for the beam with a large height to length ratio. However, as it was mentioned in Subsection 4.2.6, this was essential for modelling of surface subsidence. Hence, an attempt to obtain the minimal error when the beam had the same size in both the x- and z-directions was performed. The density of the mesh was changed keeping two cube-shaped zones and altering the size of the beam in the out-of-plane direction (y-direction). Subsection 4.2.2 shows that the number of elements provided no slenderness issues and the large size of the beam into the page did not influence the result. In this study, sizes X and Z were equal. Figure 4.9 presents the relationships between stress and displacement errors and zone sizes. Instead of mesh density, the zone size was depicted to improve the visibility of the graph. It is clear that when the zone size increased, the total number of zones decreased.

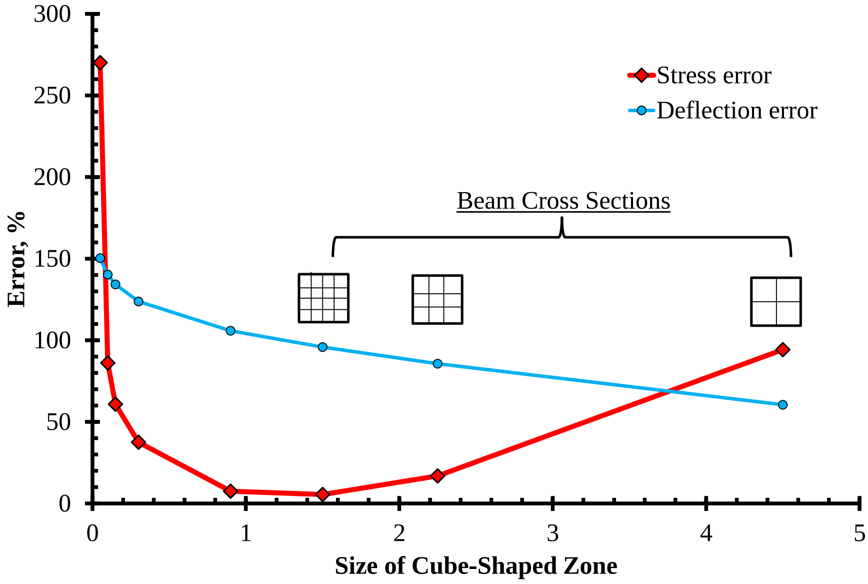

Figure 4.9: Errors versus Zone Size When $X = Z = 9$m

Figure 4.9 shows that the deflection error monotonically decreased with increasing zone size (decreasing the mesh density). However, the stress error changed its behaviour from decreasing to increasing at a size of 1.5m. Therefore, the errors were not due to non-linear stress gradients. The shape of the curves with a small size of the cube-shaped zone is inversely exponential. Surprisingly, the greatest error in displacement was found when the mesh was dense, and the largest error of stress was also seen when the mesh was dense. In Figure 4.9, it was concluded that the beam with a square in-plane shape could not reliably simulate the beam deflection. When the denser mesh was used, the displacement error reduced; however, the stress error increased.

The attempt of improving the prediction of the analytical results with the square beam failed. However, as Table 4.2 shows, the displacement error was constant for different mesh densities (starting from 24x24x24) of the square beam. This gives the idea that the deflection of the beam was calculated by FLAC3D correctly, and as it has been mentioned, the theory of the beam was not applicable to the 'square' beam and mesh density of 24x24x24 and higher could be recommended to model surface subsidence.

4.2.8 Stress

The previous results show that the minimum displacement error was obtained with the cube-shaped zones or the zones in which two sides were three times larger than the third one, i.e. y/x=3 and z/x=3, were used. In this subsection, these zone ratios were used to check the errors in stresses starting with the investigation of the mesh with the cube-shaped zones. To check the influence of the number of zones in the bending direction, the number of zones was continually increased in the z-direction of the beam, whilst the number of zones in both the x- and y-directions was held constant. Figure 4.10 shows the dependence between stress error and the number of zones in the z-direction.

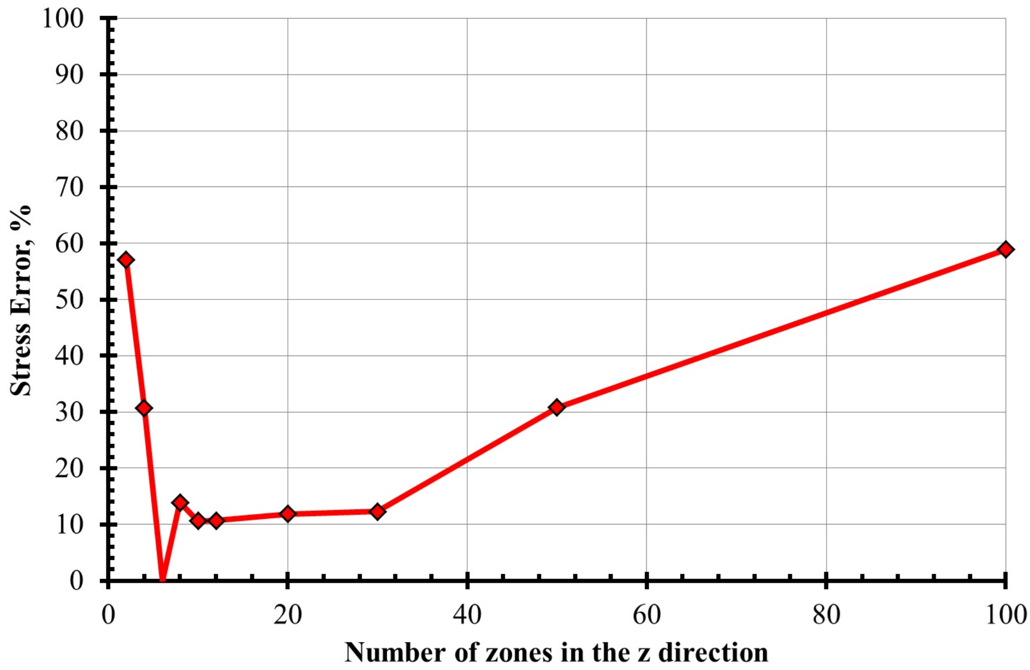

Figure 4.10: Stress Error versus Number of Zones in the z-Direction

Figure 4.10 shows that the minimum stress error was found when the mesh was six zones high. The model also correctly predicted displacements. The same study was carried out for the mesh with zones of $z/x = 3$ and $z/y = 3$. It was found that this mesh arrangement could not provide a satisfactory accuracy, and a consistent error of approximately 20% was obtained for all cases. Therefore, the recommendation for the mesh configuration in the goaf is six cube-shaped zones in the height of the goaf.

4.3 Thin Hollow Cylinder

The mesh configuration in the domain of the host rock or soil was also important. To exclude the influence of the goaf mesh, the null model was assigned to the goaf domain of the model which was developed in Chapter 3. The null model automatically set all stresses to zero. In Chapter 3, the required goaf height (RH) was obtained by adjusting γ in the double-yield model or pre-consolidation pressure and specific volume in the modified Cam-clay. In the null model, the required height (RH) was adjusted to 0.28m (derived in Subsection 3.3.2) by altering the GSI of the overburden. The reduction of the GSI weakened the calculated rock properties. Therefore, the reduced value of the GSI resulted in a reduction in the goaf height after the simulation.

After this, the mesh was densified two times to compare the impact of the mesh densities of the overburden and the whole domains. The goaf height after the simulation became 1.4m, i.e. 6.5 times higher. At the same time, the increase of the mesh density of the whole domain (overburden and goaf) caused 50% increase of the goaf height after the simulation (Figure 3.15). Therefore, the influence of the mesh density of the overburden was higher than the mesh density of the whole domain.

To analyze the influence of the configuration of the overburden mesh, the research on the optimal mesh configuration was extended for a hollow cylinder. A thin cylinder of 5m radius and 0.25m thickness was made of the same elastic material as the cantilever considered in Section 4.2. A force of 200kN was placed across a diameter to one of the ends of the quarter of the cylinder. One-quarter of the cylinder was modelled due to the symmetry of the problem. The roller boundaries were applied to both ends of the cylinder quarter. The out-of-plane displacements (y-direction) were fixed to be equal to zero. The model layout is depicted in Figure 4.11, where the black arrow indicates the direction of the applied force.

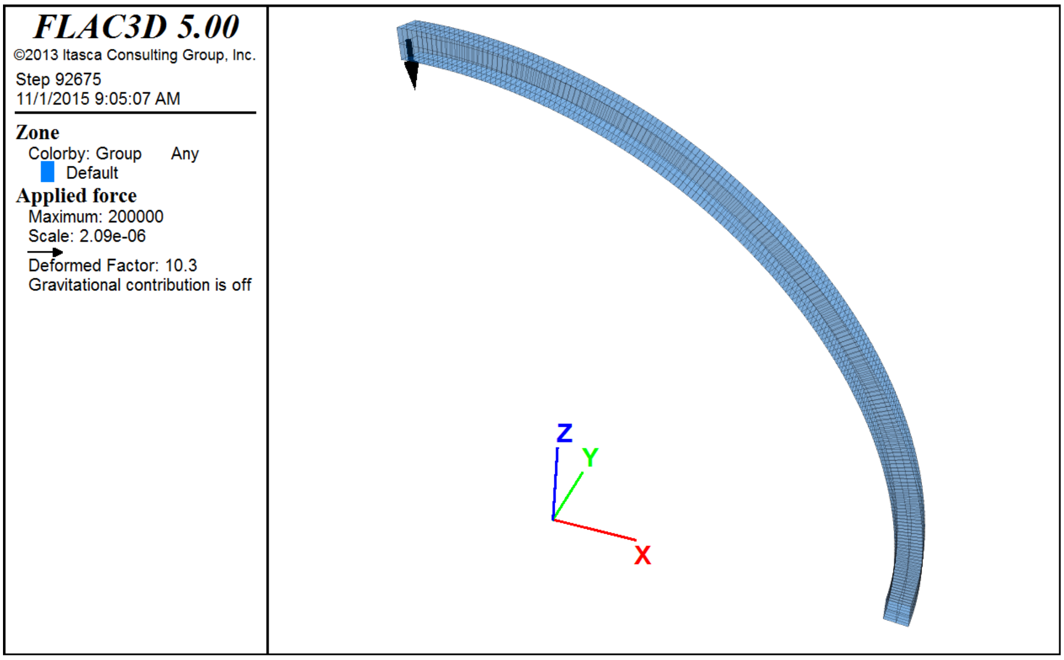

Figure 4.11: Layout of the Thin Walled Cylinder Model

The previous mesh analysis on the cantilever showed that both the shape of the zones and the number of zones in-plane (x- and z-directions) played an important role. To broaden the investigation, the number of zones around the circumference and in the height of the cross-section (x- and z-directions) were altered. Since the size of the cylinder was unchangeable, the shape of zones also changed in all directions. Figure 4.12 presents an area chart type with the number of zones axes in radial and perimeter directions and displacement error, which was calculated according to the theoretical value of Pound (2006) 49.22mm. The vertical axis is the displacement error and two horizontal axes are a number of zones in the radial and tangential directions.

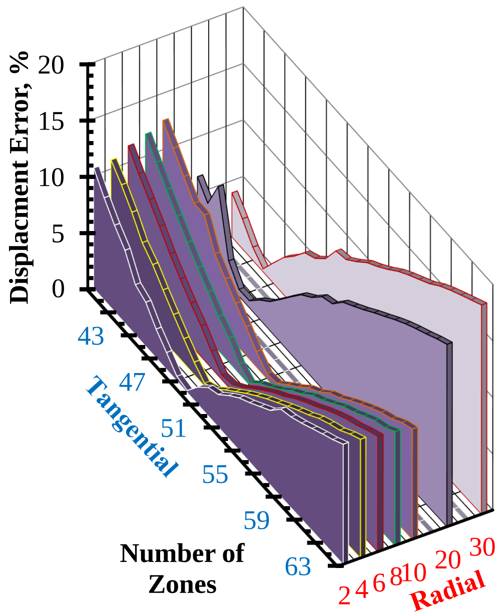

Figure 4.12: Displacement Error vs Number of Zones

Figure 4.12 indicates small errors in the mesh arrangements when 44-50 zones were used in the tangential direction because the shape of the zone was close to a cube. It can be noticed that only a mild increase in error was caused by decreasing the number of zones in the radial direction for 43-50 zones interval. With the increasing number of zones in the radial direction, this interval of the number of zones in the radial direction shifted to the less number of zones in the tangential direction. This happened because the zone size in the out-of-plane direction became too large in this case. The smallest error of 0.16% was obtained for the mesh 2x2x48, when the zones were approximating curvilinear cubes ($x \approx y \approx z$). Figure 4.12 also shows some inconsistency, the most noticeable example was the cylinder of 20 zones in the radial direction and 39-41 zones in the circumference direction. The error suddenly decreased in the monotonically increasing part of the curve at 41 zones in the radial direction. Therefore, there was a need to study mesh arrangements for the wider interval of the number of zones (5 zones - 200 zones) in the radial direction. Figure 4.13 illustrates the results.

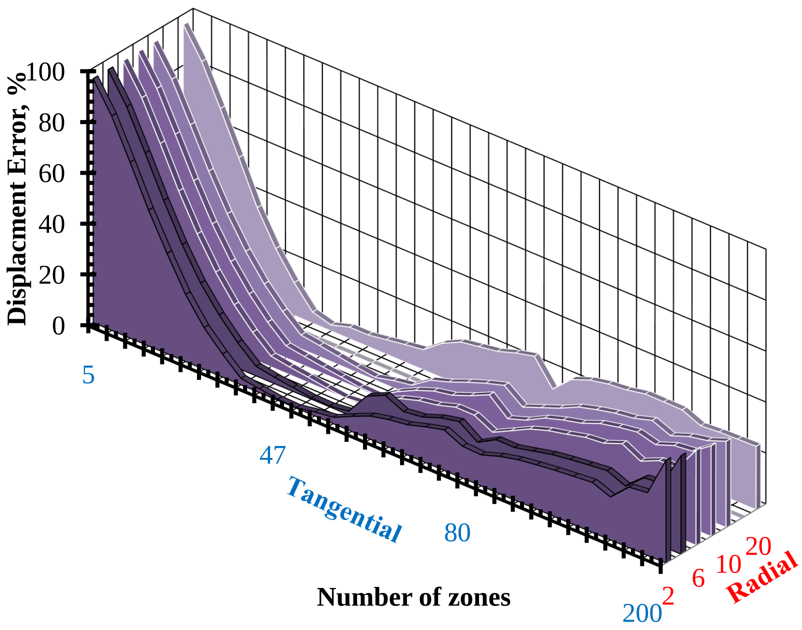

Figure 4.13: Displacement Error vs Number of Zones (larger interval)

Figure 4.13 demonstrates that the error was influenced by the number of zones in radial and tangential directions. The smallest error 0.09% was obtained for the model with the cube-shaped mesh 6x6x49. The error increased when leaving this mesh configuration. However, unexpected decreases of error were noticed with a mesh of 80 and 166 zones around the circumference.

The result of Figure 4.12 and Figure 4.13 concluded that the best mesh arrangement that represents the theoretical displacement solution was 6x6x49 when the element form was close to cube and six zones were used in the cross-section. The optimal element arrangement in terms of accuracy and speed of computation was 2x2x47. These zone arrangements showed that two cuboid-shaped zones with the larger side in the direction of bending and six cube-shaped zones yielded results with the smallest errors. This analysis did not offer any new findings when compared to the analysis in Section 4.2 because it was a point load providing a bending moment, which was very similar to the last example.

4.4 Thick Hollow Cylinder

4.4.1 Model Description

The investigation was broadened by simulating an 'Expansion of a Hollow Cylinder' problem, a classical problem in the theory of elasticity (Timoshenko and Goodier, 1970). The purpose of this analysis was to investigate how the finite-difference simulations react to pressure instead of a point load on a structure. For this, half of a cylinder (Figure 4.14) with an inner radius (r_0) of 4m and an outer radius (r) of 6m, was used. The zones were fixed in the out-of-plane (y-) direction, and roller boundary conditions were implemented at the ends of the half-cylinder. The elastic modulus (E) was 1.5e+10Pa, and the Poisson's ratio (μ) was 0.25. An internal pressure (p_i) of 1e+9Pa was applied uniformly to the inner side of the cylinder as indicated by the black arrows in Figure 4.14.

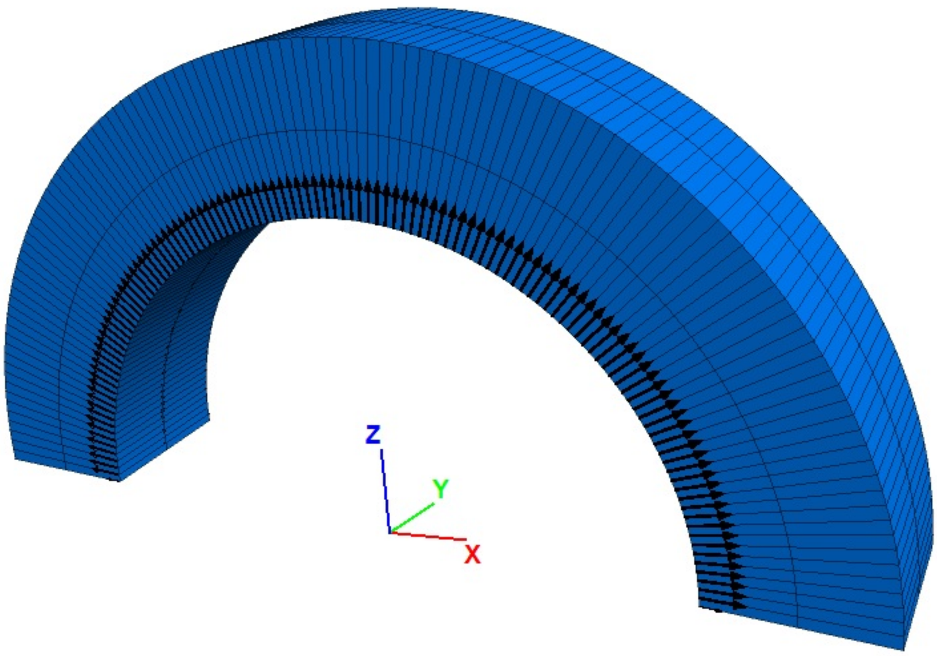

Figure 4.14: Layout of the Thick Walled Cylinder Model

A theoretical displacement of 7.6E-2m was calculated according to the following equation:

$$u_r = \frac{p_i r_i^2 r}{E(r_0^2 - r_i^2)} \left[(1-\mu) + (1+\mu)\frac{r_o^2}{r^2} \right] \tag{4.3}$$

In the beginning, the influence of the number of zones in the cross-section on the modelled result was investigated. Then the out-of-plane size was considered.

4.4.2 Number of Zones in the Cross-Section

Subsection 4.2.5 showed that the number of out-of-plane zones (y-direction) did not influence on the analysis of a structure subjected to a point load. To prove this result for the cylinder under pressure, the number of zones in the y-direction was gradually increased from one to 20 zones. The shape of the zone was kept close to both a curvilinear cube and to the optimal zone configuration (one perpendicular to load side with the zone which was three times smaller than the other sides). Table 4.3 presents the influence of the number of zones on the error.

Table 4.3: Error of the Model of Thick Walled Cylinder

Number of Zones in x- y- z- directions	**Zone Size, m** x-y-z	**Error, %**
60-20-480	0.033-0.033-0.033	6.8
60-10-480	0.033-0.033-0.033	6.8
60-5-480	0.033-0.033 0.033	6.8
60-2-480	0.033-0.033-0.033	6.8
60-1-480	0.033-0.033-0.033	6.8
20-20-48	0.1-0.33-0.33	3.7
20-10-48	0.1-0.33-0.33	3.7
2-1-48	0.1-0.33-0.33	3.7

Two conclusions can be drawn from Table 4.3. Firstly, Table 4.3 indicates that the error was not influenced by the number of zones in the out-of-plane direction, even if only one zone was used. Secondly, Table 4.3 shows that the sufficiently large out-of-plane size (0.033m) did not influence the result. The out-of-plane size was also changed according to the aforementioned multiplications because the size of the zone was constant and the number of zones altered.

Sections 4.2 and 4.3 indicated that the smallest error would be obtained when the number of zones in the radial direction was equal to six. In this investigation, the number of zones in the radial direction was increased starting from 1 and up to 100, and the size of the half-cylinder was kept constant. To keep a cube-shaped zone, the number of zones in the circumferential direction was altered. The out-of-plane size of the cylinder was also adjusted for each analysis so that each analysis used just one zone in the out-of-plane direction and the shape was a curvilinear cube. Section 4.3 showed that the error was not influenced by this size of the cylinder for sufficiently large (0.033m) out-of-plane sizes. In the current investigation, the maximum X/Y ratio was 100. Figure 4.15 presents the calculated displacement error, the relationships between the number of zones in the radial and circumferential directions for three sizes of the thin cylinder, i.e. inner radius = 4m, and outer radius = 5m, 6m, and 7m.

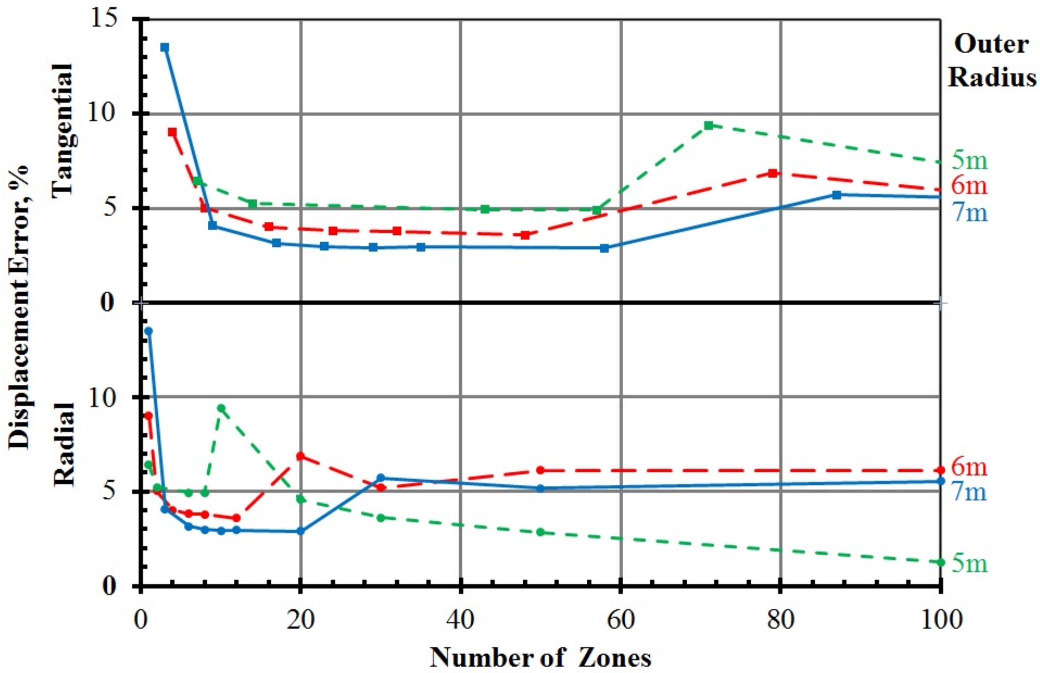

Figure 4.15: Displacement Error vs Number of Zones for 2m Thick Cylinder (inner radius = 4m, outer radius = 6m)

Figure 4.15 shows that the minimal error (3.6%) was calculated when six zones were used in the radial direction across the cylinder of 4m inner and 6m outer diameters. From four to 12 zones in the radial direction caused the minimal error. Figure 4.15 also presents that this minimal error occurred when 48 zones were in the tangential direction. In attempt to reduce the remaining error; the model was checked if this error was due to the six zone arrangements in the radial direction or due to the 48 zone arrangement around the circumference. Keeping the same size of the zones, the outer radius of the cylinder was increased from 6m to 7m. Figure 4.15 shows that the minimal error was when six zones were used across the cross-section of the cylinder. The minimal error was probably due to the 46-zones arrangement around the circumference. One more cylinder of 4m inner and 5m outer diameters was investigated. Figure 4.15 shows that the displacement errors of this cylinder is smaller, except cases for the extreme small number of zones (two) and starting from 30 zones the radial displacement error became bigger than the error of the cylinder of 4m inner and 5m outer diameters.

Although the behaviour of the graph is different, i.e. the error reduced constantly with increasing number of zones in the radial direction, two main principals were still at hand. The six zones in the radial and around 46 zones in the circumference directions resulted in small errors. This mesh arrangement of six cubic zones in the radial direction and about 48 zones in the circumference directions was consistent with previous findings indicating that the zone arrangement was not sensitive to the type of loading applied.

4.4.3 Out-of-Plane Size of the Cylinder

Although large out-of-plane sizes did not influence the result of the calculation of displacement, the previous investigation pointed out that the small out-of-plane dimension could influence the accuracy. The cylinder from the previous investigation had the optimal mesh configuration, i.e. the radial size (r) of the zone was three times larger than the size along the circumference, and two zones in the height of the cylinder cross-section and one zone into the page. The size of the zone (y) was altered. The size of the zone was equal to the size of the cylinder (Y) in-page because there was only one zone in-page. Using a logarithmic scale, the relationship of the displacement error vs the ratio between the out-of-plane and radial zone size (r) is presented in Figure 4.16.

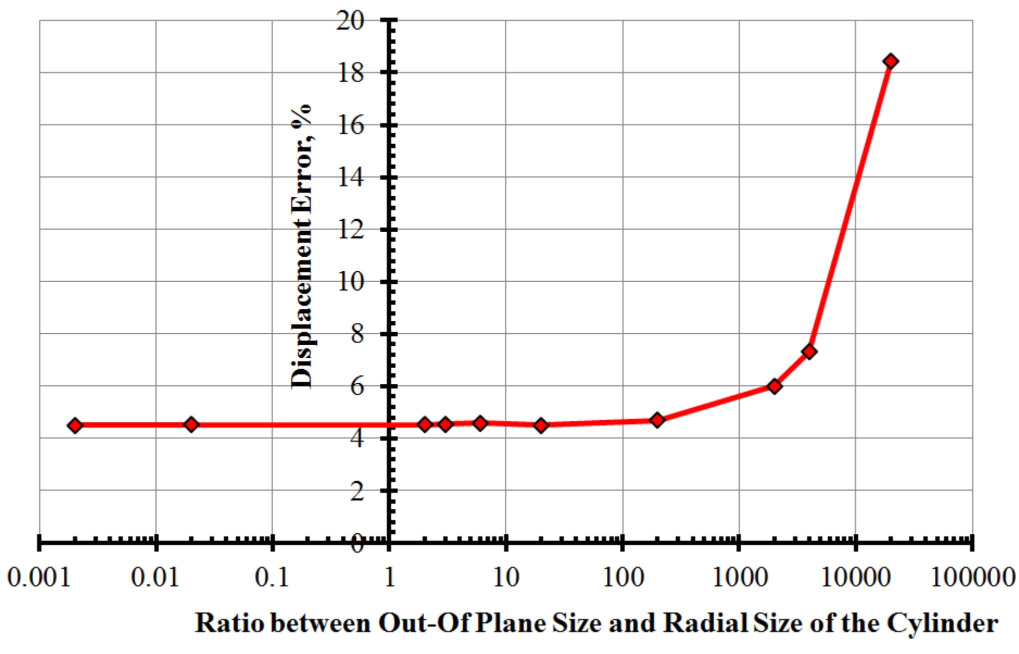

Figure 4.16: Error against the Thickness of the Cylinder

Figure 4.16 indicates that when the ratio between the cylinder depth and radius reduced to less than 1:1000, then errors significantly rose. Conversely, no improvement in the calculated error was seen if this ratio reduced below 1:100. To investigate if the error increased due to the thickness of the cylinder or due to the ratio of the zone, the mesh was altered to have two and ten zones in the out-of-plane direction, and the simulation was repeated. This reduced the zone size y twice and ten times respectively, in other words, the ratio between the out-of-plane and radial size (r) of the zone reduced. As it was shown in Subsection 4.4.2, number of zones in the y-direction did not influence the result (Figure 4.17).

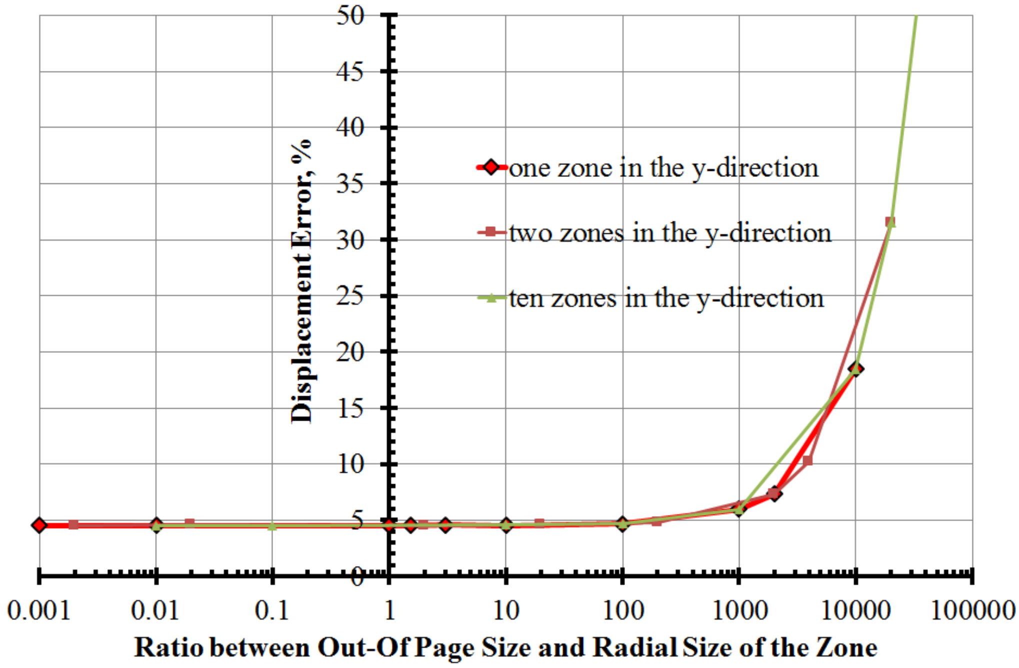

Figure 4.17: Error against Radial Size of the Zone

Figure 4.17 depicts three identical curves for three mesh arrangements. The error for zone ratio r/y of less than 1:100 was small and the error exponentially rose for a ratio of more than 1:100 This means the error increased due to the ratio of the zone (r/y).

4.5 Cylindrical Hole in an Infinite Hoek-Brown Medium

4.5.1 Problem Statement

To extend the analysis of the influence of the configuration of the mesh of the overburden, the Cylindrical Hole in an Infinite Hoek-Brown Medium problem from the FLAC3D manual (Itasca, 2011) was implemented because this problem enable the research to study the mesh density when the internal pressure was reduced imitating the overburden response to the coal mining. In FLAC3D, a cylindrical hole of the problem in an infinite Hoek-Brown medium was represented as a cylinder hole of 2m radius (b) which was inserted into the 40m radius cylinder as shown in

Figure 4.18.

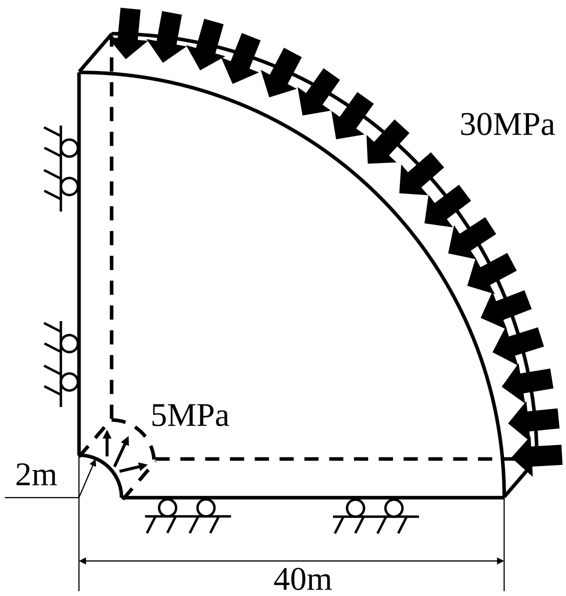

Figure 4.18: Cylindrical Hole in an Infinite Medium

The symmetry of the problem was used and only one quarter of the cylinder was considered by imposing the roller boundary conditions on the cutting edges. The elastic properties were bulk modulus (K)=3.667MPa and shear modulus (S)=2200MPa. The Hoek-Brown parameters were s=0.0039, m_b=1.7, σ_{ci}=30MPa, a=0.5, and σ_s^{cv}=0. A density of 2000kg/m^3 was assigned throughout the whole domain. A uniform compressive stress (σ_0) of 30MPa was applied through the domain and on the edge. A stress (p_i) of 5MPa was applied to the inner wall of the cylinder. The domain was fixed in the out-of-plane direction. The original thickness of the model in the out-of-plane direction was 0.2m as in FLAC3D manual (Itasca, 2011). This size was subject to change to check the its influence on the modelling error. The original mesh configuration was one zone in the out-of-plane direction and 60 zones in the radial and tangential directions. The radial direction controlled by a ratio of 1.05 to increase the size of the zone side from the hole to the outer side of the cylinder as shown in Figure 4.19.

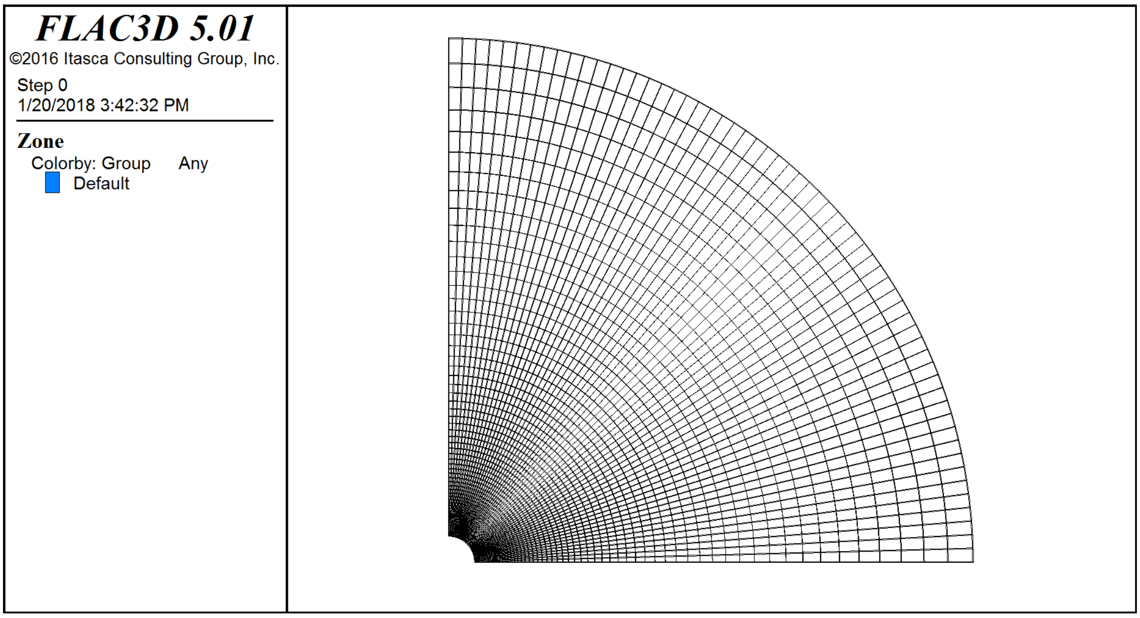

Figure 4.19: Mesh with a Ratio of 1.05

Table 4.4 presents the zone sizes, i.e. r, t, and y in the radial, tangential, and out-of-plane directions respectively. Table 4.4 also includes the ratio r/t.

Table 4.4: Sizes of the Zones

Zone #	**Size r, m**	**mean Size t, m**	r/t	Zone #	**Size r, m**	**mean Size t, m**	r/t
	Outer side of the cylinder			31	0.44	0.12	3.79
1	1.91	0.51	3.74	32	0.42	0.11	3.79
2	1.82	0.49	3.74	33	0.40	0.11	3.80
3	1.73	0.46	3.74	34	0.38	0.10	3.80
4	1.65	0.44	3.74	35	0.36	0.10	3.80
5	1.57	0.42	3.75	36	0.35	0.09	3.81
6	1.50	0.40	3.75	37	0.33	0.09	3.81
7	1.43	0.38	3.75	38	0.31	0.08	3.82
8	1.36	0.36	3.75	39	0.30	0.08	3.82
9	1.29	0.35	3.75	40	0.29	0.07	3.83
10	1.23	0.33	3.75	41	0.27	0.07	3.83
11	1.17	0.31	3.75	42	0.26	0.07	3.84
12	1.12	0.30	3.75	43	0.25	0.06	3.84
13	1.06	0.28	3.75	44	0.23	0.06	3.85
14	1.01	0.27	3.76	45	0.22	0.06	3.85
15	0.97	0.26	3.76	46	0.21	0.06	3.86
16	0.92	0.24	3.76	47	0.20	0.05	3.87
17	0.88	0.23	3.76	48	0.19	0.05	3.87
18	0.83	0.22	3.76	49	0.18	0.05	3.88
19	0.79	0.21	3.76	50	0.18	0.04	3.89
20	0.76	0.20	3.76	51	0.17	0.04	3.90
21	0.72	0.19	3.77	52	0.16	0.04	3.91
22	0.69	0.18	3.77	53	0.15	0.04	3.92
23	0.65	0.17	3.77	54	0.14	0.04	3.93
24	0.62	0.16	3.77	55	0.14	0.03	3.94
25	0.59	0.16	3.77	56	0.13	0.03	3.95
26	0.56	0.15	3.78	57	0.12	0.03	3.96
27	0.54	0.14	3.78	58	0.12	0.03	3.97
28	0.51	0.14	3.78	59	0.11	0.03	3.99
29	0.49	0.13	3.78	60	0.11	0.03	4.00
30	0.46	0.12	3.79		Inner side of the cylinder		

Table 4.4 shows that r/t for all zones was about three-four. It was clear that once the radial geometrical ratio was used as one instead of 1.05, the ratio r/t would vary for the zones in along the radial direction. The results of this investigation are presented later.

The previous sections show that the size of the domain, number of zones, and size of the zones influence the result in FLAC3D. After study on the mesh and zone quality in the cylinder hole and rough strip footing in FLAC3D, Abbasi et al. (2013) concluded that the aspect ratio between one and three3 caused errors of less than 5%. However, as the previous sections showed that the number of zones in any directions influenced the result too. First, the section focused on the out-of-plane direction, number of zones, and sizes. Then the number of zones in the radial and tangential directions were considered. The error was calculated for displacement, tangential, and radial stresses based on the closed-form solution by Carranza-Torres and Fairhurst (1999).

4.5.2 Analytical Solution

The analytical solution was carried out according to the work of Carranza-Torres and Fairhurst (1999) for the elastic and plastic regions. Following the FLAC3D manual (Itasca, 2011), the extent of the failure zone (b_{pl}) for the given Hoek-Brown properties is $1.62b$. The analytical radial and tangential stresses (σ_r and σ_θ) and displacement (u_r) could be found by the following equations which were presented by Carranza-Torres and Fairhurst (1999):

for the elastic region:

$$\sigma_r(r) = \sigma_0 - (\sigma_0 - p_i^{cr}) \left(\frac{b_{pl}}{r}\right)^2 \tag{4.4}$$

$$\sigma_\theta(r) = \sigma_0 + (\sigma_0 - p_i^{cr}) \left(\frac{b_{pl}}{r}\right)^2 \tag{4.5}$$

$$u_r = \sigma_0 + \frac{(\sigma_0 - p_i^{cr})}{2G}\frac{b_{pl}^2}{r} \tag{4.6}$$

where p_i^{cr}=15.8MPa for the given Hoek-Brown properties according to the FLAC3D manual (Itasca, 2011).

for the plastic region:

$$\sigma_r(r) = \left(S_r(r) - \frac{s}{m_b^2}\right) m_b \sigma_{ci} \tag{4.7}$$

where

$$S_r(r) = \left(\sqrt{P_i^{cr}} + \frac{1}{2} ln\left(\frac{r}{b_{pl}}\right)\right)^2 \tag{4.8}$$

where P_i^{cr}=0.311 for the given Hoek-Brown properties (Itasca, 2011).

$$\sigma_\theta(r) = \left(S_\theta(r) - \frac{s}{m_b^2}\right) m_b \sigma_{ci} \tag{4.9}$$

where

$$S_\theta(r) = S_r(r) + \sqrt{S_r(r)} \tag{4.10}$$

$$
\begin{aligned}
u_r = & \frac{\sigma_0}{2G}\left(1-\frac{p_i^{cr}}{\sigma_{ci}}\right)\left[\frac{b_{bl}}{b}\frac{A_1+1}{A_1-1}\frac{r}{b_{pl}}+\frac{D}{2(S_0-P_i^{cr})(1-A_1)^3}\left(\frac{r}{b_{pl}}\right)^{A_1}\right. \\
& -\frac{2}{A_1-1}\left(\frac{r}{b_{pl}}\right)^{A_1}+\frac{C}{4(S_0-P_i^{cr})(1-A_1)}\frac{r}{b_{pl}}\left(ln\frac{r}{b_{pl}}\right)^2 \\
& \left.+\frac{D}{2(S_0-P_i^{cr})(1-A_1)^3}\frac{r}{b_{pl}}\left((1-A_1)ln\frac{r}{b_{pl}}-1\right)\right]
\end{aligned}
\tag{4.11}
$$

where $A_1 = -K_\psi$;

$A_2 = 1 - \nu - \nu K_\psi$;

$A_3 = \nu - (1-\nu)K_\psi$;

$C = A_2 - A_3$;

$D = A_2\left[2(1-A_1)\sqrt{P_i^{cr}} - 1\right] - A_3\left[2(1-A_1)\sqrt{P_i^{cr}} - A_1\right]$;

$K_\psi = \frac{1+sin\psi}{1-sin\psi}$.

ψ is the dilation angle and ν is the Poisson's ratio.

4.5.3 Out-Of-Plane Cylinder Size *Y*

First, the analytical solutions were compared with the results obtained by increasing the model size Y in the out-of-plane direction. The out-of-plane size Y of the cylinder was increased from 0.001m to 1m where the stabilization of the error could be seen. Figure 4.20 presents results of this investigation.

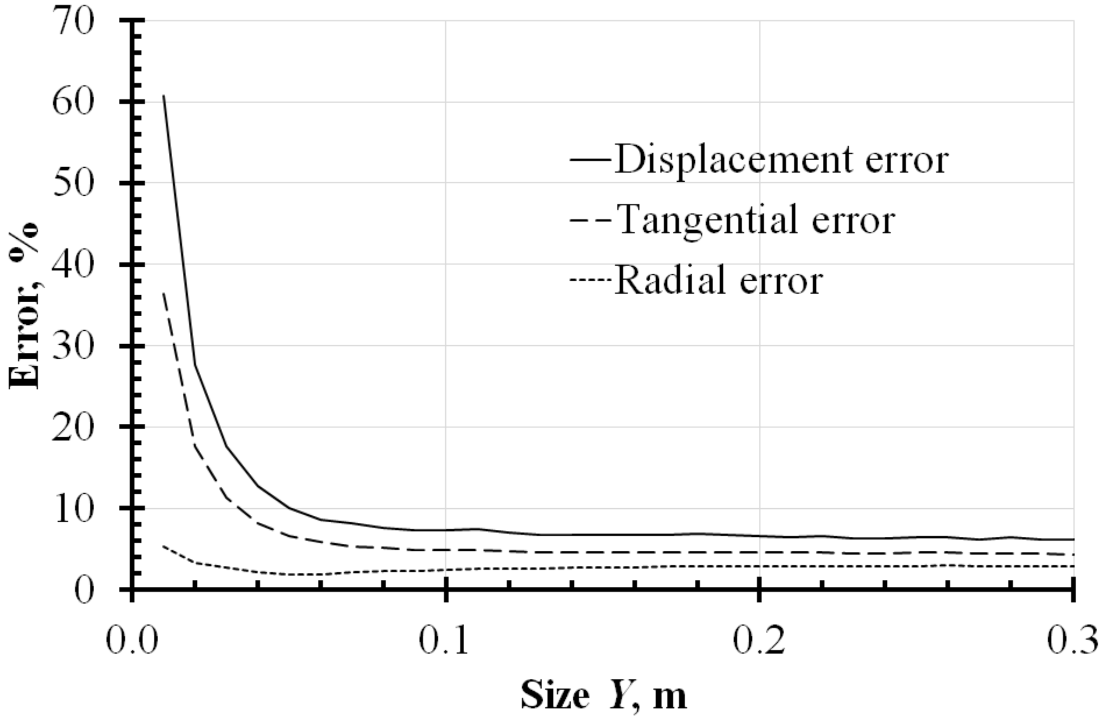

Figure 4.20: Error vs Out-Of Plane Cylinder Size

Figure 4.20 depicts three curves of radial, tangential, and displacement errors. All errors decreased dramatically for the cylinder with a thickness of 0.08m and smaller. In the case of 0.08m thickness, the zone size ratio y/t=0.2-3.0. This finding contradicted to the earlier finding for the beam in Subsection 4.2.3 in the following way:

t is the tangential size of the zone which is perpendicular to the load. For the beam, this size of the zone was called x. Figure 4.3 shows that the error dramatically increased for the ratio y/x=0.5. In Figure Figure 4.20, the error became small if the ratio y/t was larger than 0.2. From this, it could be concluded that the thickness of the hole domain was crucial, not the thickness of the zone.

4.5.4 Out-Of-Plane Number of Zones, Constant Zone Size

To check the influence of the number of zones in out-of-plane directions and the thickness of the model, the number of zones in the out-of-plane direction was increased together with the thickness (Y) of the cylinder. Zones of three thicknesses, i.e. 0.1m 0.2 and 0.3m, were considered. The 0.1m-thick zones was considered to prove the conclusions on modelling error. For 0.2m- and 0.3m-thick zones, Figure 4.21 illustrates the modelled results.

Figure 4.21: Error vs Out-Of-Plane Zone Number

Figure 4.21 shows six curves of radial, tangential, and displacement errors vs the number of zones in the out-of-plane direction for the 0.2m- and 0.3m-thick zones. For the 0.2m-thick zones, All errors increased dramatically for the cylinder of more than five zones in the out-of-plane direction or for the cylinder which was thicker than 1m because five 0.2m-thick zones constituted 1m-thick cylinder. To check the consistency of the raised error when more than five zones in the out-of-plane direction were used, the 0.1m- and 0.3m-thick models were run. Contradictory to the earlier research, the 0.1m thick model predicted small errors with more than five zones in the out-of-plane. At the same time, the 0.3m thick model showed consistency with the 0.2m-thick model (Figure 4.21) in the way that more than 1m-thicker cylinder had a large error too. Figure 4.21 shows the increase in the error when there were more than three zones in the out-of-plane direction. Three 0.3m zones in the out-of-plane direction constituted 0.9m-thick cylinder. So, in other words, the error rose when the cylinder was thicker than 0.9m. These errors were unexpected and probably caused by some error in Itascas code.

4.5.5 Tangential Number of Zones

The influence of the number of zones in the tangential direction was also investigated. Itasca used 60 zones in the tangential direction. In this study, the number of zones was changed from 12 to 300. 12 zones in the tangential direction was chosen as the first test because the smaller number of zones caused an instant error. 300 zones were chosen because this number of zones allowed to observe the general trend of errors with increasing number of zones in the radial direction. Meshes with 12 zones and 100 zones (300 zones are not visible in the plot) in the tangential direction are shown in Figure 4.22a and Figure 4.22b respectively.

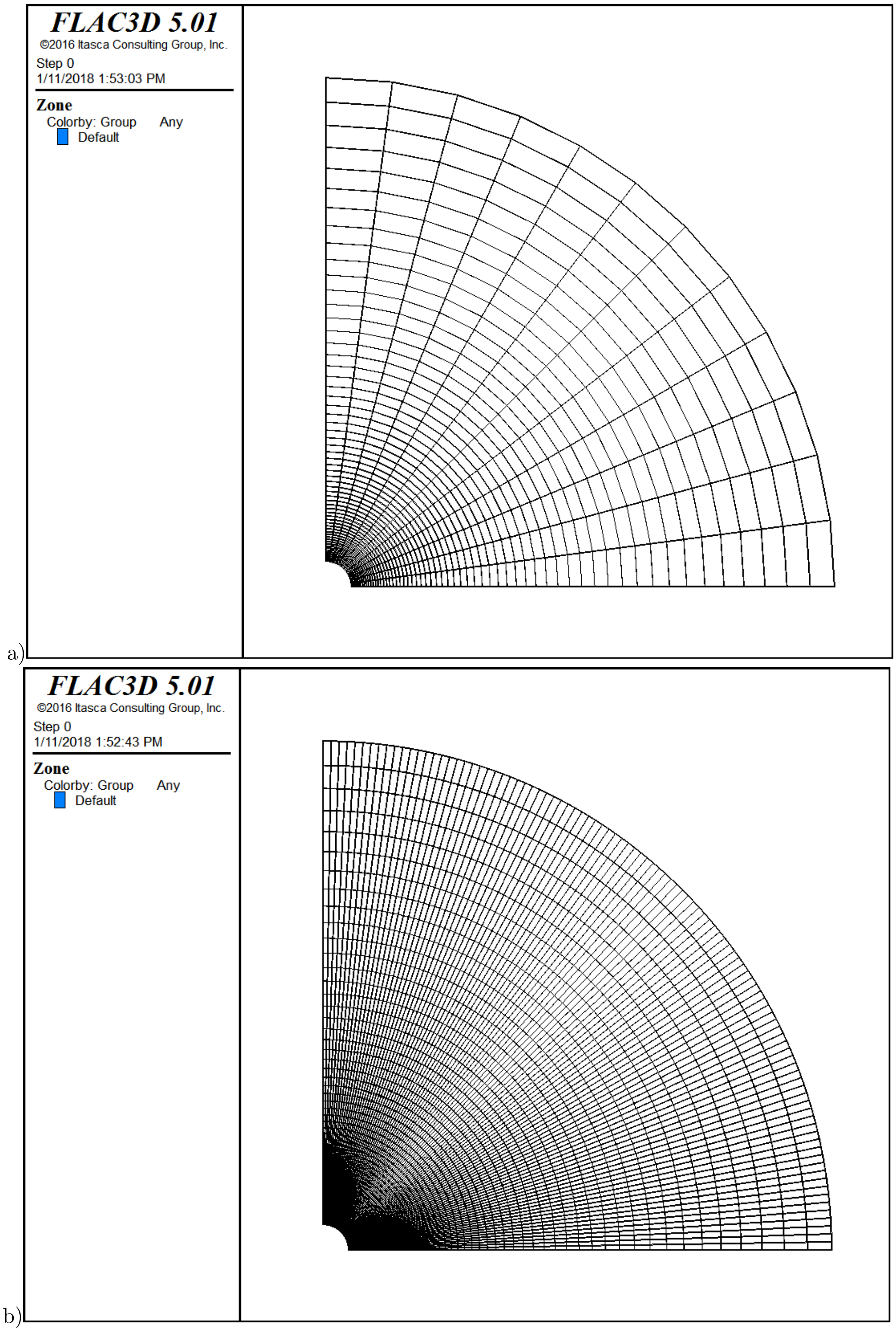

Figure 4.22: The Mesh with 12 (a) and 100 (b) Zones in the Tangential Direction

Figure 4.22 also shows that the Itascas original mesh layout of the zone number was kept constant, i.e. ratio of 1.05, one zone in the out-of-plane direction, 0.2m-thick model. Figure 4.23 depicts the errors vs the zone number in the tangential direction.

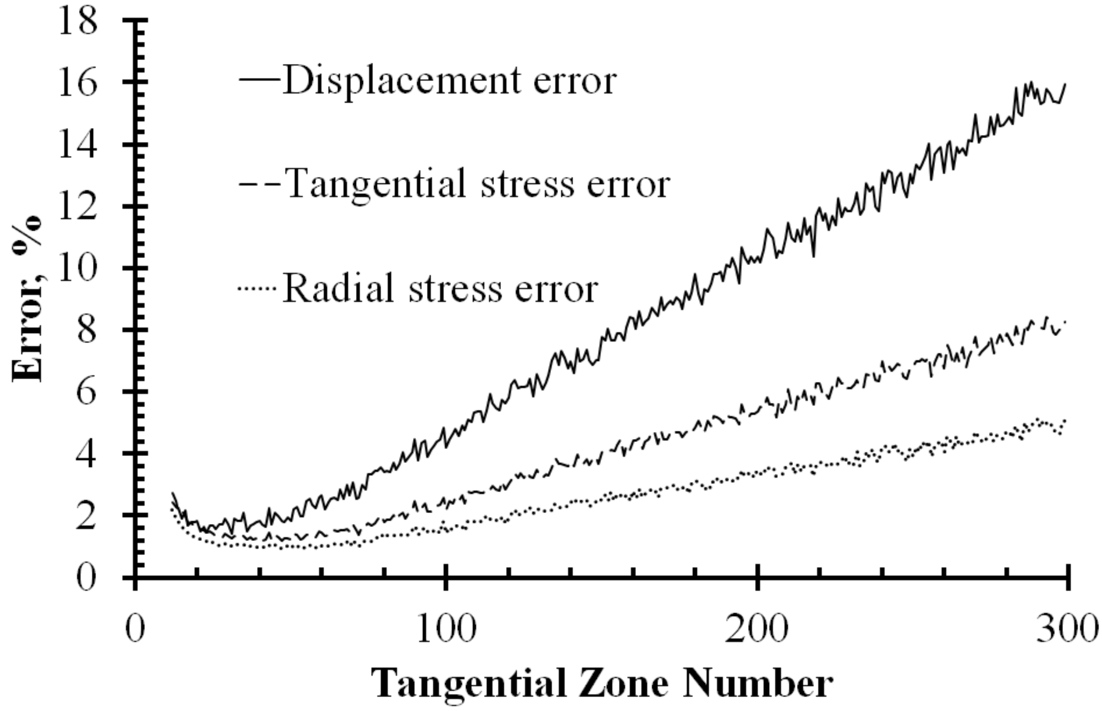

Figure 4.23: Error vs Tangential Zone Number

Figure 4.23 shows that the error decreased and hit the minimum at values of approximately 20-40 zones. Then the errors, especially displacement errors, rose up to 18%. The reason for big errors was that the size of the zone in the parallel direction to the applied pressure was smaller than the size of the zone which was perpendicular to the pressure. The next subsection addresses the errors that were caused by flat zones to the applied pressure of forces.

4.5.6 Radial Number of Zones

This subsection investigated the influence of the number of zones in the radial direction. For this, the radial ratio was set from 1.05 to one, as shown in Figure 4.19. As stated in Subsection 4.6, this ratio increased the size of the zone side from the hole to the outer side of the cylinder. When the ratio was one, the zones were equally distributed through the tangential direction as shown in Figure 4.24. For the model zone, this means the ratio r/t was changing in the radial direction.

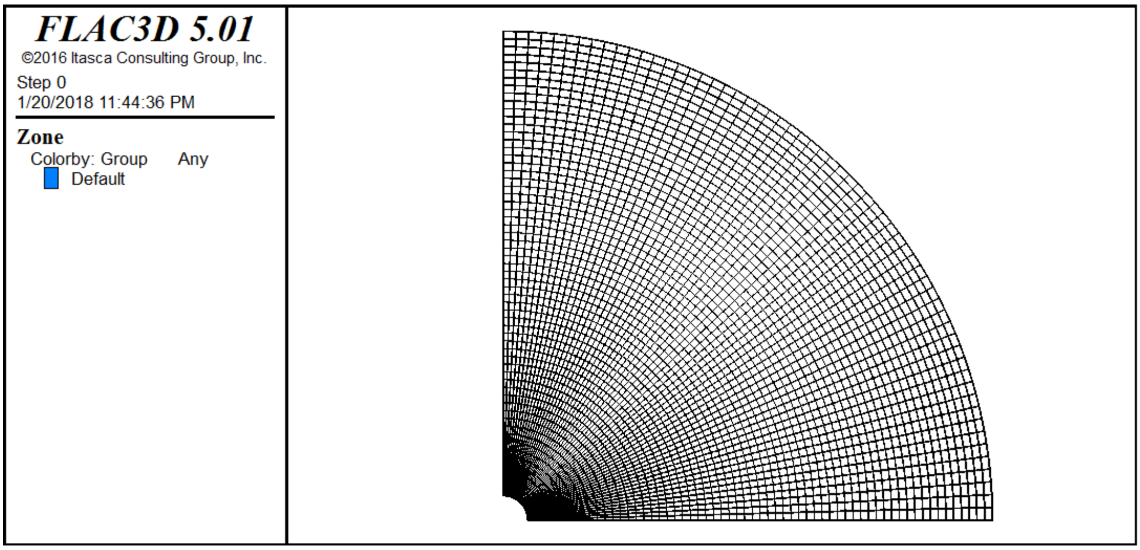

Figure 4.24: Mesh with a Ratio of 1.0

Then the number of zones was changed in the radial direction from just five zones to 100 in the radial direction to investigate the change in error. Five zones were the minimum possible. 100 zones were a number of zones when the error became constant. The meshes with five and 100 zones are shown in Figure 4.25a and Figure 4.25b respectively.

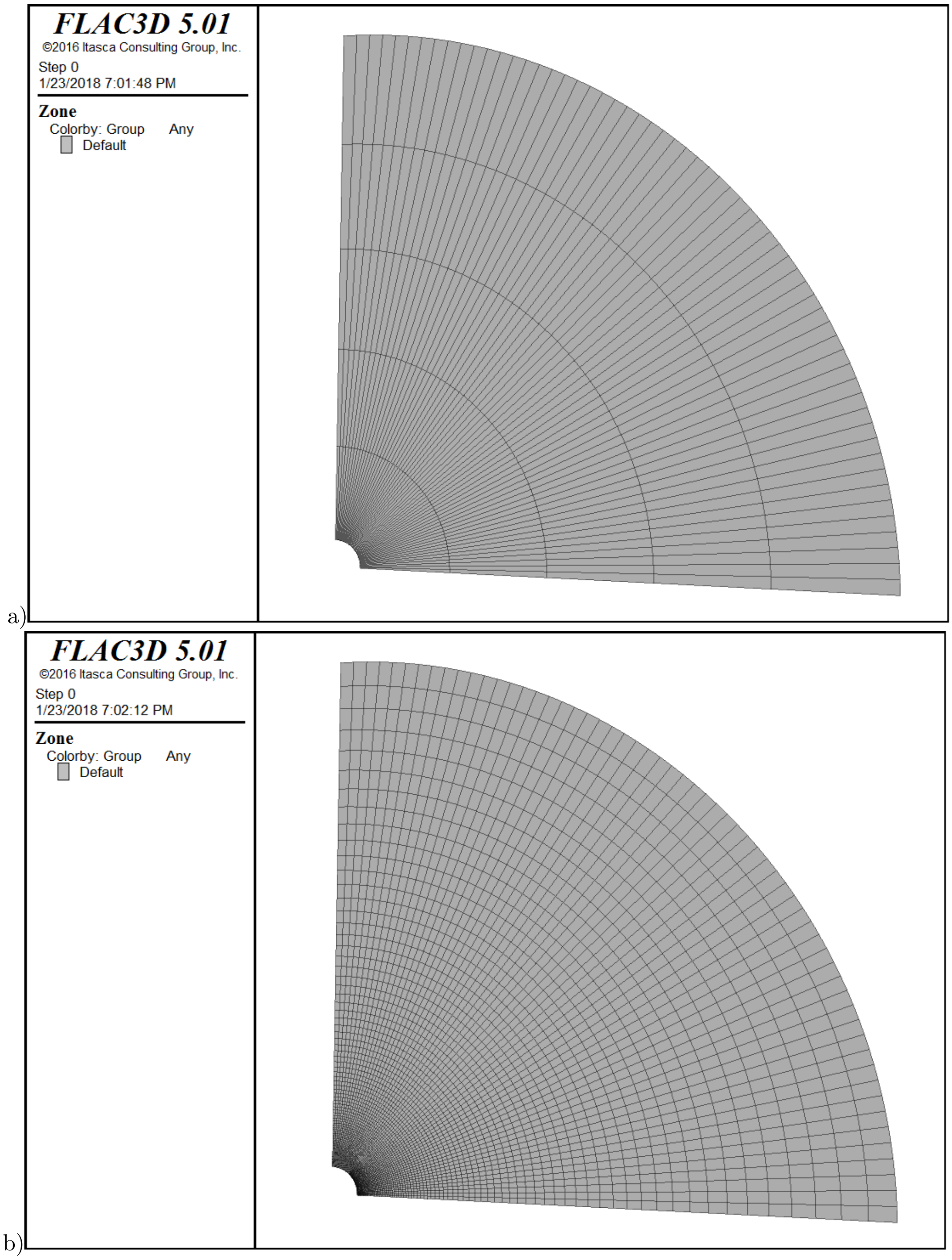

Figure 4.25: The Mesh with Five (a) and 100 (b) Zones in the Radial Direction

When increasing the number of zone from five to 100 in the radial direction as shown in Figure 4.25, the displacement error reduced from extremely high to 30% (displacement error) as shown in Figure 4.26. Since the size of the cylinder was kept, the size of the zone decreased with the increasing number of zones. The ratio r/t was not constant in contrast with the model where the locations of the zones were controlled by the geometrical ratio 1.05.

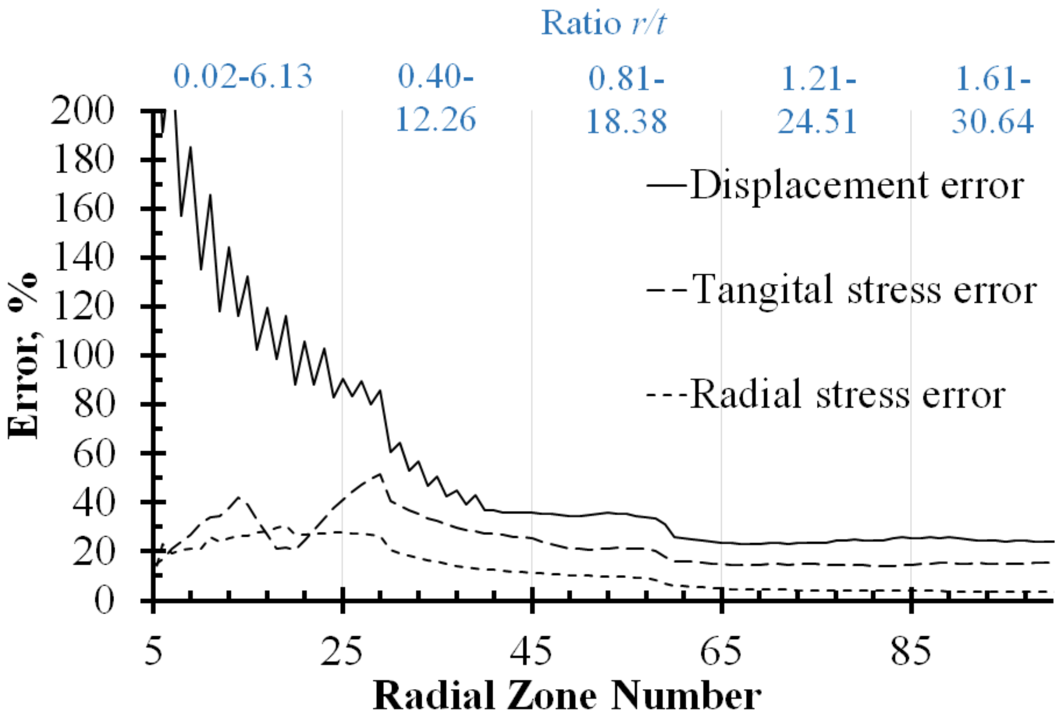

Figure 4.26: Error vs Radial Zone Number

An error of 30% was still high, but as it was noticed the reduction of the displacement from 30% to 200% happened due to the ratio r/t of larger than one. Figure 4.26 depicts the interval of the ratio r/t for the tangential number of zones. The most interesting zone numbers are from 45 to 85. For tangential numbers of between 45-65, the ration r/t increased from 0.81 to 18.38 from the outer side of the cylinder. At the same time, for tangential numbers of between 45-65, the ration r/t increased from 1.21 to 24.51. So, if the zone had the larger side, which was perpendicular to the force applied, then the side, which was parallel to the applied force, the error was inevitable large. This was true even for the zones which were far from the largest deformations.

4.6 Rough Strip Footing on a Cohesive Frictionless Material

To extend the mesh analysis for modelling of the surface subsidence, FLAC3D's 'Rough Strip Footing on a Cohesive Frictionless Material' problem (Itasca, 2011) was investigated. The problem is illustrated in Figure 4.27.

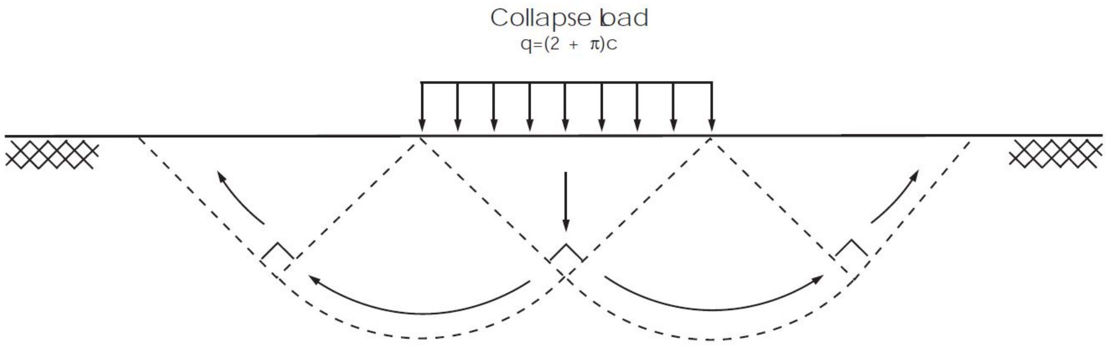

Figure 4.27: Prandtl Mechanism for a Strip Footing (Itasca, 2011)

Figure 4.27 illustrates the surface and a collapse load ($q = (2+\pi)c$, where $c =$ the cohesion) on it. Figure 4.27 also depicts the directions of deformations. The symmetry of the problem was used resulting in the domain 100m width (x) and the roller boundary condition imposed on the cutting symmetry line as shown in Figure 4.28.

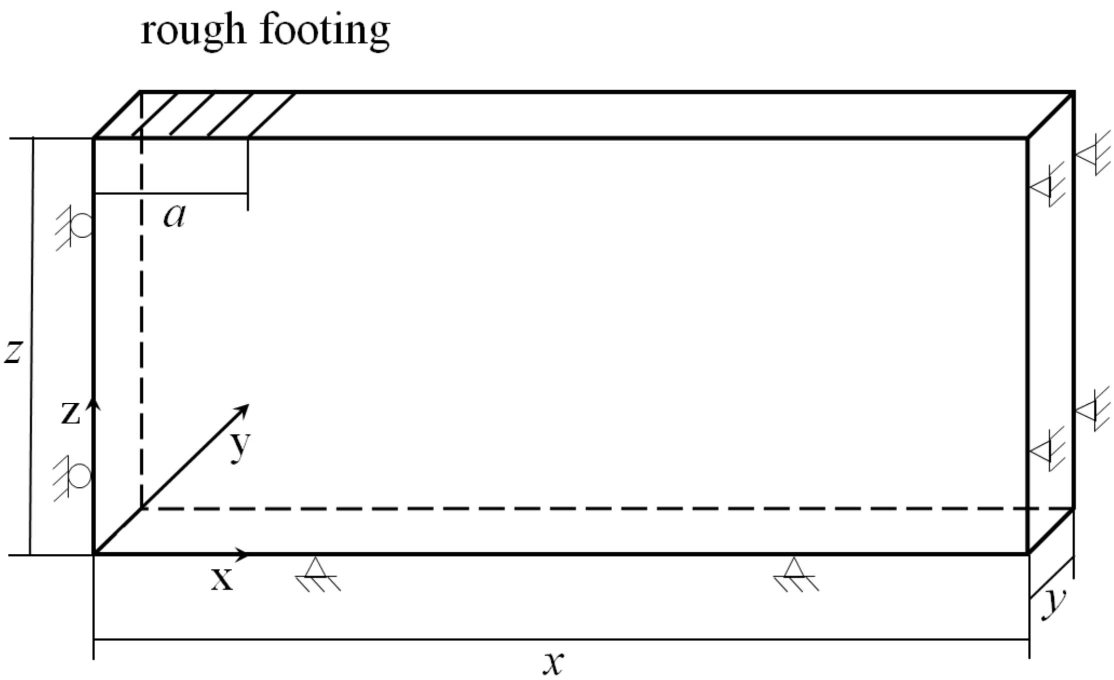

Figure 4.28: Domain for Simulation of Rough Footing

Figure 4.28 shows that the right side and bottom of the domain were fixed. The problem 'Rough Strip Footing' is plane-strain; therefore, the domain was fixed in the out-of-plane direction. The height of the domain (z) was 60m. The thickness of the domain (y) was 1m. The bulk and shear moduli were 0.2MPa and 0.1MPa, respectively. The cohesion (c) was 0.1MPa. The footing was represented by the dashed area of 20m (a) half-width in Figure 4.28 and by a velocity of 0.00005m/step for a total of 25 000 calculation steps. The 20m-wide footing could represent a 20m-wide half-goaf. Terzaghi and Peck (1967) deduced the average footing pressure at failure (q) from the problem 'Prandtl's wedge' (Prandtl, 1924):

$$q = (2 + \pi)c \tag{4.12}$$

The theoretical solution was compared with the modelled results obtained with different model mesh densities, the original mesh density with 1m cube-shaped zone, 0.5m, 0.25m, and 0.125m cube-shaped zone. Figure 4.29 presents the modelled results.

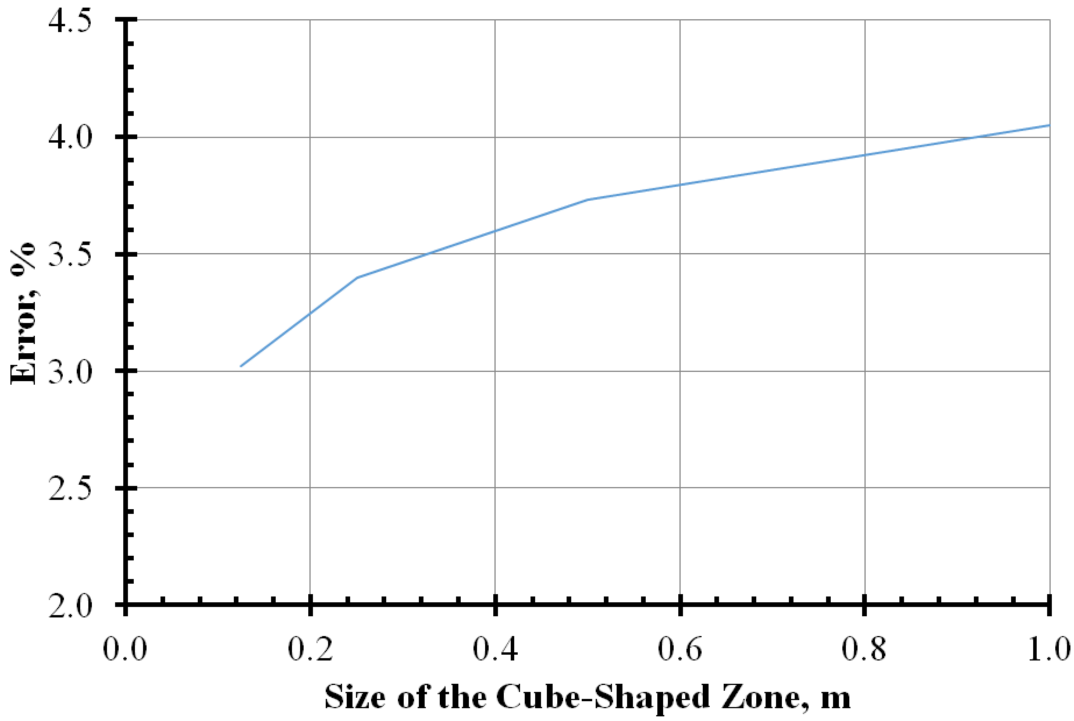

Figure 4.29: Rough Footing, Different Mesh Densities

Figure 4.29 shows that the error decreased from 4.05% to 3.02% with decreasing the size of the cube-shaped zone from 1m to 0.125m. In other words, the error decreased insignificantly with increasing mesh densities. The error was acceptable (less than 5%) with any considered mesh configurations; therefore, any mesh densities at hand could be used to model the overburden behaviour after a collapse of a mine.

4.7 Summary

The study showed that 6 zones in the height of the goaf should be advised. The 200x60x1 and denser mesh with the cube-shaped zones should be recommended to model surface subsidence. For these recommendations on goaf and domain mesh to model surface subsidence, five classical problems were chosen to investigate model mesh in FLAC3D, i.e. the cantilever, the thin and thick hollow cylinders, the cylindrical Hole in an infinite Hoek-Brown medium, and the rough strip Footing on a cohesive frictionless material.

The investigation on the cantilever showed that the aspect ratios between the side that was perpendicular to the applied forces and the side that was parallel to the applied forces should be larger than one to one during the simulation of a plane-strain object. The ratio between the length and the height of the beam should be more than 0.025. The beam, whose shape was close to the square in-plane, resulted in large errors because this shape of the beam should be considered as a plate. At the same time, the error was constant when the mesh was denser than 24x24x24. Therefore, the mesh in the mining simulation should be densified more than 24x24x24.

The study on the beam and both thick and thin cylinders showed that a number of zones in the y-direction was not important; however, a number of zones in the z-direction should be chosen carefully. The thinnest zone that could be used out-of-plane was when the ratio between the out-of-plane and in-plane dimensions of the zone was not less than 1:1000. Starting from the domain arrangement of 1:100, the error stayed at a constant value of less than 5%. Contrary to the beam study, the study on the Hoek-Brown cylinder showed that the thickness in the out-of-plane direction should be less than 1m and more than 0.08m. This thickness could be recommended for the mesh to model surface subsidence.

The study on the thin- and thick-walled hollow cylinder presented that the mesh with an aspect ratio of 1:3 and with two zones in the direction of bending had the smallest displacement error. However, a mesh with an aspect ratio of 1:3 could not calculate the theoretical stress. Therefore, a mesh for surface subsidence simulations should consist of cube-shaped zones. For the cantilever and hollow cylinders, the number of out-of-plane zones did not play a significant role. The error was minimal when the number of elements in the vertical direction was six. The six-zones configuration corresponded to the findings for the 2D model from Pound (2006), which said that 6 zones in the vertical direction were optimal to obtain good predictions. The number of zones around the quarter of the circumference should be around 45.

The study on the Hoek-Brown cylinder noticed that the thickness (out-of-plane) of the whole domain played a more important role rather than the out-of-plane zone size. Considering the modelling surface subsidence, the thickness of the model should be recommended as more than 0.1m and equal or less than 1m with one zone in the out-of-plane direction.

The study on the mesh of the rough strip footing showed that 200mx60mx1m mesh with the 1m cube-shaped zones resulted in error of less than 1%. The increasing mesh density caused a slight reduction in error. Therefore, this mesh or more dense should be recommended to model surface subsidence.

Chapter 5

Implementation of a User-Defined Constitutive Model

In this chapter, the author collected his experience on the implementation of the UDCM in FLAC3D. Programming the UDCM was started from the simplest constitutive model, i.e. an isotropic, elastic model. Then the programme was increased in complexity by considering linear plastic models, such as the von Mises, Drucker-Prager, Tresca, and Mohr-Coulomb models. Finally, CASM (Yu, 1998) and the bubble model (Al-Tabbaa and Wood, 1989) were programmed to implement them into modelling surface subsidence at the UCG site.

5.1 Overview

Chapter 3 showed that the constitutive models embedded in FLAC, Mohr-Coulomb, modified Hoek-Brown, strain softening, double-yield, and modified Cam-clay models, did not predict surface subsidence correctly. The modelled surface subsidence trough was shallower and wider than the measurements. To improve predictions, more advanced models should be programmed, embedded in FLAC3D, verified and only then used to model surface subsidence. This work considers CASM and the bubble model. Both models can be reduced to the modified Cam-clay model, which was originally embedded in FLAC. This lets validate the programmed models against the modified Cam-clay model. The bubble model can later be extended to more complex bounding surface models, which have not been considered in this work. CASM can simulate granular materials in contrast to the modified Cam-clay model. The granular materials commonly comprise overburdens. The bubble model handles the destruction of the soil and its elastic behavior in a more efficient way than the modified Cam-clay model. Different compressibilities of disturbed and undisturbed clays were already acknowledged many years ago, for example, by Casagrande (1932). Many works (for example, Atkinson and Richardson (1985), Vanapalli and Oh (2010), and etc) on the elasticity of the soil reveal complicated elastic behaviour of the soil.

FLAC is capable of the implementation of user-defined constitutive models (UDCM). In FLAC2D, the UDCM can be programmed in FISH, which is a programming language embedded into FLAC. In FLAC2D and FLAC3D, the UDCM is written in C++ and compiled as a DLL file (dynamic link library). The UDCM in FISH is easier to use, but it takes longer to run than the UDCM when it is implemented as a DLL file in FLAC3D. After programming, the verification of the models was required. During verification, two difficulties were encountered, i.e. yield surface drift and singularities at the corners of the yield surfaces, and solved with the help of work by Potts and Gens (1985) and Abbo (1997), respectively.

In this work, the verifications of the Drucker-Prager, and Mohr-Coulomb models were carried out using FLAC's verification problem 'Cylindrical Hole in an Infinite Mohr-Coulomb Material' (Itasca, 2011). The results of the UDCMs were compared with the results of the models embedded in FLAC3D. The verification problem was extended by changing the cylindrical hole for the spherical hole and checking the performance of the UDCMs in three dimensions. After obtaining identical results between the UDCMs and the built-in models, the Critical State models, i.e. the modified Cam-clay model and CASM, were programmed as UDCM. These models were verified using the numerical triaxial test. The results were compared with the results of the built-in modified Cam-clay model, with CASM's results obtained in a finite element model CRISP by Khong (2004), and with experimental data. Finally, the bubble model was verified by comparisons with the modified Cam-clay model, FLAC's verification problem 'Embankment Loading on a Cam-Clay Foundation' (Itasca, 2011) and results obtained by the author in FLAC2D using FISH 2D code by Ni (2007). The verification was conducted by comparison substep, step, and solve results.

In FLAC3D, any constitutive model runs ten substeps per zone in one step. The user defines zones in the domain. During the run, FLAC3D automatically subdivides each zone into two overlaid groups of five tetrahedra (Figure 5.1) to provide accurate solutions for plasticity analyses.

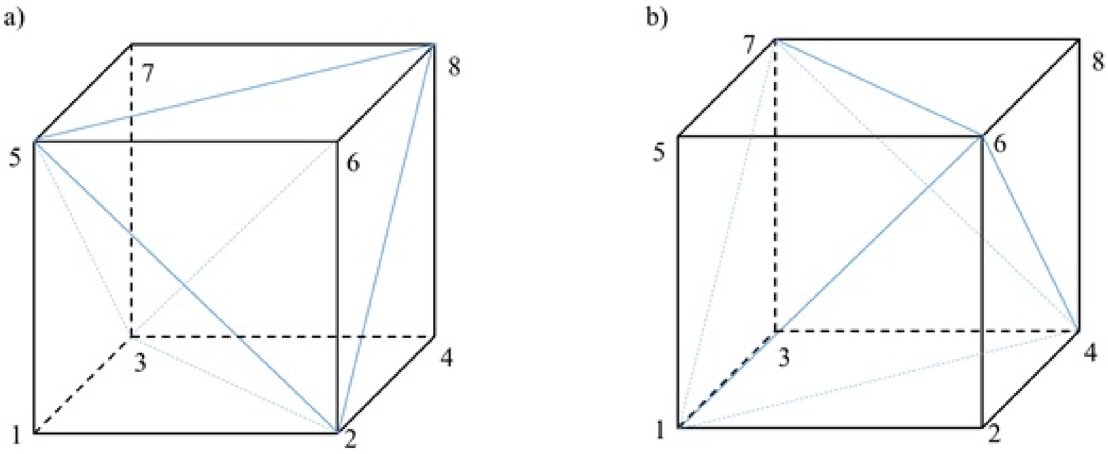

Figure 5.1: Tetrahedra with the Numbered Vertices in One Zone

In Figure 5.1a, there are five tetrahedron: (1 2 3 5), (2 3 5 8), (2 5 6 8), (2 3 4 8), and (3 5 7 8). In Figure 5.1b, there are five overlaid tetrahedron: (1 2 4 6), (1 3 5 7), (1 5 6 7), (1 4 7 6), and (4 6 7 8). Results of one zone are averaged over the ten subzones. The code of any constitutive model in FLAC3D consists of two parts. One part is called each time, the other part is run once in ten times, where the average values are calculated.

5.2 Elastic Model

The programming of the calculations in the constitutive models starts with a general form of stress-strain relationship for an elastic guess using (Itasca, 2011):

$$\dot{\sigma} = D^e \dot{\varepsilon} \tag{5.1}$$

where D^e is the stiffness matrix. The superimposed dot denotes time differentiation.

In FLAC3D, the incremental stress update is performed:

$$\begin{pmatrix} \Delta\sigma_{xx} \\ \Delta\sigma_{yy} \\ \Delta\sigma_{zz} \\ \Delta\sigma_{xy} \\ \Delta\sigma_{xz} \\ \Delta\sigma_{yz} \end{pmatrix} = \begin{pmatrix} \alpha_1 & \alpha_2 & \alpha_2 & 0 & 0 & 0 \\ \alpha_2 & \alpha_1 & \alpha_2 & 0 & 0 & 0 \\ \alpha_2 & \alpha_2 & \alpha_1 & 0 & 0 & 0 \\ 0 & 0 & 0 & 2G & 0 & 0 \\ 0 & 0 & 0 & 0 & 2G & 0 \\ 0 & 0 & 0 & 0 & 0 & 2G \end{pmatrix} \begin{pmatrix} \Delta\varepsilon^e_{xx} \\ \Delta\varepsilon^e_{yy} \\ \Delta\varepsilon^e_{zz} \\ \Delta\varepsilon^e_{xy} \\ \Delta\varepsilon^e_{xz} \\ \Delta\varepsilon^e_{yz} \end{pmatrix} \tag{5.2}$$

where α_1 and α_2 are the elastic constants or Lame's constants:

$$\alpha_1 = 4G/3 + K \tag{5.3}$$

$$\alpha_2 = -2G/3 + K \tag{5.4}$$

where K is the bulk modulus and G is the shear modulus.

5.3 Plastic Model

After taking an elastic guess, the failure function $f(\sigma)$ is calculated. If $f(\sigma) \geq -FTOL$ (Failure TOLerance), where $FTOL$ is a small positive tolerance when a material fails. In order to stipulate the relative magnitudes of the plastic strain after failure, the flow rule is used. The plasticity theory widely accepted that the relationship between the plastic potential g and the plastic strains ε^p is given by:

$$\varepsilon^p = \lambda \frac{dg}{d\sigma} \tag{5.5}$$

where λ is the scalar quantity termed the non-negative plastic multiplier.

Clearly, the function g is critical to describe the way that the material behaves after yielding. Different expressions of g can be found in the literature. In early plasticity, the theoretical framework was derived from the observation of metals yielding and the associated flow rule was postulated. This flow rule assumes that g is equal to the failure criterion f. It is clear from geomechanics that the associated flow rule does not model the post-yield displacement of soil with sufficient accuracy. This has led to the postulation of the non-associated flow rule in which g is very similar to f, but with only a small variation. The non-negative plastic multiplier λ can be derived using the assumption that the relative directions of the plastic strains are given from the derivative of the flow rule.

There are two common assumptions made in the plasticity theory. The first assumption is that the strain increments can be decomposed into the sum of elastic and plastic parts, i.e.

$$\dot{\varepsilon} = \dot{\varepsilon}^e + \dot{\varepsilon}^p \tag{5.6}$$

The second assumption is that the stress state stays on the failure surface during yielding. For example,

$$\dot{f} = \dot{\sigma}\frac{\partial f}{\partial \sigma} = 0 \tag{5.7}$$

Using both of these assumptions, we can now derive an expression for the non-negative plastic multiplier λ.

$$\dot{f} = \frac{df}{d\sigma} D^e \dot{\varepsilon}^e = 0 \tag{5.8}$$

$$\frac{df}{d\sigma} D^e \left(\dot{\varepsilon} - \lambda \frac{dg}{d\sigma} \right) = 0 \tag{5.9}$$

$$\lambda = \frac{\left(\frac{df}{d\sigma}\right)^T D^e \dot{\varepsilon}}{\left(\frac{df}{d\sigma}\right)^T D^e \frac{dg}{d\sigma}} \tag{5.10}$$

The calculation of the plastic multiplier allows us to determine how much elastic strain has occurred during an increment of work and adjust the internal stress accordingly.

To find the stress tensor using the strain tensor, the elastic-plastic stiffness matrix D^{ep} is required. A nonlinear model may be expressed as follows:

$$\dot{\sigma} = D^{ep} \dot{\varepsilon} \tag{5.11}$$

Using the previous derivation it can be seen that

$$\frac{df}{d\sigma} D^e \left(\dot{\varepsilon} - \lambda \frac{\partial g}{\partial \sigma} \right) = 0 \tag{5.12}$$

$$\frac{df}{d\sigma} \left(D^e - \frac{D^e \frac{\partial g}{\partial \sigma} \left(\frac{\partial f}{\partial \sigma}\right)^T D^e}{\left(\frac{\partial f}{\partial \sigma}\right)^T D^e \frac{\partial g}{\partial \sigma}} \right) \dot{\varepsilon} = 0 \tag{5.13}$$

Recall that during yielding we have $\dot{\sigma}\frac{df}{d\sigma} = 0$, hence we have proved that

$$\dot{\sigma} = \left(D^e - \frac{D^e \frac{\partial g}{\partial \sigma} \left(\frac{\partial f}{\partial \sigma}\right)^T D^e}{\left(\frac{\partial f}{\partial \sigma}\right)^T D^e \frac{\partial g}{\partial \sigma}} \right) \dot{\varepsilon} \tag{5.14}$$

$$D^{ep} = D^e - \frac{D^e \frac{\partial g}{\partial \sigma} \left(\frac{\partial f}{\partial \sigma}\right)^T D^e}{H} \tag{5.15}$$

where $H = \left({}^{\partial f}/_{\partial \sigma}\right)^T D^e {}^{\partial g}/_{\partial \sigma}$. For an isotropic hardening material, i.e. $f(\sigma, h) = 0$, $H = \left({}^{\partial f}/_{\partial \sigma}\right)^T D^e {}^{\partial g}/_{\partial \sigma} + {}^{\partial f}/_{\partial h} {}^{\partial h}/_{\partial \varepsilon^p} {}^{\partial g}/_{\partial \sigma}$.

5.4 Yield Surface Drift

Unfortunately, due to inaccuracies associated with numerical computation, stresses in a state of failure start to drift away when they ought to remain within $FTOL$ as described in Section 5.3. The drift can be corrected by reducing a model time step; however, this increases the runtime of the model. Potts and Gens (1985) evaluated several schemes for correcting the stress state back to the yield surface and compared those to the correct solution which was calculated using an incredibly small time step. Potts and Gens (1985) argued that changes in elastic strains must be considered when the stress is corrected back to the yield surface and proved that the following formulae effectively corrects stresses back to the yield surface.

$$\sigma^{correct} = \sigma - \alpha D^e \frac{\partial g}{\partial \sigma} \tag{5.16}$$

where

$$\alpha = \frac{F(\sigma, h)}{\left({}^{\partial f}/_{\partial \sigma}\right)^T D^e {}^{\partial g}/_{\partial \sigma} - {}^{\partial f}/_{\partial h} \Delta h {}^{\partial g}/_{\partial \sigma}} \tag{5.17}$$

The effect of the yield surface drift is shown in Section 5.8.

5.5 Rounded Mohr-Coulomb Model (Abbo, 1997)

One more numerical difficulty was encountered whilst programming the von Mises, Drucker-Prager, Tresca, and Mohr-Coulomb models. Figure 5.2 explains the nature of this numerical difficulty.

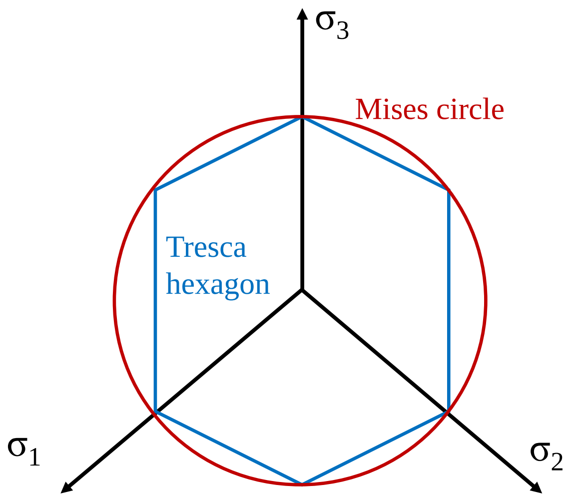

Figure 5.2: Tresca and von Mises Yield Function in Principal Stress Space

Figure 5.2 illustrates that the von Mises model has a circle yield surface, whereas the Tresca model has a hexagon-shaped yield surface. At a Lode angle of $\pm 30^{\circ}$, the Tresca yield function and plastic potential cannot be differentiated. If a model for frictional material is considered, then one more place of the singularity appears at the locus of the Mohr-Coulomb yield surface (Figure 5.3 where $I_1 = 0$).

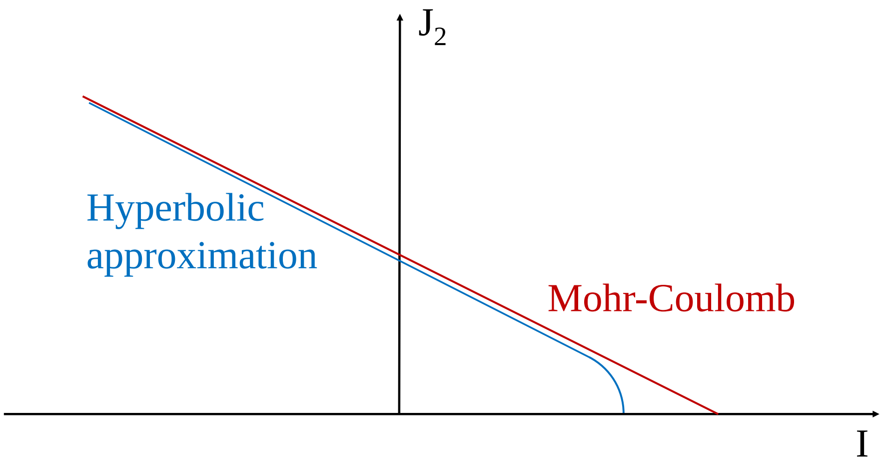

Figure 5.3: Approximation to Mohr-Coulomb Yield Function after Abbo (1997)

Fortunately, this difficulty was overcome by Sloan and Booker (1986) by rounding the yield surface. The Mohr-Coulomb yield criterion is convenient to express in the approximated form:

$$f = \sqrt{J_2} sin\phi + I_1 K(\theta) - c \cdot cos\phi = 0 \tag{5.18}$$

where J_2 and I_1 are the stress invariants that represent the magnitude of shear stress and the effect of mean stress, respectively. $K(\theta)$ is the function of the Lode angle:

$$K(\theta) = cos\theta - \frac{1}{\sqrt{3}} sin\phi \cdot sin\theta \tag{5.19}$$

where ϕ is the friction angle, and θ is the Lode angle.

The three stress invariants are defined by

$$I_1 = \frac{1}{3}(\sigma_{xx} + \sigma_{yy} + \sigma_{zz}) \tag{5.20}$$

$$\sqrt{J_2} = \sqrt{\frac{1}{2}\left((\sigma_{xx} - I_1)^2 + (\sigma_{yy} - I_1)^2 + (\sigma_{zz} - I_1)^2\right) + \tau_{xy}^2 + \tau_{yz}^2 + \tau_{xz}^2} \tag{5.21}$$

$$\theta = \frac{1}{3} sin^{-1}\left(-\frac{3\sqrt{3}}{2}\frac{J_3}{\sqrt{J_2^3}}\right), (-30^\circ \leq \theta \leq 30^\circ) \tag{5.22}$$

where

$$J_3 = (\sigma_{xx} - I_1)(\sigma_{yy} - I_1)(\sigma_{zz} - I_1) + 2\tau_{xy}\tau_{yz}\tau_{xz} - (\sigma_{xx} - I_1)\tau_{yz}^2 - (\sigma_{yy} - I_1)\tau_{xz}^2 - (\sigma_{zz} - I_1)\tau_{xy}^2 \tag{5.23}$$

In the vicinity of the vertices at $\theta = \pm 30$, the modified form K is used:

$$K(\theta) = A - B \cdot sin3\theta \tag{5.24}$$

where

$$A = \frac{1}{3} cos\theta_T \left(3 + tan\theta_T tan3\theta_T + \frac{1}{\sqrt{3}} sign(\theta)\left(tan3\theta_T + 3tan\theta_T\right) sin\phi\right) \tag{5.25}$$

$$B = \frac{1}{3cos3\theta_T}\left(sign(\theta) sin\theta_T + \frac{1}{\sqrt{3}} sin\phi \cdot cos\theta_T\right) \tag{5.26}$$

$$sign(\theta) = \begin{cases} +1, & \text{for } \theta \geq 0. \\ -1, & \text{for } \theta < 0. \end{cases} \tag{5.27}$$

Against the singularity at the tip of the surface (Figure 5.3), Zienkiewicz and Pande (1977) implemented a hyperbolic approximation. Just only one new parameter a was introduced into Equation 5.18:

$$f = I_1 + \sqrt{J_2 K^2(\theta) + a^2 sin^2\phi} - c \cdot cos\phi = 0 \tag{5.28}$$

The parameter a is adjustable to bring the function (Equation 5.28) closer to the original Mohr-Coulomb yield function as desired. Moreover, the Mohr-Coulomb yield function is recovered if a is set to zero.

The gradients of the yield surface and plastic potential play an essential role in elastoplastic finite element analysis:

$$\frac{\partial f}{\partial \sigma} = \frac{\partial f}{\partial I_1}\frac{\partial I_1}{\partial \sigma} + \frac{\partial f}{\partial \sqrt{J_2}}\frac{\partial \sqrt{J_2}}{\partial \sigma} + \frac{\partial f}{\partial J_3}\frac{\partial J_3}{\partial \sigma} \tag{5.29}$$

Abbo (1997) presented the solution of the rounded hyperbolic Mohr-Coulomb gradients.

$$\frac{\partial f}{\partial \sigma} = C_1\frac{\partial I_1}{\partial \sigma} + C_2\frac{\partial \sqrt{J_2}}{\partial \sigma} + C_3\frac{\partial J_3}{\partial \sigma} \tag{5.30}$$

where the first term:

$$C_1\frac{\partial I_1}{\partial \sigma} = \frac{1}{3}\left\{\begin{array}{c} sin\phi \\ sin\phi \\ sin\phi \\ 0 \\ 0 \\ 0 \end{array}\right\} \tag{5.31}$$

where $\frac{\partial J_2}{\partial \sigma}$ in the second term:

$$\frac{\partial J_2}{\partial \sigma} = \left\{\begin{array}{c} \sigma_{xx} - I_1 \\ \sigma_{yy} - I_1 \\ \sigma_{zz} - I_1 \\ 2\tau_{xy} \\ 2\tau_{yz} \\ 2\tau_{xz} \end{array}\right\} \tag{5.32}$$

and where $\frac{\partial J_3}{\partial \sigma}$ in the third term:

$$\frac{\partial J_3}{\partial \sigma} = \left\{ \begin{array}{c} (\sigma_{yy} - I_1)(\sigma_{zz} - I_1) - \tau_{yz}^2 \\ (\sigma_{xx} - I_1)(\sigma_{zz} - I_1) - \tau_{xz}^2 \\ (\sigma_{xx} - I_1)(\sigma_{yy} - I_1) - \tau_{xy}^2 \\ 2(\tau_{yz}\tau_{xz} - (\sigma_{zz} - I_1)\tau_{xy}) \\ 2(\tau_{xz}\tau_{xy} - (\sigma_{xx} - I_1)\tau_{yz}) \\ 2(\tau_{xy}\tau_{yz} - (\sigma_{yy} - I_1)\tau_{xz}) \end{array} \right\} + \frac{\sqrt{J_2}}{3} \left\{ \begin{array}{c} 1 \\ 1 \\ 1 \\ 0 \\ 0 \\ 0 \end{array} \right\} \tag{5.33}$$

The constants C_2 and C_3 need special treatments.

Away from the corners of the Mohr-Coulomb yield criterion ($|\theta| \leq \theta_T$, where θ_T= the angle of tolerance), the constant C_2 and C_3 are found by differentiating Equation 5.18.

$$C_2 = K - tan3\theta \frac{dK}{d\theta} \tag{5.34}$$

$$C_3 = -\frac{\sqrt{3}}{2cos3\theta J_2} \frac{dK}{d\theta} \tag{5.35}$$

where $K = K(\theta)$ is defined by 5.24 and

$$\frac{dK}{d\theta} = -sin\theta - \frac{1}{\sqrt{3}} sin\phi cos\theta \tag{5.36}$$

At a corner of the Mohr-Coulomb yield surface ($|\theta| \leq \theta_T$) , Equation 5.27 should be substituted into Equations 5.34 and 5.35.

$$C_2 = A + 2Bsin3\theta \tag{5.37}$$

$$C_3 = \frac{3\sqrt{3}B}{2J_2} \tag{5.38}$$

It can be easily shown that coefficients C_2 and C_3 in Equation 5.30 resulting differentiating Equation 5.28 differs from the coefficients C_2 and C_3 found earlier by α, where

$$\alpha = \frac{\sqrt{J_2}K}{\sqrt{J_2K^2 + a^2sin^2\phi}} \tag{5.39}$$

Finally, two terms of Equation 5.30, which includes C_2 and C_3, can be rewritten as:

$$C_2 \frac{\partial \sqrt{J_2}}{\partial \sigma} := \frac{1}{2} \bar{\alpha} C_2 \begin{Bmatrix} \sigma_{xx} - I_1 \\ \sigma_{yy} - I_1 \\ \sigma_{zz} - I_1 \\ 2\tau_{xy} \\ 2\tau_{yz} \\ 2\tau_{xz} \end{Bmatrix} \tag{5.40}$$

$$C_3 \frac{\partial J_3}{\partial \sigma} := \bar{\alpha} J_2 C_3 \left\{ \frac{1}{\sqrt{J_2}} \begin{Bmatrix} (\sigma_{yy} - I_1)(\sigma_{zz} - I_1) - \tau_{yz}^2 \\ (\sigma_{xx} - I_1)(\sigma_{zz} - I_1) - \tau_{xz}^2 \\ (\sigma_{xx} - I_1)(\sigma_{yy} - I_1) - \tau_{xy}^2 \\ 2(\tau_{yz}\tau_{xz} - (\sigma_{zz} - I_1)\tau_{xy}) \\ 2(\tau_{xz}\tau_{xy} - (\sigma_{xx} - I_1)\tau_{yz}) \\ 2(\tau_{xy}\tau_{yz} - (\sigma_{yy} - I_1)\tau_{xz}) \end{Bmatrix} + \frac{\sqrt{J_2}}{3} \begin{Bmatrix} 1 \\ 1 \\ 1 \\ 0 \\ 0 \\ 0 \end{Bmatrix} \right\} \tag{5.41}$$

where $\bar{\alpha} = {}^{K}/\sqrt{J_2K^2 + a^2 sin^2\phi}$

The perturbation of $\sqrt{J_2}$ is done to minimize the effect of division by $\sqrt{J_2}$ by small values.

5.6 Cylindrical Hole Cut into the Cube

Once the models were programmed, they should have been tested. The results of the UDCMs were compared with the results of the Itasca's models embedded in FLAC3D using an example of the 'Cylindrical Hole in a Semi-Infinite Mass Simulation' from the FLAC3D manual (Itasca, 2011). At the beginning of the verification, the elastic, isotropic model with a bulk modulus of 3.5e+8Pa and a shear modulus of 2.1e+8Pa, which corresponded to an elastic modulus of 5.25e+8Pa and Poissons ratio of 0.25, was developed. The symmetry of the problem was used, and only one quarter of the object was modeled. The domain of this model and boundary conditions are presented in Figure 5.4.

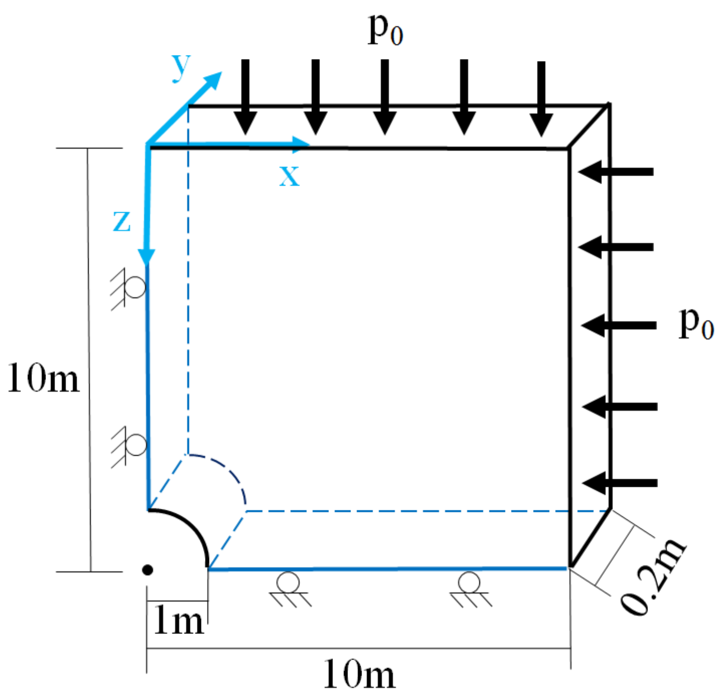

Figure 5.4: Domain and Boundary Conditions for Simulation of Cylindrical Hole Cut into the Cube

Following the FLAC3D manual (Itasca, 2011), the domain was a 0.2m-thick 10mx10m cuboid, which was discretized into one layer of 900 zones or 1922 grid points. In the cuboid corner, a quarter-cylindrical hole was placed as shown in Figure 5.4. The out-of-plane direction was fixed. Two cutting walls of symmetry were fixed in the literal direction. The initial stress (p_0) of 30MPa was applied throughout the domain in the beginning, and then the hole was removed from the domain. The normal stress of 30MPa was applied to the rest of unfixed walls. It took seconds to reach the equilibrium solution on a 3.4GHz Intel(R) Core(TM)i7-3770 CPU computer. The results (stresses and displacements) of the built-in models and the UDCM were drawn for each type of stress and displacement. These plots are presented in Appendix A.1.1, and they show the results of both models to coincide, except shear stresses in the xy- and yz- directions. These disagreements were caused by numerical instability because these stresses were much smaller than the stresses in other directions. For the Mohr-Coulomb analyses, the cohesion was of 3.45MP and the friction angle was of 30°. The non-associated flow rules were used, the dilation angle was of 0°. The results agreed well and are presented in Appendix A.1.2. At the same time, the numerical instability of small shear stresses was noticed in the Mohr-Coulomb model.

5.7 Spherical Hole Cut into the Cube

To avoid the numerical instability mentioned in Section 5.6, the previous FLAC example was extended to three dimensions by increasing the out-of plane side of the cuboid, and the cylindrical hole was replaced with the spherical hole. The domain of this model and boundary conditions are presented in Figure 5.5.

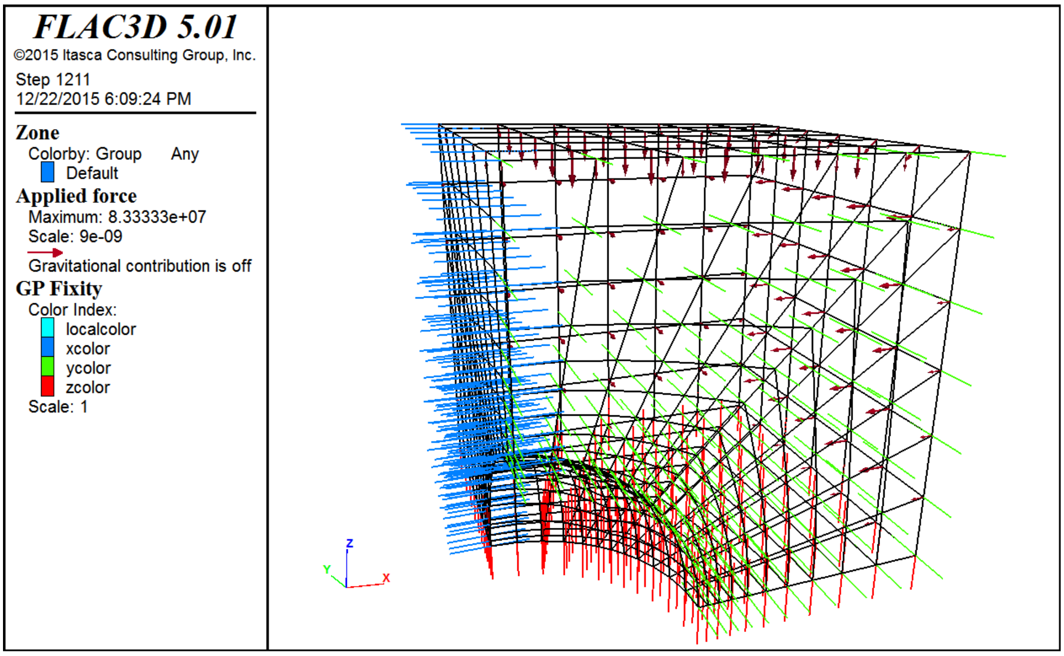

Figure 5.5: Domain and Boundary Conditions for Simulation of Spherical Hole Cut into the Cube

The domain was a 10m cube, into which a spherical hole of radius 4m was cut as shown in Figure 5.5. This domain had 1080 zones and 1397 grid points. Three cutting walls of symmetry were fixed in the lateral direction. Since the previous model highlighted some encountered difficulties with small stresses, the initial stresses were reduced. The initial stress of 3Pa was applied throughout the domain at the beginning, and then the hole was removed. The normal stress of 3Pa was applied to the remaining unfixed walls. Appendix A.2.1 and Appendix A.2.2 demonstrate the full sets of the results of the FLAC's elastic and Drucker-Prager models and UDCMs in close agreement for small stresses. After that, the stresses were increased to a value of the previous problem with the cylindrical hole. The results (Appendix A.2) of the built-in elastic, Drucker-Prager, and Mohr-Coulomb models and UDCMs were in close agreement for different stresses.

5.8 Smooth Circular Footing on an Associated Mohr-Coulomb Material

Since the UDCMs and the built-in models had identical results, the Mohr-Coulomb UDCM was tested for analytical solutions. Following Cox et al. (1961), the analytical average pressure over the footing at failure for a friction angle of 20°and cohesion of 0.1MPa was 20.1MPa (Itasca, 2011). The quarter segment domain and boundary conditions of the model are sketched in Figure 5.6.

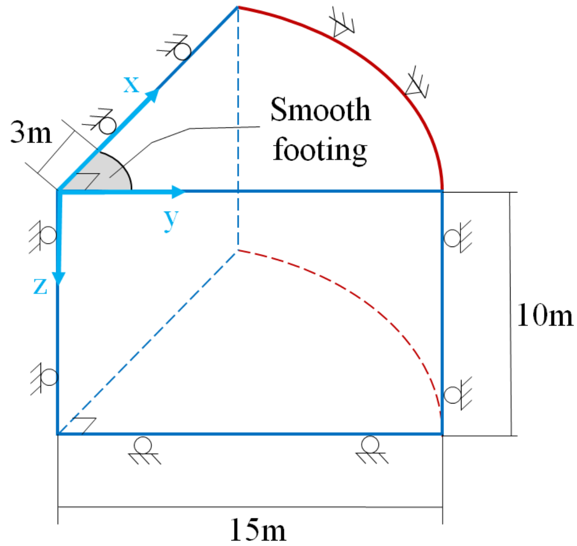

Figure 5.6: Domain and Boundary Conditions for Simulation of Smooth Circular Footing on an Associated Mohr-Coulomb Material after Itasca (2011)

Figure 5.6 depicts roller boundary conditions on all sides of the model except for the semicircular sides, which were fixed. A system of coordinate axes was selected in such a way that the x- and y-axes were in the plane of the cylinder upper-base, and the z-axis pointed downwards along the cylinder axis. The slab was represented by a disk segment with a radius of 3m. The radius of the domain was 15m, and its height was 10m. A downward velocity of 2x10 ^{5}m/step was applied to the grid points representing the extent of the footing in the positive z-direction for a total of 9600 timesteps.

This domain with the built-in Mohr-Coulomb model resulted in pressure over the footing of 20.3MPa, which was in an error of 0.94%. At the same time, the programmed Mohr-Coulomb model oppositely underestimated the pressure with a slightly larger error of 0.99% (19.9MPa). The impact of the fixed boundary conditions was also checked by replacing the fixed semicircular sides of the model with roller boundary conditions. The error increased insignificantly by 1.03%.

The difference in the results obtained with UDCM and the built-in model is believed to be due to different algorithms of avoiding the yield surface drift. FLAC's model solves the quadratic equation each time landing stresses on the yield surface. The UDCM implements the algorithm of the drift correction which was described in Section 5.4.

The UDCM was largely affected by yield surface drift. Figure 5.7 illustrates the results with and without the drift correction.

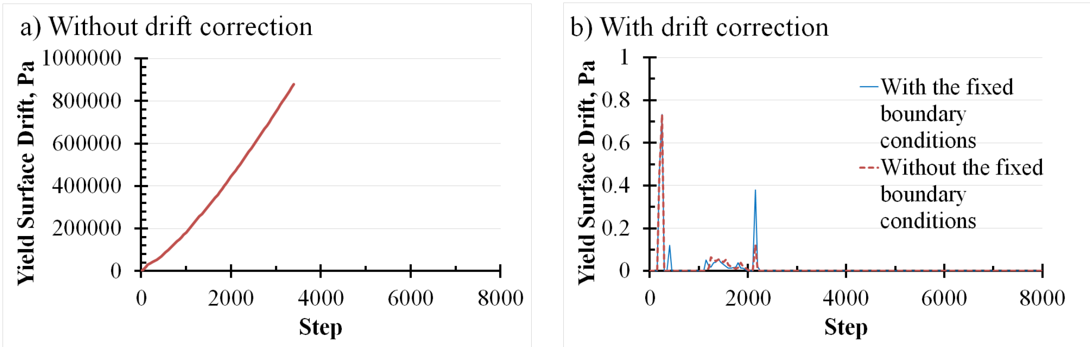

Figure 5.7: Yielding Surface Drift

Figure 5.7a shows that the stresses of the model without correction drift away from the yield surface while stepping, and the model crashes. The stresses of the model with the drift correction return to the yield surface in Figure 5.7b. The figure presents the drift correction for two models, i.e. the model with the fixed boundary conditions on the semicircular sides and the model exclusively with the roller boundary conditions. The less constraint model caused smaller yield surface drift, which can be seen as the spikes in Figure 5.7b.

5.9 Critical State Model

The Mohr-Coulomb failure criteria fail to adequately model many basic features of soil and soft rock behavior, such as differing the volumetric response of soil depending on its stress history and Critical State stress relationship. The Critical State models were a significant breakthrough in geomechanics (Gens and Potts, 1988). The Critical State of granular materials is described by two equations:

$$q = Mp \tag{5.42}$$

$$\Gamma = \nu + \lambda ln(p) \tag{5.43}$$

The constants M, Γ, and λ represent basic soil-material properties. M is a component of the failure criterion. Γ, and λ are responsible for hardening and softening relations. The parameters ν, p, and q are the specific volume, the mean effective stress, and deviatoric stress, which have the following relations with the stress invariants: $p = I_1/3$ and $q = \sqrt{(3J_2)}$. The first elastic-plastic Critical State models, Cam-clay and modified Cam-clay, were developed at the University of Cambridge by Roscoe and his co-workers. The Cam-clay yield surface is a logarithmic curve. The modified Cam-clay yield surface is plotted as an elliptical curve, which is more convenient in numerical analysis. Here, the modified Cam-clay model is considered because it is available in FLAC. The Critical State concept for the modified Cam-clay function (Equation 5.44) is presented in Figure 5.8, where the NCL, SW, and CSL stand for the Normal Consolidation Line, the unloading-reloading (Swelling) line and the Critical State Line, respectively. The stress moves down along the NCL when the soil sample is first loaded. Once the sample is unloaded, the stress moves up along the SW. The CSL, where the soil distorts with no volume change, is parallel to the NCL.

$$f(q,p) = q^2 + M^2 p(p - p_0) \tag{5.44}$$

where p_0 is the pre-consolidation pressure.

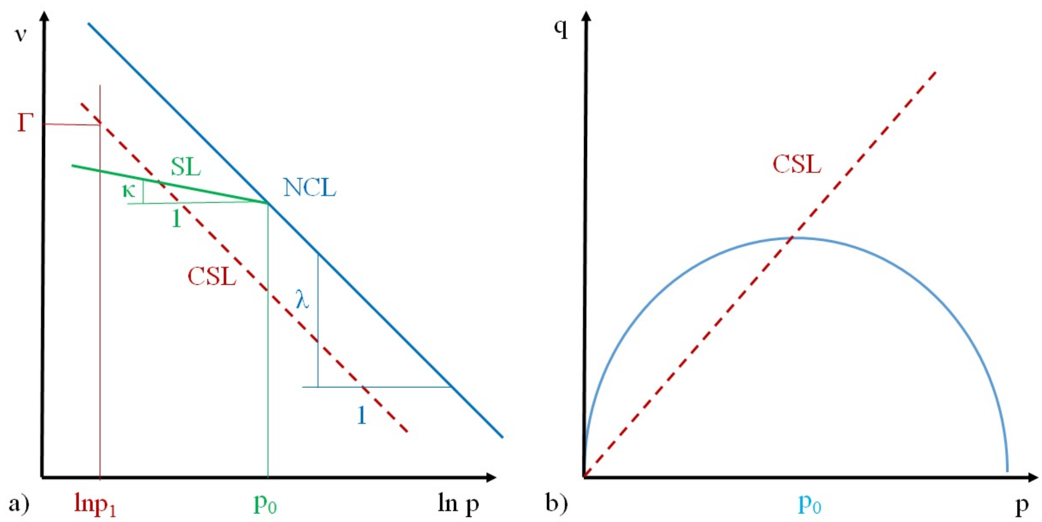

Figure 5.8: Critical State Concept and Modified Cam-clay Failure Criterion after Yu (2007)

Figure 5.8 illustrates the modified Cam-clay yield function (Equation 5.44) in the q-p space. The yield function is intersected by the CSL at the top of the yield locus. This point is called the Critical State point. In the modified Cam-clay model, the bulk modulus, K, changes as a function of the specific volume and the mean stress:

$$K = \frac{\nu p}{\kappa} \tag{5.45}$$

where κ is the angle of the swelling line.

One of the main shortcomings of the modified Cam-clay model is that the Critical State point often does not lie at the top of the yield locus; instead, it lies to the left of the peak. Observations indicate that the deviatoric stress often reaches a local peak before approaching the Critical State for sands Khong (2004). The Clay And Sand Model (CASM) does not have this shortcoming.

CASM was introduced by Yu (1995) and can be considered as the next step in programming the more sophisticated constitutive models. CASM is an extension of the modified Cam-clay model. It has two additional parameters r, which specifies the Critical State point, and n, which controls the shape of the yield surface. The yield surface function for CASM can be expressed:

$$f(q,p) = \left(\frac{q}{Mp}\right)^n + \frac{ln(p/p_0)}{lnr} \tag{5.46}$$

As seen from Equation 5.46, the shape of the yield surface is not perfectly elliptical. This makes the Critical State point shift to the left as shown in Figure 5.12. This excludes the drawback of the modified Cam-clay. CASM approximates the observed behaviour of sand and any other granular soils better.

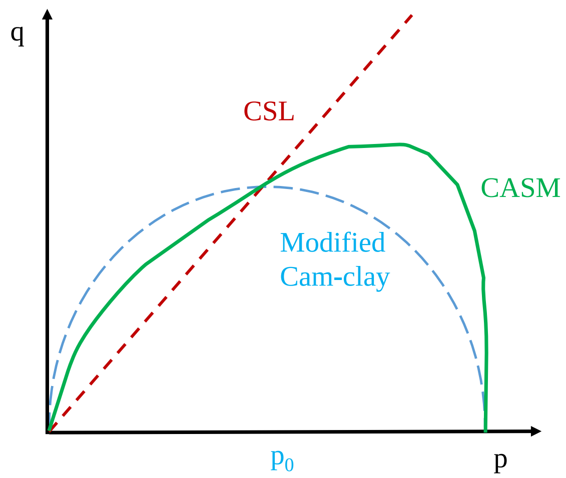

Figure 5.9: CASM Yield Surface

5.10 Triaxial Compression Test on Cam-Clay Material

In the beginning, the modified Cam-clay UDCM was validated, and only then CASM was tasted. For the validation of the modified Cam-clay UDCM, a one-zone cube model was developed to exclude the influence of the mesh density and to minimize the effect of its size. The plane sketch of the model is presented in Figure 5.10.

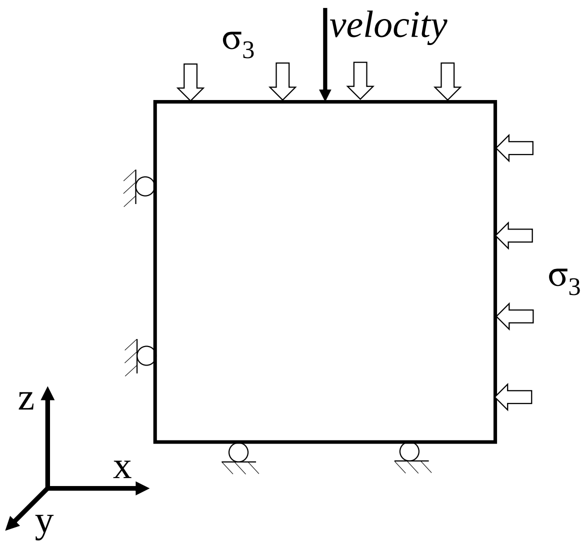

Figure 5.10: Representation of the Triaxial Test in FLAC

The model was fixed in the y-direction. The roller boundary conditions were imposed on the bottom and left side of the model. On the top and right side of the model, the compression pressure was assigned. The velocity, which corresponds to the desired displacement as the number of steps divided by the desired displacement, was assigned on the top of the model. After the FLAC3D manual (Itasca, 2011), the properties of the lightly-over-consolidated clay ($\sigma_3 = 1.6 \cdot p_0$) were used:

Shear modulus (G) 250kPa;

Maximum bulk modulus, (K_{max}) 8000kPa;

Frictional constant (M) 1.02;

Slope of normal consolidation line (λ) 0.2;

Slope of elastic swelling line (κ) 0.05;

Pre-consolidation pressure (p_0) 5.0kPa;

Reference pressure (p_1) 1.0kPa;

Specific volume at reference pressure

on normal consolidation line (ν_λ) 3.32.

For these properties, the graphs of deviatoric stress and plastic volumetric strain vs strain were plotted in Figure 5.11.

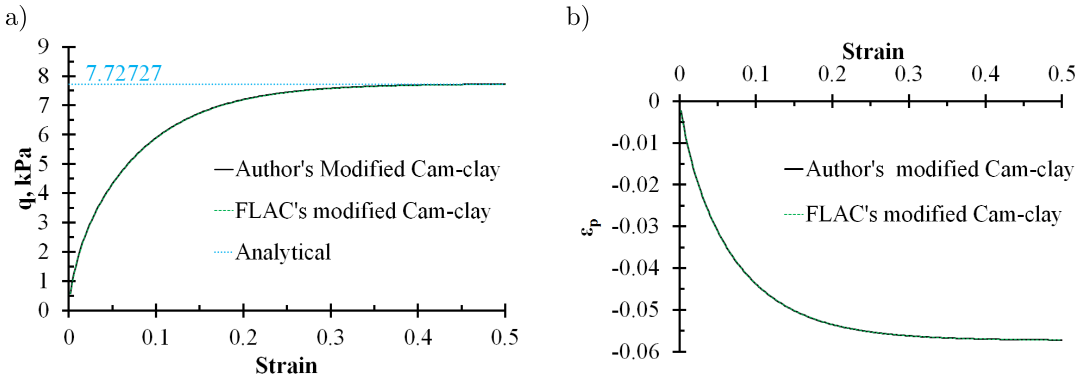

Figure 5.11: Comparison between the UDCM and Built-in Modified Cam-Clay Model

In Figure 5.11, the results of both models are identical. The modelled results of the triaxial compression were also compared with a closed-form solution in the FLAC3D manual (Itasca, 2011).

$$p = \frac{3p_0}{3-M} \tag{5.47}$$

$$q = Mp \tag{5.48}$$

$$\nu_{cr} = \nu_\lambda - \lambda ln(2p/p_1) + \kappa ln2 \tag{5.49}$$

The following results were obtained by the closed-form solution and by Itasca's modified Cam-clay model:

Analytical: $p = 7.57576$ $q = 7.72727$ $\nu = 2.81104$

Numerical: $p = 7.57575$ $q = 7.72725$ $\nu = 2.81104$

Error (%): $p = 0.00010054$ $q = 0.000295992$ $\nu =$ 1.75728e-05

and the results of the modified Cam-clay UDCM are

Analytical: $p = 7.57576$ $q = 7.72727$ $\nu = 2.81104$

Numerical: $p = 7.57573$ $q = 7.72714$ $\nu = 2.81104$

Error (%): $p = 0.000420829$ $q = 0.00172148$ $\nu =$ 8.08028e-05

The analytical deviatoric stress is presented in Figure 5.11. The comparison with the analytical results indicates relative errors of less than 2% for both Itacsa's model and the UDCM. As can be seen, errors of p and q are slightly increased for the UDCM, but at the same time, an error of v is decreased.

5.11 Triaxial Compression Test on CASM Material

User-defined CASM is validated using test data performed on remoulded Weald clay at Imperial College, London by Bishop and Henkel (1957). This clay was used by Khong (2004) to validate the CASM model which was incorporated into a finite element package CRISP. Khong (2004) assigned the following parameters:

Poisson's ratio (μ) 0.3;
Frictional constant (M) = 0.9;
Slope of normal consolidation line (λ) 0.093;
Slope of elastic swelling line (κ) 0.025;
Pre-consolidation pressure (p_0) 250kPa for normally consolidated soil and
Reference pressure (p_1) 1.0kPa;
Specific volume at reference pressure
on normal consolidation line (ν_λ) 2.06;
Stress-state coefficient (n) 4.5
Spacing ratio (r) 2.718.

The following analytical and numerical results were obtained:

Analytical: $p = 357.143$ $q = 321.429$ $\nu = 1.4662$
Numerical: $p = 338.746$ $q = 265.267$ $\nu = 1.48182$
Error (%): $p = 5.1513$ $q = 17.4724$ $\nu = 1.06508$

The results of CASM indicated relative errors of 5.1513%, 17.4724%, and 1.06508% for mean and deviatoric stresses and volumatric strain, respectively. The error of CASM increased in comparison with the earlier results of the modified Cam-clay model in Section 5.10 because the analytical solution was drawn from the theory of the Cam-clay plasticity; therefore for CASM validation, the laboratory data is required.

Khong (2004) validated CASM using deviatoric stress (q) and volumetric plastic strain(ϵ_p) of the laboratory tests reported by Bishop and Henkel (1957). Figure 5.12 compares the results of user-defined CASM, and triaixial test data Khong (2004).

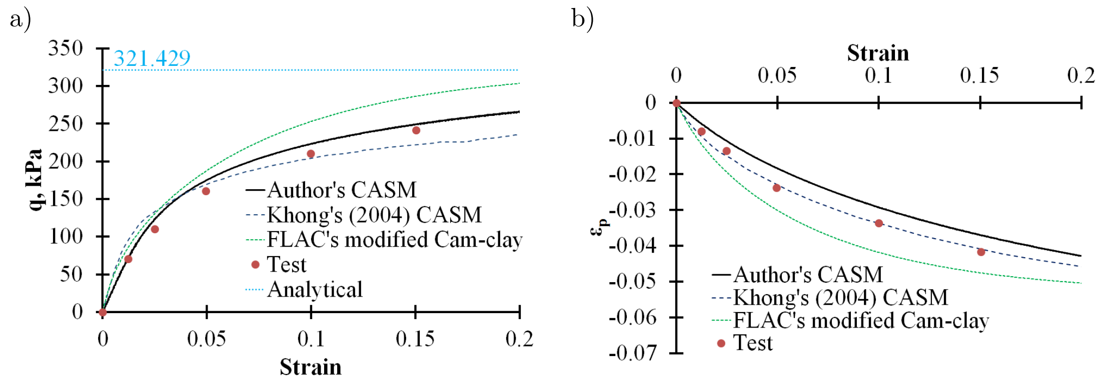

Figure 5.12: Comparison between CASM and the Test Data for Normally Consolidated Clay

Figure 5.12a illustrates three curves of the deviatoric stress versus strain and Figure 5.12b presents three curves of the plastic volumetric strain versus strain. The curves were obtained by the author in FLAC3D using the modified Cam-clay model and the user-defined CASM, and by Khong (2004) in CRISP (Britto and Gunn, 1987). In Figure 5.12a and Figure 5.12a, the dots represent the laboratory results. Figure 5.12a also depicts the analytical solution. Figure 5.12a reveals that the deviatoric stress that was modelled by the author using CASM agreed in the closest way with the laboratory results. Disgustingly from the other curves, the curve of the deviatoric stress that was modelled by Khong (2004) had a slightly different shape. The analytical solution and the modified Cam-clay model overestimated the laboratory deviatoric stress.

Contrary to the closest agreement of the deviatoric stress that was modelled by the author's CASM, Figure 5.12b depicts wider disagreement between the plastic volumetric strain that was modelled by the author's CASM and the laboratory results than the disagreement between the plastic volumetric strain that was simulated by Khong (2004) and the laboratory results. However, the disagreement was very small, within a thousandth of plastic volumetric strain. The different outcomes of these two identical models can be explained by the choice of the numerical solution of the partial differential equations. Khong (2004) programmed the model into CRISP, which utilizes the finite-element method, but the author used the finite-difference software FLAC3D. The modified Cam-clay model overestimated plastic volumetric strain and the deviatoric stress. At the same time, CASM could better capture the behaviour of the clay under triaxial loading.

5.12 Theory of the Bubble Model (Rouainia and Muir Wood, 2000)

Since user-defined CASM was verified, the programme could be sophisticated by a more complex constitutive model. The more complicated bubble model exploits the Cam-clay plasticity and is an extension of the modified Cam-clay model in line with CASM. The bubble model is complicated by kinematic hardening, bounding surface plasticity, and destructuration. The idea of two-surface models is to reduce the elastic domain by introducing an inner surface (bubble) inside an outer surface (bounding surface or structure surface), which encloses the elastic region. It was first introduced by Al-Tabbaa and Wood (1989), and then it was extended by Wood (1995) for structured soil. To describe the behaviour of the structured soil, the bubble model contains three elliptical surfaces in stress space: a reference surface (f), a kinematic yield surface or bubble (f_b), and a structure surface (F) as shown in Figure 5.13. The bubble surface separates the elastic and plastic regions. Once the failure occurs, the bubble moves towards the structure surface.

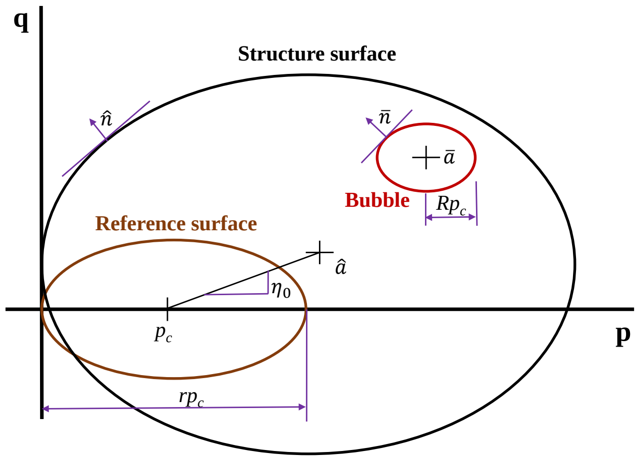

Figure 5.13: Bubble Model in Deviatoric Space after Ni (2007)

The surfaces are subject to change in size and in location when plastic strain occurs. Their analytical equations in mean principal stress - deviatoric stress tensors (p - s) space are Equations 5.50, 5.52, and 5.53. The reference surface is responsible for internal behaviour of the reconstituted soil. The surface is subject to change in size when volumetric plastic strain occurs according to the isotropic hardening rule (Equation 5.63). The reference surface is described by

$$f = \frac{3}{2M_\theta^2}(s)(s) + (p - p_c)^2 - (p_c)^2 = 0 \tag{5.50}$$

where p_c is the distance from the origin of the p, q coordinate system to the centre of the reference surface on the p axis; $p := \frac{1}{3}tr[\sigma]$ and $s := \sigma - pI$ where $tr[\cdot]$ is the trace operator of $[\cdot]$ and I is the second-rank identity tensor; M_θ is the function of the Lode angle (θ):

$$M_\theta = \frac{2mM}{(1+m) - (1-m)sin(3\theta)} \tag{5.51}$$

where m is the ratio of extension and compression strengths. It should be between 0.7 and 1.0 to ensure the convexity of the reference surface. M is the critical state stress ratio for axisymmetrical compression.

In contrast to the reference surface, which is always centered on the p axis (Figure 5.13), the bubble moves around within the structure surface according to the kinematic hardening rule (Equation 5.64). The analytical equation of the bubble is given by

$$f_b = \frac{3}{2M_\theta^2}(s - s_{\bar{a}}) : (s - s_{\bar{a}}) + (p - p_{\bar{a}})^2 - (Rp_c)^2 = 0 \tag{5.52}$$

where $\{p_{\bar{a}}, s_{\bar{a}}\}^T = \bar{a}$ denotes the location of the centre of the bubble in the stress space;
R is the ratio between the sizes of the bubble and the reference surface.

The structure surface could be considered as a bounding surface where the bubble moves around. Destruction of the structure surface is controlled by kinematic and isotropic hardening. After the destruction, the surface is only controlled by isotropic hardening. The structure surface is defined as

$$F = \frac{3}{2M_\theta^2}(s - (r-1)\eta_0 p_c) : (s - (r-1)\eta_0 p_c) + (p - rp_c)^2 - (rp_c)^2 = 0 \tag{5.53}$$

where η_0 is a dimensionless deviatoric tensor controlling the structure surface;
$\{rp_c(r-1)\eta_0 p_c\}^T = \hat{a}$ denotes the centre of the structure surface;
r is the ratio between the sizes of the structure and the reference surfaces, which represents the process of the progressive destructuration of a structured soil as a monotonically decreasing function of the plastic strain:

$$r = 1 + (r_0 - 1)exp\left[\frac{-k\varepsilon_d}{\lambda^* - \kappa^*}\right] \tag{5.54}$$

where λ^* is the slope of the normal compression line expressed in a logarithmic specific volume –

logarithmic mean stress compression plane (i.e. $ln\nu \sim lnp$ plane);
κ^* is the slope of swelling line;
r_0 is the initial size of the structure surface;
k is a parameter controlling the rate of destruction with strain;
ε_d is an assumed destructuration strain.

The incremental form of the destructuration law is written as,

$$\dot{r} = -\frac{-k}{\lambda^* - \kappa^*}(r-1)\dot{\varepsilon_d} \tag{5.55}$$

where $\dot{\varepsilon}_d$ is the destructuration strain rate.

$$\dot{\varepsilon}_d = \left[(1-A)\left(\dot{\varepsilon}^p_\nu\right)^2 + A\left(\dot{\varepsilon}^p_q\right)^2\right]^{1/2} \tag{5.56}$$

A is a non-dimensional scaling parameter, $\dot{\varepsilon}^p_\nu$ is the plastic volumetric strain rate and $\dot{\varepsilon}^p_q$ is the equivalent plastic shear strain rate.
When the yield function is zero, plastic strain occurs:

$$\dot{\varepsilon}^p = \frac{1}{H}(\bar{n} : \dot{\sigma})\bar{n} \tag{5.57}$$

where $\dot{\sigma}$ is the stress rate and $\bar{n}$ denotes a unit vector representing the normalised stress gradient on the bubble at the current stress state;
H is the scalar plastic modulus expressed as follows:

$$H = H_c + \frac{1}{\|n\|^2}\frac{BR^2p_c^3}{(\lambda^* - \kappa^*)}\left(\frac{b}{b_{max}}\right)^\psi \tag{5.58}$$

where n is the stress gradient on the bubble at the current stress state and $\|n\| = [n : n]^{1/2}$;
B is a material parameter controlling the magnitude of plastic modulus;
ψ is a material parameter controlling the rate of decay of plastic modulus;
H_c is the plastic modulus associated with the conjugate stress state σ_c on the structure surface. It is given by

$$H_c = \frac{rp_c\left\langle T\left[(p-p_{\bar{a}}) + \frac{3}{2M_\theta^2}(s-s_{\bar{a}}) : \eta_0 + Rp_c\right] - \frac{3}{2M_\theta^2}(p-p_{\bar{a}})(s-s_{\bar{a}}) : \frac{\eta_0}{r}\right\rangle}{(\lambda^* - \kappa^*)\left[(p-p_{\bar{a}})^2 + \frac{3}{2M_\theta^2}(s-s_{\bar{a}}) : (s-s_{\bar{a}})\right]} \tag{5.59}$$

where the quantity T is given by

$$T = (p - p_{\bar{a}}) - k\left(\frac{r-1}{r}\right)\left[(1-A)(p-p_{\bar{a}})^2 + \frac{3A}{2M_\theta^2}(s - s_{\bar{a}}) : (s - s_{\bar{a}})\right]^{1/2} \tag{5.60}$$

In Equation 5.58, b is a normalised distance between current stress point σ on the bubble and the conjugate stress point σ_c on the structure surface, and b_{max} is obtained when the bubble is touching the structure surface at a point diametrically opposite to the conjugate stress point. b and b_{max} are expressed as follows:

$$b = \bar{n} : (\sigma_c - \sigma) \tag{5.61}$$

$$b_{max} = 2\left(\frac{r}{R} - 1\right)\bar{n} : \bar{\sigma} \tag{5.62}$$

In line with the Cam-clay model, *isotropic hardening* is controlled only by the plastic volumetric strain rate which is given by

$$\frac{\dot{p}_c}{p_c} = \frac{\dot{\varepsilon}_\nu^p}{(\lambda^* - \kappa^*)} \tag{5.63}$$

when plastic strain occurs, the bubble translates inside the structure surface according to the *kinematic hardening* rule given by

$$\dot{\bar{a}} = \dot{\hat{a}} + (\bar{a} - \hat{a})\left(\frac{\dot{r}}{r} + \frac{\dot{p}_c}{p_c}\right) + \frac{\bar{n}\left\{\dot{\hat{\sigma}} - \hat{\sigma}\left[\left(\frac{\dot{r}}{r}\right) + \left(\frac{\dot{p}_c}{p_c}\right) + \bar{\sigma}\left(\frac{\dot{r}}{r}\right)\right]\right\}}{\bar{n} : (\sigma_c - \sigma)}(\sigma_c - \sigma) \tag{5.64}$$

where $\hat{\sigma} = \sigma - \hat{a}$ is the normalised stress with respect to the centre of the structure surface.

In the bubble model, the elastic bulk and shear moduli, K and G, are defined as

$$K = \frac{p}{\kappa^*} \tag{5.65}$$

$$G = \frac{3(1-2\mu)}{2(1+\mu)K} \tag{5.66}$$

where μ is the constant Poisson's ratio.

Despite the rather difficult equations and a high number of parameters, the bubble model has an effective extension from the modified Cam-clay model. The bubble model includes a kinematic hardening rule and a reduced elastic zone due to the bubble surface. According to the discussions in Section 2.4 on the implementation of the constitutive models to simulate surface subsidence, the bubble model should be programmed into FLAC3D to run surface subsidence simulations.

5.13 Bubble Model in FLAC3D

The bubble model was written in C++ and compiled as a DLL file for FLAC3D in contrast to the code in FISH for FLAC2D developed by Ni (2007). The code of the model is presented in Appendix B. The programme includes subroutines of the initialization, run section, and necessary functions, such as raising a number to a power correctly, returning the sign of the function, computing the deviatoric stress. The flow chart of the programme is shown in Figure 5.14.

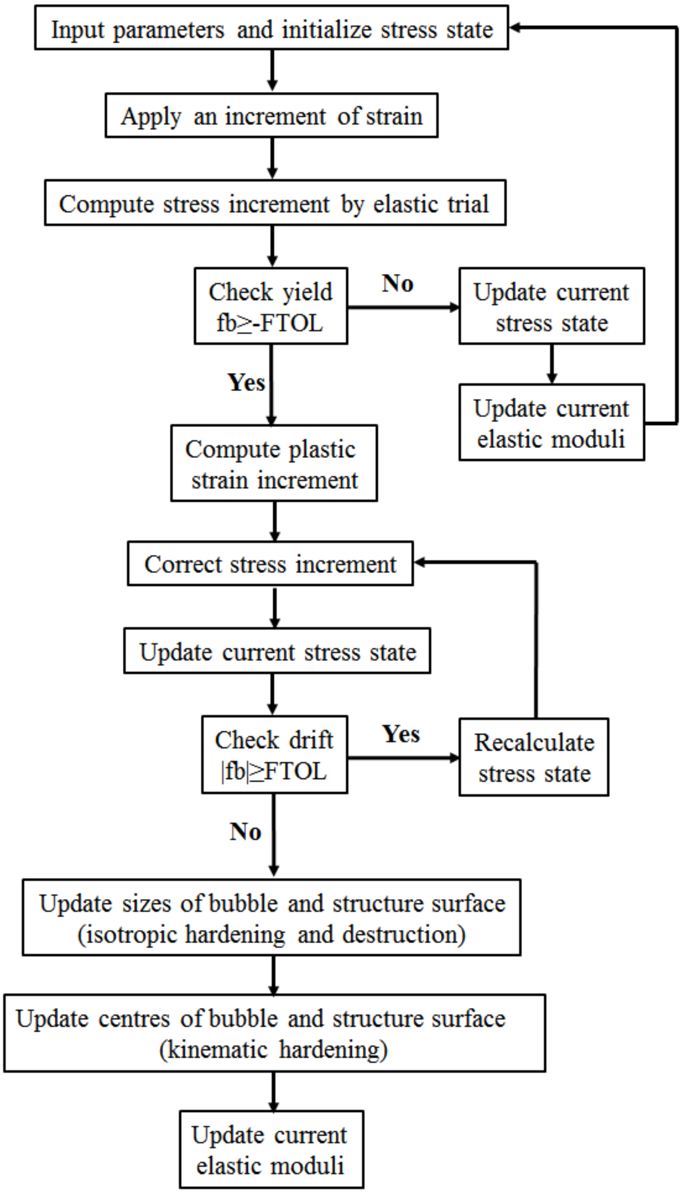

Figure 5.14: Flow Chart of the Programmed Bubble Model modified after Ni (2007)

Like all previous models, the run of the bubble model starts with an elastic guess. If this guess corresponds to the failure of material ($f_b \geq -FTOL$), the normalized stress gradient, hardening modulus, conjugate stress on the structure surface, the distance between the conjugate stress and current stress are computed.

The stress gradient is calculated as follows

$$\frac{\partial f_b}{\partial \sigma_{ij}} = \frac{-6}{M_\theta^3}\bar{J}_2\frac{\partial M_\theta}{\partial \sigma_{ij}} + \frac{3}{M_\theta^2}\frac{\partial \bar{J}_2}{\partial \sigma_{ij}} + 2(p - p_{\bar{a}})\frac{\partial p}{\partial \sigma_{ij}} \tag{5.67}$$

where

$$\frac{\partial p}{\partial \sigma_{ij}} = \frac{1}{3}\begin{Bmatrix} 1 \\ 1 \\ 1 \\ 0 \\ 0 \\ 0 \end{Bmatrix} \tag{5.68}$$

$$\frac{\partial M_\theta}{\partial \sigma_{ij}} = \frac{-12sqrt3m(1-m)M}{\left[2(1+m) + 3\sqrt{3}(1-m)\frac{J_3}{J_2^{\frac{3}{2}}}\right]^2}\frac{\partial\left[\frac{J_3}{J_2^{3/2}}\right]}{\partial \sigma_{ij}} \tag{5.69}$$

$$\frac{\partial\left[\frac{J_3}{J_2^{3/2}}\right]}{\partial \sigma_{ij}} = \frac{J_2^{3/2}\frac{\partial J_3}{\partial \sigma_{ij}} - \frac{3}{2}J_2^{1/2}J_3\frac{\partial J_2}{\partial \sigma_{ij}}}{J_2^3} \tag{5.70}$$

The other required terms of Equation 5.70 can be found in Section 5.5, i.e. J_2 is Equation 5.21, J_3 is Equation 5.23, and their derivatives $\frac{\partial J_2}{\partial \sigma_{ij}}$ and $\frac{\partial J_3}{\partial \sigma_{ij}}$ are Equations 5.32 and 5.33, respectively.

To ensure the non-intersection translation of the bubble through the structure surface, the programme calculates the maximum distance between the conjugate stress and stress when the bubble is touching the structure surface at a point diametrically opposite to the conjugate stress. The maximum distance is computed according to Equation 5.62. Then the plastic modulus is calculated using Equation 5.59. Out of this, the plastic strain increment is computed according to Equation 5.57. Then the elastic part of strain is found, and the stress rate is corrected. After this, the stresses are checked for the yield surface drift discussed as in Section 5.4. Once the drift is corrected, sizes (isotropic hardening) and centres (kinematic hardening) of the bubble and structure surface are updated using Equations 5.63 and 5.64. The step of the programme ends with updating the current elastic moduli (Equations 5.65 and 5.66). After the programming is completed, the validation is required.

5.14 Numerical Triaxial Test on Bubble Material

5.14.1 Bubble and Modified Cam-Clay Models

At the beginning of the validation, the bubble UDCM was compared with the modified Cam-clay model embedded in FLAC3D. Theoretically, the bubble model is recovered to the modified Cam-clay model when $R = 0.998$, r_0 =1.0 and ν_0=0, and the following set of parameters were used for each of the models (Ni, 2007):

Table 5.1: Bubble Properties Corresponding to Modified Cam-clay

Bubble model	**Modified Cam-clay model**
$\lambda^* = 0.3$ $\kappa^* = 0.02$ $M = 1$ $m = 1$ $\mu = 0.25$	$\lambda = 0.426$ $\kappa = 0.0284$ $M = 1$ $\mu = 0.25$
$B = 400$ $\psi = 0.5$	$p_1 = 50kPa$ $v_1 = 2.0$ (reference point)
$pc_0 = 200kPa$ $\sigma_3 = 200kPa$	$pc_0 = 400kPa$ $\sigma_3 = 200kPa$

The specimens, which properties are presented in Table 5.1, underwent triaxial compression. In FLAC3D, the numerical representation of the triaxial test was a single zone cube model in the axisymmetric configuration as shown in Figure 5.10 from Section 5.10. The grid was fixed in the z-direction. The roller boundary conditions were imposed on the bottom and the left side of the model. An initial isotropic compressive stress and a constant lateral confining pressure at the top and the right side of the model were applied according to the confining pressures (σ_3) from Table 5.1. A velocity boundary condition was applied at the top of the model. These settings of the models in FLAC2D and FLAC3D with the bubble UDCM and the built-in modified Cam-clay model resulted in the curves of deviatoric stress versus strain and volumetric strain versus strain, which are presented in Figure 5.15a and Figure 5.15b respectively.

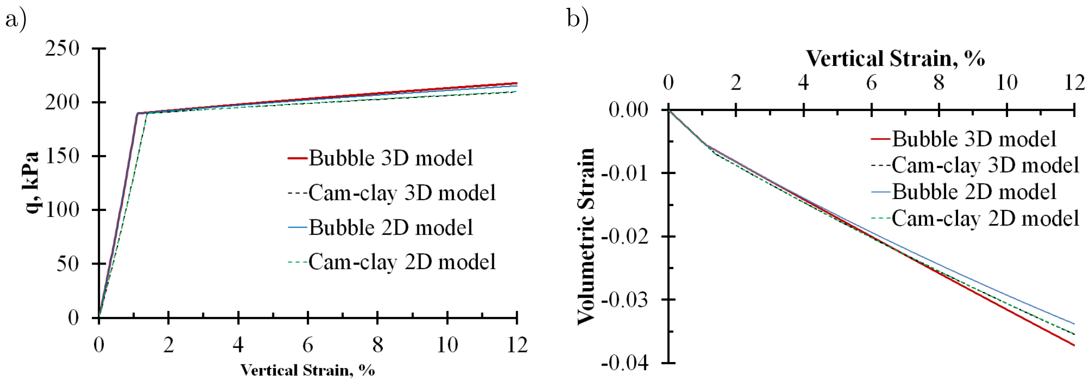

Figure 5.15: Comparison between the Bubble and Modified Cam-clay Models

There are four curves in Figure 5.15a and in Figure 5.15b. Due to the very close agreement between the results that were obtained with FLAC2D and FLAC3D four curves merged into two curves in Figure 5.15a. The curves that were obtained using the bubble model and modified Cam-clay model had very small discrepancy. In Figure 5.15b, the curves merge only once between the results that were obtained with Cam clay in 2D and 3D. The bubble model resulted in slightly different volumetric strain.

Some discrepancies between stress and volumetric strain results, which were modelled with the modified Cam-clay and bubble models, were caused by the model parameters. The modified Cam-clay parameters were adjusted to the bubble model with some approximation error. Some small differences were also noticeable between the volumetric strain results of the bubble models in FLAC2D and FLAC3D (Figure 5.15b). In FLAC3D, the volumetric shear strain is calculated in all direction; therefore, FLAC3D predicted slightly larger volumetric strain; however, these small deviations were considered to be negligible, and the validation of the bubble model could be carried out with the properties, which made the bubble model perform in its full capacity.

5.14.2 Experiment on Fine Uniform Sand

The next step of the validation was to check if the model could predict the triaxial measurements. The model was tested for its ability to reproduce triaxal test results, which were reported by Lee and Seed (1967) and used for validation of the bubble model in FLAC2D by Ni (2007). The soil, which was used in their experiment, was drained fine uniform sand with a density of 2.68kg/m^3 and limiting void ratio of 0.61 and 1.03. The loose sample had an initial void ratio of 0.87, a relative density of 38% and a frictional angle of 34°. For confining pressures of 100kPa, 450kPa, and 2000kPa, B and pc_0 parameters are presented in Table 5.2, respectively. Herewith, under-consolidated, normally consolidated, and over-consolidated samples were considered. The set of the bubble model parameters were taken from the validation of the bubble model in FLAC2D conducted by Ni (2007):

Standard parameters λ^*=0.3 κ^*=0.02 M=1 m=1 μ=0.3;

Bubble size R_{bub}=0.15;

Hardening modulus parameters ψ=1.0;

Initial conditions η_0=0 r_0=2.0.

Table 5.2: B and pc_0 Parameters for Different Confining Pressures

σ_3,	B	pc_0, kPa
100	600	300
450	1800	900
2000	25000	1200

For these properties and three confining pressures, Figures 5.16, 5.17, and 5.18 present the test data and the results modelled with the bubble models in FLAC2D and FLAC3D. The figures denoted 'a' were graphs between principal stress ratio and vertical strain. The figures denoted 'b' are graphs between volumetric strain and vertical strain.

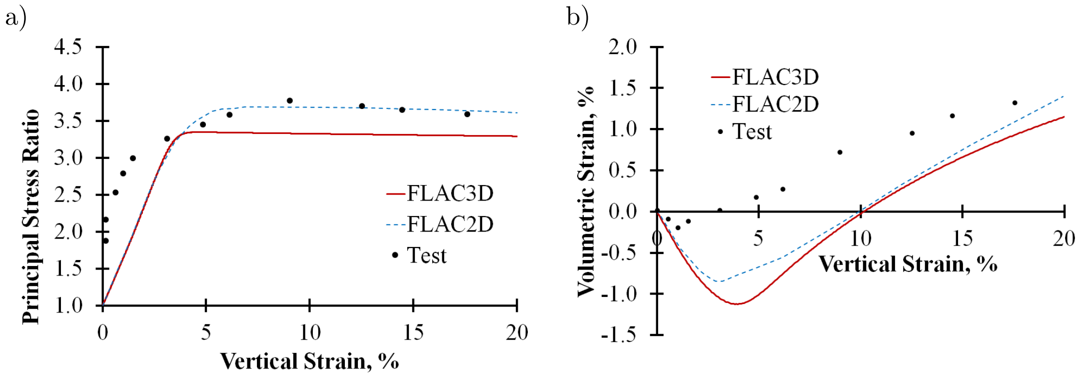

Figure 5.16: Stress-Strain and Volumetric Behaviour under a Confining Pressure of 100kPa

Figure 5.16 shows the behaviour of the sample under a confining pressure of 100kPa. FLAC3D predicted smaller stress than FLAC2D and laboratory experiment did (Figure 5.16a). The models overestimated a reduction in the volume during shearing before exhibiting dilation (Figure 5.16b).

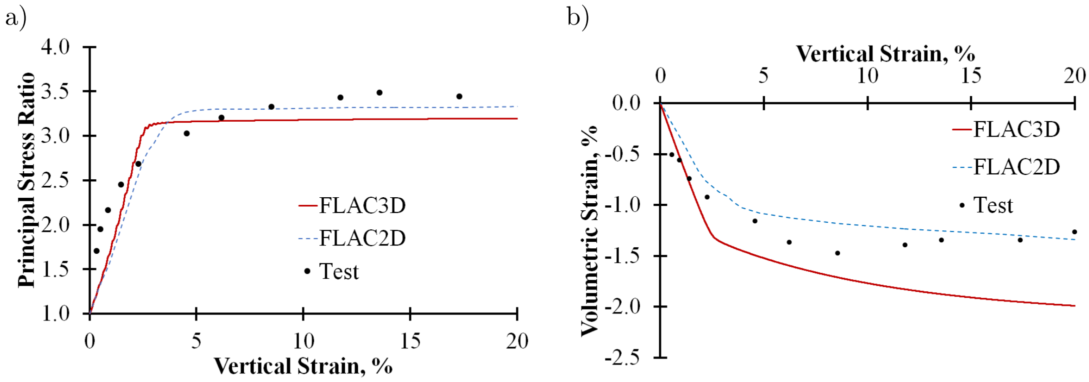

Figure 5.17: Stress-Strain and Volumetric Behaviour under a Confining Pressure of 450kPa

Figure 5.17a presents that the stress response to a confining pressure of 450kPa was also underestimated by FLAC3D, but the difference in the results of FLAC2D and FLAC3D was smaller. Figure 5.17a shows a small difference between the test and modelled results. Figure 5.17b depicts that FLAC3D overestimated volumetric strain and FLAC2D underestimated volumetric strain measured in the laboratory.

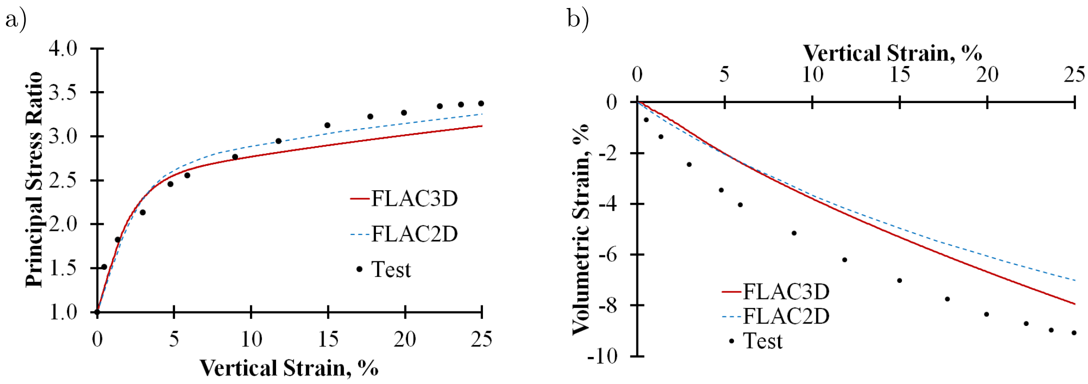

Figure 5.18: Stress-Strain and Volumetric Behaviour under a Confining Pressure of 2000kPa

Figure 5.18a presents very close stress results between FLAC2D, FLAC3D predictions and test. The volumetric strain was predicted smaller by FLAC2D and FLAC3D than the laboratory measurements.

In Figures 5.16, 5.17, and 5.18, some discrepancy can be seen between the results of Ni (2007) and the authors results. The reason was that the author used the 3D model where stress gradients had to be calculated in all directions, whereas in FLAC2D the stress gradient was considered as zero in the out-of-plane direction.

In most cases, the agreement between the model predictions and the experimental data was good. The best agreement was noticed under the initial mean confining pressure of 450kPa, when the sample was normally consolidated. Under the higher confining pressure of 2000kPa, the model underestimated a reduction in the volume. This deficiency of the bounding surface plasticity models was known and reported, for example, by Chávez and Alonso (2003).

For the best prediction when the specimen was under a confining pressure of 450kPa Figures 5.19 depicts a graphical representation of movements of the bubble and structure surfaces, stress and conjugate stress.

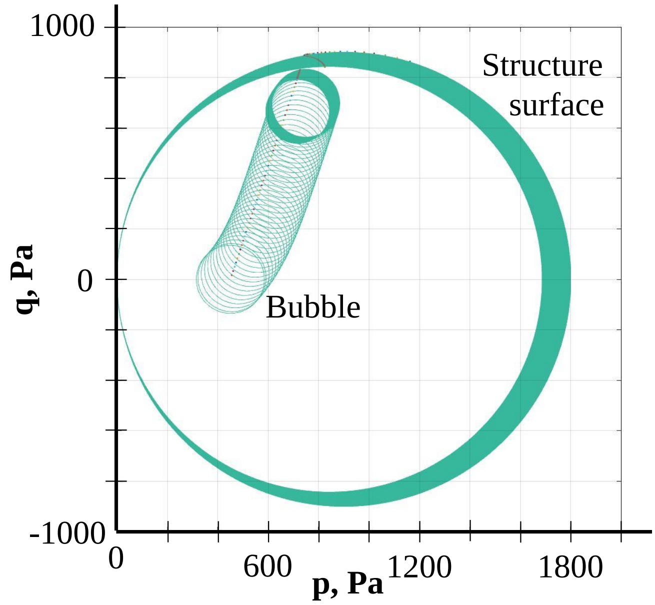

Figure 5.19: Surfaces at 25% Strain Stress-Strain under a Confining Pressure of 450kPa

Figure 5.19 shows the bubble surface moved towards the Structure surface. The bubble moved according to the kinematic hardening law. When the bubble touched the structure surface, the intensive isotropic hardening started and the structure surface was increasing in size.

5.15 Embankment Loading on a Cam-Clay Foundation

To extend the validation of the bubble model by using a more sophisticated equilibrium example, the 'Embankment Loading on a Cam-clay Foundation' described in the FLAC manual (Itasca, 2011) was considered. The saturated soil (undrained clay) foundation loaded by an embankment was 10 meters deep. The groundwater free surface was at the ground level. The embankment was 8 meters wide. The model domain consisted of 200 cube zones as shown in Figure 5.20. This domain mesh was used for the primary investigation. Since the mesh of this validation problem consists of more than one zone and Chapter 4 showed that the mesh density had a great impact on the result, this model was studied for the mesh sensitivity.

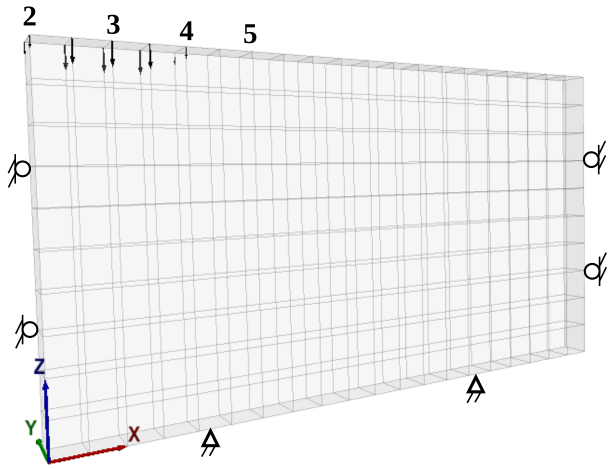

Figure 5.20: Model Geometry with Applied Forces and Points of Interest

Figure 5.20 presents four monitoring points 2, 3, 4, and 5. The mechanical boundary conditions corresponded to roller boundaries on both sides of the plane of analysis (y-direction), roller boundaries along the symmetry line and the far boundary of the model (x-direction), and to fixed displacements in the x-, y- and z-direction at the model base as shown in Figure 5.20. The ratio of horizontal to vertical effective stress is 6/13. A density of 2000kg/m^3 was used throughout the domain. An applied surcharge simulated the weight of the embankment. Water was drained through the soil surface. The Cam-clay properties of the soil are shown in Table 5.3.

Table 5.3: Bubble and Modified Cam-Clay Properties

Modified Cam-Clay Model	**Bubble Model**
$\lambda = 0.161$ $\kappa = 0.062$ $M = 0.888$ $\mu = 0.3$	$\lambda^* = 0.077$ $\kappa^* = 0.03$ $M = 0.888$ $m = 1$ $\mu = 0.3$
$p_1 = 1.6e5kPa$ $\nu_1 = 2.858$ (reference point)	$B = 50$ $\psi = 0.5$ $pc_0 = 800kPa$
$pc_0 = 400kPa$ $\sigma_3 = 200kPa$	

Table 5.3 also presents the bubble model properties, which correspond to the given Cam-clay model properties. As mentioned in Subsection 5.14.1, the bubble model was reduced to the modified Cam-clay model when $R = 0.998$, $r_0 = 1$ and $\nu = 0$. For the bubble model reduced to the modified Cam-clay, parameters k, m, A had no influence on model calculations. This can be easily shown by substitution in the equations of the bubble model in Section 5.12. Out of this, only bubble parameters λ^*, κ^*, B, and ψ should be estimated from the modified Cam-clay parameters. These parameters were derived following the algorithm presented by Ni (2007). For small strain problems,

values of λ^* and κ^* could be estimated by

$$\lambda^* \frac{\lambda}{\nu_0} \tag{5.71}$$

$$\kappa^* \frac{\kappa}{\nu_0} \tag{5.72}$$

where ν_0 is the initial specific volume corresponding to the initial mean effective principal stress p_0, which can be calculated as

$$\nu_0 = \nu_1 - \lambda \cdot ln \left(\frac{p}{p_1} \right) \tag{5.73}$$

where p is the current mean effective stress.

Parameter $\psi = 0.5$ was taken from the model described in Subsection 5.14.1. Parameter B depends on ψ and p_0. Ni (2007) found the relationship between B and p_0 for $\psi = 0.5$:

$$\nu_0 = \nu_1 - \lambda \cdot ln \left(\frac{p}{p_1} \right) \tag{5.74}$$

The displacements of the monitoring points were plotted against the groundwater time (discharge) in Figure 5.21.

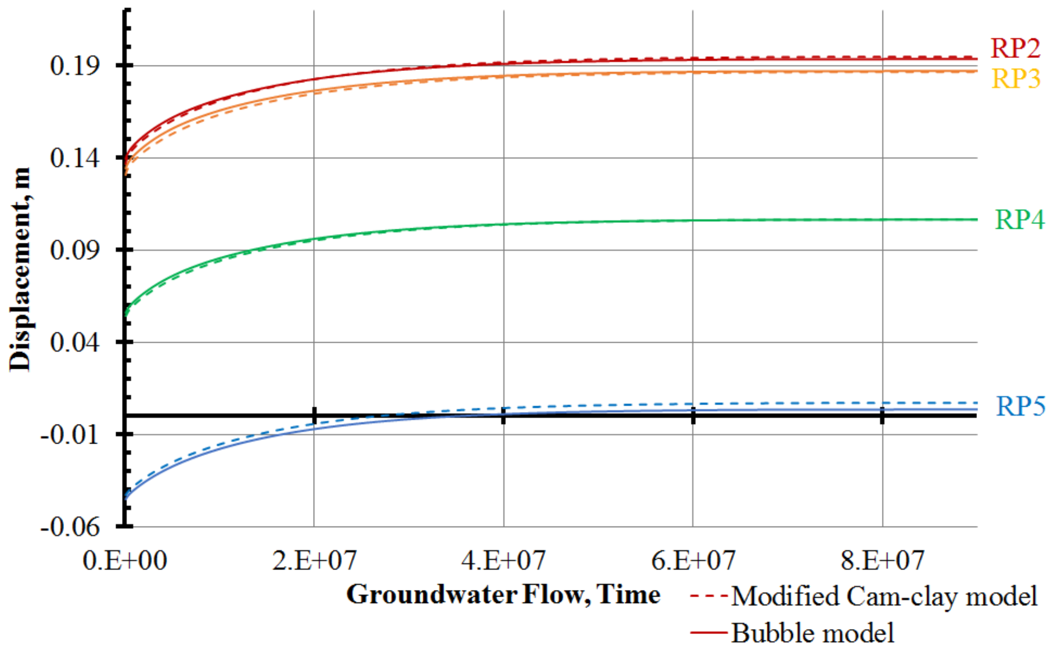

Figure 5.21: Vertical Displacement Histories

Figure 5.21 shows good agreement of modelled displacements that were simulated by both models. However, some small discrepancy between the results of the modified Cam-clay model and the bubble model could be noticed for point 5, where displacements occurred in the opposite direction (squeezing). Displacements of two monitoring points 2 and 3 were compared with the analytical solution from the FLAC manual (Itasca, 2011). Table 5.4 presents that the error was negligible (less than 5%) for both the modified Cam-clay and bubble models if the results were compared with the analytical solution.

Table 5.4: Bubble and Modified Cam-clay models vs Analytical Solution

	Error of the Modified Cam-clay (%)	Error of the Bubble model (%)
Point 2	2.53411	0.887831
Point 3	0.751566	3.43067

The close agreement of the results of the two models was challenged by altering mesh density. The errors of the models are presented in Table 5.5.

Table 5.5: Bubble and Modified Cam-clay models vs Analytical Solution

	Error of the Modified Cam-clay (%)	Error of the Bubble model (%)
Point 2	8.62568	12.6853
Point 3	14.8571	1.89427

Table 5.5 shows that the errors increased up to almost 15% from 5% when the mesh density was densified twice. The further densification of the mesh was not possible because the models crashed due to a lack of computer memory.

5.16 Summary

After overcoming two challenges, i.e. singularities at the corners of the yield surface and yield surface drift, the validation of the UDCMs indicated that the programmed models were capable of reproducing FLAC's models and predicting analytical and laboratory results. The user-defined popular models, i.e. the von Mises, Drucker-Prager, Tresca, Mohr-Coulomb, modified Cam-clay models were verified by comparison with the results of FLAC's built-in models, i.e. Mohr-Coulomb, and modified Cam-clay, and laboratory triaxial data. CASM and the bubble model were verified against the built-in modified Cam-clay model, laboratory data and results of these models which were earlier used for validation by Khong (2004) and by Ni (2007). The programmed von Mises, Drucker-Parger, Tresca and Mohr-Coulomb models, and modified Cam-clay models could perform on par with the built-in models. The sophisticated UDCMs, CASM and the bubble model, were compared with the built-in modified Cam-clay model under certain parameters which reduced

CASM and the bubble model to the modified Cam-clay model. CASM could perform better than the modified Cam-clay model in the triaxial loading of clay. The comparison of CASM results with the results obtained earlier in the CRISP software by Khong (2004) showed close agreement. The results of the bubble model were compared with the laboratory test data and the results that were obtained with the earlier developed FISH code by Ni (2007) in FLAC2D. The validation footing problem, which had more than one zone, was checked for the mesh sensitivity. The best results were obtained for normally consolidated clay. Along with the conclusions of Chapter 4, the study on 'Embankment Loading on a Cam-clay Foundation' in this chapter showed that the mesh density should be selected with great care.

Chapter 6

Improved Surface Subsidence Simulations

This chapter presents a model of surface subsidence after the collapse of a UCG reactor. The chosen site is the Shatsk UCG station in the Moscow basin. The field data was well-documented by Turchaninov and Sazonov (1958). In 18 years after this UCG experience, Turchaninov I.A. with two other coauthors wrote a book 'Principals of Rock Mechanics' (Turchaninov et al., 1979), which is still cited, for example, by Hudson and Harrison (2000) from the University of London. The description of the Shatsk UCG station is also unique because a project of such a scale is still unusual. This data enables the comparison of modelled results against field measurements. Field measurements of the conventional coal mine, Bolokhovsk mine, from the same basin by Proskuryakov (1947) are also used for comparison. Proskuryakov (1947) summarized the general experience of mining in the Moscow basin, and unfortunately, the overburden description is absent. The model cannot be developed without this information, and the chapter therefore only deals with modelling the surface subsidence at the Shatsk UCG station.

The chapter starts with an introduction to the Shatsk station and surface subsidence there. Then the process of simulation of the surface subsidence after a collapse of the UCG reactor is described. FLAC3D's built-in Mohr-Coulomb and modified Cam-clay models are applied to the overburden of the Shatsk UCG station. The chapter considers UCG features, which distinguish surface subsidence after the collapse of a mine and a UCG reactor. The features are ash left in the reactor, a complicated shape of the UCG reactor, and thermal stresses. After this, the UDCMs, i.e. CASM and the bubble model, are used to improve subsidence predictions. The chapter ends with discussions and conclusions on modelling results.

6.1 UCG Station

The Shatsk station was located about 180 km away from Moscow near the city of Tula in the Moscow basin in the Central Russian Upland as shown in Figure 6.1 on the next page.

Figure 6.1 is a map of surficial geology with locations of the station and the European clays considered in this work, i.e. the London clay, the Weald clay, and the Norrköping clay. Figure 6.1 illustrates that the genesis of the clay in the Moscow basin (Cretaceous K) is closer to the genesis of the London clay (Paleogene Pg) than to the Norrköping clay (Precambrian pCm), and the Weald clay is the same genesis as the Moscow clay. Therefore, the properties of the clay in the Moscow basin are closer to the properties of the London clay and the Weald clay than to the properties of the Norrköping clay as demonstrated in Section 6.4 and in Section 6.5. However, the properties of the Norrköping clay for the bubble model are used throughout the chapter since they are available in the literature.

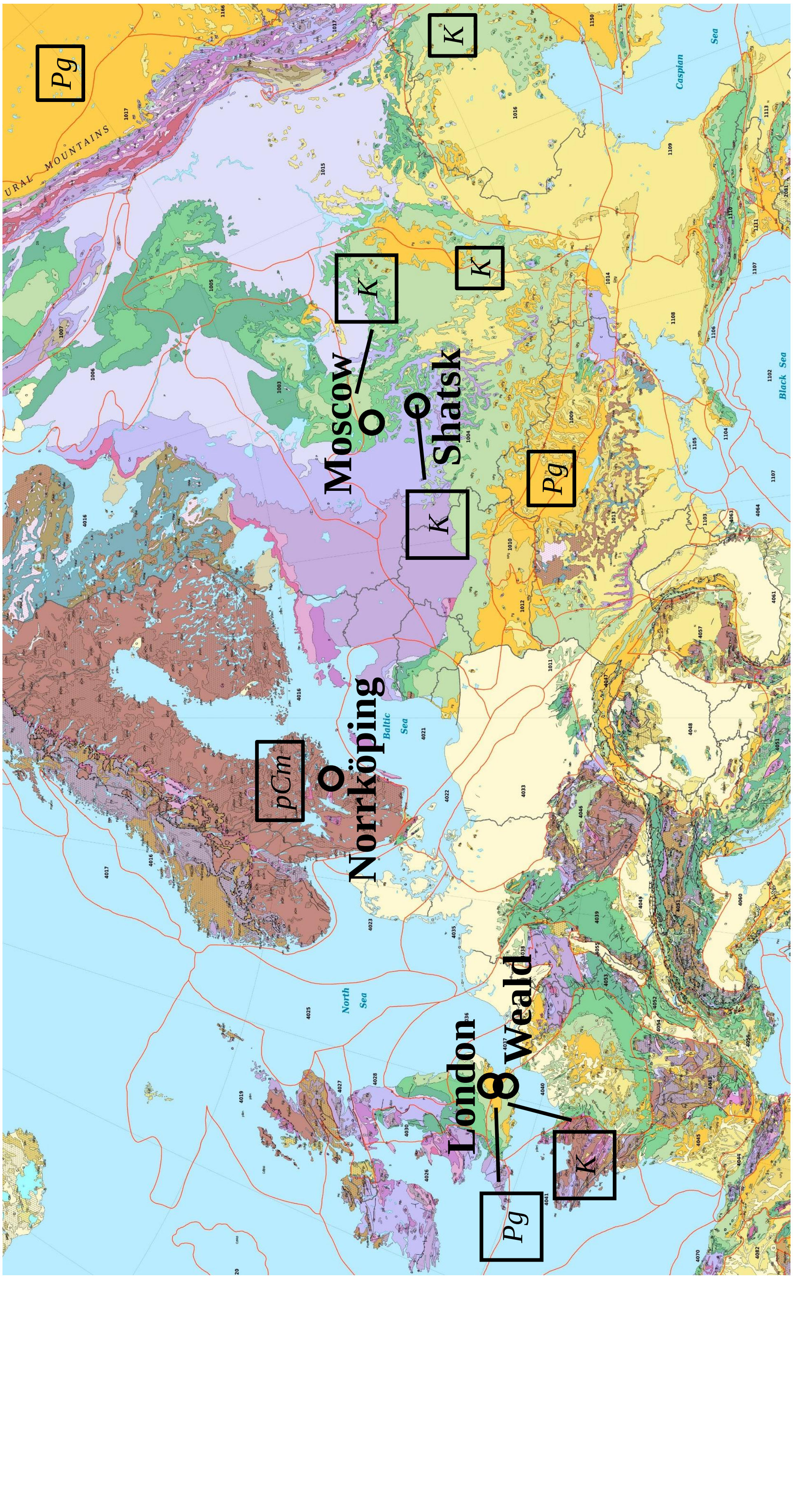

Figure 6.1: Surficial Geology and Locations of the UCG Station and Places of Interest after Everipedia (2016)

At the site of the Shatsk UCG station, the overburden is mostly clay, and 20% overburden is fractured weak limestone. There are five underground water aquifers there. The 3m thick coal seam is at a depth of 45 meters. Figure 6.2 depicts a stratigraphic column of the site with ranges of thicknesses and mean depths.

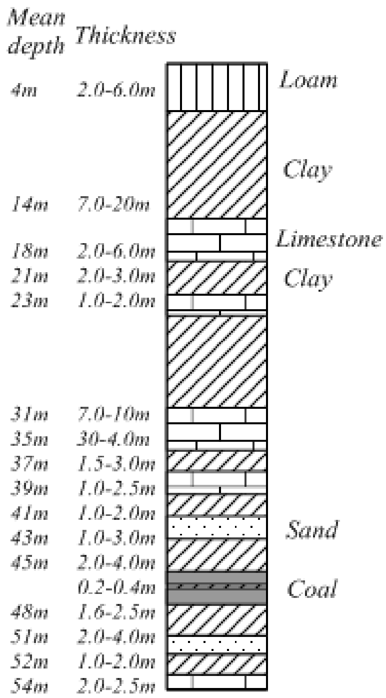

Figure 6.2: Stratigraphic Column after Turchaninov and Sazonov (1958)

The first subsurface layer is a 2-6 meter thick quaternary loam deposit. This deposit covers a 7-20 meter Mesozoic clay layer. The soil under the Mesozoic layer is paleozoic. This soil includes fractures limestone, clay, and a coal seam at a mean depth of 48 meters. The total competency of limestone constitutes 20% of the stratigraphic column.

The work on UCG was started in July 1955. At the end of 1956, the UCG process began working under normal conditions. The first surface subsidence was noticed on August 9, 1955, after 34 days of coal combustion. According to engineering calculations, 300 tonnes of coal had been gasified at that time (Turchaninov and Sazonov, 1958). The velocity of the surface subsidence was constant at 25mm/day. During UCG, the measured moisture of the syngas was constantly between 300 and 500g/mm^3. This shows that there was no sudden water leakage into the reactor in spite of the five aquifers above. In turn, this means that large crevices, which could conduct water, did not occur, and the surface subsidence was smooth. Figure 6.3 shows contours of surface subsidence on October 1, 1957.

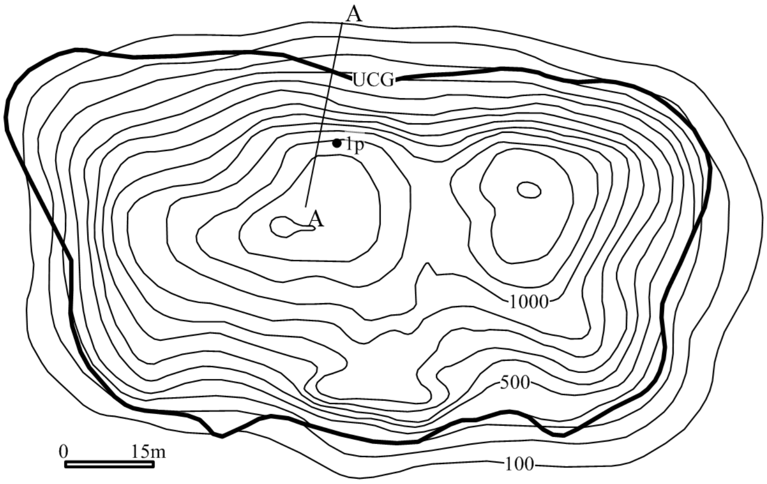

Figure 6.3: Surface Subsidence Contours (in mm) after Turchaninov and Sazonov (1958)

In Figure 6.3, the bold UCG contour is the border of the UCG reactor. Figure 6.3 also depicts cutting line A-A, which is used to create the simulation of the subsidence, and borehole 1p, where the displacements were measured at four points underground. The deepest measurements were in the seam roof.

As stated in Chapter 2, caving of the roof was not considered in the model. During UCG, the roof sank steadily, and this made caving insignificant (Turchaninov and Sazonov, 1958). For conventional coal mining, the heights of the caving zone were also small in the Moscow basin. Proskuryakov (1947) studied caving of the mines in the Moscow basin and argued that the caving was not high there.

6.2 Modelling Surface Subsidence

This section introduces the process of modelling surface subsidence by considering cutting along the line A-A (Figure 6.3) at the Shatsk UCG station. In this section, a popular Mohr-Coulomb constitutive model is considered for the overburden, and a double yield model is implemented in the goaf. The sketch of the numerical model is shown in Figure 6.4.

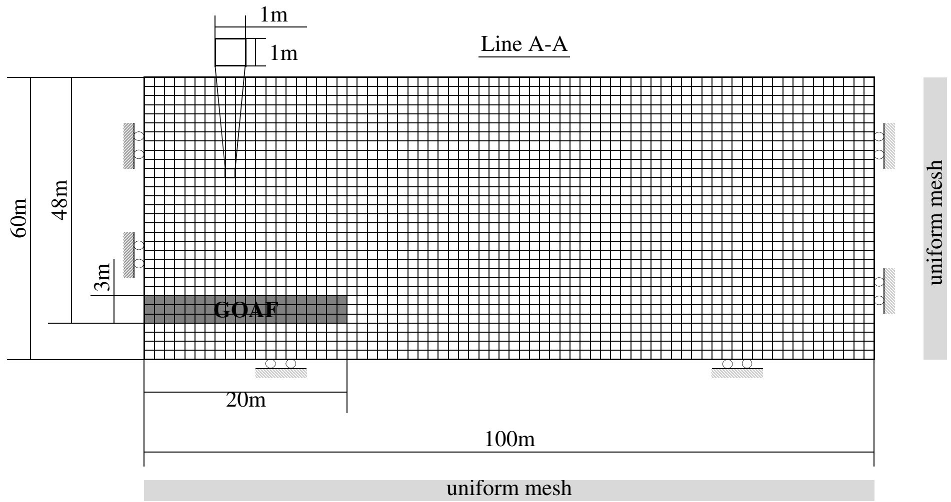

Figure 6.4: Layout of the Shatsk Model (Not drawn to scale)

The setting of the model was similar to the model at the Naburn site described in Chapter 3, e.g., no thermal effect for the first modelling attempts, a rectangular goaf, and boundary conditions. The roller boundary conditions were applied to the bottom, the left and right sides of the model. The model was fixed in the out-of-plane direction. The size of the model was 100m wide and 60m high. A hydrostatic stress field was imposed on the mesh. One zone was in the out-of-plane direction. The domain had 10800 zones. The size of the cube-shaped zone was 0.5m. This zone size created a mesh with six zones in the goaf height because Chapter 4 stated that six zones in the goaf height were the optimal mesh configuration for the goaf. The seam was at a depth of 48m and was burnt to a width of 20m forming the reactor. When the reactor collapsed, the goaf occurred. The double-yield model represented the behaviour of the goaf. The Mohr-Coulomb model represented the behaviour of the overburden. The Mohr-Coulomb properties for the overburden were calculated using the stratigraphic column (Figure 6.2) and the method described in Section 3.2. The elastic properties were calculated according to Equation 3.3 assuming the Poisson's ratio is 0.2. The tensile strength, cohesion, and friction angle were estimated according to Equations 3.10, 3.15, and 3.14 respectively and presented in Table 6.1.

Table 6.1: Rock Properties at the Shatsk UCG Station (if not mentioned, in Pa)

Depth (m)	Geomaterial	Bulk modulus	Shear modulus	Friction (degree)	Cohesion	Tensile strength
2	loam	1.00E+06	8.00E+05	30	5.00E+06	5.00E+05
6	clay	1.00E+06	8.00E+05	30	5.00E+06	1.53E+06
16	limestone	7.78E+08	5.83E+08	49.6	1.53E+07	5.00E+05
20	clay	1.00E+06	8.00E+05	30	5.00E+06	1.53E+06
23	limestone	7.78E+08	5.83E+08	49.5	1.53E+07	5.00E+05
25	clay	1.00E+06	8.00E+05	30	5.00E+06	1.53E+06
33	limestone	7.78E+08	5.83E+08	49.3	1.53E+07	5.00E+05
37	clay	1.00E+06	8.00E+05	30	5.00E+06	1.53E+06
39	limestone	7.78E+08	5.83E+08	49.2	1.53E+07	5.00E+05
41	clay	1.00E+06	8.00E+05	30	5.00E+06	0.00E+00
43	sand	1.00E+06	8.00E+05	30	1.00E+06	5.00E+05
45	clay	1.00E+06	8.00E+05	30	5.00E+06	8.14E+04
47	coal	4.60E+07	3.50E+07	55	2.50E+06	2.79E+04
50	clay	1.00E+06	8.00E+05	30	5.00E+06	2.79E+04
53	sand	1.00E+06	8.00E+05	30	1.00E+06	2.79E+04
60	clay	1.00E+06	8.00E+05	30	5.00E+06	1.38E+06

The model ran approximately 30 minutes on a 3.4GHz Intel(R) Core(TM)i7-3770 CPU computer. The results were compared against both the field observations at the UCG station and at the Bolokhovsk mine utilizing conventional coal excavation. The Bolokhovsk mine was located in the Moscow basin as the Shatsk UCG station, but the seam was slightly deeper (51m vs 48m) and about twice thinner (1.6m vs 3.0m) than the Shatsk UCG reactor. Keeping these differences in mind, firstly, the displacements of the surface were compared with modelled results and measurements at both sites in Figure 6.5

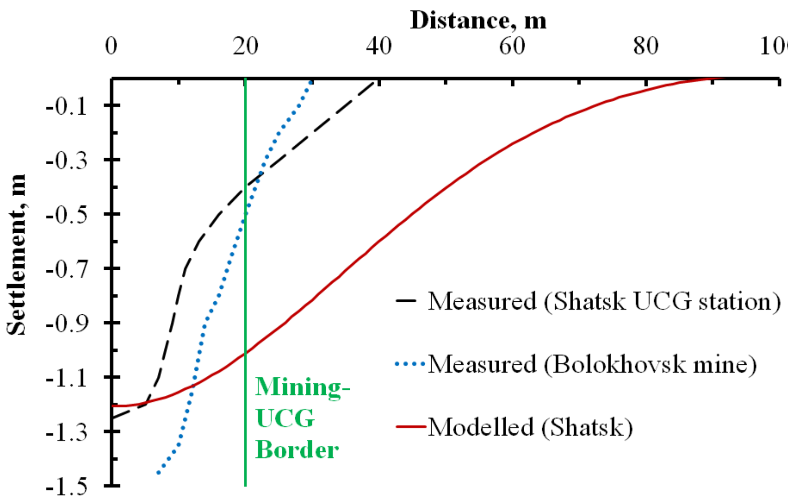

Figure 6.5: Surface Settlement Half-Profiles

Figure 6.5 shows that the modelled subsidence trough is much wider than the measurements at the UCG station and at the conventional mine in the same basin. The subsidence trough of the conventional Bolokhovsk mine is narrower and deeper than the surface subsidence after UCG in spite of the thinner seam. This can be explained by the UCG features, such as the ash left after coal burning in the UCG reactor, the complicated shape of the reactor, and thermal stress.

To compare measurements and modelling results underground, four monitoring points were considered in the borehole. Figure 6.6 shows the placement of these underground monitoring reference points (RP) in borehole 1p (Figure 6.3).

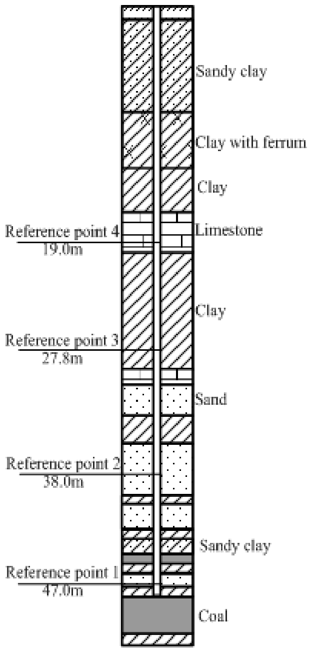

Figure 6.6: Placement of the Reference Points in Borehole 1p after Turchaninov and Sazonov (1958)

According to Figure 6.6, the reference points were located at a distance of approximately 10m from each other. RP1 was located at the roof of the seam. RP4 was at a depth of 19m. Table 6.2 presents the vertical displacements in these points, which were measured on the 1st October 1957, after 25 months of the coal burning.

Table 6.2: Vertical Displacements of the Reference Points

Reference point	**Measured (m)**	**Modelled (m)**
RP 4	1.2	1.22
RP 3	1.25	1.26
RP 2	1.25	1.46
RP 1 (Roof)	1.7	2.01

Table 6.2 also presents the modelled results at the reference points. The displacements of the shallowest reference points (RP3 and RP 4) agree with the modelled results. The modelled settlement of the deepest reference point (RP 1), which is located at the roof of the reactor, is 0.3m smaller than the measured displacement. This is also applicable to the modelled displacement of RP2, which is 0.2m smaller. Thus, the modelling error is increasing with depth.

The results of further investigation of the underground displacements are presented in Figure 6.7, which compares displacements normalized to the seam thickness in the roof at a conventional mine against predictions. It should be noted that measurements of the displacements in the roof were done relative to the upper corner of the goaf. The measurements at the Bolokhovsk mine were used because they are not available at the Shatsk station. It should be noted that both sites are in the Moscow basin.

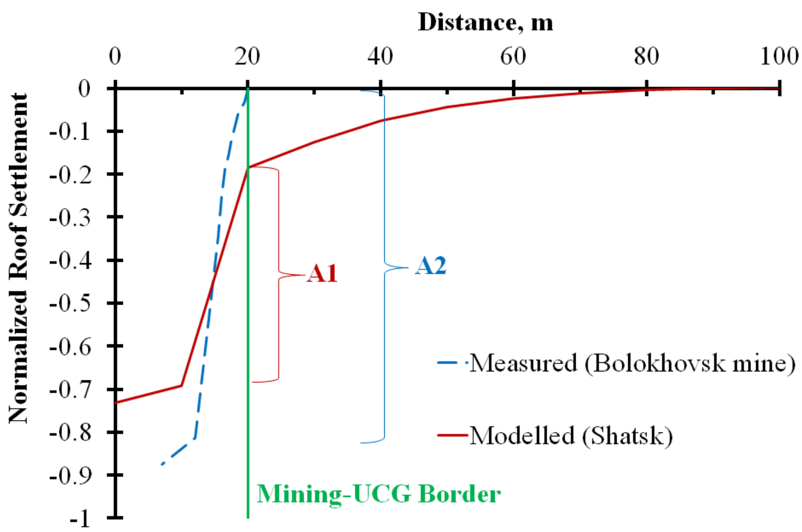

Figure 6.7: Roof Settlement Half-Profile after Proskuryakov (1947)

Since the amplitude of the measured settlement is larger than the modelled displacements ($A2 > A1$), this gives the idea that the double yield model does not represent the goaf behaviour correctly.

This investigation on the correctness of the simulations was broadened by considering stresses in the goaf. Figure 6.8 shows the modelled stresses along the roof at the Shatsk UCG station and measured stresses at the conventional Bolokhovsk mine. Unfortunately, the measurements were done only at a very short distance.

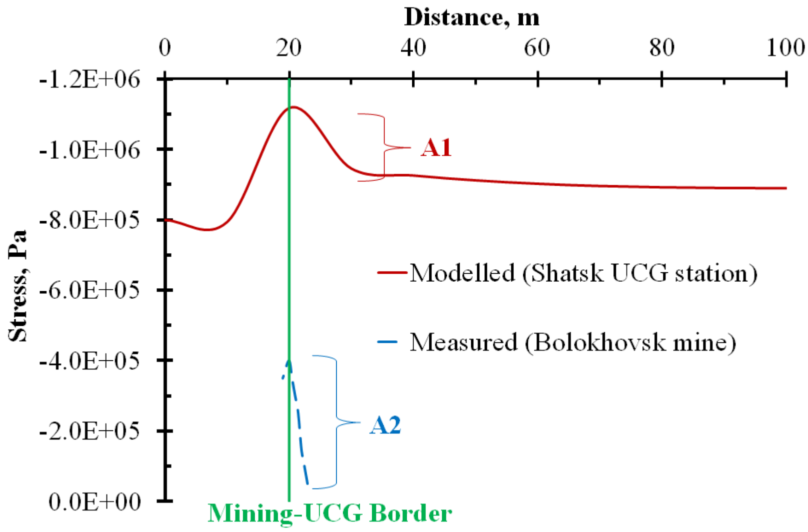

Figure 6.8: Roof Stress Half-Profile after Proskuryakov (1947)

Figure 6.8 depicts the magnitude of the measured stress, which differs from the modelled results. Figure 6.8 also shows that the jump of the measured stresses between the seam and goaf is larger than the modelled jump ($A2 > A1$). These observations cast doubt on predictions of the double yield model. The information in the section forces us to look for some solutions to improve the predictions. One of them could be the utilization of some other constitutive models to simulate the rock-soil behaviour.

6.3 Implementation of the Modified Cam-Clay Model

As it has been mentioned, the Critical State models were a significant breakthrough in geomechanics. The modified Cam-clay model is the Critical State model built-in FLAC3D, and it can be easily implemented. Since the input parameters for the modified Cam-clay model and for the more advanced models are difficult to obtain, simulation of the surface subsidence at the Shatsk site was simplified by assuming the same properties for all layers. In order to check the predictions of the modified Cam-clay model, Norrköping clay was considered due to the availability of the properties for the bubble model considered later. The following properties were assigned to the modified Cam-clay model: λ =0.76, $\kappa = 0.055$, M=1.35, μ=0.22, ν=3 (Westerberg, 1999). Figure 6.9 depicts the subsidence profile obtained by two models, i.e. the modified Cam-clay and Mohr-Coulomb models.

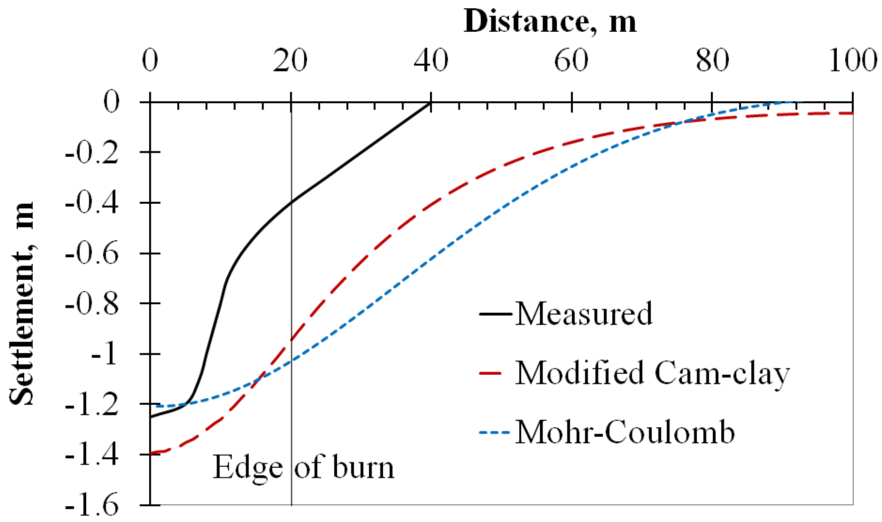

Figure 6.9: Surface Settlement Half-Profile Obtained with the Mohr-Coulomb and Modified Cam-clay Models

Figure 6.9 shows that the modified Cam-clay curve mirrors the shape of the measured subsidence trough better than the Mohr-Coulomb curve. However, the modelled subsidence trough was still 10m or 50% wider than the measurements. The depth of the subsidence trough was also overestimated by 0.2m. The reason for the too deep modelled subsidence trough could be the mitigation effects of the ash left in the reactor after combustion.

6.3.1 Ash Impact

The ash left in the UCG reactor can be considered as stowing in the conventional mine because the ash contributes to forming a goaf and can reduce the depth of the surface subsidence. Especially, this should be considered for coal with high ash content. Gregg et al. (1976) reported that the coal of the Moscow basin had the highest ash content of up to 60%. Table 3.8 shows that the subsidence factor for the stowing goaf should be increased from 0.9 to 0.5. Therefore, the required height of the goaf after the simulation should be increased from 10% for conventional mining to 50% of the height of extracted coal. Figure 6.10 shows the results for the model with the increased required height of the goaf.

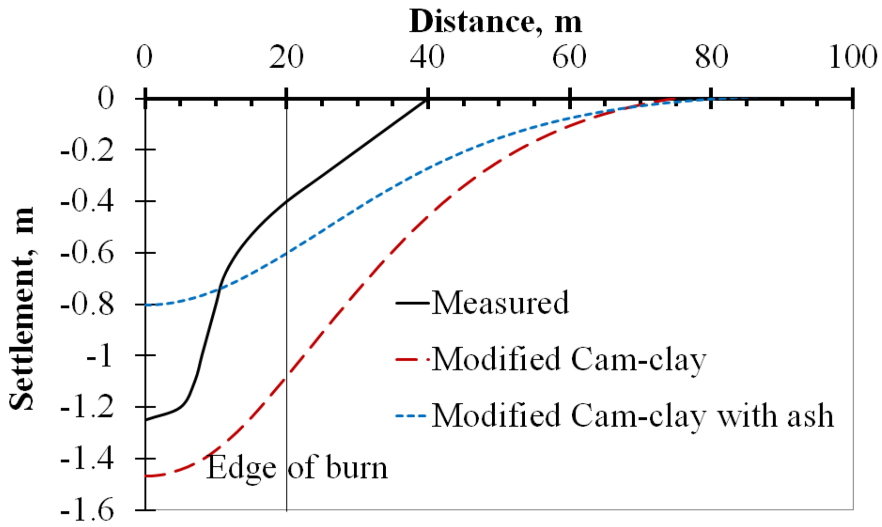

Figure 6.10: Ash Effect on the Surface Subsidence

Figure 6.10 illustrates that the depth of the modified Cam-clay with ash curve was 45% less than the modified Cam-clay curve. Thus, the height of the goaf after the simulation was proportional to the maximum subsidence. At the same time, the widths of the modelled subsidence troughs were identical and wider than the field data. Therefore, the way to reduce the width and increase the depth of the subsidence trough should be found.

6.3.2 Impact of the Reactor Shape

One more feature of UCG, i.e. a complicated shape of the reactor, should be recalled. Subsection 2.3.3 demonstrated that the shape of the UCG reactor is different from the rectangular shape of the mine, and it is more like a trapezium. In Figure 6.5, the subsidence trough measured at the Shatsk UCG station is wider and has a more complicated shape than the subsidence trough at the traditional Bolokhovsk mine. This means that the shape of the reactor is not rectangular. However, Tian (2013) argues that current studies take a rectangular shape of the reactor for modelling purposes. In the model at hand, the complicated shape of the reactor was taken into account by reducing the goaf width. The rectangular goaf adopted to substitute the complicated shape of the reactor is shown in Figure 6.11.

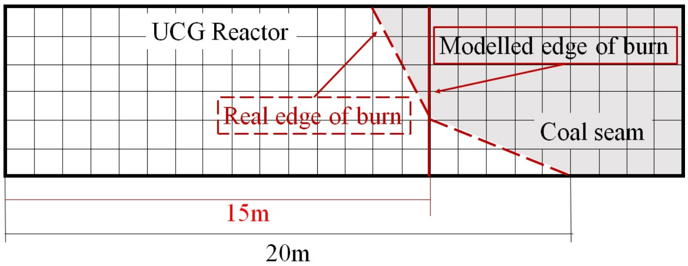

Figure 6.11: Vertical Cross-Section of the UCG Reactor

Figure 6.11 depicts an approximate contour of the UCG reactor from Figure 2.9 and the reduction of the goaf width from 20m to 15m. To check the influence of the goaf width on the subsidence trough, three simulations were run for the goaf of widths 20m, 15m, and 10m. Figure 6.12 presents the subsidence troughs for these three different widths of the goaf.

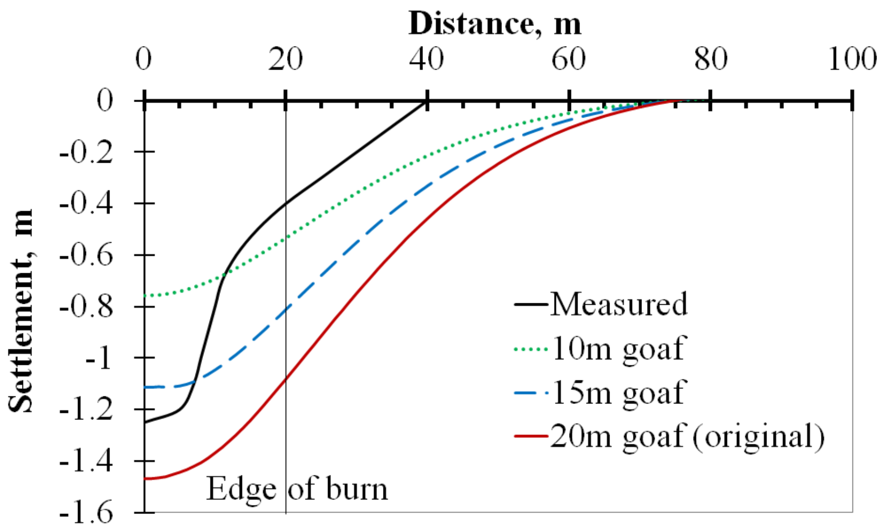

Figure 6.12: Surface Settlement Half-Profile Obtained with Different Widths of the Goaf

Figure 6.12 shows that the reduction of the goaf width from 20m to 15m, and then to 10m causes a decrease in the depth of the subsidence trough from -1.4m to -0.8m, respectively. Figure 6.12 also depicts that the goaf width of 15m, as shown in Figure 6.11, is closest to the correct depth to the depth of the measured subsidence trough. Unfortunately, the width of the subsidence trough is unchangeable by altering the width of the goaf and disagree with the measurements. Therefore, the way to reduce the width of the subsidence trough still should be looked for.

6.3.3 Thermal Analysis

One more feature of UCG should be examined, i.e. the thermal impact. FLAC3D incorporates the thermal conduction model by subtraction of the thermal strain from the total strain. Thermal-strain increments which correspond to temperature increment ΔT is derived from

$$\Delta\epsilon_{ij} = \alpha_t \Delta T \delta_{ij} \tag{6.1}$$

where α_t [t°C] is the coefficient of linear thermal expansion, and δ_{ij} is the Kronecker delta.

To predict temperature distribution, FLAC uses Fourier's transport low and the energy-balance equation (Itasca, 2011). Fourier's law defines the relation between the heat-flux vector q_i and the temperature gradient:

$$q_i = kT_{,j} \tag{6.2}$$

where T is the temperature [°C], and k is the thermal conductivity in [W/m°C].
The energy-balance equation is given in FLAC3D as

$$-q_{i,j} + q_\nu = \rho C_\nu \frac{\partial T}{\partial t} \tag{6.3}$$

where q_i is the heat-flux vector in [W/m^2], q_ν is the volumetric heat-source intensity in [W/m^3], ρ is the mass density of the medium in [kg/m^3], and C_ν is the specific heat at constant volume in [J/kg°].

For these equations, thermal parameters of the soil were adapted from the work on the nuclear waste disposal by Rutqvist et al. (2011), i.e. conductivity (k)=0.925W/m°C, thermal expansion (α_t)=1.5e-4°C^{-1}, specific heat(C_p)=2498J/kg°C. The initial temperature was 1250°C in the reactor. The initial temperature of the overburden was 5°C. FLAC's thermal model was run for a period of 27 months before the reactor collapsed because surface subsidence (Figure 6.3) was measured after 27 months of coal combustion at the Shatsk station (Turchaninov and Sazonov, 1958). Figure 6.13 presents the distribution of the temperature near the reactor along the depth.

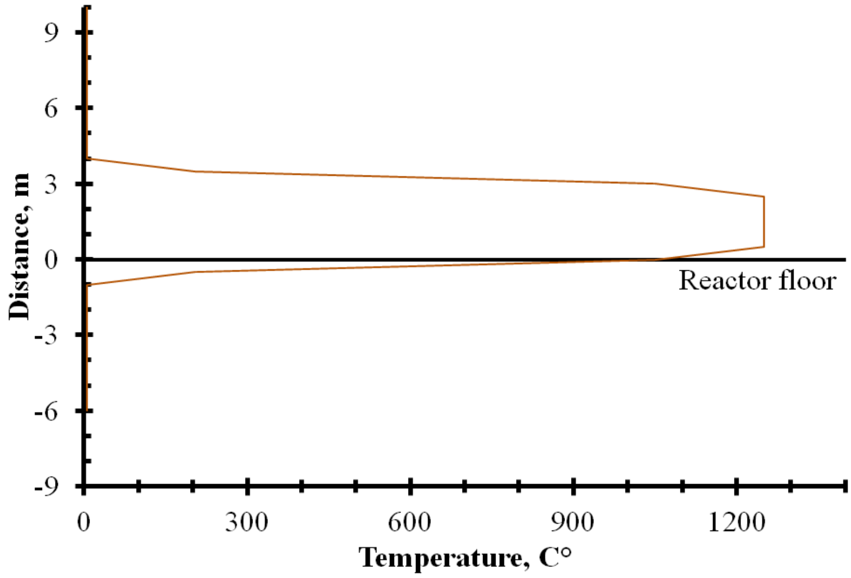

Figure 6.13: Modelled Distribution of Temperature

Figure 6.13 is a graph where the x-axis is temperature, and the y-axis is the vertical distance with respect to the reactor floor. The negative distance is the distance downwards from the reactor floor in the underburden. Figure 6.13 illustrates that the temperature does not spread more than 1m from the reactor for 27 months. Subsection 2.3 also says that the thermal impact is limited within a short distance from the UCG reactor. According to Figure 2.6, the high temperatures did not spread more than 6m from the reactor at the Lysychansk station. The modelling results indicated that temperature did not distribute far from the place of the combustion. Figure 6.14 depicts the whole domain of the model and temperature contours.

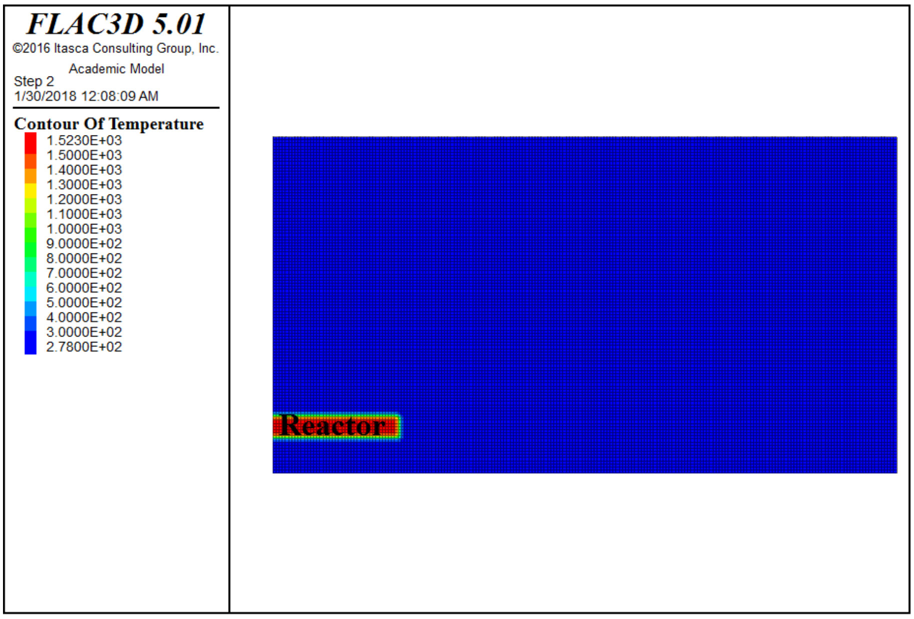

Figure 6.14: Temperature (in Kelvin) Contour in the Model

Figure 6.14 shows that high temperature (in Kelvin) was higher near the reactor. The highest temperature was 1523K (1250°C) in the reactor. Then the effect of the high temperature on the overburden decreased sharply with the distance from the reactor to an in situ temperature of 278K or 5°C (SNIP 2.01.01-82, 1982).

Once, the temperature distribution was set, the double-yield model was implemented in the UCG reactor part of the model. Coupling mechanical and thermal models through Equation 6.1 allowed the reformulation of the stress-strain rate relations. Figure 6.15 presents two curves which were obtained with the modified Cam-clay model. One of the curves (the dotted curve) was modelled without consideration of the thermal and ash impact of UCG. having worse predictions of the measurements.

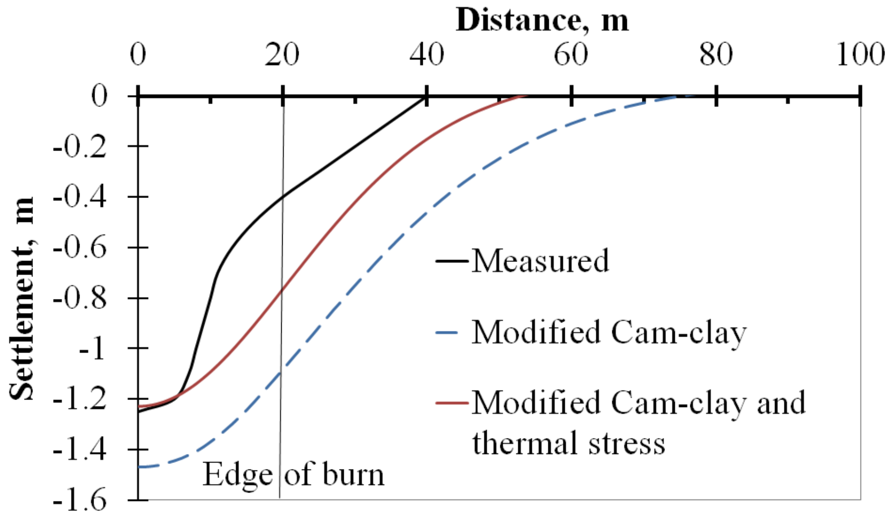

Figure 6.15: Surface Settlement Half-Profile Obtained with Thermal Analysis

Figure 6.15 depicts three curves that represent the measured subsidence trough and troughs modelled withthe modified Cam-clay model with and without thermal stresses. The modelled curves repeated the shapes of each other. The depth of the trough modelled with the thermal stresses was lower and closer to the measurements than the trough obtained without thermal stresses. The width of the trough modelled with thermal stresses was also lower in contrast to the previous investigation of the impact of the UCG features, where the reduction of the depth of the trough did not induce the reduction of the simulated width.

The information above shows that the complicated shape of the reactor and ash reduced the depth of the modelled subsidence trough. At the same time, the thermal stresses in the simulation reduced both the width and depth of the subsidence trough. However, the UCG features obviously did not change the shape of the subsidence trough. Therefore, the way of improving the predictions should be further investigated. The improvement could include the implementation of different constitutive models to simulate overburden. The next section considers the UDCM, i.e CASM.

6.4 Implementation of CASM

CASM is an extension of the modified Cam-clay model with two extra parameters k and n. Unfortunately, CASM could not handle tensile stresses. Therefore, thermal analyses during the simulation of surface subsidence were not possible because high temperatures caused the extension of the overburden. The properties of the Weald clay were implemented to simulate surface subsidence in the Moscow basin. Based on the work of Khong (2004), the following CASM properties were assigned to the model: λ =0.093, κ = 0.025, M=0.9, μ=0.3, ν=2.06, n=4.5, k=2.718. Figure 6.16 illustrates a measured subsidence trough and two subsidence troughs obtained with the modified Cam-clay model and CASM.

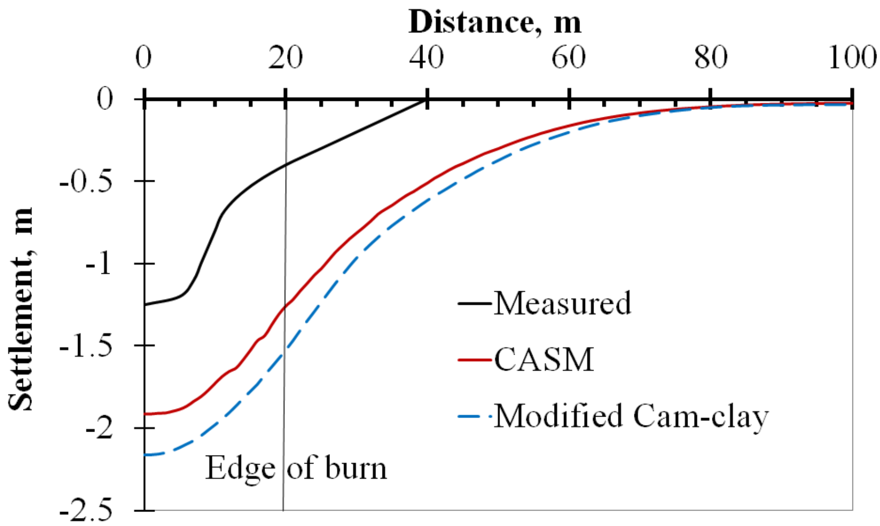

Figure 6.16: Surface Settlement Half-Profile Obtained with the Modified Cam-Clay Model and CASM

Figure 6.16 shows that although CASM predicted a slightly shallower subsidence trough, the shapes of CASM and the modified Cam-clay curves were similar. At the same time, Figure 6.16 demonstrates deeper subsidence troughs than Figure 6.15 does. Thus, the properties of the Weald clay caused the deeper subsidence than the properties of the Norrköping clay. If the information presented in Subsections 6.3.1, 6.3.1, and 6.3.3 is recalled, which said that the UCG features reduced the depth of the subsidence trough, then it could be seen that the properties of the Weald clay corresponds better to the properties of the clay of the Moscow basin because the property of the Norrköping clay caused a shallower subsidence trough. At the same time, it could be seen that none of the considered models predicted the measured shape of the subsidence trough. Therefore, the adjustment of the properties could not help obtain the correct subsidence trough. Probably, the enhancement of the model could be in the implementation of some more advanced constitutive model.

6.5 Implementation of the Bubble Model

To improve predictions of the shape of the subsidence, trough the bubble model was implemented in the overburden. Despite the advantages of the bubble model which could help to capture the correct behaviour of the overburden, one important disadvantage of the model is difficult to obtain the bubble model parameters. As mentioned before, there are ten parameters (excluding the initial conditions) in the bubble model:

Size of the bubble R_{bub};

Plastic modulus parameters B and ψ;

Standard parameters: Poissons ratio μ, Critical State parameters: λ^* and κ^*, m, M;

Destructuration parameters A and k; and

Initial conditions size of the structure surface r_0, ν_0, p_{c0}.

To understand the impact of the parameters of the bubble model and to show the capability of the bubble model to change the shape of the subsidence trough, the impact of the key parameter of the bubble model R_{bub}, which changes the bubble size and can recover the bubble model to the modified Cam-clay model, on the subsidence trough was investigated. For this, the typical parameters of the bubble model for non-structured soil (r_0=1 and ν_0=0), given by Ni (2007), were assigned: $R_{bub} = 0.2$, $\lambda^* = 0.3$, $\kappa^* = 0.02$, $\mu = 0.25$, $M = 1.0$ $B = 600$, $m = 1$, $\psi = 0.5$, $\nu_0 = 0$, $r_0 = 1$, $A = 0.5$, $k = 4$.

The size of the bubble was slightly increased from 0.2, which was presented by Ni (2007) to 0.3 to avoid crashing the model. So, the performance of the model was checked for two radii of 0.3 and 0.998 as a minimum and maximum possible sizes of the bubble. The results are depicted in Figure 6.17.

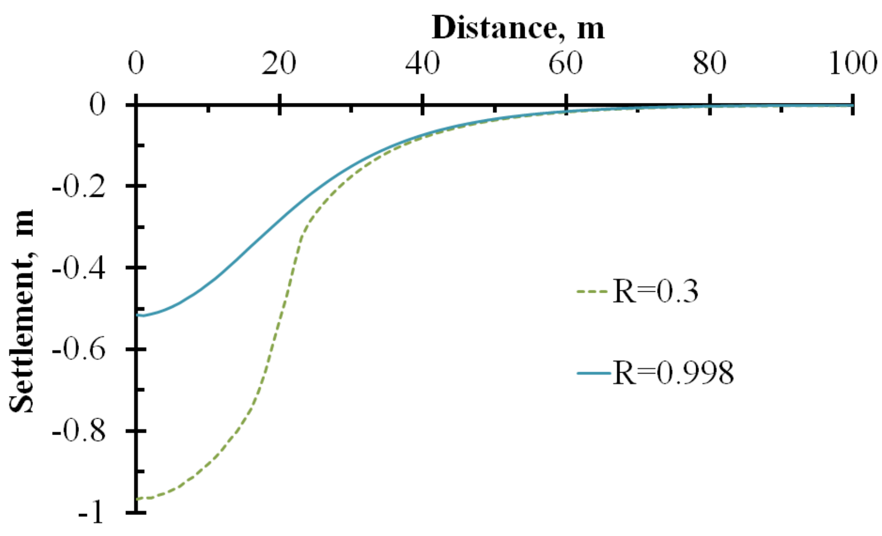

Figure 6.17: Surface Settlement Half-Profile Obtained with the Bubble Model with the Different Bubble Radii

The simulations show that the bubble size has the largest influence on the width and depth of the subsidence trough. In Figure 6.17, it can be seen that the reduction of the bubble size considerably deepens the subsidence trough and reduces the width. However, the reactor does not collapse under the typical bubble parameters. Therefore, weaker soil should be considered.

The properties of Norrköping clay was tested. The bubble parameters of Norrköping clay was taken from the research of Rouainia and Muir Wood (2000): $\lambda^* = 0.3$, $\kappa^* = 0.02$, $\mu = 0.25$, M =1.0, m =1.0, B=4, $\psi = 1.0$, ν_0=0.0, r_0 =1.0, $A = 0.5$, $k = 8$.

Under this properties, the reactor collapsed. Figure 6.18 presents two curves obtained with the bubble model and measurements. One curve 'Norrköping clay' is derived for the goaf of width 20m, the other is derived for the goaf of width 15m.

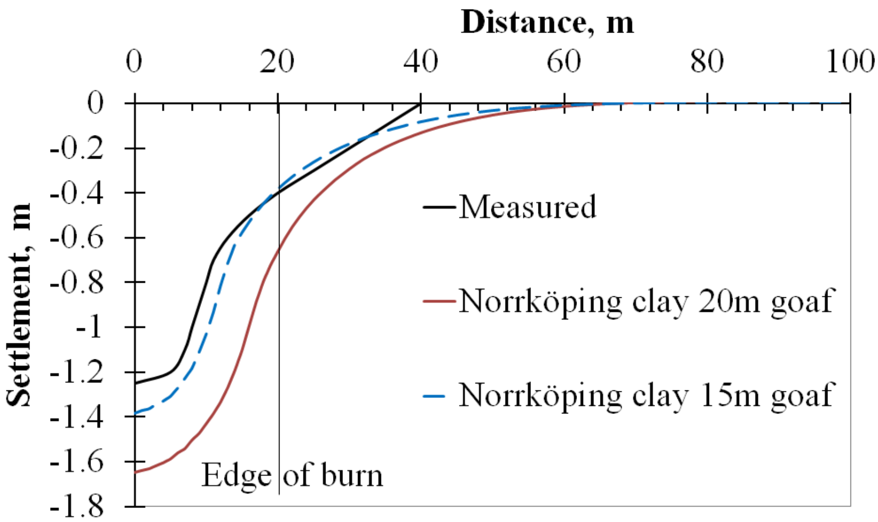

Figure 6.18: Surface Settlement Half-Profile Obtained with the Bubble Model

Figure 6.18 depicts the curve Norrköping clay 15m goaf is shallower than the curve Norrköping clay 20m goaf for more than 0.2m and coincides better with the measurements. At the same time, both curves have identical shapes to the measurements. The results obtained for 15m goaf agreed well with the measurements; however, only one UCG feature, the complicated geometry of the reactor was considered. Previously, it was shown that the features of UCG, i.e. ash in the reactor and thermal stresses, reduced the depth of the subsidence trough. Obviously, the properties of the Norrköping clay results in an underestimation of the depth of the subsidence trough once all features are implemented. Therefore, the parameters of the bubble model which correspond to the Moscow clay better should be found.

For obtaining better parameters for the Moscow clay, the parametric study of the bubble model was continued by investigation of the influence of the Critical State parameter λ^* on the surface subsidence trough. Butterfield (1979) suggested a table of typical values of λ^* and confirming κ^* for different soils:

Table 6.3: Values of λ^* and κ^* (Butterfield, 1979)

Soil	λ^*	κ^*
Mexico City Clay	0.498	0.025
London Clay	0.083	0.037
Newfoundland peat	0.214	0.117
Newfoundland silt	0.103	0.016
Chicago Clay	0.154	0.045
Boston blue Clay	0.122	0.024
Drammen Clay, plastic	0.14	0.016
Drammen Clay, lean	0.104	0.018

Table 6.3 shows that values of lambda λ^* range from 0.498 for Mexico clay to 0.083 for London clay. Because the parameters of the bubble model of the Moscow clay were unknown, the maximum and minimum values of λ and corresponding to the values of κ from Table 6.3 were considered. Since using the Critical State parameters for different clays in the given set of the bubble model parameters of the Norrköping clay caused numerical instability for deep subsidence troughs, Subsection 6.3.1 on the ash impact was recalled and the required goaf height after the simulation was increased by 50% of the goaf. Subsection 6.3.1 justified that at the UCG site, the goaf height after the simulation should be increased because the ash left after UCG in the reactor acted as stowing. The comparison of obtained subsidence troughs with different critical parameters is shown in Figure 6.19.

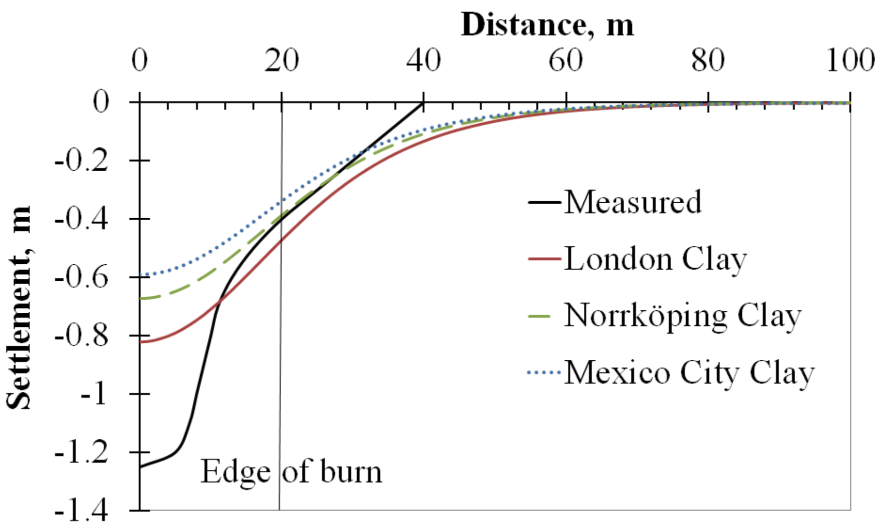

Figure 6.19: Surface Settlement Half-Profile Obtained with the Bubble Model for Different Clays

Figure 6.19 illustrates that the London clay curve was the deepest, whereas the Mexico City clay curve is the shallowest. Since it is known from previous research that the features of UCG result in shallower subsidence trough, London clay is likely to be the most suitable for the Moscow basin. However, obviously, the parameters of the bubble model which would be suitable to model behaviour of the Moscow clay should be estimated. The minimum required data could be obtained from three triaxial compression tests and one isotropic compression test (Lade, 2005).

6.6 Summary

The chapter described the UCG station in the Moscow basin and the modelling of surface subsidence after a UCG reactor collapsed. It investigated the impact of various UCG features such as complicated geometry of the reactor, thermal stresses, and ash remaining in the reactor, on surface subsidence. It was shown that these features resulted in shallower subsidence troughs. The chapter also studied the implementation of the Critical State models. The modified Cam-clay model and CASM resulted in almost identical deeper and narrower subsidence troughs than the trough predicted by the Mohr-Coulomb model. However, the modelled results did not agree with the measurements well. Further investigation was carried on using a more advanced constitutive model, the bubble model. It was shown that the bubble model resulted in a closer subsidence trough to the measurements.

The bubble model was implemented using parameters of the Norrköping clay (due to availability) and including only one UCG feature, the complicated shape of the UCG reactor since the bubble model could not deal with the tensile stresses. However, the chapter also considered the influence of the UCG features, i.e. ash left in the void after burning, thermal stresses and the complicated geometry of the UCG reactor, on the subsidence trough using the modified Cam-clay model. These features reduced the surface subsidence depth. Therefore, the bubble model predictions should be deeper. A study on the influence of the Critical State parameters showed that λ and κ for the London clay would be better to use because they resulted in a deeper subsidence trough. Ideally, the parameters of the bubble model should be estimated from the lab tests.

Chapter 7

Conclusions and Further Work

7.1 Conclusions

This thesis presented the procedure and recommended improvements of simulation of surface subsidence caused by underground mineral extraction, i.e. Longwall coal mining and UCG. Explanations of the modelling procedure started with the method of deriving model parameters of the geomaterial from the borehole descriptions. Two sites with available borehole descriptions and measured surface subsidence were considered, i.e. a coal mine at Naburn in North Yorkshire and the Shatsk UCG station in the Moscow basin, to model surface subsidence. The simulations were conducted with FLAC2D and FLAC3D software. The modelling results were compared with field observations and with theoretical expectations, which were calculated according to NCB (1975). The simulations showed that the popular constitutive models, which are available in most commercial software including FLAC such as Mohr-Coulomb, modified Hoek-Brown, strain softening, and modified Cam-clay, could not predict the measurements for the conventional coal mining at Naburn. The modelled trough was much wider and shallower than the field observations.

During simulations of the surface subsidence at Naburn, one more difficulty was noticed, i.e. the influence of mesh density and zone shape on the results especially in the area of large deformations. This area is a goaf during modelling surface subsidence. Detailed mesh analysis was carried out with the conclusions that the best mesh arrangement in the goaf was the six cubic zone height of the goaf. This mesh arrangement in the goaf was used to model surface subsidence at the Shatsk UCG station. Herewith, the 200x60x1 mesh of the whole domain of the model at the Shatsk UCG station caused an error of less than 1% in the footing problem; therefore, it was suitable to model surface subsidence. The simulations with popular constitutive models, i.e. Mohr-Coulomb, modified Hoek-Brown, strain softening, and modified Cam-clay models, showed different results from the measurements. The implementation of the thermal analyses enhanced predictions of the surface subsidence at the Shatsk UCG station.

The next step of improvements in the simulation of surface subsidence at the Shatsk UCG station was the implementation of the advanced constitutive models, i.e. CASM and the bubble model. For this, the constitutive models were programmed sequentially from simple to more complicated in C++ and embedded in FLAC3D. In the beginning, the isotropic elastic model was programmed, then the von Mises, Drucker-Prager, Tresca, Mohr-Coulomb, and modified Cam-clay models followed. The results were verified with the results of the built-in models. Based on this successful programming experience, CASM and the bubble model were programmed. Since CASM and the bubble model can be reduced to the modified Cam-clay model by choosing the appropriate parameters, the results of these models were compared with the results of the modified Cam-clay model embedded in FLAC3D. Then the results of full performances of CASM and the bubble model were compared with the laboratory experiments and the results from other packages, i.e. CRISP and FLAC2D. The validations showed the capability of CASM and the bubble model to predict the expected results.

After validation, CASM and the bubble model were deployed to model surface subsidence after a collapse of the UCG reactor at the Shatsk station in the Moscow basin. The properties were taken from the Weald and Norrköping clays because of their availability in the literature. It was shown that CASM prediction was not better than that of the modified Cam-clay. In opposite to CASM, the bubble model resulted in a narrower and deeper subsidence trough, which was closer to the field measurements, than any other troughs modelled by popular constitutive models, i.e. Mohr-Coulomb, modified Hoek-Brown, strain softening, and modified Cam-clay models.

7.2 Further Work

The considered model of surface subsidence at the Shatsk UCG station showed that the bubble model was capable of simulating the surface subsidence more precisely than popular models embedded in the commercial software. At the same, it is a challenge to derive the parameters for the bubble model. Five parameters (A, B, k, R, r_0, ψ) cannot be obtained directly by laboratory testing. More numerical investigation of laboratory test data is required. Once the investigation on the bubble parameters is fulfilled. The thermal impact on these properties should be studied to include the UCG effect. Additionally, there are some difficulties to implement thermal analyses in the bubble model because the model cannot handle tensile stresses. Therefore, including tensile stresses into the bubble model is a worthwhile buildup of the model. The useful extension of this work could be also an implementation of the other bounding surface models that were developed for specific applications, for example, particle crushing of the goaf material. The further crushing of the disturbed geomaterial is known to occur at pressures of 300-500kPa and investigations in Chapter 3 shows that the stresses reach these values in the goaf. So, the implementation of the constitutive models that consider particle crushing in the goaf is a worthwhile extension of this study.

Bibliography

ABAQUS, C. (2012). Analysis users manual, version 6.12.

Abbasi, B., Russell, D., and Taghavi, R. (2013). FLAC3D mesh and zone quality. In *Proceedings of the 3rd International FLAC/DEM Symposium*, pages 1–12.

Abbo, A. J. (1997). *Finite element algorithms for elastoplasticity and consolidation.* PhD thesis, University of Newcastle Upon Tyne.

Agroskin, A. and Kazak, V. (1959). Heating a coal seam and overburden during underground coal gasification. *Underground coal gasification*, 2:10–15.

Aiman, W., Thorsness, C., Hill, R., and Stephens, D. (1980). An underground coal gasification experiment: Hoe creek II. *Combustion Science and Technology*, 21(3-4):97–107.

Al-Tabbaa, A. and Wood, D. M. (1989). An experimentally based Bubble model for clay. *Numerical models in geomechanics. NUMOG III*, pages 91–99.

Andersson, J. and Ljunggren, C. (1997). A geostatistical approach to evaluate differences in results between hydraulic fracturing and overcoring. In *Proceedings of the International Symposium on Rock Stress*, pages 223–227.

Antonova, R., Bezhanishvili, A., Blinderman, M., Grabskaya, E., Gusev, A., Kazak, V., Kapralov, V., and Fominyh, V. (1990). *Underground Coal Gasification.* Central Research Institute of Economics and Santific-Technical Information of Coal Industry.

Arjang, B. (1989). Pre-mining stresses at some hard rock mines in the Canadian Shield. In *Proceedings of the 30th US Symposium on Rock Mechanics (USRMS)*, pages 33–47. American Rock Mechanics Association.

Arjang, B. and Herget, G. (1997). In situ ground stresses in the Canadian hardrock mines: an update. *International Journal of Rock Mechanics and Mining Sciences*, 34(3-4):15.e1–15.e16.

Atkinson, J. and Richardson, D. (1985). Elasticity and normality in soilexperimental examinations. *Géotechnique*, 35(4):443–449.

Balmer, G. (1952). A general analytic solution for Mohr envelope.

Batchelor, A., Kwakwa, K., Proughten, A., and Davies, N. (1997). Determination of the in situ stresses at Sellafield, UK: A case study. In *Proceedings of the International Symposium on Rock Stress*, pages 265–276.

Bell, F. G. and Donnelly, L. J. (2006). *Mining and its Impact on the Environment*. CRC Press.

Benson, R. P. (1970). *Rock mechanics aspects in the design of the Churchill Falls underground powerhouse, Labrador*. PhD thesis, University of Illinois at Urbana-Champaign.

Bhutto, A. W., Bazmi, A. A., and Zahedi, G. (2013). Underground coal gasification: From fundamentals to applications. *Progress in Energy and Combustion Science*, 39(1):189–214.

Bieniawski, Z. T. (1967). Mechanism of brittle fracture of rock: Part I – theory of the fracture process. *International Journal of Rock Mechanics and Mining Sciences*, 4(4):395 – 406.

Bieniawski, Z. T. (1984). *Rock Mechanics Design in Mining and Tunneling*. Balkema.

Bishop, A. W. and Henkel, D. J. (1957). *The measurement of soil properties in the triaxial test*. Edward Arnold (Publishers) Ltd; London.

BP (2017). British Petroleum statistical review of world energy. June 2017. `https://www.bp.com/content/dam/bp-country/de_ch/PDF/bp-statistical-review-of-world-energy-2017-full-report.pdf` accessed on 10/10/2017.

Brady, B. H. and Brown, E. T. (2013). *Rock mechanics: for underground mining*. Springer Science & Business Media.

Bräuner, G. (1973). *Subsidence due to underground mining*. US Department of the Interior, Bureau of Mines.

Britto, A. M. and Gunn, M. J. (1987). *Critical state soil mechanics via finite elements*.

Brown, E. and Hoek, E. (1978). Trends in relationships between measured in situ stresses and depth. *International Journal of Rock Mechanics and Mining Science*, 15(4):211–215.

BS 5930:1981 (1981). Code of practice for site investigations. *British Standards Institution, London*, page 147.

Burton, E., Friedmann, J., and Upadhye, R. (2006). Best practices in underground coal gasification. *Lawrence Livermore National Laboratory*, page 119.

Butterfield, R. (1979). A natural compression law for soils. *Géotechnique*, 29(4):469–480.

Campbell, G., Brandenburg, C., and Boyd, R. (1974). Preliminary evaluation of underground coal gasification at Hanna, Wyoming. Technical report, Bureau of Mines, Washington, DC (USA).

Carranza-Torres, C. and Fairhurst, C. (1999). The elasto-plastic response of underground excavations in rock masses that satisfy the Hoek–Brown failure criterion. *International Journal of Rock Mechanics and Mining Sciences*, 36(6):777–809.

Casagrande, A. (1932). The structure of clay and its importance in foundation engineering. *Boston Society Civil Engineers Journal*.

Chávez, C. and Alonso, E. (2003). A constitutive model for crushed granular aggregates which includes suction effects. *Soils and Foundations*, 43(4):215–227.

Chernyak, I., Burchakov, Y., and Berman, D. (1981). Failure of the roof of the development working of the deep mines. *Coal*, 11:20–23.

Chuen, L. (1979). Practice and knowledge of coal mining under water bodies. In *Proceedings of the 10th World Mining Congress*, pages 200–203.

Cox, A. D., Eason, G., and Hopkins, H. G. (1961). Axially symmetric plastic deformations in soils. *Philosophical Transactions of the Royal Society of London A: Mathematical, Physical and Engineering Sciences*, 254(1036):1–45.

Cui, X., Wang, J., and Liu, Y. (2001). Prediction of progressive surface subsidence above longwall coal mining using a time function. *International Journal of Rock Mechanics and Mining Sciences*, 38(7):1057 – 1063.

D'Applonia Consulitng Engineers (1981). DAPROK user's manual, draft version.

Dashko, R. E. and Malov, N. D. (1997). Engineering and geological aspects of the accident in the saint petersburg subway. *Razv. Okhr. Nedr*, 3:59–75.

Deck, O. and Anirudh, H. (2010). Numerical study of the soil–structure interaction within mining subsidence areas. *Computers and Geotechnics*, 37(6):802–816.

Deere, D. (1968). Geological considerations. *Rock mechanics in engineering practice*, pages 1–20.

Derbin, G. (2018). Personal communication.

Esterhuizen, E., Mark, C., and Murphy, M. M. (2010). Numerical model calibration for simulating coal pillars, gob and overburden response. In *Proceeding of the 29th international conference on ground control in mining, Morgantown, WV*, pages 46–57.

Everipedia (2016). Geology of Europe. `https://everipedia.org/wiki/Geology_of_Europe/` accessed on 10/10/2017.

Fakhimi, A., Salehi, D., and Mojtabai, N. (2004). Numerical back analysis for estimation of soil parameters in the resalat tunnel project. *Tunnelling and Underground Space Technology*, 19(1):57 – 67.

Fawcett, R., Hibberd, S., and Singh, R. (1986). Analytic calculations of hydraulic conductivities above Longwall coal faces. *International journal of mine water*, 5(1):45–60.

Frydman, S. and Burd, H. J. (1997). Numerical studies of bearing-capacity factor N γ. *Journal of geotechnical and geoenvironmental engineering*, 123(1):20–29.

Gan, D., Lu, H., Lu, H., and Yu, H. (2012). Retention goaf stability influence comprehensive analysis on existing building. In *Proceedings of the 2nd International Conference on Electronic & Mechanical Engineering and Information Technology*, pages 652–656.

Ganow, H. (1984). Results of long term ground surface measurements at the Hoe Creek III site. Technical report, Lawrence Livermore National Lab., CA (USA).

Gens, A. and Potts, D. (1988). Critical state models in computational geomechanics. *Engineering Computations*, 5(3):178–197.

Gentry, D. W. and Abel, J. F. (1978). Surface response to Longwall coal mining in mountainous terrain. *Association of Engineering Geologists Bulletin*, 15(2):191–220.

Gerdov, M. (1940). Some results of the thermal study of the strata bearing coal seams. *Bulletin on the issues of underground coal gasification*, 1:1–23.

Ghabraie, B., Ghabraie, K., Ren, G., and Smith, J. V. (2017). Numerical modelling of multistage caving processes: insights from multi-seam Longwall mining-induced subsidence. *International Journal for Numerical and Analytical Methods in Geomechanics*, 41(7):959–975.

Gregg, D., Hill, R., and Olness, D. (1976). Overview of the Soviet effort in underground gasification of coal. Technical report, Lawrence Livermore National Lab., CA (USA).

Guarascio, M., Fabris, M., and Castelli, E. (1999). Numerical model simulation of the subsidence induced by solution mining cavities. In *The international FLAC symposium on numerical modeling in geomechanics*, pages 225–232.

Gunn, R. (1977). Problems solved and problems not solved in UCG. Technical report, Energy Research and Development Administration, Laramie, WY (USA). Laramie Energy Research Center.

Guo, H., Yuan, L., Shen, B., Qu, Q., and Xue, J. (2012). Mining-induced strata stress changes, fractures and gas flow dynamics in multi-seam Longwall mining. *International Journal of Rock Mechanics and Mining Sciences*, 54:129–139.

Hansen, T. (1988). Rock properties. *Norwegian Tunnelling Today*, pages 41–44.

Hasenfus, G., Johnson, K., and Su, D. (1988). A hydrogeomechanical study of overburden aquifer response to Longwall mining. In *Proceedings of the 7th international conference on ground control in mining*, pages 108–118.

Hedley, D. and Grant, F. (1972). Stope-and-pillar design for Elliot Lake Uranium Mines. *Canadian Mining and Metallurgical Bulletin*, 65(723):37.

Herget, G. (1974). Ground stress determinations in Canada. *Rock Mechanics*, 6(1):53–64.

Herget, G. (1987). Stress assumptions for underground excavations in the Canadian Shield. *International journal of rock mechanics and mining sciences*, 24(1):95–97.

Herget, G. (1990). *Rock stresses and rock stress monitoring in Canada.* Mining Research Laboratories.

Herrero, C., Muñoz, A., Catalina, J., Hadj-Hassen, F., Kuchenbecker, R., Spreckels, V., Juzwa, J., Bennett, S., Purvis, M., Bigby, D., et al. (2012). Prediction and monitoring of subsidence hazards above coal mines (presidence), rfcs final report 2012. Technical report, RFCR-CT-2007-00004, EUR 25057 EN, European Commission, Brussels, 131 pp.

Hoek, E. (1994). Strength of rock and rock masses. *International Society of Rock Mechanics News Journal*, 2(2):4–16.

Hoek, E. and Brown, E. T. (1980). *Underground excavations in rock*. CRC Press.

Hoek, E. and Brown, E. T. (1997). Practical estimates of rock mass strength. *International Journal of Rock Mechanics and Mining Sciences*, 34(8):1165–1186.

Hoek, E., Carranza-Torres, C., and Corkum, B. (2002). Hoek-Brown failure criterion—2002 edition. *Proceedings of the 5th North American Rock Mechanics Symposium*, 1:267–273.

Hoek, E. and Diederichs, M. S. (2006). Empirical estimation of rock mass modulus. *International journal of rock mechanics and mining sciences*, 43(2):203–215.

Hoek, E., Kaiser, P. K., and Bawden, W. F. (2000). *Support of underground excavations in hard rock*. CRC Press.

Hoek, E., Wood, D., and Shah, S. (1992). A modified Hoek-Brown failure criterion for jointed rock masses. In *Proceedings of the Rock Mechanic Symposium. International Society of Rock Mechanics Eurock*, pages 209–214. Thomas Telford Publishing.

Hofmann, R. (1976). STEALTH, a Lagrange explicit finite difference code for solids, structure, and thermohydraulic analysis.

Hu, H.-T. and Schnobrich, W. C. (1989). Constitutive modeling of concrete by using nonassociated plasticity. *Journal of Materials in Civil Engineering*, 1(4):199–216.

Hudson, J. A. and Harrison, J. P. (2000). *Engineering rock mechanics: an introduction to the principles*. Elsevier.

Indraratna, B. and Salim, W. (2002). Modelling of particle breakage of coarse aggregates incorporating strength and dilatancy. *Proceedings of the Institution of Civil Engineers-Geotechnical Engineering*, 155(4):243–252.

Iofis, M. and Shmelev, A. (1985). *Engineering geomechanics under mining*. Nauka.

ISRM (1988). International Society of Rock Mechanics. commission on standardisation laboratory and field results. Suggested methods for determining hardness and abrasiveness of rocks. *Int. J. Rock Mech. Min. Geomech. Abstr.*, 15:89–97.

Itasca (2008). FLAC — Fast Lagrangian Analysis of Continua, user's guide. *Itasca Consulting Group*.

Itasca (2011). FLAC3D —Fast Lagrangian Analysis of Continua in 3D dimensions, users guide. *Itasca Consulting Group*.

Iwanec, A. S., Carter, J., and Hambleton, J. (2016). Geomechanics of subsidence above single and multi-seam coal mining. *Journal of Rock Mechanics and Geotechnical Engineering*, 8(3):304–313.

Kapralov, V. (2013). *Geotechnical aspects of estimation of the deposits for underground coal gasification*. Kniga and Biznes.

Kapusta, K., Stańczyk, K., Wiatowski, M., and Chećko, J. (2013). Environmental aspects of a field-scale underground coal gasification trial in a shallow coal seam at the Experimental Mine Barbara in Poland. *Fuel*, 113:196–208.

Karacan, C. Ö. (2010). Prediction of porosity and permeability of caved zone in Longwall gobs. *Transport in porous media*, 82(2):413–439.

Karfakis, M. and Akram, M. (1993). Effects of chemical solutions on rock fracturing. In *International journal of rock mechanics and mining sciences & geomechanics abstracts*, volume 30, pages 1253–1259.

Kavalov, B. and Peteves, S. D. (2007). The future of coal. *Institute for Energy (IFE).*

Kazak, V., Kapralov, V., and Kreinin, E. (1990). Ways of reducing heat losses under underground coal gasification. *Physical-Chimical Problems of Mining*, 6:91–96.

Kazak, V. and Semenenko, D. (1960). Study of geological factors determining the underground coal gasification process. Management of the seam roof under underground coal gasification. *Scientific Work of All-Soviet Research Institute of Underground Coal Gasification*, 1:72–83.

Kendrich, R. (1973). Induction caving URAD mine. *SME mining engineering handbook: American Institute of Mining, Metallurgical, and Petroleum Engineers*, 1:12.203–12.210.

Khadse, A., Qayyumi, M., Mahajani, S., and Aghalayam, P. (2007). Underground coal gasification: A new clean coal utilization technique for India. *Energy*, 32(11):2061–2071.

Khan, M. M., Mmbaga, J. P., Shirazi, A. S., Liu, Q., and Gupta, R. (2015). Modelling underground coal gasification - A review. *Energies*, 8(11):12603–12668.

Khong, C. D. (2004). *Development and numerical evaluation of unified critical state models.* PhD thesis, University of Nottingham.

Klimenko, A. Y. (2009). Early ideas in underground coal gasification and their evolution. *Energies*, 2(2):456–476.

Knothe, S. (1953). Effect of time on formation of basin subsidence. *Archives of Mining and Steel Industr*, 1(1):1–7.

Kolesnikov, P. (1935). On the question of stratum thermal conductivity. *Underground coal gasification*, 2:9–12.

Kratzsch, H. (1983). Mining subsidence engineering. *Spring-Verlag Berlin, Heildelberg, Newyork.*

Kreinin, E., Antonova, R., Dvornokova, Y., and Guryanova, E. (2010). Underground coal gasification and preservation of the environment. In *Proceedings of the Scochinski Mining Institute*, pages 199–203.

Kreinin, E. V. (2010). *Underground coal gasification. Foundation theory and practice.* Korinaofseta.

Kuznetsov, A. (1935). Report on the first experience on underground coal gasification in an anthracite mine. Technical report, Podzemgas Moscow.

Lade, P. V. (2005). Overview of constitutive models for soils. In *Soil constitutive models: Evaluation, selection, and calibration*, pages 1–34.

Lama, R. (1973). Subsidence in the near-vicinity of a Longwall face. In *International Journal of Rock Mechanics and Mining Sciences & Geomechanics Abstracts*, volume 10, pages 273–280.

Lama, R. and Vutukuri, V. (1978). *Handbook on mechanical properties of rocks — testing techniques and results*, volume 3.

Laouafa, F., Farret, R., Vidal-Gilbert, S., and Kazmierczak, J. (2016). Overview and modeling of mechanical and thermomechanical impact of underground coal gasification exploitation. *Mitigation and Adaptation Strategies for Global Change*, 21(4):547–576.

Lee, F. and Abel, J. (1983). Subsidence from underground mining environmental analysis and planning considerations. Technical report, Geological Survey Circular 876.

Lee, K. L. and Seed, H. B. (1967). Drained strength characteristics of sands. *Journal of the Soil Mechanics and Foundations Division*, 93(6):117–141.

Lel, Y., Sandrigailo, I., and EuYu, T. (2000). Mining-geological and mining conditions of deep quarries development.

Lenin, V. (1913). One of the great victories of technology. *Newspaper Pravda*, 91.

Lloyd, P., Mohammad, N., and Reddish, D. (1997). Surface subsidence prediction techniques for UK coalfields-An innovative numerical modelling approach. In *Proceeding of the 15th Mining Congress of Turkey*, pages 6–9.

Lomtadze, V. (1984). *Engineering geology.* Nedra.

Majdi, A., Hassani, F. P., and Nasiri, M. Y. (2012). Prediction of the height of destressed zone above the mined panel roof in Longwall coal mining. *International Journal of Coal Geology*, 98:62–72.

Marinos, P., Hoek, E., et al. (2000). GSI: a geologically friendly tool for rock mass strength estimation. International Society for Rock Mechanics.

Martin, C. (1990). Characterizing in situ stress domains at the AECL underground research laboratory. *Canadian Geotechnical Journal*, 27(5):631–646.

Martin, C., Kaiser, P., and Christiansson, R. (2003). Stress, instability and design of underground excavations. *International Journal of Rock Mechanics and Mining Sciences*, 40(7):1027–1047.

McGarr, A. and Gay, N. (1978). State of stress in the earth's crust. *Annual Review of Earth and Planetary Sciences*, 6(1):405–436.

Mead, S., Wang, F., Ganow, H., and Stuermer, D. (1981). Environmental studies of underground coal gasificaion experiments in northeastern Wyoming. Technical report, Lawrence Livermore Laboratory.

Mellors, R., Foxall, W., and Yang, X. (2012). Detecting and monitoring UCG subsidence with InSAR. Technical report, Lawrence Livermore National Laboratory (LLNL), Livermore, CA.

Mitchell, J. (1976). Soil behavior. *Jehn Wiley & Sons, New York.*

Mohammadi, H., Jalalifar, H., and Ebrahimi, M. A. (2013). Prediction of damaged zone in Longwall working panels. pages 59–67.

Najafi, M., Jalali, S. M. E., and KhaloKakaie, R. (2014). Thermalmechanicalnumerical analysis of stress distribution in the vicinity of underground coal gasification (ucg) panels. *International Journal of Coal Geology*, 134-135:1 – 16.

NCB (1963). UK national Coal Board. principles of subsidence engineering. *Production Department, London.*

NCB (1975). UK national Coal Board. Subsidence Engineers Handbook. *Production Department, London.*

Nguyen, T. and Selvadurai, A. (1995). Coupled thermal-mechanical-hydrological behaviour of sparsely fractured rock: implications for nuclear fuel waste disposal. In *International Journal of Rock Mechanics and Mining Sciences & Geomechanics Abstracts*, volume 32, pages 465–479. Pergamon.

Ni, B. (2007). *Implementation of a Bubble model in FLAC and its application in dynamic analysis.* PhD thesis, University of Auckland.

Nusimov, G. (1941). Undeground coal gasification. *Gostoptechizdat.*

Ovchinikov, V., Tyutin, F., and Semenenko, D. (1966). Features of the rock deformation and its performance during underground gasification of the steep coal seam in the Kuznetsk basin. *Underground coal gasification in the Kuznetsk basin*, 1:130–146.

Palchik, N. S., Laing, T. J., Connell, K. J., Daltroy, L. H., Friedman, C. P., Hull, A. L., Mazzuca, S. A., Palella, T. D., Ragsdale, C. G., and Stross, J. (1991). Research priorities for arthritis professional education. *Arthritis & Rheumatology*, 34(2):234–240.

Palchik, V. (1989). Analytical and empirical prognosis of rock foliation in rock masses. *J Coal Ukraine*, 7:45–46.

Palchik, V. (2002). Influence of physical characteristics of weak rock mass on height of caved zone over abandoned subsurface coal mines. *Environmental Geology*, 42(1).

Palchik, V. (2003). Formation of fractured zones in overburden due to Longwall mining. *Environmental Geology*, 44(1):28–38.

Palmström, A. (1995). *A Rock Mass Characterization System for Rock Engineering Purpose*. PhD thesis, University of Oslo.

Palmström, A. and Singh, R. (2001). The deformation modulus of rock massescomparisons between in situ tests and indirect estimates. *Tunnelling and Underground Space Technology*, 16(2):115–131.

Pei, P., Korom, S. F., Ling, K., and Nasah, J. (2016). Cost comparison of syngas production from natural gas conversion and underground coal gasification. *Mitigation and adaptation strategies for global change*, 21(4):629–643.

Peng, S. S. and Chiang, H. S. (1984). *Longwall mining*. John Wiley and Sons, New York, NY, USA.

Pongpanya, P., Sasaoka, T., Shimada, H., Hamanaka, A., and Wahyudi, S. (2017). Numerical study on effect of Longwall mining on stability of main roadway under weak ground conditions in Indonesia. *Journal of Geological Resource and Engineering*, 3:93–104.

Potts, D. and Gens, A. (1985). A critical assessment of methods of correcting for drift from the yield surface in elasto-plastic finite element analysis. *International Journal for Numerical and Analytical Methods in Geomechanics*, 9(2):149–159.

Pound, C. (2006). The performance of FLAC zones in bending. In *Proceedings of the 4th International FLAC Symposium*, pages 1–7.

Pourhosseini, O. and Shabanimashcool, M. (2014). Development of an elasto-plastic constitutive model for intact rocks. *International Journal of Rock Mechanics and Mining Sciences*, 66:1–12.

Prandtl, L. (1924). Stress distribution in plastic bodies. In *Proceedings of the 1st International Congress on Applied Mechanics*, pages 43–54.

Proskuryakov, V. A. (1947). Experience of the calculation of the rock stress in the faces at the Moscow basin. *Coal*, 9:10–15.

Ren, G., Whittaker, B., and Reddish, D. (1989). Mining subsidence and displacement prediction using influence function methods for steep seams. *Mining Science and Technology*, 8(3):235–251.

Rouainia, M. and Muir Wood, D. (2000). A kinematic hardening constitutive model for natural clays with loss of structure. *Géotechnique*, 50(2):153–164.

Russell, A. R. and Khalili, N. (2004). A bounding surface plasticity model for sands exhibiting particle crushing. *Canadian Geotechnical Journal*, 41(6):1179–1192.

Russo, Y. and Kazak, V. (1958). Changes of physico-mechanical properties of the roof of the coal seam during underground coal gasification. *Underground coal gasification*, 4:36–41.

Rutqvist, J., Ijiri, Y., and Yamamoto, H. (2011). Implementation of the Barcelona Basic Model into TOUGH–FLAC for simulations of the geomechanical behavior of unsaturated soils. *Computers & geosciences*, 37(6):751–762.

Salamon, M. (1983). Rockburst hazard and the fight for its alleviation in South African gold mines. *Rockbursts: prediction and control. IMM, London*, pages 11–36.

Salamon, M. (1990). Mechanism of caving in Longwall coal mining. In *Rock Mechanics Contributions and Challenges: Proceedings of the 31st US Symposium on Rock Mechanics*, pages 161–169.

Semenenko, D. and Turchaninov, I. (1957). Rock performance under underground coal gasification. *Underground coal gasification*, 3:31–39.

Serafim, J. L. and Pereira, J. P. (1983). Considerations of the geomechanics classification of Bieniawski. In *Proceedings of the International Symposium on Engineering Geology and Underground Construction*, volume 1, pages 1133–1142.

Shafirovich, E. and Varma, A. (2009). Underground coal gasification: a brief review of current status. *Industrial & Engineering Chemistry Research*, 48(17):7865–7875.

Shell, A. and France, H. (1977). In situ gasification: what it looks like from sitting on top. In *Proceedings of the 3rd annual underground coal conversion symposium*, pages 127–140.

Singh, G. and Singh, U. (2011). Assessment of goaf characteristics and compaction in Longwall caving. *Mining Technology*, 120(4):222–232.

Singh, K. B. and Dhar, B. B. (1997). Sinkhole subsidence due to mining. *Geotechnical & Geological Engineering*, 15(4):327–341.

Singh, M. and Kendorski, F. (1981). Strata disturbance prediction for mining beneath surface water and waste impoundments. In *Proceedings of the 1st Conference on Ground Control in Mining*, pages 76–89. West Virginia University, Morgantown, WV.

Singh, R. and Singh, T. (1999). Investigation into the behaviour of a support system and roof strata during sublevel caving of a thick coal seam. *Geotechnical and Geological engineering*, 17(1):21–35.

Singh, R. and Yadav, R. (1995). Subsidence due to coal mining in India. *IAHS Publications-Series of Proceedings and Reports-Intern Assoc Hydrological Sciences*, 234:207–214.

Skafa, P. (1960). *Underground coal gasificaion*. Gosgortechizdat.

Sloan, S. and Booker, J. (1986). Removal of singularities in Tresca and Mohr–Coulomb yield functions. *International Journal for Numerical Methods in Biomedical Engineering*, 2(2):173–179.

Smart, B. and Aziz, N. (1989). The influence of caving mechanism on powered support rating. *Aust. IMM Bull. Proc*, 294(4):77–84.

SNIP 2.01.01-82 (1982). Building climatology USSR. *Building Code, Stroyisdat, Moscow.*

Stephenson, D., Dass, S., and Shaw, D. (1983). Numerical modeling of subsidence induced by underground coal gasification including thermal effects. *In Situ*, 7(1):27–51.

Strokova, L. A. (2009). Numerical model of surface subsidence during subway tunneling. *Soil Mechanics and Foundation Engineering*, 46(3):117–119.

Styler, N. et al. (1984). Prediction of inter-strata movements above Longwall faces. In *The 25th US Symposium on Rock Mechanics (USRMS)*. American Rock Mechanics Association.

Su, F., Nakanowataru, T., Itakura, K., Ohga, K., and Deguchi, G. (2013). Evaluation of structural changes in the coal specimen heating process and UCG model experiments for developing efficient UCG systems. *Energies*, 6(5):2386–2406.

Sury, M., White, M., Kirton, J., Carr, P., Woodbridge, R., Mostade, M., Chappell, R., Hartwell, D., Hunt, D., and Rendell, N. (2004). Review of environmental issues of underground coal gasification. *WS Atkins Consultants Ltd., University of Liège Belgium, FWS Consultants Ltd*, 126:1–126.

Terzaghi, K. and Peck, R. (1967). Settlement of point bearing pile foundation;, settlement of floating pile foundation. *Soil Mechanics in Engineering Practice*, pages 540–555.

Tian, H. (2013). *Development of a thermo-mechanical model for rocks exposed to high temperatures during underground coal gasification.* PhD thesis, RWTH Aachen University.

Timoshenko, S. P. and Goodier, J. N. (1970). *Theory of elasticity.* McGraw-Hill, New York London.

Trent, B. and Langland, R. (1983). Subsidence modeling for underground coal gasification. *In Situ*, 7(1):53–85.

Turchaninov, I. (1957a). On nature of underground coal gasification and deformation of the rock during underground coal gasification in the Moscow basin. *Underground coal gasification*, 2:74–78.

Turchaninov, I. (1957b). Solutions of control of the roof during underground coal gasification. *Underground coal gasification*, 3:39–42.

Turchaninov, I., Iofis, M., and Kasparyan, E. (1977). *Principles of rock mechanics.* Nedra, Leningrad.

Turchaninov, I., Iofis, M., and Kasparyan, E. (1979). *Principles of rock mechanics.* Terraspace Inc., Rockville, MD, USA.

Turchaninov, I. and Sazonov, V. (1958). Some features of gasification of the coal seam and movements of the overburden during UCG at the Shatsk station. *Underground coal gasification*, 3:11–16.

Turchaninov, I. and Zabrovsky, A. (1958). Rock deformation and its influence on the process of underground gasification of the thick and steep coal seam. *Underground coal gasification*, 2:7–11.

US Department of Energy (1979). Underground coal conversion. *Program description.*

Vanapalli, S. and Oh, W. (2010). A model for predicting the modulus of elasticity of unsaturated soils using the soil-water characteristic curve. *International Journal of Geotechnical Engineering*, 4(4):425–433.

Virgona, J. E. (1978). Environmental research for underground coal gasification. In *Proc. Environmental Assessment of Solid Fossil Fuel Processes Symposium of the 71st Annual American Institute Chemical Engineers Meeting, Nov*, pages 12–16.

Vyazmensky, A., Elmo, D., Stead, D., and Rance, J. R. (2007). Combined finite-discrete element modelling of surface subsidence associated with block caving mining. In *Proceedings of 1st Canada-US Rock Mechanics Symposium*, pages 467–475.

Wagoner, J. (2011). Wulanchabu ucg site data-status report. Technical report, Lawrence Livermore National Laboratory (LLNL), Livermore, CA.

Westerberg, B. (1999). *Behaviour and modelling of a natural soft clay: triaxial testing, constitutive relations and finite element modelling.* PhD thesis, Luleå tekniska universitet.

Wilson, A. (1982). Pillar stability in Longwall mining. *State-of-the-Art of Ground Control in Longwall Mining and Mining Subsidence*, pages 85–95.

Wood, M. D. (1995). Kinematic hardening model for structured soil. *Numerical Models in Geomechanics*, pages 83–88.

Wu, D., Zhang, Y., Zhao, R., Deng, T., and Zheng, Z. (2017). A coupled thermal-hydraulic-mechanical application for subway tunnel. *Computers and Geotechnics*, 84:174–182.

Xu, N., Kulatilake, P. H., Tian, H., Wu, X., Nan, Y., and Wei, T. (2013). Surface subsidence prediction for the wutong mine using a 3-d finite difference method. *Computers and Geotechnics*, 48:134 – 145.

Yang, D., Sarhosis, V., and Sheng, Y. (2014). Thermalmechanical modelling around the cavities of underground coal gasification. *Journal of the Energy Institute*, 87(4):321 – 329.

Youngberg, A., Sinks, D., Craig, G., Ethridge, F., and Burns, L. (1983). Postburn evaluation for Hanna II, phases 2 and 3. Underground coal gasification experiments, Hanna, Wyoming. *United States Office of Scientific and Technical Information, Technical Information Center. Under cooperative contract.*

Younger, P. L. (2011). Hydrogeological and geomechanical aspects of underground coal gasification and its direct coupling to carbon capture and storage. *Mine Water and the Environment*, 30(2):127–140.

Yow, J. and Hunt, J. (2002). Coupled processes in rock mass performance with emphasis on nuclear waste isolation. *International Journal of Rock Mechanics and Mining Sciences*, 39(2):143 – 150.

Yu, H. (1995). A unified critical state model for clay and sand. *Civil Engineering Research Report No 112.08.*

Yu, H.-S. (1998). CASM: A unified state parameter model for clay and sand. *International journal for numerical and analytical methods in geomechanics*, 22(8):621–653.

Yu, H.-S. (2007). *Plasticity and geotechnics. Advances in Mechanics and Mathematics*, volume 13. Springer Science & Business Media.

Zamzow, K. (2010). Underground coal gasification: history, environmental issues, and the proposed project at Beluga. *Center for Science in Public Participation, Alaska.*

Zhang, D., Fan, G., Ma, L., and Wang, X. (2011). Aquifer protection during Longwall mining of shallow coal seams: a case study in the Shendong Coalfield of China. *International Journal of Coal Geology*, 86(2):190–196.

Zhou, Y. (1991). Evaluating the impact of multiseam mining on recoverable coal reserves in an adjacent seam. *Minerals and Energy, Pub*, (104).

Zhukov, V. and Orlov, G. (1964). Surface subsidence during underground gasification of the coal seam at the industrial gas reactor 3 at the Angren station 'Podzemgaz'. *Scientific Work of All-Soviet Research Institute of Underground Coal Gasification*, 12:68–74.

Zienkiewicz, O. and Pande, G. (1977). Time-dependent multilaminate model of rocks - a numerical study of deformation and failure of rock masses. *International Journal for Numerical and Analytical Methods in Geomechanics*, 1(3):219–247.

Appendix A

Validation of Elastic and Perfectly Plastic Models

This Appendix presents the charts of comparison between UDCM and build-in models for two problems: 'Cylindrical Hole Cut into the Cube' and 'Spherical Hole Cut into the Cube' for two different initial stresses, i.e. 3Pa and 30MPa. The models at hand are isotropic, elastic, Drucker-Prager, and Mohr-Coulomb models.

A.1 Cylindrical Hole Cut into the Cube

A.1.1 Elastic, Isotropic Model

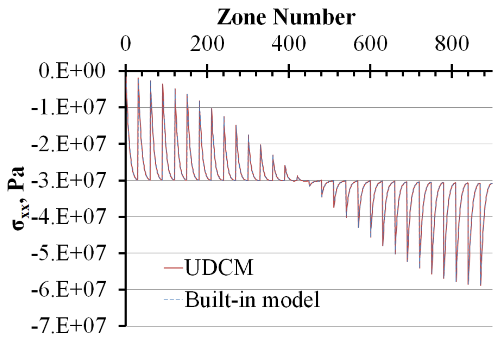

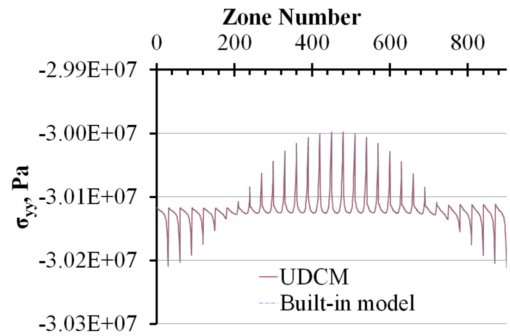

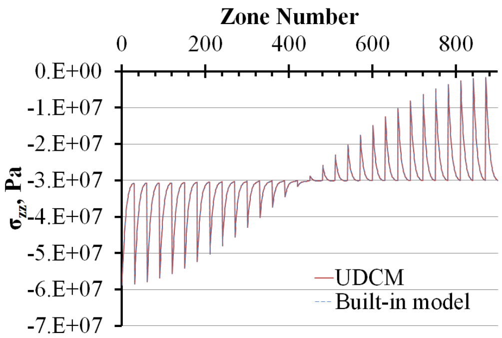

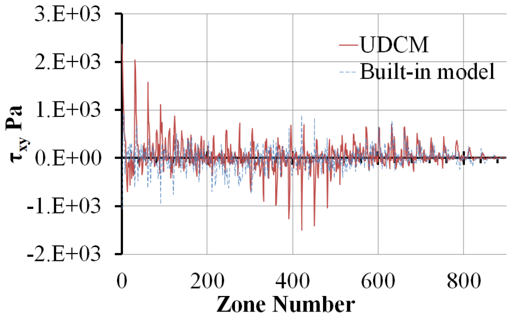

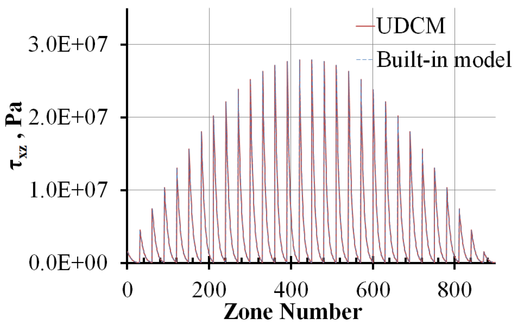

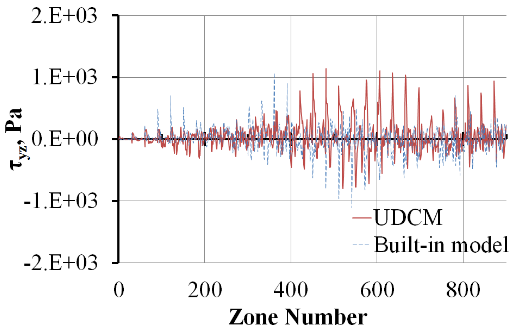

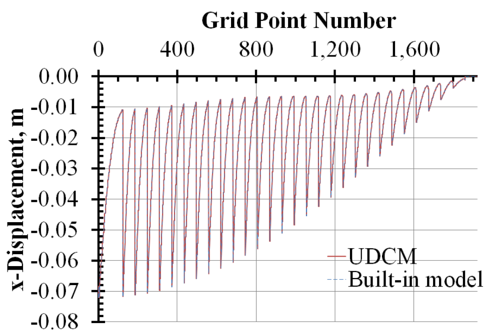

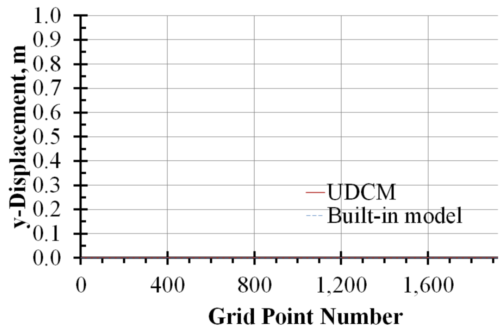

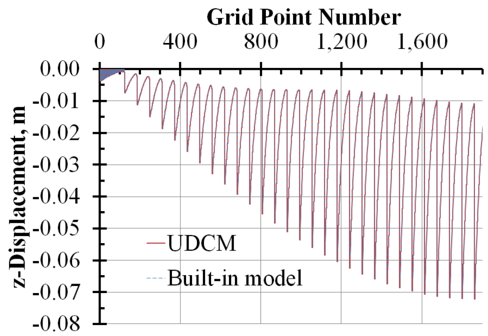

A.1.2 Mohr-Coulomb Model

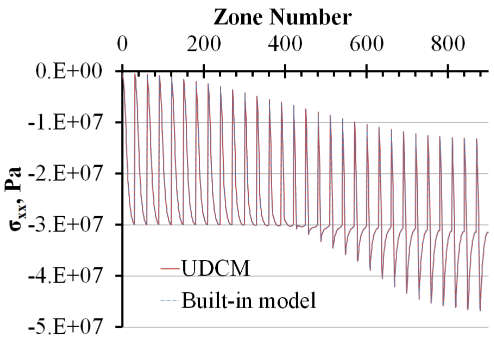

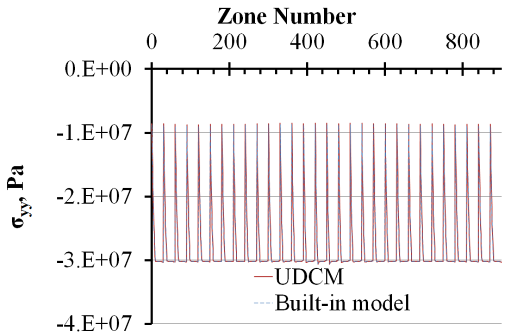

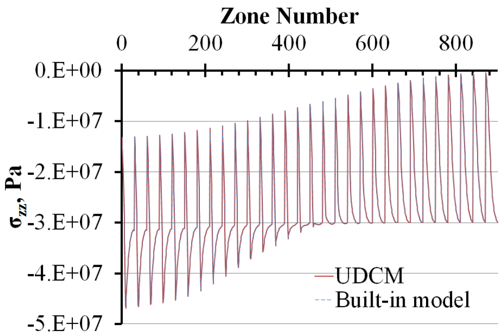

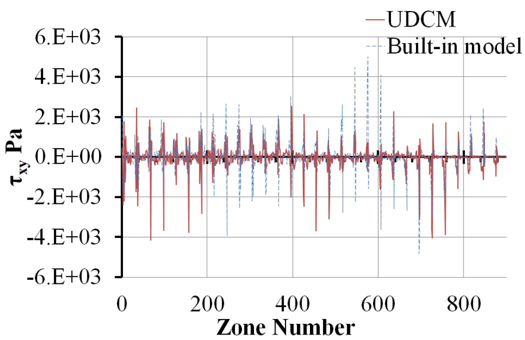

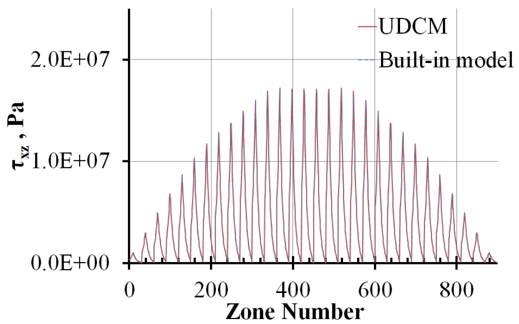

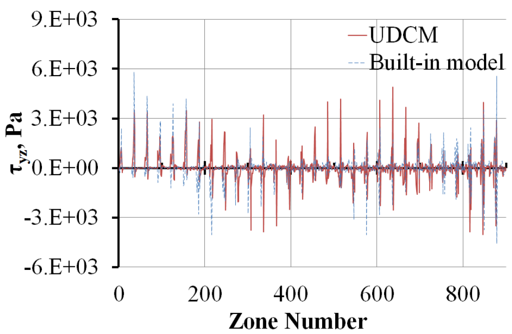

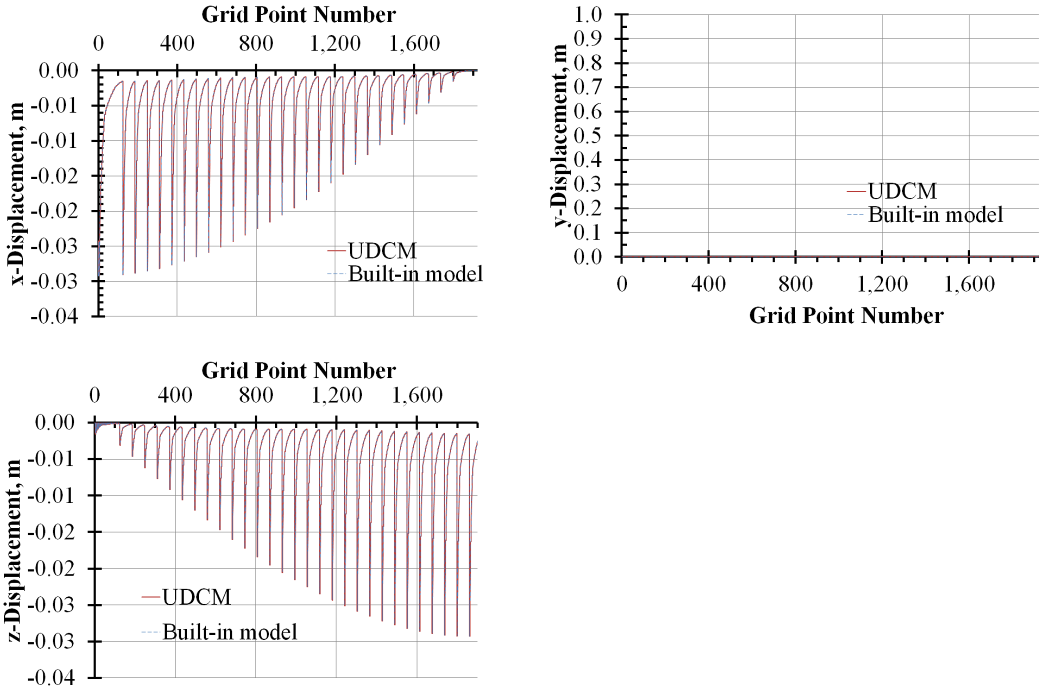

A.2 Spherical Hole Cut into the Cube

A.2.1 Elastic, Isotropic Model (Small Stress)

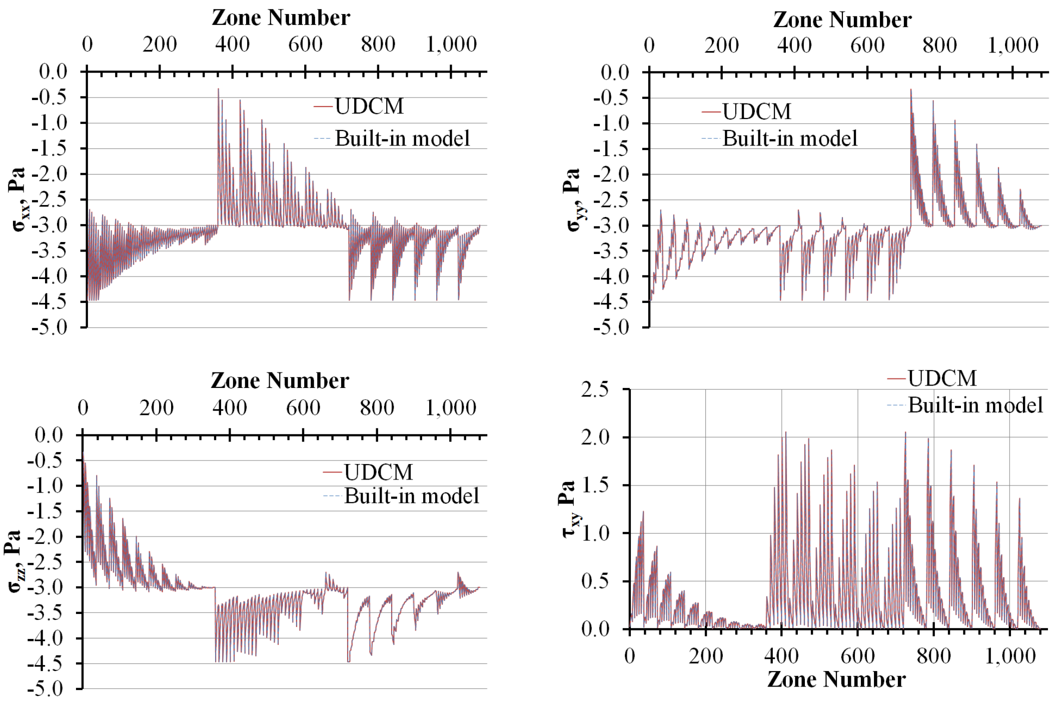

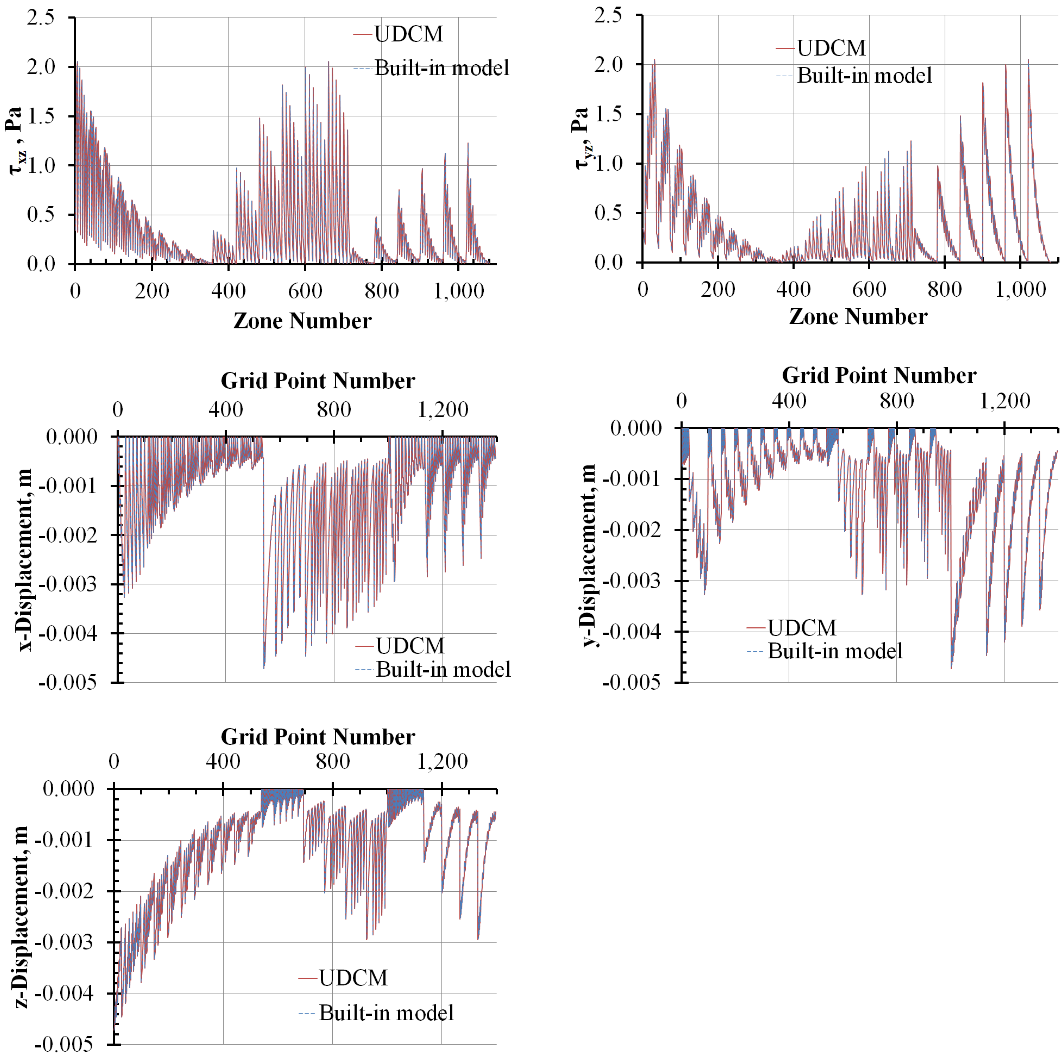

τxz , Pa
Zone Number
UDCM
Built-in model
τyz, Pa
Zone Number
UDCM
Built-in model
Grid Point Number
x-Displacement, m
UDCM
Built-in model
Grid Point Number
y-Displacement, m
UDCM
Built-in model
Grid Point Number
z-Displacement, m
UDCM
Built-in model

A.2.2 Drucker-Prager Model (Small Stress)

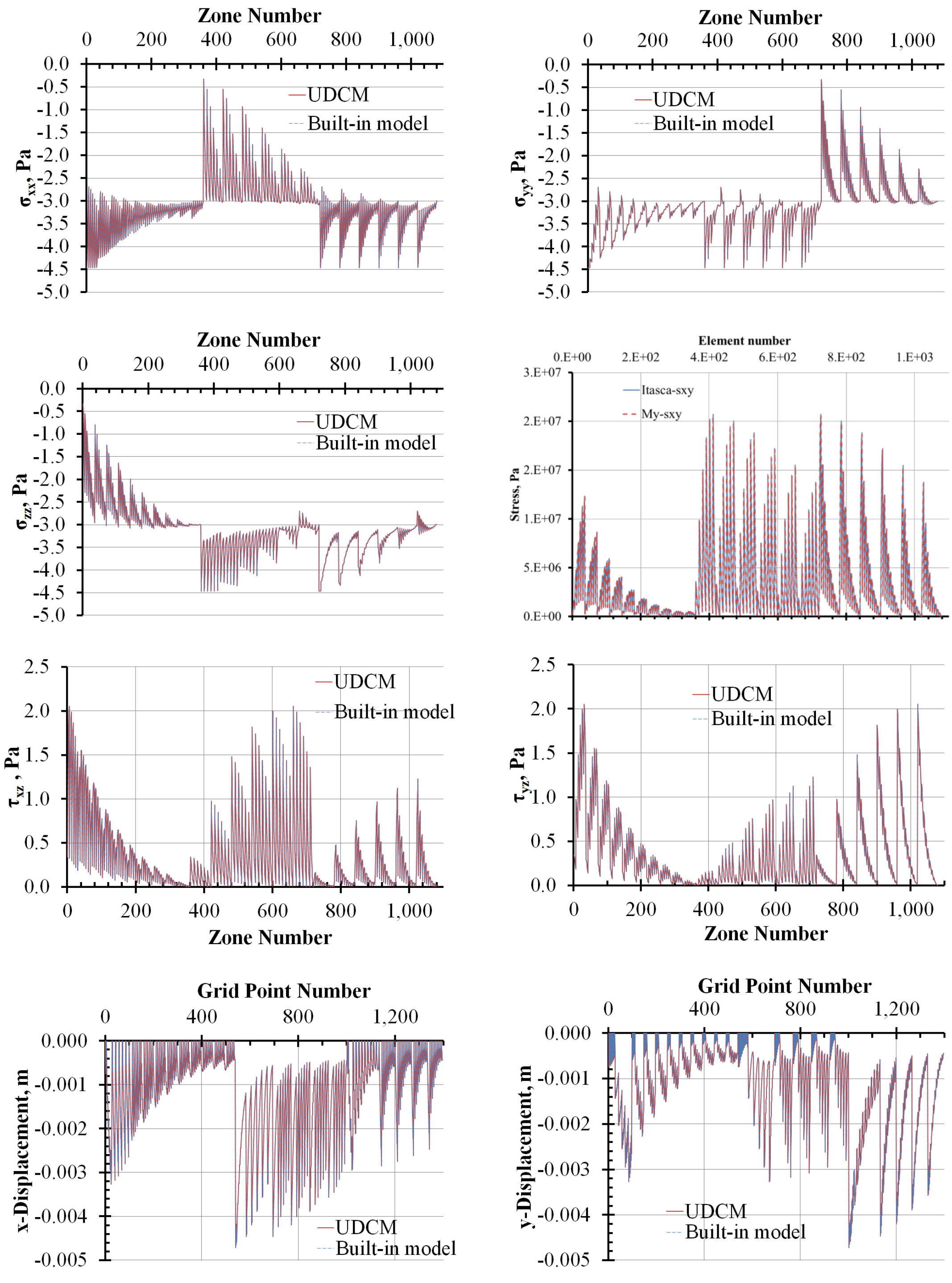

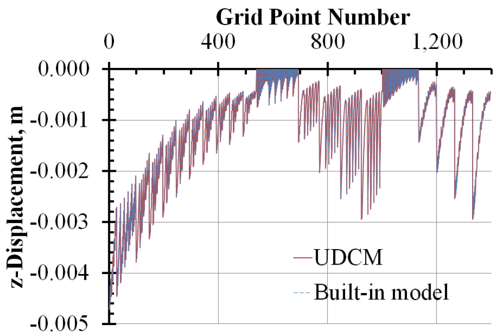

A.2.3 Elastic, Isotropic Model

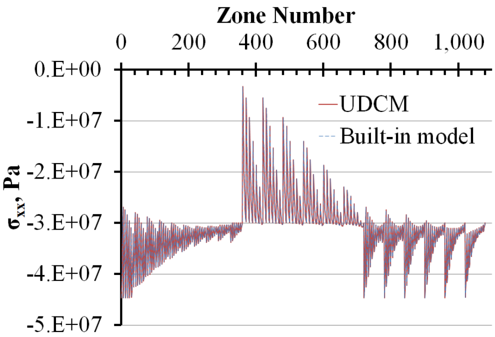

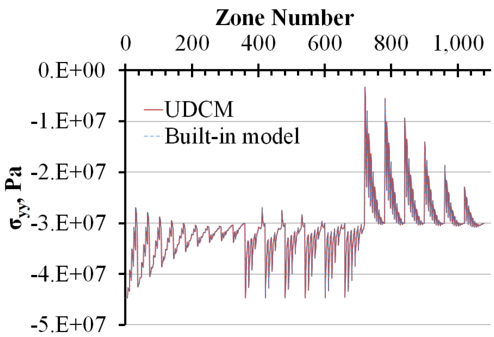

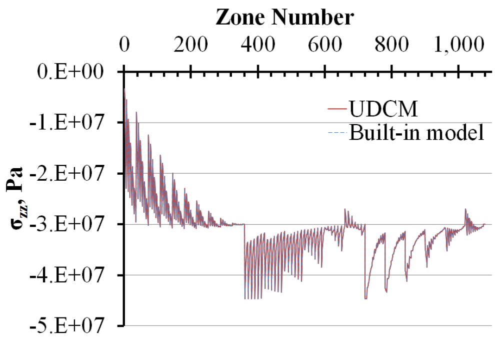

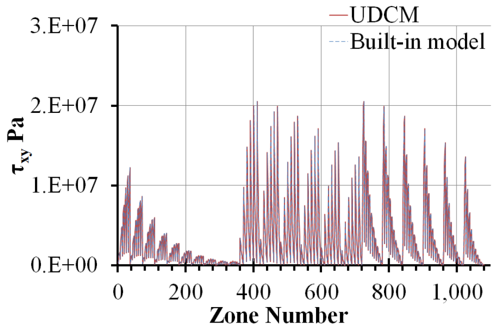

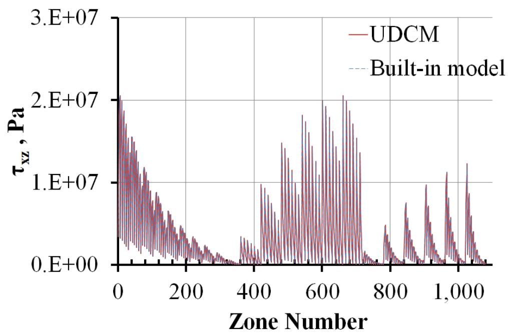

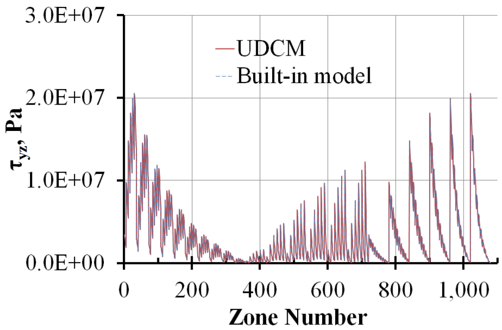

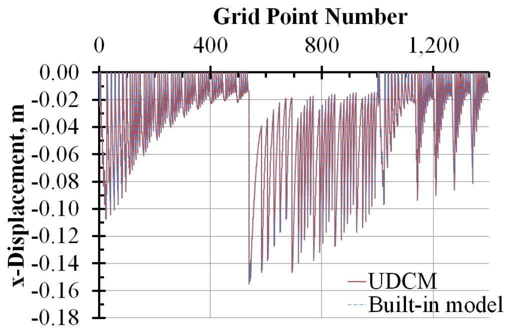

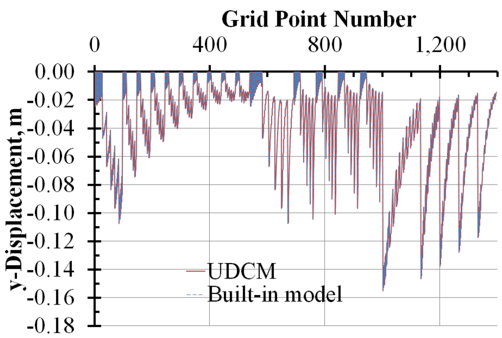

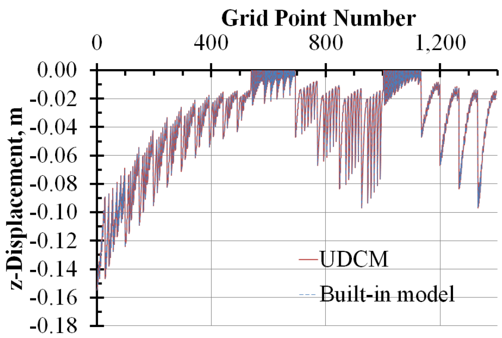

A.2.4 Drucker-Prager Model

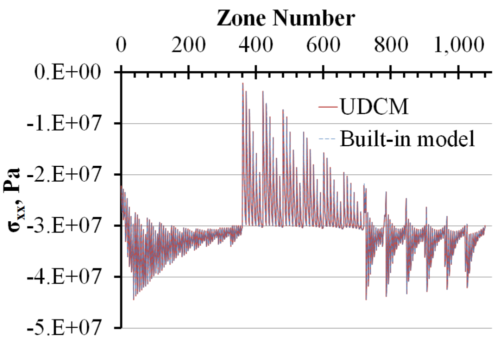

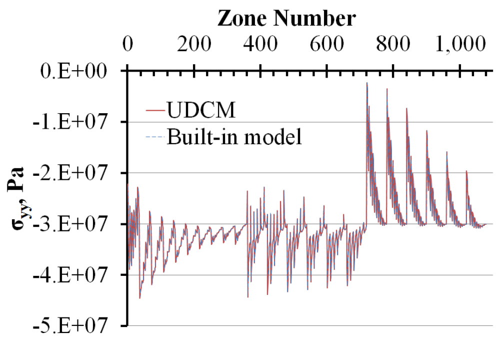

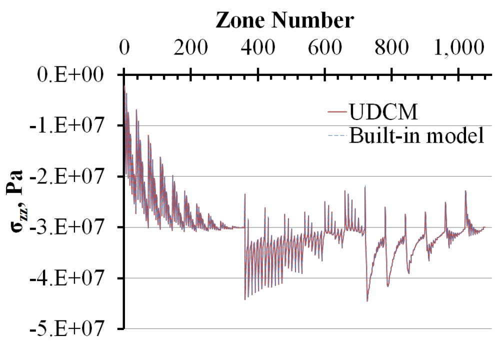

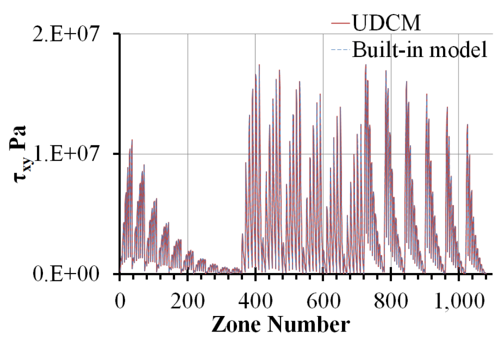

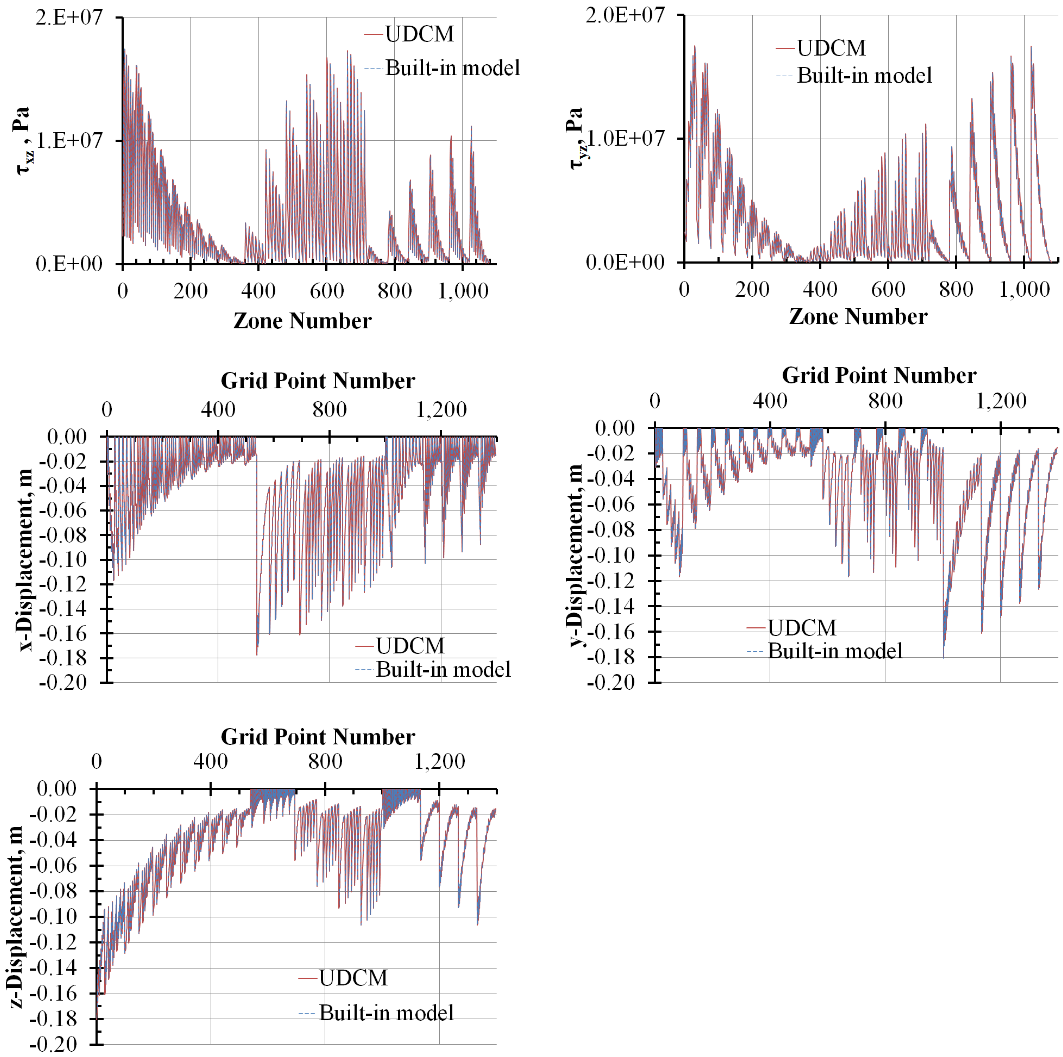
τxz , Pa
Zone Number
UDCM
Built-in model
τyz, Pa
Zone Number
UDCM
Built-in model
Grid Point Number
x-Displacement, m
UDCM
Built-in model
Grid Point Number
y-Displacement, m
UDCM
Built-in model
Grid Point Number
z-Displacement, m
UDCM
Built-in model

A.2.5 Mohr-Coulomb Model

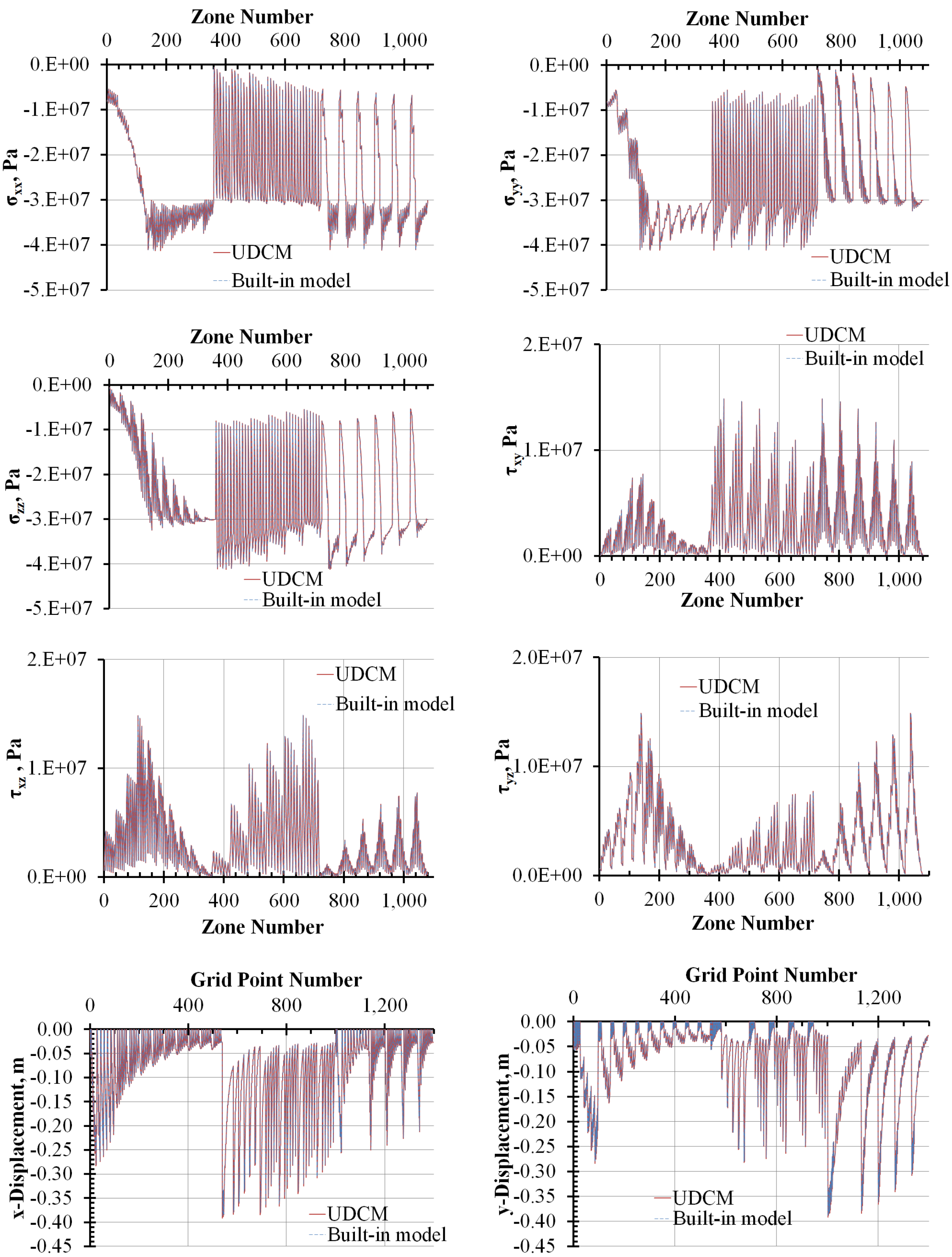

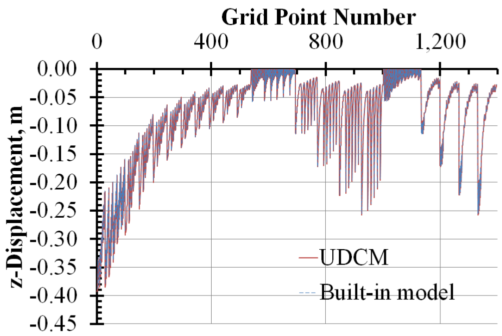
Grid Point Number
0
400
800
1,200
0.00
-0.05
-0.10
-0.15
-0.20
-0.25
-0.30
-0.35
-0.40
-0.45
z-Displacement, m
UDCM
Built-in model

Appendix B

C++ Code of the Bubble Model

The following code is a programmed bubble model with yield surface drift for FLAC3D. It includes three parts: functions, initialization, and run sections.

B.1 Functions

```
//Correctly raises a number to a power without causing a NaN
double Modelbubble::power(const double a, const double b) {
  double output;
  double tempa, tempb;
  output = pow(a, b);
  if (output != output) {
    if (a == 0.0) output = 0.0;
    else if (b < 0.0) {
      tempb = -1.0*b;
      output = 1.0 / pow(a, tempb);
      if (output != output) {
        tempa = -1.0*a;
        output = -1.0 / pow(tempa, tempb);
      }
    }
    else {
      tempa = -1.0*a;
      output = -1.0*pow(tempa, b);
    }
    if (b == 0.0) output = 1.0;
  }
```

```
    if (output >= DBL_MAX) output = DBL_MAX;
    if (output <= -DBL_MAX) output = -DBL_MAX;
    if ((output >= -DBL_MIN) && (output <= DBL_MIN)) output = 0.0;
    return output;
}
//Returns the sign
double Modelbubble::Sign(const double Value) {
    if (Value == 0.0) return 0.0;
    if (Value > 0.0) return 1.0;
    else return -1.0;
}
//Inverts a 6x6 matrix
bool Modelbubble::xmatinv(double b[6][6]) {
    bool flag;
    Double bii, bji;
    UInt n = 6;
    UInt i, j, k;
    flag = true;
    for (i = 0; i < n; i++) {
        bii = b[i][i];
        if (bii == 0.0) {
            flag = false;
            return(flag);
        }
        for (k = 0; k < n; k++) b[i][k] = b[i][k] / bii;
        b[i][i] = 1.0 / bii;
        for (j = 0; j < n; j++) {
            if (j != i) {
                bji = b[j][i];
                for (k = 0; k < n; k++) b[j][k] = b[j][k] - bji * b[i][k];
                b[j][i] = -bji * b[i][i];
            }
        }
    }
    return(flag);
}
//Calculates deviatoric stress
double Modelbubble::q(const double sxx, const double syy, const double szz,
    const double txy, const double txz, const double tyz) {
        double a = sxx - syy;
        double b = sxx - szz;
        double c = syy - szz;
        double half = ((a*a) + (b*b) + (c*c)) / 6.0;
        double J2 = (txy*txy) + (txz*txz) + (tyz*tyz) + half;
```

```
    return power((3.0*J2), 0.5);
}
```

B.2 Initialization

```
for (UInt i = 0; i < 6; i++) {
   for (UInt j = 0; j < 6; j++) {
      k[i][j] = 0.0;
      S[i][j] = 0.0;
   }
}
//Initial distance from the origin of the p, q coordinate system
//to the centre of the reference surface on the p axis
pc = ipc0*(-1.0);
r_str = ir_str0; //Initial relative size of the structure surface
//A dimensionless tensor denoting the initial anisotropy of the structure surface
nambda0 = nambda0 / 1.732;
$p = (s->stnS_.s11() + s->stnS_.s22() + s->stnS_.s33()) / 3.0;
//Initial stress in p-q space
$s = nambda0*(r_str - 1.0)*pc; //Centre of structure surface
s_p = r_str*pc; //Centre of the strcuture surface in deviatoric stress space
s_zs11c = s_p;  //Centre of the structure surface in general stress space
s_zs22c = s_p;
s_zs33c = s_p;
s_zs12c = $s;
s_zs13c = $s;
s_zs23c = $s;
//Bubble model is reduced to the modified Cam-clay model
if (r_bub > 0.95) {
   b_zs11c = pc;
   b_zs22c = pc;
   b_zs33c = pc;
   b_zs12c = 0.0;
   b_zs13c = 0.0;
   b_zs23c = 0.0;
}
bub_p = (b_zs11c + b_zs22c + b_zs33c) / 3.0;
//Checking if the bubble intersects structure surface
if (fabs(bub_p) <= fabs(r_bub*pc)){
   b_zs11c = r_bub*pc;
   b_zs22c = b_zs11c;
```

```
    b_zs33c = b_zs11c;
    $p = (s->stnS_.rs11() + s->stnS_.rs22() + s->stnS_.rs33()) / 3.0;
}
if (fabs(bub_p) >= fabs(2.0 * ir_str0*pc - r_bub*pc)) {
    b_zs11c = 2.0 * ir_str0*pc - r_bub*pc;
    b_zs22c = b_zs11c;
    b_zs33c = b_zs11c;
    $p = (s->stnS_.rs11() + s->stnS_.rs22() + s->stnS_.rs33()) / 3.0;
}
//Centre of the bubble in deviator stress space
b_ds11c = b_zs11c - bub_p;
b_ds22c = b_zs22c - bub_p;
b_ds33c = b_zs33c - bub_p;
b_ds12c = b_zs12c;
b_ds13c = b_zs13c;
b_ds23c = b_zs23c;
//Initial bulk and shear moduli
b_mod = fabs($p) / b_kappa + b_bod0;
s_mod = 3.0*b_mod*(1.0 - 2.0*b_poss) / (2.0*(1.0 + b_poss));
```

B.3 Run

```
// Builds the compliance matrix [S]
S[0][0] = k[0][0] = (3.0*b_mod + s_mod) / (9.0*b_mod*s_mod);
S[0][1] = k[0][1] = (2.0*s_mod - 3.0*b_mod) / (18.0*b_mod*s_mod);
S[0][2] = k[0][2] = (2.0*s_mod - 3.0*b_mod) / (18.0*b_mod*s_mod);
S[1][0] = k[1][0] = k[0][1];
S[2][0] = k[2][0] = k[0][2];
S[1][2] = k[1][2] = (2.0*s_mod - 3.0*b_mod) / (18.0*b_mod*s_mod);
S[2][1] = k[2][1] = k[1][2];
S[1][1] = k[1][1] = (3.0*b_mod + s_mod) / (9.0*b_mod*s_mod);
S[2][2] = k[2][2] = (3.0*b_mod + s_mod) / (9.0*b_mod*s_mod);
S[3][3] = k[3][3] = 1.0 / s_mod;//getShearModulus();
S[4][4] = k[4][4] = 1.0 / s_mod;//getShearModulus();
S[5][5] = k[5][5] = 1.0 / s_mod;//getShearModulus();
xmatinv(k); // Inverts to build the stiffness matrix [k]
//Initializes stress and strain state
zde11 = s->stnE_.s11();
zde22 = s->stnE_.s22();
zde33 = s->stnE_.s33();
zde12 = s->stnE_.s12();
```

```
zde13 = s->stnE_.s13();
zde23 = s->stnE_.s23();
zs11 = s->stnS_.s11();
zs22 = s->stnS_.s22();
zs33 = s->stnS_.s33();
zs12 = s->stnS_.s12();
zs13 = s->stnS_.s13();
zs23 = s->stnS_.s23();
//Total volumatric strain
$sum_zde11 = $sum_zde11 + zde11;
$sum_zde22 = $sum_zde22 + zde22;
$sum_zde33 = $sum_zde33 + zde33;
$sum_zde12 = $sum_zde12 + zde12;
$sum_zde13 = $sum_zde13 + zde13;
$sum_zde23 = $sum_zde23 + zde23;
//Trial stresses rate
$dzs11 = s->stnE_.s22()*k[0][1] + s->stnE_.s33()*k[0][2] + s->stnE_.s11()*k[0][0];
$dzs22 = s->stnE_.s11()*k[1][0] + s->stnE_.s33()*k[1][2] + s->stnE_.s22()*k[1][1];
$dzs33 = s->stnE_.s11()*k[2][0] + s->stnE_.s22()*k[2][1] + s->stnE_.s33()*k[2][2];
$dzs12 = s->stnE_.s12()*k[3][3] * 2.0;
$dzs13 = s->stnE_.s13()*k[4][4] * 2.0;
$dzs23 = s->stnE_.s23()*k[5][5] * 2.0;
//Trial stresses
$zs11 = s->stnS_.rs11() + $dzs11;
$zs22 = s->stnS_.rs22() + $dzs22;
$zs33 = s->stnS_.rs33() + $dzs33;
$zs12 = s->stnS_.rs12() + $dzs12;
$zs13 = s->stnS_.rs13() + $dzs13;
$zs23 = s->stnS_.rs23() + $dzs23;
$p = ($zs11 + $zs22 + $zs33) / 3.0;
//Deviator stress
$ds11 = $zs11 - $p;
$ds22 = $zs22 - $p;
$ds33 = $zs33 - $p;
$ds12 = $zs12;
$ds13 = $zs13;
$ds23 = $zs23;
//Deviator stress wrt the bubble centre
$b_ds11 = $ds11 - b_ds11c;
$b_ds22 = $ds22 - b_ds22c;
$b_ds33 = $ds33 - b_ds33c;
$b_ds12 = $ds12 - b_ds12c;
$b_ds13 = $ds13 - b_ds13c;
$b_ds23 = $ds23 - b_ds23c;
```

```

$J2r = ($ds11*$ds11 + $ds22*$ds22 + $ds33*$ds33 + 2.0 * $ds12*$ds12);
$J2r = ($J2r + 2.0 * $ds13*$ds13 + 2.0 * $ds23*$ds23) / 2.0;
double $J3 = $ds11*$ds22*$ds33 + 2.0*$ds12*$ds13*$ds23 - $ds33*$ds12*$ds12;
$J3 = $J3 - $ds22*$ds13*$ds13 - $ds11*$ds23*$ds23;
$J2c = $b_ds11*$b_ds11 + $b_ds22 * $b_ds22 + $b_ds33 * $b_ds33;
$J2c = $J2c + 2.0 * $b_ds12 *$b_ds12 + 2.0 * $b_ds13 * $b_ds13;
$J2c = ($J2c + 2.0 * $b_ds23 * $b_ds23) / 2.0;
//Lode angle
if ($J2r == 0.0) {
   $M = (2.0 * b_mm / (1.0 + b_mm))*b_M;
}
else {
   $c1 = -2.59807*$J3 / power(($J2r), 1.5);
   if (fabs($c1) == 1.0) {
      if ($c1 == 1.0) $M = b_M;
      if ($c1 == -1.0) $M = b_M*b_mm;
   }
   else {
      $c1 = std::min(fabs($c1), 0.99999)*Sign($c1);
      $theta = atan($c1 / power((1.0 - $c1*$c1), 0.5)) / 3.0;
      $M = 2.0 * b_mm*b_M / ((1.0 + b_mm) - (1.0 - b_mm)*sin(3.0*$theta));
   }
}
//Inner product of deviator stress wrt bubble centre
$sp = 2.0 * $J2c;
// Bubble yield function
$fb = 1.5*$sp / ($M *$M) + ($p - bub_p)*($p - bub_p) - r_bub*r_bub * pc*pc;
//Test for failure
if ($fb >= -0.001) {
   $c1 = -12.0 * 1.732*b_mm*(1.0 - b_mm)*b_M;
   $c2 = 2.0 * (1.0 + b_mm);
   $c3 = 3.0 * 1.732*(1.0 - b_mm);
   $c4 = power($J2r, 0.5);
   $c5 = 1.0 / ($c2 + $c3*$J3 / $J2r / $c4);
   $c5 = $c1*$c5*$c5;
   $c6 = $ds12*$ds12 + $ds13 * $ds13 + $ds23 *$ds23;
   $c7 = $ds11*$ds22 + $ds11*$ds33 + $ds22*$ds33;

   double $M11 = (3.0*$ds22*$ds33 - $c7 + $c6) / 3.0;
   $M11 = 1.0 / ($c4*$c4*$c4)*$M11;
   $M11 = $M11 - 3.0 / 2.0 / ($c4*$c4*$c4*$c4*$c4)*$J3*$ds11;
   if ($M11 != $M11) throw std::runtime_error("bubble: $M11=NaN");
   $M11 = $c5*$M11;
```

```

double $M22 = (3.0*$ds11*$ds33 - $c7 + $c6) / 3.0;
$M22 = 1.0 / ($c4*$c4*$c4)*$M22;
$M22 = $M22 - 3.0 / 2.0 / ($c4*$c4*$c4*$c4*$c4)*$J3*$ds22;
$M22 = $c5*$M22;

double $M33 = (3.0*$ds22*$ds11 - $c7 + $c6) / 3.0;
$M33 = 1.0 / ($c4*$c4*$c4)*$M33;
$M33 = $M33 - 3.0 / 2.0 / ($c4*$c4*$c4*$c4*$c4)*$J3*$ds11;
$M33 = $c5*$M33;

double $M12 = -2.0 / ($c4*$c4*$c4)*$ds12*$ds33;
$M12 = $M12 - 3.0 / ($c4*$c4*$c4*$c4*$c4)*$J3*$ds12;
$M12 = $c5*$M12;

double $M13 = -2.0 / ($c4*$c4*$c4)*$ds13*$ds22;
$M13 = $M13 - 3.0 / ($c4*$c4*$c4*$c4*$c4)*$J3*$ds13;
$M13 = $c5*$M13;

double $M23 = -2.0 / ($c4*$c4*$c4)*$ds23*$ds11;
$M23 = $M23 - 3.0 / ($c4*$c4*$c4*$c4*$c4)*$J3*$ds23;
$M23 = $c5*$M23;

double $J11 = $b_ds11;
double $J22 = $b_ds22;
double $J33 = $b_ds33;
double $J12 = 2.0 * $b_ds12;
double $J13 = 2.0 * $b_ds13;
double $J23 = 2.0 * $b_ds23;

$n11 = -6.0 / ($M*$M*$M) * $J2c*$M11;
$n11 = $n11 + 3.0 / ($M*$M) * $J11 + 2.0 / 3.0*($p - bub_p);
$n22 = -6.0 / ($M*$M*$M) * $J2c*$M22;
$n22 = $n22 + 3.0 / ($M*$M) * $J22 + 2.0 / 3.0*($p - bub_p);
$n33 = -6.0 / ($M*$M*$M) * $J2c*$M33;
$n33 = $n33 + 3.0 / ($M*$M) * $J33 + 2.0 / 3.0*($p - bub_p);
$n12 = -6.0 / ($M*$M*$M) * $J2c*$M12;
$n12 = $n12 + 3.0 / ($M*$M) * $J12;
$n13 = -6.0 / ($M*$M*$M) * $J2c*$M13;
$n13 = $n13 + 3.0 / ($M*$M) * $J13;
$n23 = -6.0 / ($M*$M*$M) * $J2c*$M23;
$n23 = $n23 + 3.0 / ($M*$M) * $J23;
//Normalise stress gradient
double pn = $n11*$n11 + $n22*$n22 + $n33*$n33 + 2.0*$n12*$n12;
```

```
pn =pn + 2.0*$n13*$n12 + 2.0*$n23*$n12;
$n = power(pn, 0.5);
$n11 = $n11 / $n;
$n22 = $n22 / $n;
$n33 = $n33 / $n;
$n12 = $n12 / $n;
$n13 = $n13 / $n;
$n23 = $n23 / $n;
$n = $n*$n;
//Stress wrt the bubble centre
$b_zs11 = $zs11 - b_zs11c;
$b_zs22 = $zs22 - b_zs22c;
$b_zs33 = $zs33 - b_zs33c;
$b_zs12 = $zs12 - b_zs12c;
$b_zs13 = $zs13 - b_zs13c;
$b_zs23 = $zs23 - b_zs23c;
//Stress wrt the structure surface centre
$s_zs11 = $zs11 - s_zs11c;
$s_zs22 = $zs22 - s_zs22c;
$s_zs33 = $zs33 - s_zs33c;
$s_zs12 = $zs12 - s_zs12c;
$s_zs13 = $zs13 - s_zs13c;
$s_zs23 = $zs23 - s_zs23c;
//Stress wrt the structure surface centre
$s_zs11cj = r_str / r_bub*$b_zs11;
$s_zs22cj = r_str / r_bub*$b_zs22;
$s_zs33cj = r_str / r_bub*$b_zs33;
$s_zs12cj = r_str / r_bub*$b_zs12;
$s_zs13cj = r_str / r_bub*$b_zs13;
$s_zs23cj = r_str / r_bub*$b_zs23;
//Conjugate stress point on the structure surface
$zs11cj = $s_zs11cj + s_zs11c;
$zs22cj = $s_zs22cj + s_zs22c;
$zs33cj = $s_zs33cj + s_zs33c;
$zs12cj = $s_zs12cj + s_zs12c;
$zs13cj = $s_zs13cj + s_zs13c;
$zs23cj = $s_zs23cj + s_zs23c;
//Plastic variables at the current point
$b = $n11*($zs11cj - $zs11);
$b = $b + $n22*($zs22cj - $zs22);
$b = $b + $n33*($zs33cj - $zs33);
$b = $b + 2.0 * $n12*($zs12cj - $zs12);
$b = $b + 2.0 * $n13*($zs13cj - $zs13);
$b = $b + 2.0 * $n23*($zs23cj - $zs23);
```

```

$bmax = $n11*$b_zs11;
$bmax = $bmax + $n22*$b_zs22;
$bmax = $bmax + $n33*$b_zs33;
$bmax = $bmax + 2.0 * $n12*$b_zs12;
$bmax = $bmax + 2.0 * $n13*$b_zs13;
$bmax = $bmax + 2.0 * $n23*$b_zs23;
$bmax = 2.0*(r_str / r_bub - 1.0)*$bmax;
$c11 = fabs($b / $bmax);
$c1 = 3.0 / (2.0*($M*$M));
$c2 = $c1 / $M *$M;
$c3 = $p - bub_p;
$T = power((((1.0 - AA)*($c3*$c3) + AA*$c2*$sp)), 0.5);
$T = $c3 - kk*(r_str - 1.0) / r_str*$T;
$c4 = nambda0 / r_str;
$c5 = $b_ds11 + $b_ds22 + $b_ds33 + 2.0 * $b_ds12 + 2.0 * $b_ds13;
$c5 = ($c5 + 2.0 * $b_ds23)*nambda0;
$c6 = $c5 / r_str;
//Plastic modulus associated with the conjugate stress state
$Hc = $T*($c3 + $c1*$c5 + r_bub*pc);
$Hc = $Hc - $c3*$c1*$c6;
$Hc = r_str*pc*$Hc;
$Hc = $Hc / (b_lambda - b_kappa);
$Hc = fabs($Hc) / ($c3*$c3 + $c2*$sp);

$H = BB*(fabs(pc*pc*pc)) * r_bub*r_bub*power($c11, psigh);
 $H = $Hc + $H/(b_lambda - b_kappa) / $n;
$dgamma = ($n11*$dzs11 + $n22*$dzs22 + $n33*$dzs33 + 2.0 * $n12*$dzs12;
$dgamma =   $dgamma + 2.0 * $n13*$dzs13 + 2.0 * $n23*$dzs23) / $H;
//Plastic strain rate
$pzde11 = $dgamma*$n11;
$pzde22 = $dgamma*$n22;
$pzde33 = $dgamma*$n33;
$pzde12 = $dgamma*$n12;
$pzde13 = $dgamma*$n13;
$pzde23 = $dgamma*$n23;
//Correctes strain rate
$zde11 = s->stnE_.s11() - $pzde11;
$zde22 = s->stnE_.s22() - $pzde22;
$zde33 = s->stnE_.s33() - $pzde33;
$zde12 = s->stnE_.s12() - $pzde12;
$zde13 = s->stnE_.s13() - $pzde13;
$zde23 = s->stnE_.s23() - $pzde23;
//Correctes stress rate
```

```
    $dzs11 = $zde22*k[0][1] + $zde33*k[0][2] + $zde11*k[0][0];
    $dzs22 = $zde11*k[1][0] + $zde33*k[1][2] + $zde22*k[1][1];
    $dzs33 = $zde11*k[2][0] + $zde22*k[2][1] + $zde33*k[2][2];
    $dzs12 = $zde12*k[3][3] * 2.0;
    $dzs13 = $zde13*k[4][4] * 2.0;
    $dzs23 = $zde23*k[5][5] * 2.0;

    $sum_pzde11 += $pzde11*dVol;
    $sum_pzde22 += $pzde22*dVol;
    $sum_pzde33 += $pzde33*dVol;
    $sum_pzde12 += $pzde12*dVol;
    $sum_pzde13 += $pzde13*dVol;
    $sum_pzde23 += $pzde23*dVol;
}  // $fb > 0.0
s->stnS_.rs11() += $dzs11;
s->stnS_.rs22() += $dzs22;
s->stnS_.rs33() += $dzs33;
s->stnS_.rs12() += $dzs12;
s->stnS_.rs13() += $dzs13;
s->stnS_.rs23() += $dzs23;

//==========================Yild surface drift
if ($fb >= -0.001){
    $p = (s->stnS_.rs11() + s->stnS_.rs22() + s->stnS_.rs33()) / 3.0;
    //Deviator stress
    $ds11 = s->stnS_.rs11() - $p;
    $ds22 = s->stnS_.rs22() - $p;
    $ds33 = s->stnS_.rs33() - $p;
    $ds12 = s->stnS_.rs12();
    $ds13 = s->stnS_.rs13();
    $ds23 = s->stnS_.rs23();
    //Deviator stress wrt the bubble centre
    $b_ds11 = $ds11 - b_ds11c;
    $b_ds22 = $ds22 - b_ds22c;
    $b_ds33 = $ds33 - b_ds33c;
    $b_ds12 = $ds12 - b_ds12c;
    $b_ds13 = $ds13 - b_ds13c;
    $b_ds23 = $ds23 - b_ds23c;

    $J2r = $ds11*$ds11 + $ds22*$ds22 + $ds33*$ds33 + 2.0 * $ds12*$ds12;
    $J2r = ($J2r + 2.0 * $ds13*$ds13 + 2.0 * $ds23*$ds23) / 2.0;
    $J3 = $ds11*$ds22*$ds33 + 2.0*$ds12*$ds13*$ds23 - $ds33*$ds12*$ds12;
    $J3 = $J3 - $ds22*$ds13*$ds13 - $ds11*$ds23*$ds23;
    $J2c = $b_ds11*$b_ds11+$b_ds22 * $b_ds22 + $b_ds33 * $b_ds33;
```

```
$J2c = $J2c + 2.0 * $b_ds12 *$b_ds12 + 2.0 * $b_ds13 * $b_ds13;
$J2c = ($J2c + 2.0 * $b_ds23 * $b_ds23) / 2.0;

//Inner product of deviator stress wrt bubble centre
$sp = 2.0 * $J2c;
//Bubble yield function
post_error = 1.5*$sp / ($M *$M) + ($p - bub_p)*($p - bub_p);
post_error = post_error - r_bub*r_bub * pc*pc;
pre_error=post_error;
UInt loop_flag = 0;
//This checks if the programm has entered the correction loop,
//not to calculate stress gradients twice
//Correction for yield surface drift
while (fabs(post_error) >= 0.001){
   loop_flag = 1;
   $c1 = -12.0 * 1.732*b_mm*(1.0 - b_mm)*b_M;
   $c2 = 2.0 * (1.0 + b_mm);
   $c3 = 3.0 * 1.732*(1.0 - b_mm);
   $c4 = power($J2r, 0.5);
   $c5 = 1.0 / ($c2 + $c3*$J3 / $J2r / $c4);
   $c5 = $c1*$c5*$c5;
   $c6 = $ds12*$ds12 + $ds13 * $ds13 + $ds23 *$ds23;
   $c7 = $ds11*$ds22 + $ds11*$ds33 + $ds22*$ds33;

   double $M11 = (3.0*$ds22*$ds33 - $c7 + $c6) / 3.0;
   $M11 = 1.0 / ($c4*$c4*$c4)*$M11;
   $M11 = $M11 - 3.0 / 2.0 / ($c4*$c4*$c4*$c4*$c4)*$J3*$ds11;
   $M11 = $c5*$M11;

   double $M22 = (3.0*$ds11*$ds33 - $c7 + $c6) / 3.0;
   $M22 = 1.0 / ($c4*$c4*$c4)*$M22;
   $M22 = $M22 - 3.0 / 2.0 / ($c4*$c4*$c4*$c4*$c4)*$J3*$ds22;
   $M22 = $c5*$M22;

   double $M33 = (3.0*$ds22*$ds11 - $c7 + $c6) / 3.0;
   $M33 = 1.0 / ($c4*$c4*$c4)*$M33;
   $M33 = $M33 - 3.0 / 2.0 / ($c4*$c4*$c4*$c4*$c4)*$J3*$ds11;
   $M33 = $c5*$M33;

   double $M12 = -2.0 / ($c4*$c4*$c4)*$ds12*$ds33;
   $M12 = $M12 - 3.0 / ($c4*$c4*$c4*$c4*$c4)*$J3*$ds12;
   $M12 = $c5*$M12;

   double $M13 = -2.0 / ($c4*$c4*$c4)*$ds13*$ds22;
```

```
        $M13 = $M13 - 3.0 / ($c4*$c4*$c4*$c4*$c4)*$J3*$ds13;
        $M13 = $c5*$M13;

        double $M23 = -2.0 / ($c4*$c4*$c4)*$ds23*$ds11;
        $M23 = $M23 - 3.0 / ($c4*$c4*$c4*$c4*$c4)*$J3*$ds23;
        $M23 = $c5*$M23;

        double $J11 = $b_ds11;
        double $J22 = $b_ds22;
        double $J33 = $b_ds33;
        double $J12 = 2.0 * $b_ds12;
        double $J13 = 2.0 * $b_ds13;
        double $J23 = 2.0 * $b_ds23;

        $n11 = -6.0 / ($M*$M*$M) * $J2c*$M11;
        $n11 = $n11 + 3.0 / ($M*$M) * $J11 + 2.0 / 3.0*($p - bub_p);
        $n22 = -6.0 / ($M*$M*$M) * $J2c*$M22;
        $n22 = $n22 + 3.0 / ($M*$M) * $J22 + 2.0 / 3.0*($p - bub_p);
        $n33 = -6.0 / ($M*$M*$M) * $J2c*$M33;
        $n33 = $n33 + 3.0 / ($M*$M) * $J33 + 2.0 / 3.0*($p - bub_p);
        $n12 = -6.0 / ($M*$M*$M) * $J2c*$M12;
        $n12 = $n12 + 3.0 / ($M*$M) * $J12;
        $n13 = -6.0 / ($M*$M*$M) * $J2c*$M13;
        $n13 = $n13 + 3.0 / ($M*$M) * $J13;
        $n23 = -6.0 / ($M*$M*$M) * $J2c*$M23;
        $n23 = $n23 + 3.0 / ($M*$M) * $J23;
        //Normalise stress gradient
        double a1 = k[0][0] * $n11 + k[0][1] * $n22 + k[0][2] * $n33;
        double a2 = k[1][0] * $n11 + k[1][1] * $n22 + k[1][2] * $n33;
        double a3 = k[2][0] * $n11 + k[2][1] * $n22 + k[2][2] * $n33;
        double a4 = k[3][3] * $n12;
        double a5 = k[4][4] * $n13;
        double a6 = k[5][5] * $n23;

        double alpha = $n11*a1 + $n22*a2 + $n33*a3 + $n12*a4 + $n13*a5 + $n23*a6;
        alpha = post_error / alpha;
        s->stnS_.rs11() -= alpha*a1;
        s->stnS_.rs22() -= alpha*a2;
        s->stnS_.rs33() -= alpha*a3;
        s->stnS_.rs12() -= alpha*a4;
        s->stnS_.rs13() -= alpha*a5;
        s->stnS_.rs23() -= alpha*a6;
        $p = (s->stnS_.rs11() + s->stnS_.rs22() + s->stnS_.rs33()) / 3.0;
        //Deviator stress
```

```
        $ds11 = s->stnS_.rs11() - $p;
        $ds22 = s->stnS_.rs22() - $p;
        $ds33 = s->stnS_.rs33() - $p;
        $ds12 = s->stnS_.rs12();
        $ds13 = s->stnS_.rs13();
        $ds23 = s->stnS_.rs23();
        //Deviator stress wrt the bubble centre
        $b_ds11 = $ds11 - b_ds11c;
        $b_ds22 = $ds22 - b_ds22c;
        $b_ds33 = $ds33 - b_ds33c;
        $b_ds12 = $ds12 - b_ds12c;
        $b_ds13 = $ds13 - b_ds13c;
        $b_ds23 = $ds23 - b_ds23c;

        $J2r = $ds11*$ds11 + $ds22*$ds22 + $ds33*$ds33 + 2.0 * $ds12*$ds12;
        $J2r = ($J2r + 2.0 * $ds13*$ds13 + 2.0 * $ds23*$ds23) / 2.0;
        $J3 = $ds11*$ds22*$ds33 + 2.0*$ds12*$ds13*$ds23 - $ds33*$ds12*$ds12;
        $J3 = $J3 - $ds22*$ds13*$ds13 - $ds11*$ds23*$ds23;
        $J2c = $b_ds11*$b_ds11 + $b_ds22 * $b_ds22 + $b_ds33 * $b_ds33;
        $J2c = $J2c + 2.0 * $b_ds12 *$b_ds12 + 2.0 * $b_ds13 * $b_ds13;
        $J2c = ($J2c + 2.0 * $b_ds23 * $b_ds23) / 2.0;
        $sp = 2.0 * $J2c;
        // Bubble yield function
        post_error = 1.5*$sp / ($M *$M) + ($p - bub_p)*($p - bub_p);
        post_error = post_error - r_bub*r_bub * pc*pc;
    }//while
    //Updates the plastic strains  for drift------------------------------------
    double pn = $n11*$n11 + $n22*$n22 + $n33*$n33 + 2.0*$n12*$n12 + 2.0*$n13*$n12;
    pn = pn + 2.0*$n23*$n12;
    $n = power(pn, 0.5);
    if ($n != $n) throw std::runtime_error("bubble: $n=NaN");
    $n11 = $n11 / $n;
    $n22 = $n22 / $n;
    $n33 = $n33 / $n;
    $n12 = $n12 / $n;
    $n13 = $n13 / $n;
    $n23 = $n23 / $n;
    $n = $n*$n;
    //Stress wrt the bubble centre
    $b_zs11 = $zs11 - b_zs11c;
    $b_zs22 = $zs22 - b_zs22c;
    $b_zs33 = $zs33 - b_zs33c;
    $b_zs12 = $zs12 - b_zs12c;
    $b_zs13 = $zs13 - b_zs13c;
```

```
$b_zs23 = $zs23 - b_zs23c;
//Stress wrt the structure surface centre
$s_zs11 = $zs11 - s_zs11c;
$s_zs22 = $zs22 - s_zs22c;
$s_zs33 = $zs33 - s_zs33c;
$s_zs12 = $zs12 - s_zs12c;
$s_zs13 = $zs13 - s_zs13c;
$s_zs23 = $zs23 - s_zs23c;

//Stresses wrt structure surface centre
$s_zs11cj = r_str / r_bub*$b_zs11;
$s_zs22cj = r_str / r_bub*$b_zs22;
$s_zs33cj = r_str / r_bub*$b_zs33;
$s_zs12cj = r_str / r_bub*$b_zs12;
$s_zs13cj = r_str / r_bub*$b_zs13;
$s_zs23cj = r_str / r_bub*$b_zs23;

//Conjugate stress point on structure surface
$zs11cj = $s_zs11cj + s_zs11c;
$zs22cj = $s_zs22cj + s_zs22c;
$zs33cj = $s_zs33cj + s_zs33c;
$zs12cj = $s_zs12cj + s_zs12c;
$zs13cj = $s_zs13cj + s_zs13c;
$zs23cj = $s_zs23cj + s_zs23c;

//Plastic variables at current point>
$b = $n11*($zs11cj - $zs11);
$b = $b + $n22*($zs22cj - $zs22);
$b = $b + $n33*($zs33cj - $zs33);
$b = $b + 2.0 * $n12*($zs12cj - $zs12);
$b = $b + 2.0 * $n13*($zs13cj - $zs13);
$b = $b + 2.0 * $n23*($zs23cj - $zs23);

$bmax = $n11*$b_zs11;
$bmax = $bmax + $n22*$b_zs22;
$bmax = $bmax + $n33*$b_zs33;
$bmax = $bmax + 2.0 * $n12*$b_zs12;
$bmax = $bmax + 2.0 * $n13*$b_zs13;
$bmax = $bmax + 2.0 * $n23*$b_zs23;
$bmax = 2.0*(r_str / r_bub - 1.0)*$bmax;
$c11 = fabs($b / $bmax);

$c1 = 3.0 / (2.0*($M*$M));
$c2 = $c1 / $M *$M;
```

```
   $c3 = $p - bub_p;
   $T = power((((1.0 - AA)*($c3*$c3) + AA*$c2*$sp)), 0.5);
   $T = $c3 - kk*(r_str - 1.0) / r_str*$T;
   $c4 = nambda0 / r_str;
   $c5 = $b_ds11 + $b_ds22 + $b_ds33 + 2.0 * $b_ds12 + 2.0 * $b_ds13;
   $c5 = ($c5 + 2.0 * $b_ds23)*nambda0;
   $c6 = $c5 / r_str;
   //plastic modulus associated with the conjugate stress state
   $Hc = $T*($c3 + $c1*$c5 + r_bub*pc);
   $Hc = $Hc - $c3*$c1*$c6;
   $Hc = r_str*pc*$Hc;
   $Hc = $Hc / (b_lambda - b_kappa);
   $Hc = fabs($Hc) / ($c3*$c3 + $c2*$sp);

   $H = BB*(fabs(pc*pc*pc)) * r_bub*r_bub*power($c11, psigh);
   $H = $Hc + $H/(b_lambda - b_kappa) / $n;
   }//-----------------------------------------------
   $dgamma = $n11*$dzs11 + $n22*$dzs22 + $n33*$dzs33 + 2.0 * $n12*$dzs12
   $dgamma = ($dgamma + 2.0 * $n13*$dzs13 + 2.0 * $n23*$dzs23) / $H;
   //Plastic strain rate
   $pzde11 = $dgamma*$n11;
   $pzde22 = $dgamma*$n22;
   $pzde33 = $dgamma*$n33;
   $pzde12 = $dgamma*$n12;
   $pzde13 = $dgamma*$n13;
   $pzde23 = $dgamma*$n23;
   //Total plastic volumetrci strain after the drift correction
   $sum_pzde11 += $pzde11;
   $sum_pzde22 += $pzde22;
   $sum_pzde33 += $pzde33;
   $sum_pzde12 += $pzde12;
   $sum_pzde13 += $pzde13;
   $sum_pzde23 += $pzde23;
}//($fb >= 0.00001)
//=====================================End of the drift correction
if (s->sub_zone_ == s->total_sub_zones_ - 1) {
   double d1dVol = 0.1;
   $zde11 = $sum_zde11 *d1dVol;
   $sum_zde11 = 0.0;
   $zde22 = $sum_zde22 *d1dVol;
   $sum_zde22 = 0.0;
   $zde33 = $sum_zde33 *d1dVol;
   $sum_zde33 = 0.0;
   $zde12 = $sum_zde12 *d1dVol;
```

```
$sum_zde12 = 0.0;
$zde13 = $sum_zde13 *d1dVol;
$sum_zde13 = 0.0;
$zde23 = $sum_zde23 *d1dVol;
$sum_zde23 = 0.0;
vertical_strain = vertical_strain + $zde22 * 100;
volumetric_strain = volumetric_strain + ($zde11 + $zde22 + zde33) * 100;
if ($fb > 0.0001) {
   $pzde11 = $sum_pzde11 *d1dVol;
   $sum_pzde11 = 0.0;
   $pzde22 = $sum_pzde22 *d1dVol;
   $sum_pzde22 = 0.0;
   $pzde33 = $sum_pzde33 *d1dVol;
   $sum_pzde33 = 0.0;
   $pzde12 = $sum_pzde12 *d1dVol;
   $sum_pzde12 = 0.0;
   $pzde13 = $sum_pzde13 *d1dVol;
   $sum_pzde13 = 0.0;
   $pzde23 = $sum_pzde23 *d1dVol;
   $sum_pzde23 = 0.0;
   //Isotropic and kinematic hardening
   $pv_zde = $pzde11 + $pzde22 + $pzde33;// plastic volumetric strain rate
   //Equivalent plastic shear strain
   $pq_zde = $pzde11 *$pzde11 + $pzde22*$pzde22 + $pzde33*$pzde33;
   $pq_zde = $pq_zde + $pzde12*$pzde12 + $pzde13*$pzde13 + $pzde23*$pzde23;
   $pq_zde = power((2.0 / 3.0*$pq_zde), 0.5);
   q_strain = q_strain + $pq_zde * 100.0;
   $dpc = $pv_zde / (b_lambda - b_kappa) *fabs(pc);
   $pq_zde = power(((1.0 - AA)*$pv_zde*$pv_zde + AA*$pq_zde*$pq_zde), 0.5);
   // destruction strain rate
   $dr_str = (-1.0)*kk / (b_lambda - b_kappa)*(r_str - 1.0)*$pq_zde;
   //Kinematic hardening(update the bubble and str surface centres)
   //Translation rate of the str surface centre
   //Change of the str surface centre in the deviator space,
   double $ds = nambda0*((r_str - 1.0)*$dpc + pc*$dr_str);
   // change of str surface centre in p axis
   double $s_dp = r_str*$dpc + pc*$dr_str;
   pc = pc + $dpc; //Isotropic hardening
   r_str = r_str + $dr_str; //Update the str surface size
   //Change of the str surface centre in the general stress space
   $s_dzs11c = $s_dp;
   $s_dzs22c = $s_dp;
   $s_dzs33c = $s_dp;
   $s_dzs12c = $ds;
```

```
    $s_dzs13c = $ds;
    $s_dzs23c = $ds;
    //Stress rate wrt the str surface centre
    $p = (s->stnS_.rs11() + s->stnS_.rs22() + s->stnS_.rs33()) / 3.0;
    if ($p >= 0.0) $p = -0.01;\\Avoids tensile stresses
    //Uses corrected stress to calculate new bubble centre
    //Recalculates deviator stresses
    $ds11 = s->stnS_.rs11() - $p;
    $ds22 = s->stnS_.rs22() - $p;
    $ds33 = s->stnS_.rs33() - $p;
    $ds12 = s->stnS_.rs12();
    $ds13 = s->stnS_.rs13();
    $ds23 = s->stnS_.rs23();
    //Recalculates deviator stress wrt the bubble centre
    $b_ds11 = $ds11 - b_ds11c;
    $b_ds22 = $ds22 - b_ds22c;
    $b_ds33 = $ds33 - b_ds33c;
    $b_ds12 = $ds12 - b_ds12c;
    $b_ds13 = $ds13 - b_ds13c;
    $b_ds23 = $ds23 - b_ds23c;
    //Recalculates stress wrt the bubble centre
    $b_zs11 = s->stnS_.rs11() - b_zs11c; //dvazhdi opredelyatesya
    $b_zs22 = s->stnS_.rs22() - b_zs22c;
    $b_zs33 = s->stnS_.rs33() - b_zs33c;
    $b_zs12 = s->stnS_.rs12() - b_zs12c;
    $b_zs13 = s->stnS_.rs13() - b_zs13c;
    $b_zs23 = s->stnS_.rs23() - b_zs23c;
    //Recalculates stress wrt the str surface centre
    $s_zs11 = s->stnS_.rs11() - s_zs11c;
    $s_zs22 = s->stnS_.rs22() - s_zs22c;
    $s_zs33 = s->stnS_.rs33() - s_zs33c;
    $s_zs12 = s->stnS_.rs12() - s_zs12c;
    $s_zs13 = s->stnS_.rs13() - s_zs13c;
    $s_zs23 = s->stnS_.rs23() - s_zs23c;
    //Recalculates conjugate stress wrt the str surface centre
    $s_zs11cj = r_str / r_bub*$b_zs11;
    $s_zs22cj = r_str / r_bub*$b_zs22;
    $s_zs33cj = r_str / r_bub*$b_zs33;
    $s_zs12cj = r_str / r_bub*$b_zs12;
    $s_zs13cj = r_str / r_bub*$b_zs13;
    $s_zs23cj = r_str / r_bub*$b_zs23;
    //Recalculates conjugate stress on the str surface
    $zs11cj = $s_zs11cj + s_zs11c;
    $zs22cj = $s_zs22cj + s_zs22c;
```

```
    $zs33cj = $s_zs33cj + s_zs33c;
    $zs12cj = $s_zs12cj + s_zs12c;
    $zs13cj = $s_zs13cj + s_zs13c;
    $zs23cj = $s_zs23cj + s_zs23c;
    //Translation rate of the bubble centre
    $c7 = $dr_str / r_str;
    $c8 = $dpc / pc + $c7;
    $b_dzs11c = ($dzs11 - $s_dzs11c) - $s_zs11*$c8 + $b_zs11*$c7;
    $b_dzs22c = ($dzs22 - $s_dzs22c) - $s_zs22*$c8 + $b_zs22*$c7;
    $b_dzs33c = ($dzs33 - $s_dzs33c) - $s_zs33*$c8 + $b_zs33*$c7;
    $b_dzs12c = ($dzs12 - $s_dzs12c) - $s_zs12*$c8 + $b_zs12*$c7;
    $b_dzs13c = ($dzs13 - $s_dzs13c) - $s_zs13*$c8 + $b_zs13*$c7;
    $b_dzs23c = ($dzs23 - $s_dzs23c) - $s_zs23*$c8 + $b_zs23*$c7;
    $c9 = $n11*$b_dzs11c + $n22*$b_dzs22c + $n33*$b_dzs33c;
    $c9 = $c9 + 2.0*$n12*$b_dzs12c + 2.0*$n13*$b_dzs13c + 2.0*$n23*$b_dzs23c;
    $c10 = $n11*($zs11cj - s->stnS_.rs11()) + $n22*($zs22cj - s->stnS_.rs22());
    $c10 = $c10 + $n33*($zs33cj - s->stnS_.rs33());
    $c10 = $c10 + 2.0 * $n12*($zs12cj - s->stnS_.rs12());
    $c10 = $c10 + 2.0 * $n13*($zs13cj - s->stnS_.rs13());
    $c10 = $c10 + 2.0 * $n23*($zs23cj - s->stnS_.rs23());

    $b_dzs11c = $c9 / $c10*($zs11cj - s->stnS_.rs11());
    $b_dzs22c = $c9 / $c10*($zs22cj - s->stnS_.rs22());
    $b_dzs33c = $c9 / $c10*($zs33cj - s->stnS_.rs33());
    $b_dzs12c = $c9 / $c10*($zs12cj - s->stnS_.rs12());
    $b_dzs13c = $c9 / $c10*($zs13cj - s->stnS_.rs13());
    $b_dzs23c = $c9 / $c10*($zs23cj - s->stnS_.rs23());

    $b_dzs11c = $s_dzs11c + (b_zs11c - s_zs11c)*$c8 + $b_dzs11c;
    $b_dzs22c = $s_dzs22c + (b_zs22c - s_zs22c)*$c8 + $b_dzs22c;
    $b_dzs33c = $s_dzs33c + (b_zs33c - s_zs33c)*$c8 + $b_dzs33c;
    $b_dzs12c = $s_dzs12c + (b_zs12c - s_zs12c)*$c8 + $b_dzs12c;
    $b_dzs13c = $s_dzs13c + (b_zs13c - s_zs13c)*$c8 + $b_dzs13c;
    $b_dzs23c = $s_dzs23c + (b_zs23c - s_zs23c)*$c8 + $b_dzs23c;
    //New bubble centre
    b_zs11c = b_zs11c + $b_dzs11c;
    b_zs22c = b_zs22c + $b_dzs22c;
    b_zs33c = b_zs33c + $b_dzs33c;
    b_zs12c = b_zs12c + $b_dzs12c;
    b_zs13c = b_zs13c + $b_dzs13c;
    b_zs23c = b_zs23c + $b_dzs23c;
    //New bubble centre on the p-axis
    bub_p = (b_zs11c + b_zs22c + b_zs33c) / 3.0;
    //New bubble centre in deviator stress space
```

```
      b_ds11c = b_zs11c - bub_p;
      b_ds22c = b_zs22c - bub_p;
      b_ds33c = b_zs33c - bub_p;
      b_ds12c = b_zs12c;
      b_ds13c = b_zs13c;
      b_ds23c = b_zs23c;
      //New centre of the structure surface
      s_zs11c += $s_dzs11c;
      s_zs22c += $s_dzs22c;
      s_zs33c += $s_dzs33c;
      s_zs12c += $s_dzs12c;
      s_zs13c += $s_dzs13c;
      s_zs23c += $s_dzs23c;
      s_p = (s_zs11c + s_zs22c + s_zs33c) / 3.0;

      s_ds11c = s_zs11c - s_p;
      s_ds22c = s_zs22c - s_p;
      s_ds33c = s_zs33c - s_p;
      s_ds12c = s_zs12c;
      s_ds13c = s_zs13c;
      s_ds23c = s_zs23c;
   }  // $fb > 0.0
   //Updates the current elastic moduli
   $p = (s->stnS_.rs11() + s->stnS_.rs22() + s->stnS_.rs33()) / 3.0;
   $q = s->stnS_.rs33() - s->stnS_.rs11();
   b_mod = fabs($p) / b_kappa + b_bod0;
   s_mod = 3.0*b_mod*(1.0 - 2.0*b_poss) / (2.0*(1.0 + b_poss));
}//(s->sub_zone_ == s->total_sub_zones_ - 1)
```

Appendix C

Publications

This work results in the following publications:

Derbin, Y., Walker, J., Wanatowski, D., and Marshall, A. (2014). Soviet experience of underground coal gasification focusing on surface subsidence. In Proceedings of the 33rd International Conference on Ground Control in Mining, China, Beijing, October 24–26, pp. 166–167.

Derbin, Y., Walker, J., Wanatowski, D., and Marshall, A. (2015). Use of borehole data for input in numerical model of surface subsidence caused by mine collapse, In Abstract Proceedings of the 7th International Conference on Mining Science and Technology, China, Xuzhou, April 26–29, p. 377.

Derbin, Y., Walker, J., Wanatowski, D., and Marshall, A. (2015). Soviet experience of underground coal gasification focusing on surface subsidence. Journal of Zhejiang University SCIENCE A, 16(10):839–850.

Derbin, Y., Walker, J., Wanatowski, D., and Marshall, A. (2016). Issues related to goaf modeling. In Proceedings of the 19th Southeast Asian Geotechnical Conference and 2nd AGSSEA Conference, Malaysia, Kuala Lumpur, Eds.: Chan, S.H., Ooi, T.A., Ting, W.H., Chan, S.F., and Ong D., May 31 - June 3, pp. 1015–1021.

Derbin, Y., Walker, J., Wanatowski, D., and Marshall, A. (2018). Numerical Simulation of Surface Subsidence After the Collapse of a Mine. In Proceedings of the 5th GeoChina International Conference 2018 Civil Infrastructures Confronting Severe Weathers and Climate Changes:

From Failure to Sustainability. Eds.: Sevi A., Neves, J., and Hand Zhao, H., China, HangZhou, July 23–25, pp. 1–8.

Derbin, Y., Walker, J., Wanatowski, D., and Marshall, A. (2018). Implementation of advanced constitutive models for the prediction of surface subsidence after underground mineral extraction. In Proceedings of the China Europe Conference on Geotechnical Engineering. Eds.: Wu, W. and Yu, HS, August 13–16, pp. 320–323.

Derbin, Y., Walker, J. and Wanatowski, D. (2018). Modelling surface subsidence during underground coal gasification. Deep Rock Mechanics: From Research to Engineering. In Proceedings of the International Conference on Geo-Mechanics, Geo-Energy and Geo-Resources I3G 2018. Eds.: Xie H., Jian Zhao J., and Ranjith, P.G., September 14-16, pp 1–6.

Derbin, Y., Walker, J., Wanatowski, D., and Marshall, A. (2019). Numerical simulation of surface subsidence after the collapse of a mine. Enhancements in Applied Geomechanics, Mining, and Excavation Simulation and Analysis. Springer International Publishing, Charm, pp. 80–97.